THÈSE

Pour obtenir le grade de

DOCTEUR DE L'UNIVERSITÉ GRENOBLE ALPES

École doctorale : PHYS - Physique
Spécialité : Physique Théorique
Unité de recherche : Institut Néel

Etude des propriétés électroniques et structurales des nickélates supraconducteurs par des méthodes ab initio : de la théorie de la fonctionnelle de la densité à l'approximation GW

Investigation of the electronic and structural properties of superconducting nickelates by first principles methods: from density functional theory to the GW approximation

Présentée par :

Jean-Baptiste DE VAULX

Direction de thèse :

Valerio OLEVANO DIRECTEUR DE RECHERCHE, CNRS DELEGATION ALPES	Directeur de thèse
Andres CANO DIRECTEUR DE RECHERCHE, CNRS DELEGATION ALPES	Co-directeur de thèse

Rapporteurs :

FRANCESCO SOTTILE
INGENIEUR HDR, ECOLE POLYTECHNIQUE
ALEXANDRE GLOTER
DIRECTEUR DE RECHERCHE, CNRS DELEGATION ILE-DE-FRANCE SUD

Thèse soutenue publiquement le **12 décembre 2025**, devant le jury composé de :

SOPHIE DE BRION, PROFESSEURE DES UNIVERSITES, UNIVERSITE GRENOBLE ALPES	Présidente
FRANCESCO SOTTILE, INGENIEUR HDR, ECOLE POLYTECHNIQUE	Rapporteur
ALEXANDRE GLOTER, DIRECTEUR DE RECHERCHE, CNRS DELEGATION ILE-DE-FRANCE SUD	Rapporteur
MATTEO D'ASTUTO, DIRECTEUR DE RECHERCHE, CNRS DELEGATION ALPES	Examinateur

Template adapted from https://github.com/JeanCollomb/Template_rapport_these/tree/master.

Final version (13/03/2026)

A ma grand-mère

Remerciements

Cette thèse, qui avait été précédée par mon stage de M2, fut une longue et belle aventure, portant sur un sujet très dynamique et compétitif. Je voudrais commencer par remercier mes deux encadrants, Andrés Cano et Valerio Olevano, qui m'ont fait confiance puis m'ont accompagné et guidé tout au long de ces trois années (presque quatre !), en faisant preuve d'une grande patience et en me laissant pleine liberté pour travailler à ma façon, sachant me donner des coups de pouces quand il le fallait sans jamais me materner. Je retiendrai évidemment des centaines de choses, mais je n'en citerai que quelques-unes pour chacun. Andrés, je retiendrai particulièrement l'un de tes mantras : «ce qui compte, c'est la tendance», et le fait que l'on peut faire de la recherche fondamentale avec une feuille de papier collée sur un écran d'ordinateur. J'espère que tu auras réussi à assouplir quelque peu mon esprit parfois trop rigoureux, sans pour autant me faire renoncer à la rigueur scientifique si chère à Valerio. Valerio, je retiendrai ta passion pour la physique au sens large et en particulier ton attachement (presque) sans concession à la description ab initio, sans artifice ni tricherie. Véritable puits de science et d'anecdotes, je me souviendrai longtemps des après-midis à discuter dans ton bureau. J'espère d'ailleurs que ce n'est pas fini et que nous pourrons continuer à converser longuement des fonctions de Green ou de bien d'autres sujets. J'ai apprécié votre complémentarité, entre la profonde connaissance de la physique des matériaux et de la supraconductivité apportée par Andrés, associée à l'expertise de Valerio en théorie des perturbations à N-corps. Au-delà de l'aspect scientifique, je retiendrai aussi les discussions éclectiques sur des sujets aussi variés que l'écologie, la nouvelle place de l'IA dans notre monde, l'actualité cycliste ou rugbystique du moment, la traversée des Alpes d'Hannibal, l'histoire de la Savoie ou encore les exploits alpins d'Edward Whymper.

Ma thèse aurait été très différente sans l'arrivée de Quintin Meier dans notre groupe, avec qui j'ai travaillé de manière très proche, en particulier sur le couplage électron-phonon. A de nombreuses reprises tu as su me pousser à aller au-delà de ce que j'avais envisagé initialement, avec ton esprit d'initiative et ton enthousiasme pour notre sujet. Par ailleurs, ta manière simple et intuitive d'appréhender et d'expliquer la physique m'a souvent aidé à m'y retrouver au sein du monde merveilleux mais complexe de la matière condensée. Tu n'es pas tellement un «simple man», comme tu aimes à le répéter avec humour mais surtout quelqu'un d'humble qui sait se mettre au niveau de ses interlocuteurs. Evidemment, je retiendrai les aventures vécues ensemble en montagne, avec en point d'orgue notre traversée du Grand Pic de Belledonne, décidée sur un coup de tête un lundi matin en arrivant au labo. En deux mots : merci, brudi.

Au sein de l'institut Néel, je voudrais également remercier Xavier Blase pour son expertise en calcul ab initio, Pierre Toulemonde pour les discussions autour de l'actualité des nickélates, Jeanne Colbois pour le dynamisme qu'elle a insufflé lors de son arrivée dans l'équipe TMC, Patrick Belmain pour la gestion du cluster de calcul et enfin Khaled, notre DJ/chanteur/ballon d'or, toujours jovial et volontaire, qui m'a aidé pendant la dernière ligne droite de ce doctorat. Enfin, une pensée pour Laurent Saminadayar qui m'avait préparé au concours de l'école doctorale il y a quatre ans. Je voudrais également remercier Marcello Civelli pour son accueil lors de ma visite au LPS en décembre 2023 et le temps qu'il m'a consacré, même si notre projet n'a finalement pas abouti.

Merci à Virginie Simonet et Jean-Philippe Poizat pour les discussions et les initiatives portant sur la sobriété dans le monde de la recherche, la dynamique que vous avez insufflé autour de cette thématique à l'institut Néel m'a permis de trouver des espaces pour approfondir ces questionnements importants qui sinon seraient restés superficiels. Merci justement aux doctorants avec qui j'ai pu discuter de ces sujets : Océane, Ali, Coline, Lucien, Raphaël et Elisa. Par ailleurs, je voudrais remercier Elodie et tous les membres de l'administration pour leur implication auprès des non-permanents et en particulier ceux affectés par les procédures liées à la ZRR.

Je souhaiterais ensuite remercier les membres de mon jury Francesco Sottile, Alexandre Gloter, Matteo d'Astuto et Sophie de Brion pour leur relecture attentive de mon manuscrit, ainsi que pour leur bienveillance lors de ma soutenance. Je souhaiterais particulièrement remercier Sophie, également membre de mon CSI, pour ses conseils notamment en ce qui concerne l'enseignement.

Impossible de ne pas évoquer les membres de notre petite promotion de doctorants : Armand, Maxime, Abel, Kyle, Bilal, Quentin, Nils, Arthur, Romy, Johannes, Jana, Justin, Rémy, Matthieu, Chafic, Florent, Raphaël et bien sûr Julien, qui bien que non-doctorant est sans doute les plus physicien d'entre nous ! Merci pour les repas partagés à H2, les interminables discussions autour d'un café ou d'une pinte, les expéditions par monts et par vaux à ski, en crampons ou à vélo, les trails et les triathlons auxquels nous avons participés ensemble, et les parties de foot des soirs d'été. Un clin d'œil aussi à Gaëtan, comme quoi la physique peut devenir une affaire de famille... certes moins importante que le parapente ! Un grand merci également à mes colocs successifs au cours de ces années grenobloises : Majid, Saddek, Sepp, Maria, Matthias, Adrien, Ashvin et Melchior, ainsi qu'à mes amis et en particulier Gatien, Côme, Olivier, les deux Dorian, Manu, Estelle, David, Hyppolite et Chris.

Enfin, le mot de la fin revient à mes parents, qui malgré mes changements de direction au cours de mes études m'ont toujours soutenu dans mon choix de poursuivre vers la recherche fondamentale. Papa, je sais que je te dois en grande partie mon goût pour la science... alors même si cette thèse te paraîtra sans doute un peu obscure, elle t'est aussi dédiée.

Abstract

The discovery of superconductivity in a neodymium nickelate in thin film under a critical temperature of 15 K in 2019 has triggered great excitement around these materials. Made of an infinite pattern of alternating nickel oxide layers and rare earth layers, they present interesting analogies with cuprates, the archetype of unconventional superconductors, whose underlying mechanism has not yet been understood. In particular, the nickel atom presents an electronic configuration d^9 similar to the one of copper in the latter, suggesting that the mechanism responsible for superconductivity in these so-called "infinite-layer" nickelates and in cuprates might be analogous. Superconductivity was then observed in other nickelates, including some which share less similarities with cuprates. In particular, the bilayer and trilayer compounds of the Ruddlesden-Popper serie present far higher critical temperatures, respectively 80 K and 30 K, and different electronic configurations. This is the real interest of these materials: they offer a new opportunity of understanding the phenomenon of unconventional superconductivity, with a different perspective. In this thesis, electronic and structural properties of some of these nickelates have been investigated by the means of ab initio calculations. Two methods have been used, namely density functional theory (DFT) and many-body perturbation theory in the GW approximation, the latter being more cumbersome but more adapted to describe electronic correlations. A first work has shown that the conventional electron-phonon interaction cannot explain the critical temperatures observed in the infinite-layer compounds, a fact that was suggested in the literature precisely by the means of GW calculations. A second work has investigated the GW electronic structure of the bilayer lanthanum nickelate, under pressure and epitaxial strain. This work has highlighted some key differences between the DFT and GW electronic structures, knowing that the description of the superconducting instability strongly depends on the details of the latter. Finally, a study at the DFT level of the single-layer lanthanum nickelate, in which superconductivity has not yet been measured, has enabled to show two things: first that barium doping has the effect to stabilize the tetragonal phase analogously to pressure, knowing that this high-symmetry structure seems necessary to the emergence of superconductivity in the bilayer and trilayer compounds, then that considering the spins enables to reproduce the non-trivial behavior of the lattice parameters experimentally observed with respect to barium doping, highlighting the singular magnetic character of this compound in comparison with the other members of the Ruddlesden-Popper serie.

Résumé

La découverte de la supraconductivité dans un nickélate de néodyme en couche mince en-dessous d'une température critique de 15 K en 2019 a provoqué une grande effervescence autour de ces matériaux. Constitués d'une alternance infinie de couches d'oxyde de nickel et de couches de terre rare, ils présentent d'intéressantes analogies avec les cuprates, des oxydes de cuivres étudiés depuis les années 80 constituant l'archétype des supraconducteurs non-conventionnels, et dont le mécanisme sous-jacent reste à ce jour inexpliqué. En particulier, l'atome de nickel présente une configuration électronique d^9 similaire à celle du cuivre dans ces derniers, laissant à penser que les mécanismes responsables de la supraconductivité dans ces nickélates dit "à infinité de couches" et dans les cuprates pourraient être analogues. La supraconductivité a ensuite été observée dans d'autres nickélates, y compris certains dont la ressemblance avec les cuprates est plus lointaine. En particulier, les composés bicouche et tricouche appartenant à la série de Ruddlesden-Popper présentent des températures critiques bien plus hautes, respectivement de l'ordre de 80 et 30 K, et des configurations électroniques différentes. C'est tout l'intérêt de ces nouveaux matériaux : ils offrent une nouvelle opportunité de comprendre le phénomène de supraconductivité non-conventionnelle, sous un angle nouveau. Dans cette thèse, les propriétés électroniques et structurales de certains de ces nickélates ont été étudiées au moyen de calculs ab initio. Deux méthodes ont été principalement employées, à savoir la théorie de la fonctionnelle de la densité (DFT) et la théorie des perturbations à N-corps dans l'approximation GW, cette dernière étant plus lourde à mettre en œuvre, mais aussi plus adaptée pour décrire les corrélations électroniques. Un premier travail a montré que l'interaction électron-phonon conventionnelle ne pouvait être responsable des températures critiques observées dans les composés à infinité de couches, ce qui avait pourtant été suggéré dans la littérature justement au moyen de calculs GW. Un deuxième travail a porté sur le composé bicouche au lanthane, sous pression ou contrainte épitaxiale, décrivant avec précision sa structure électronique au niveau GW. Ce travail a permis de mettre en exergue certaines différences clés entre les structures électroniques DFT et GW, sachant que la description de l'instabilité supraconductrice dépend fortement des détails de celles-ci. Enfin, un travail mené au niveau DFT sur le composé monocouche au lanthane, dans lequel la supraconductivité n'a à ce jour pas été détectée, a permis de montrer deux choses: tout d'abord qu'un dopage au baryum avait pour effet de stabiliser la phase tétragonale de manière analogue à la pression, sachant que cette structure de haute symétrie semble nécessaire à l'émergence de la supraconductivité dans les composés bicouche et tricouche, ensuite que la prise en compte des spins permettait de reproduire le comportement non-trivial des paramètres de maille en fonction du dopage observé expérimentalement, soulignant le caractère magnétique singulier de ce composé par rapport aux autres membres de la série de Ruddlesden-Popper.

Contents

Remerciements v

Abstract ix

Résumé x

Contents xi

1 Introduction 1

1.1 Superconductivity in a nutshell . . . 1
1.2 Historical overview . . . 2
1.3 Nickelates . . . 4
1.3.1 Ruddlesden-Popper and layered square-planar series . . . 4
1.3.2 Chronology . . . 9
1.3.3 Further comparison with cuprates . . . 10
1.4 Motivation . . . 13
1.5 Organization of the manuscript . . . 14
References . . . 15

I Theoretical framework and methods 19

2 The quantum many-electron problem 21

2.1 The many-body hamiltonian . . . 22
2.2 The many-body wavefunction . . . 23
2.2.1 Antisymmetry condition for fermions . . . 23
2.2.2 Exponential wall . . . 23
2.3 Methods . . . 24
2.3.1 Independent electrons . . . 25
2.3.2 Hartree approximation and self-consistent field . . . 25
2.3.3 Hartree-Fock approximation and exchange . . . 27
References . . . 29

3 Density Functional Theory 31

3.1 General idea . . . 31
3.2 Hohenberg-Kohn theorem . . . 32
3.2.1 One-to-one correspondence between V_{ext}, Ψ and n . . . 32
3.2.2 Variational principle . . . 33
3.3 The Kohn-Sham method . . . 34
3.3.1 Interpretation of the Kohn-Sham eigenvalues . . . 35
3.4 Exchange-correlation functionals . . . 36
3.4.1 Local density approximation (LDA) . . . 37
3.4.2 Generalized gradient approximation (GGA) and PBE . . . 37
3.4.3 Hybrid functionals and HSE06 . . . 38

3.4.4 Wrap-up on functionals . . . 38
References . . . 40

4 Many-body perturbation theory **41**
4.1 Green's functions . . . 41
4.1.1 Definition . . . 41
4.1.2 Lehmann representation in frequency domain . . . 42
4.2 Many-body perturbation theory . . . 43
4.2.1 Self-energy and quasiparticles . . . 43
4.2.2 Dyson equation . . . 44
4.2.3 Spectral function . . . 45
4.2.4 Quasiparticle energies . . . 47
4.2.5 Quasiparticle lifetime . . . 49
4.2.6 Quasiparticle equation . . . 49
4.3 Photoemission and inverse photoemission . . . 49
References . . . 51

5 The *GW* approximation **53**
5.1 On the importance of screening . . . 53
5.2 Hedin's equations . . . 54
5.3 RPA-*GW* approximation . . . 56
5.3.1 Random-phase approximation to the polarizability . . . 56
5.3.2 *GW* approximation to the self-energy . . . 56
5.4 One-shot G_0W_0 . . . 58
5.5 *GW* in practice . . . 59
5.5.1 Starting point . . . 59
5.5.2 Frequency dependence of W . . . 59
5.6 Discussions . . . 62
References . . . 64

6 Theories and methods for superconductivity **67**
6.1 BCS theory . . . 67
6.2 Eliashberg theory . . . 69
6.2.1 Electron-phonon coupling . . . 69
6.2.2 McMillan–Allen-Dynes formula . . . 70
6.3 Unconventional superconductivity . . . 71
References . . . 72

II Research work on nickelates **75**

7 Electron-phonon coupling in the infinite-layer nickelates RNiO$_2$ **77**
7.1 Introduction . . . 77
7.2 Inconsistency of electronic structures with respect to literature . . . 78
7.2.1 Slow convergence of the self-energy with the HL PPM . . . 78
7.2.2 On and off-shell approximations . . . 80
7.3 Methodology for electron-phonon coupling calculations . . . 81
7.4 Study for different plasmon-pole models . . . 82
7.4.1 Hole-doped $Nd_{0.8}Sr_{0.2}NiO_2$ . . . 82
7.4.2 Parent compounds $NdNiO_2$ and $LaNiO_2$ . . . 85
7.5 Evolution with respect to pressure . . . 86
7.5.1 Hole-doped $Nd_{0.8}Sr_{0.2}NiO_2$ . . . 87

7.5.2 Parent compounds $NdNiO_2$ and $LaNiO_2$ . . . 87
7.6 Variation with respect to the starting DFT functional . . . 88
7.6.1 Electronic structure . . . 89
7.6.2 Phonons . . . 90
7.7 Conclusion . . . 91
References . . . 92

Appendix . . . 95
7.A Technical details . . . 95

8 *GW* electronic structure of the bilayer nickelate $La_3Ni_2O_7$ 97
8.1 Introduction . . . 97
8.2 Calculation details . . . 98
8.2.1 Numerical methods . . . 98
8.2.2 Crystal structure and Brillouin zone . . . 99
8.3 Results . . . 100
8.3.1 Electronic structure at 29.5 GPa . . . 100
8.3.2 Evolution with pressure . . . 105
8.3.3 $La_3Ni_2O_7$ under epitaxial strain . . . 107
8.4 Conclusions . . . 108
References . . . 109

Appendix . . . 112
8.A Convergence in the number of bands . . . 112
8.B Orbital character projection: pure atomic orbitals vs Wannier functions . . . 112
8.C Fermi energy calculation: standard bisection vs DOS integration . . . 114
8.D Crystal structures . . . 115
8.D.1 Influence of the tilt: *Amam* vs $I4/mmm$ bandplots . . . 116
8.E Bloch state plots . . . 118
8.F Additional orbital character projections . . . 118

9 Pressure, doping and magnetism in the single-layer nickelate La_2NiO_4 121
9.1 Introduction . . . 121
9.2 Methods . . . 122
9.3 Pressure and compositional effects . . . 123
9.3.1 Pressure . . . 123
9.3.2 Chemical pressure via Ba substitution . . . 124
9.4 Electronic structure . . . 125
9.4.1 Parent compound La_2NiO_4 . . . 125
9.4.2 Doped compound $La_{1.5}Ba_{0.5}NiO_4$ . . . 126
9.5 Magnetism . . . 128
9.5.1 Parent compound La_2NiO_4 . . . 128
9.5.2 Doped compound $La_{1.5}Ba_{0.5}NiO_4$ . . . 129
9.6 Discussion . . . 130
9.7 Conclusions . . . 131
References . . . 134

10 Additional results and perspectives 135
10.1 Self-doping tendency . . . 135
10.1.1 An effect triggered by both *GW* corrections and pressure . . . 135
10.1.2 Relative and absolute *GW* corrections . . . 136
10.1.3 Sensitiveness to internal atomic positions . . . 137
10.1.4 Band engineering . . . 138

10.1.5 Sensitiveness to the tilt of the octahedra . . . 139
10.1.6 Electron-phonon coupling . . . 139
10.2 Spectral weights behavior . . . 141
10.3 Stability of the *GW* corrections . . . 142
References . . . 143

Conclusion **145**
References . . . 148
Conclusion (en français) **149**

List of publications **153**
List of symbols **155**
List of abbreviations **157**

1 Introduction

My best dreams are those where I am skiing downhill in good powder snow.

Karl Alexander Müller,
co-discoverer of superconductivity in the cuprates

This introductory chapter explains the scientific context in which this thesis took place. It starts with a short introduction on superconductivity and its history, with a specific attention to cuprates. The next section is dedicated to nickelates, details their structure and properties, the chronology of the discovery of superconductivity in them and their link to cuprates. Finally, the motivation of this PhD thesis is given, and the organization of the manuscript explained.

1.1 Superconductivity in a nutshell

Superconductivity is a physical phenomenon in which a material conducts the electrical current without any resistance, hence its name. Beside the vanishing resistivity, the other hallmark which characterizes superconductivity is the Meissner effect involving the expulsion of a magnetic field from the superconductor, often demonstrated in experiments where a little magnet levitates above a cooled superconductor. These two effects, despite always going together in the known superconductors, are independent of each other. A superconductor is characterized by its critical temperature T_c under which it enters the superconducting state, as well as its critical field H_c above which superconductivity is destroyed. Related to H_c, there exists a critical current j_c which is the maximum current density that can flow through the superconducting material. From a more fundamental perspective, superconductivity is the macroscopic manifestation of a quantum coherent state, which is obtained by lowering down the temperature – sometimes close to absolute zero (-273.15°C) – and potentially by increasing the pressure. Beside the electrical conductivity and the magnetic susceptibility, other physical properties such as specific heat, thermal conductivity, etc. are strongly affected at the superconducting phase transition.

Existing applications Despite the low temperatures required, superconductors are already used in many technological applications. Their main use is to generate high magnetic fields, since they can conduct extremely strong electrical currents (not limited by the Joule heating but only by j_c). A known example is the magnetic resonance imaging (MRI) scanners coils which are permanently cooled down at 4 K by liquid helium. Levitating trains can also make use of superconducting electromagnets to levitate above the track and to be propelled, but they are not yet commercially used. In the field of research, one can cite the coils of tokamaks used to confine the plasma in nuclear fusion, or the ones of the Large Hadron Collider (LHC) at CERN which guide the beams of particles. On a smaller scale, SQUIDs (superconducting quantum interference devices) are widely used as highly sensible magnetometers able to measure ultra weak magnetic fields. Last but not least, the ongoing and dynamic research on quantum computers relies on basic components – the famous quantum bits or qbits – often made of superconducting circuits.

Potential applications Even for the so-called high-T_c superconductors, the working temperatures are still way too low for a wider use. There is nevertheless the hope, among physicists and industrialists, that superconductivity at room temperature and ambient pressure is possible. If so, and under the condition that this hypothetical superconducting material should be easy enough to produce and shape[1], it will trigger a technological revolution. The absence of Joule heating would be an enormous advantage in electrical transport, as well as in electronics where cooling down computing units is extremely important and becomes a major issue at the datacenters scale. The generation of high magnetic fields by superconducting electromagnets could also be done without the need of a complex cooling system.

1.2 Historical overview

Discovery This phenomenon was discovered in 1911 by Kamerlingh Onnes who, after developing a new system to liquefy helium, used this system to study physical properties at unprecedentedly low temperatures, electrical resistivity in particular. He measured that below a critical temperature T_c of 4.2 K, the electrical resistivity of solid mercury suddenly drops to zero [Kamerlingh Onnes1911]. The Meissner effect was subsequently discovered in 1933 by Meissner and Ochsenfeld, who indirectly detect it by measuring an enhanced magnetic field outside tin and lead samples [Meissner1933].

The quest for a theory The new mysterious phenomenon of superconductivity required the development of a new conceptual framework to explain it. In 1935 the London brothers developed a phenomenological theory based on electromagnetism which was able to explain the Meissner effect. In 1950, Gingzburg and Landau proposed a theory which describes the superconducting phase transition, introducing a complex order parameter that can be interpreted as the wavefunction of the superconducting electrons. This theory later enabled Abrikosov to predict the mixed state of type-II superconductors, and Josephson the effect that bears his name, which is the basis of today's superconducting quantum computing technologies.

In 1956, Cooper showed that an arbitrarily weak attractive interaction between electrons in

[1] Which is not the case for the high-T_c superconductors known so far (rare-earth based materials, often difficult to synthesize, brittle, etc.).

a small shell above the Fermi sea results in the formation of bound states, called Cooper pairs, and that the Fermi sea is unstable against the formation of these pairs [Cooper1956]. Finally in 1957, Bardeen, Cooper and Schrieffer published two articles in which a consistent microscopic theory was exposed [Bardeen1957a, Bardeen1957b]. They explained the phenomenon of superconductivity as due to the emergence of a new ground state in which the Cooper pairs "condense", which is at the basis of the macroscopic quantum coherence. In this so-called BCS theory, the interaction responsible for the formation of Cooper pairs can be in principle from any origin, but the authors suggested the quantum vibrations of the lattice – the phonons – to be responsible for this pairing. This theory – for which they received the 1972 physics Nobel Prize – succeeded to explain the superconductivity phenomenon in all the superconductors known at that time, which are now called conventional superconductors, phonon-mediated superconductors or by a misuse of language, BCS superconductors[2]. In 1959 Gor'kov proved that the Gingzburg-Landau theory, considered as phenomenological, can in fact be derived from the BCS theory with a clear physical interpretation: the Gingzburg-Landau order parameter corresponds to the Cooper pair wavefunction [Gor'Kov1959]. While the BCS theory stays at the model level, Eliashberg established in 1960 the complete microscopic theory of phonon-mediated superconductivity based on the field theory formalism [Eliashberg1960].

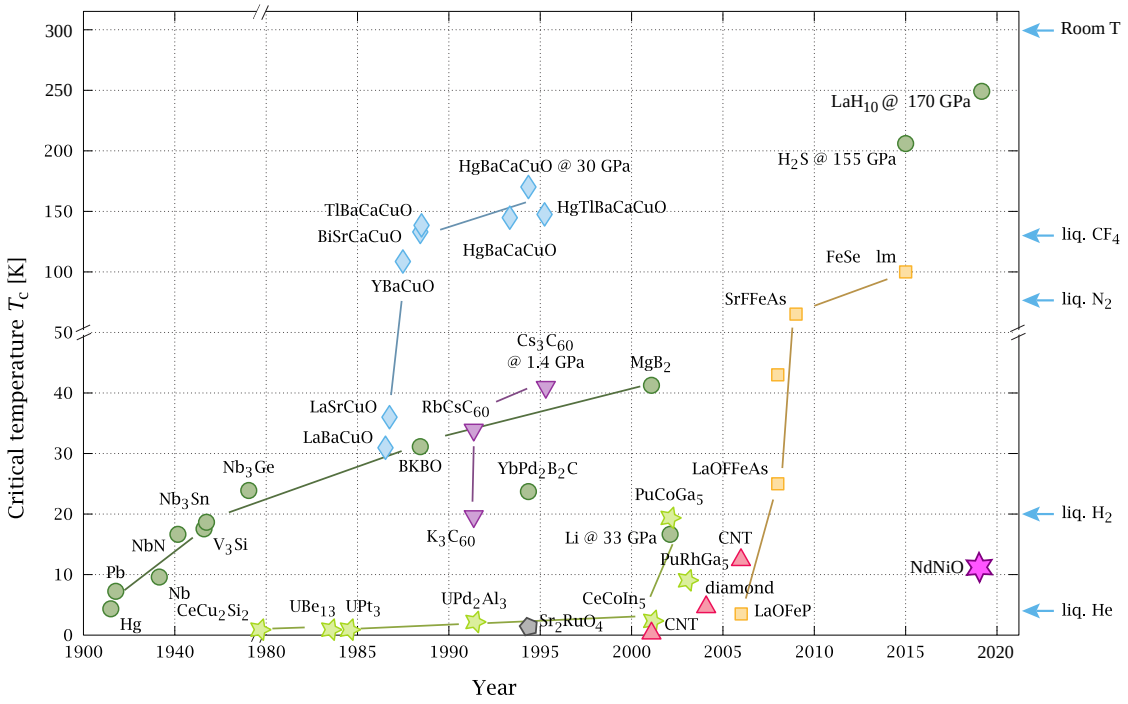

Figure 1.1: Timeline of the superconductor discoveries with the associated critical temperatures. The color identifies the different families, among others: conventional superconductors (deep green), cuprates (blue), heavy-fermions (light green), iron-based pnictides (orange) and finally the first nickelate (purple star). Originally from [Ray2016], regularly updated on the Wikipedia page [HTSCwiki].

Discovery of superconductivity in cuprates For a very long time, superconductivity was limited to these extremely low temperatures, not exceeding 23 K in Nb_3Ge. In 1986, Bednorz and Müller discovered superconductivity in barium-doped La_2CuO_4 (LaBaCuO), a copper-based oxide ceramic, with a record T_c of 35 K [Bednorz1986]. Inspired by their work, another group

[2] This is a misuse of language since the BCS theory and in particular the Cooper pairing mechanism is valid in principle for other kinds of interactions than the one mediated by phonons. Hence, the BCS theory is still relevant in the context of unconventional superconductivity.

of experimentalists soon after obtained a substantially higher T_c of 93 K in $Y_{0.6}Ba_{0.4}CuO_4$ (YBaCuO) [Wu1987]. This new family of superconductors, the so-called cuprates, have opened the era of high-temperature superconductivity. With such high critical temperatures, cuprates can be cooled down with liquid nitrogen – which have a boiling temperature of 77 K (-196°C) – to enter the superconducting state.

Bednorz and Müller received the 1987 physics Nobel Prize, that is the year right after their breakthrough, which was the shortest time ever from a discovery to a Nobel Prize in Physics and illustrates how game-changing it was (for details about the cuprates discovery, see [Garisto2023, Bednorz1987]). It opened an active period during which other cuprates were investigated and discovered superconducting, as it can be seen in Fig. 1.1 where cuprates appear in blue. They remain nowadays the materials with the higher T_c's at ambient pressure – the record being hold by HgBaCaCuO with 135 K – but still far below room-temperature.

The mystery of unconventional superconductivity In this new type of high-temperature superconductors, so-called unconventional, the coherent phonon mechanism cannot be responsible for the Cooper pairing, being overwhelmed by the random lattice vibrations due to thermal agitation. The Coulomb repulsion between electrons is supposed to play an important role in the normal state from which unconventional superconductivity emerges, and the interaction between spins is one of the main candidates for the coupling mechanism. But since 1986, no complete and convincing theory have been proposed, despite undeniable progresses. Besides cuprates, others families of materials were discovered superconducting, such as heavy fermions (plotted in light green in Fig. 1.1) or iron-based superconductors (in orange), but the unconventional superconductivity mechanism remains nowadays one of the most significant problems of modern physics, and no one knows if superconductivity can even exist at room temperature and ambient pressure. Since the discoveries of superconductivity in cuprates almost forty years ago, there was a background activity aimed to find materials analogous to cuprates, and nickel-based materials were among the possible candidates.

1.3 Nickelates

In 2019, a thin film of strontium-doped nickel oxide was measured superconducting with a T_c of about 15 K, opening the "nickel age" of superconductivity. The introduction of these nickelates has triggered great excitement around these materials, as they give a welcome opportunity to address the mystery of high-temperature superconductivity with a new perspective.

1.3.1 Ruddlesden-Popper and layered square-planar series

Let us first introduce the two families of nickelates on which superconductivity research focuses, namely the Ruddlesden-Popper (RP) and square-planar (SP) series. This section proceeds in this order to ease the explanation from a material synthesis point of view, which does not correspond to the chronological order of superconductivity discovery in these materials. The latter will be clarified in Sec. 1.3.2.

Ruddlesden-Popper (RP) nickelates are perovskite-like structures with nickel oxide layers (NiO_2) lying in between spacers made of rare-earth and oxygen atoms, with an octahedral coordination for the nickel one. Hence, they are sometimes called octahedral nickelates. Their

general chemical formula (per unit cell) reads:

$$R_{n+1}\mathrm{Ni}_n\mathrm{O}_{3n+1} \tag{1.1}$$

with R the rare-earth atom (La, Nd, Pr, Sm). The integer n corresponds to the number of elementary perovskite blocks stacked on top of each other. This stacking is interrupted by the spacer and starts again upper, but shifted by $(a/2, b/2)$ in the xy plane (see Fig. 1.2). Hence, n also corresponds to the number of NiO_2 planes stacked on top of each others. One speaks about single-layer (SL) for $n=1$, bilayer (BL) for $n=2$, trilayer (TL) for $n=3$, etc. When n tends to infinity, the cubic perovskite $R\mathrm{NiO}_3$ is formally recovered, as shown in Fig. 1.2.

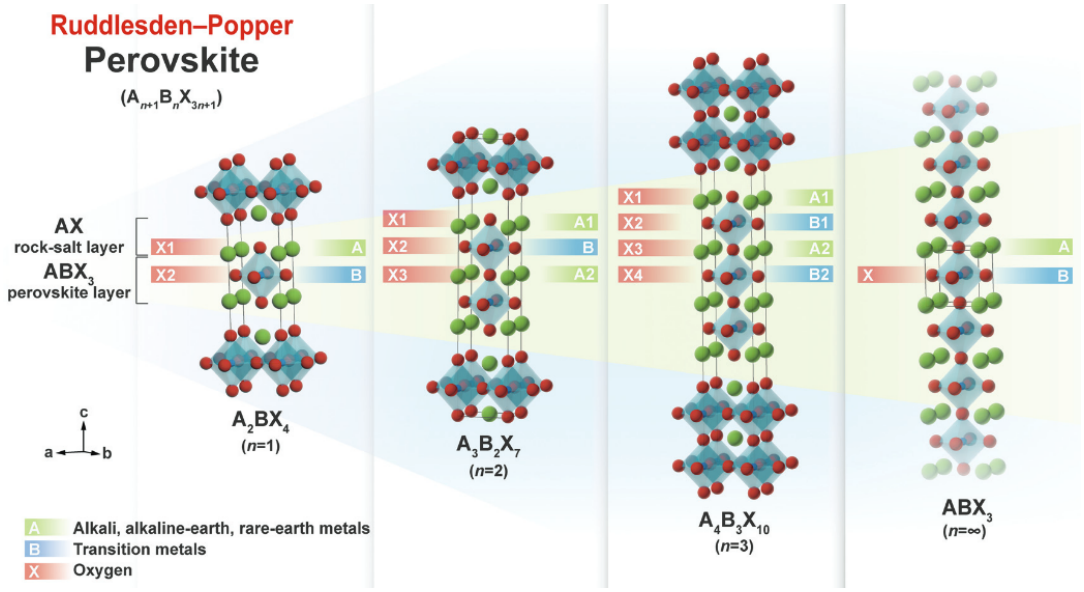

Figure 1.2: Ruddlesden-Popper serie for generic A and B atoms showing from left to right the SL, BL and TL compounds, plus the perovskite structure on the right corresponding to $n \to \infty$. From [Xu2020].

Layered square-planar (SP) compounds are the oxygen reduced counterpart of the RP. The coordination of the nickel atom with the oxygens is square-planar, hence their name. They are also referred to as oxygen deficient RPs. Their chemical formula (per unit cell) writes

$$R_{n+1}\mathrm{Ni}_n\mathrm{O}_{2n+2} \tag{1.2}$$

The reduction is said topotactic: it is a "soft" chemical reaction with a clear continuity between the initial and the final phases. In other words, the crystallographic framework of the parental phase is preserved (see Fig. 1.3). Indeed, the reaction takes place at relatively low temperature (typically 260-280°C for the IL $Nd_{0.8}Sr_{0.2}NiO_2$) compare to usual solid-state synthesis temperatures [Meng2023], and the oxygens are removed typically by annealing using CaH_2 as a reducing agent. Note that the ILs, the compounds which have triggered the interest for nickelates, are directly obtained from the reduction of the perovskite (without the need to synthesize first a RP parent with a finite n).

1.3.1.1 Tuning of the nickel electronic configuration

One of the distinctive features of the cuprates is the $3d^9$ electronic configuration of the copper atom. There has been a continuous effort of finding additional materials in which this special configuration is realized, and nickelates were one of them.

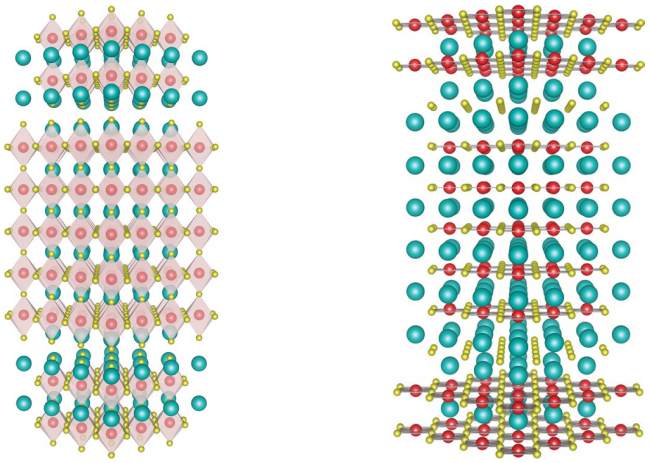

Figure 1.3: RP-pentalayer (left) which gives after a topotactic reduction of the apical oxygens the square-planar pentalayer (right). From [Pan2022].

Oxidation state In crystals, molecules or in solution, the electrons in the outer shells of each atom — the valence electrons — are shared by the atoms of the system, depending on their respective electronegativity. Some atoms will more likely lose or gain electrons. The electronic configuration of the isolated nickel atom writes [Ni] = [Ar] $3d^8\,4s^2$ since the two *s*-electrons are the less tightly bound and hence the most susceptible to go away. Indeed, the 2+ oxidation state [Ni^{2+}] = [Ar] $3d^8$ is the most common for the nickel ion, but other configurations exist. Straightforwardly, Ni^{3+} which loses one electron more present a [Ar]$3d^7$ configuration. For Ni^{1+}, only one of the original *s*-electrons is actually removed, and the remaining one moves into the *d*-shell, ending up in a rearranged configuration [Ar]$3d^9$. As nickel and copper atoms are neighbors in the *d*-block of the periodic table (with respectively 28 and 29 electrons), their nominal electronic configurations only differ by one electron. Indeed, the nominal electronic configuration of copper is [Cu] = [Ar] $3d^9 4s^2$, and its more stable oxidation state is Cu^{2+} with a d^9 configuration.

Tuning the filling by dimensionality One interesting property of these RP and square-planar series is that the *nominal* oxidation state of the nickel atom depends on the number of layers *n*. The oxygens being very electronegative, they acquire two more electrons to have the electronic configuration of neon ($v_O = 2-$). On their part the rare-earth atoms are said trivalent[3], that is they lose three electrons ($v_R = 3+$). The nickel nominal oxidation state v_{Ni} should adapt to ensure the neutrality of the system, which is calculated by solving this simple equation:

$$N_R v_R + N_{Ni} v_{Ni} + N_O v_O = 0 \tag{1.3}$$

with N_{elmt} the number of atoms of each element in one unit-cell, which depends on *n*. The formulas of the nominal oxidation state for the two series reads:

$$v_{Ni}^{RP}(n) = 3 - \frac{1}{n} \quad ; \quad v_{Ni}^{SP}(n) = 1 + \frac{1}{n} \tag{1.4}$$

where one see that they behave in an opposite manner. The adjective *nominal* is used since this calculation is obviously only a first guess and does not take into account the complete physics, as we will see later. Tab. 1.1 and Fig. 1.4 show the evolution of this nominal oxidation

[3] The rare-earth elements (scandium, yttrium and the 15 lanthanides) present a most favorable 3+ oxidation state with a striking uniformity. Only cerium and europium have other accessible oxidation states, respectively 4+ and 2+.

state with respect to n, as well as the corresponding filling of the Ni-3d shell (calculated by filling $= 10 - v_{Ni}$). One can notice that the SL is the only common member to the two series with an oxidation state Ni^{2+}.

n	v_{Ni}^{RP} (filling)	v_{Ni}^{SP} (filling)
1	2+ (d^8) **SL**	2+ (d^8)
2	2.5+ ($d^{7.5}$) **BL**	1.5+ ($d^{8.5}$)
3	2.67+ ($d^{7.33}$) **TL**	1.33+ ($d^{8.67}$)
4	2.75+ ($d^{7.25}$)	1.25+ ($d^{8.75}$)
5	2.8+ ($d^{7.2}$)	1.2+ ($d^{8.8}$) **PL**
6	2.83+ ($d^{7.17}$)	1.17+ ($d^{8.83}$)
∞	3+ (d^7) **perovskite**	1+ (d^9) **IL**

Table 1.1

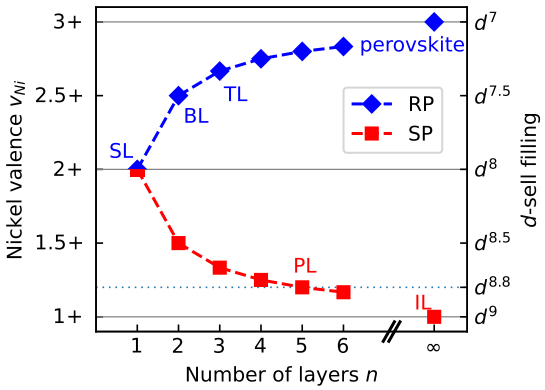

Figure 1.4

Nominal oxidation states and fillings of the Ni-3d shell in the RP and square-planar series. The $d^{8.8}$ configuration of superconducting doped cuprates is indicated by the thin dashed line. Abbreviations for the material names used all along this manuscript are indicated.

Hence, one can play with n to fill more or less the Ni-3d shell, which is a sort of intrinsic doping via the system dimensionality. This filling can be further modified by adding holes via "real" chemical doping of the rare-earth by a divalent (2+) ion such as strontium, barium, calcium or europium[4]. An additional self-doping effect by a rare-earth band also comes into play in nickelates, which also modifies the filling of the nickel d-shell. This effect will be discussed in Sec. 1.3.3.2.

Cuprates It is important to note that if some cuprates belong to the RP or square-planar series, many of them present a more complex structure. But they all have as a common trait a *fixed* d^9 (2+) configuration for the copper ion in their parent phase. Therefore in cuprates, there is no possibility to tune the filling of the copper d-shell via the number of layers, but only via chemical doping. As they are not superconducting in their parent phase, this chemical doping is required (by electrons or holes), the highest T_c's being reached for a hole-doping rate of about 20%, that is for a $d^{8.8}$ configuration.

Atomic energy levels The picture given by these simple filling values is of course incomplete and one needs to consider orbitals and crystal field splitting to go beyond. Fig. 1.5 shows the crystal field splitting of the five d-orbitals, from an octahedral environment to a square-planar one, via the deformation of the octahedron. In a perfect octahedral environment, like in a perovskite, the orbitals split into two sets, labelled $e_g = \{x^2-y^2, z^2\}$ and $t_{2g} = \{xy, xz, yz\}$. The t_{2g} orbitals are lower in energy since their lobes lie in between the ligands, contrary to the e_g orbitals. In an octahedron symmetrically deformed along the z direction, like it is the case in the RP SL[5], a further splitting within these sets occurs, since the energy of the orbitals out of the xy plane (namely xz, yz and z^2) are lowered. In the limit of a square-planar coordination

[4] These doping atoms do not have the exact same size than the original rare-earth, which generates a so-called chemical pressure. It will be studied for the barium-doped SL La_2NiO_4 in Chap. 9

[5] For members of the RP serie with $n > 1$, the octahedra are deformed in a non-symmetrical way, and the splitting is slightly more complex.

the energy of the z^2 and xy levels are exchanged.

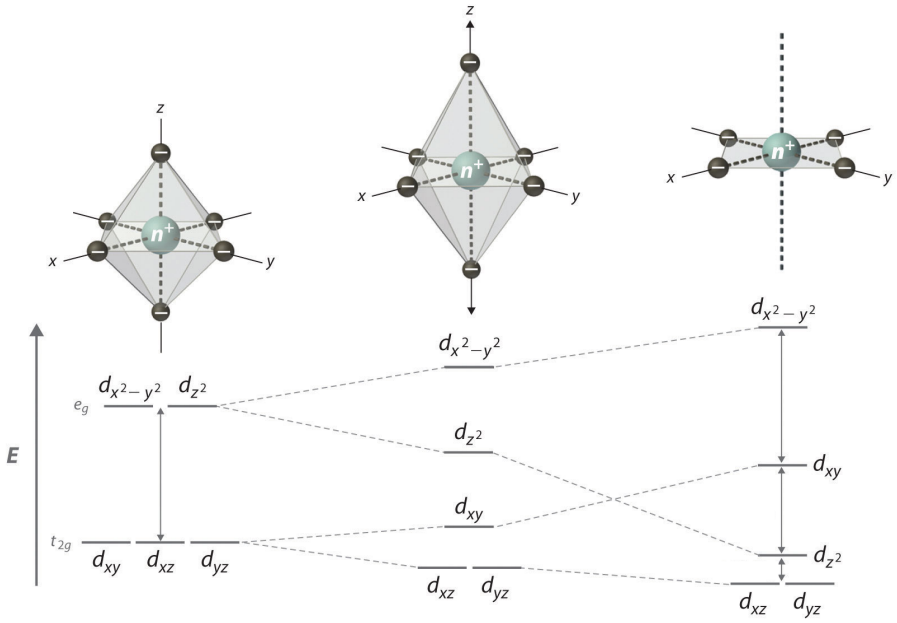

Figure 1.5: Crystal field splitting of the d-orbitals of the central metal ion within an octahedral environment, showing the e_g-t_{2g} splitting (left). If the distance with the apical ligands increases, another splitting occurs within these two sets (center). In the square-planar limit, the energy of the z^2 and xy levels are exchanged (right). From [Averill2012].

These energy levels have to be filled by the number of electrons available. Fig. 1.6 shows the orbital configuration of the nickel ion in the IL (d^9) – analogous to the one in cuprates – and in the BL ($d^{7.5}$). Since for the BL, the unit cell contains two octahedra stacked on top of each other in the z-direction, the number of electrons is doubled and one observes a bonding-antibonding splitting of the z^2 orbitals (whose lobes overlap in the z-direction).

The active states, that is the one close to the Fermi level, are the x^2-y^2 orbitals for both cuprates and square-planar nickelates, which suggests a common superconducting mechanism between these two families of materials. While in the RP case, the x^2-y^2 and z^2 orbitals are both active. Their respective role and their eventual interplay is at the center of the discussion about the superconducting mechanism in the RP nickelates.

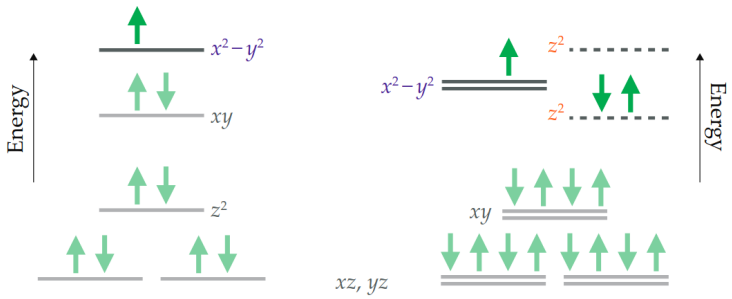

Figure 1.6: Orbital configurations of square-planar ILs and cuprates (left) and of the RP BL (right). The passive orbitals are grayed out. This schematic picture does not take into account the bandwidth due to dispersion in reciprocal space. Adapted from [Goodge2025].

1.3.2 Chronology

As we have now defined the RP and square-planar series and their specificities, as well as their link with cuprates, let us remind the chronology of the events regarding nickelates superconductivity. The year of the discovery of superconductivity in each compound together with the associated critical temperature are reported in Fig. 1.7. The literature on nickelates being already overabundant, this short historical review cannot be exhaustive but the key stages are given. It might need to be updated soon since the research on these materials is extremely dynamic, but gives the picture of the field at the time this PhD thesis was written.

The initial quest in the ILs When they started their quest for superconductivity in transition metal oxides in the 80's, Bednorz and Müller first suspected nickel-based materials to host superconductivity, among others the perovskite $LaNiO_3$. As it finally did not look promising, they replaced nickel by copper with the success we know [Garisto2023, Bednorz1987][6]. The interest about nickelates in the framework of superconductivity was revived in 1999 when analogies between the electronic structures of some nickelates and superconducting cuprates were featured by density functional theory (DFT) calculations [Anisimov1999]. In this paper, the aim of the authors was to find nickelates with a Ni^{1+} oxidation state, that is with the same d^9 configuration than the parents of the superconducting cuprates. They suggested the square-planar compounds and in particular the ILs as candidates to host superconductivity. The problem is that the Ni^{1+} ion inherent to the IL structure is relatively unstable, hence these compounds are difficult to synthesize directly. It is necessary to grow first the much more stable perovskite where the oxidation state is Ni^{3+}, then to dope it, and finally to perform the topotactic reduction. The refinement of this process took 20 years, but in 2019 a thin-film of strontium-doped $NdNiO_2$ has eventually been measured superconducting with a maximum onset critical temperature of 15 K and a doping rate of 20% [Li2019]. It triggered an avalanche of work, both experimental and theoretical, to reproduce, refine, explain and find other superconducting nickelates. During the following years, two other strontium-doped ILs in thin-film, namely $PrNiO_2$ and $LaNiO_2$, were measured superconducting with respective T_c's of 12 and 9 K [Osada2020, Osada2021]. In the latter article, some indications of superconductivity in the undoped lanthanum compound were also found, attributed to the self-doping effect typical of nickelates. The PL compound $Nd_6Ni_5O_{12}$ in thin-film was on its turn measured superconducting with a T_c of 13 K [Pan2022], reproducing again the $d^{8.8}$ configuration but *without* doping and validating the dimensionality-tuning approach.

Superconductivity in the RP compounds The history of nickelates has experienced a major and unexpected rebound when an above liquid nitrogen T_c of 78 K was measured in the undoped lanthanum BL compound $La_3Ni_2O_7$ with its $d^{7.5}$ nominal electronic configuration [Sun2023]. Beside this unprecedented T_c, it was also the first bulk nickelate to achieve superconductivity, but requiring for that high pressure. It held the record T_c for more than a year, only beaten by its lanthanum-samarium counterpart $La_2SmNi_2O_7$ and its T_c of 93 K, under high pressure as well [Li2025]. In the meantime, the lanthanum trilayer (TL) $La_4Ni_3O_{10}$ was also measured superconducting in the bulk under super high pressure, although at a lower temperature of 30 K [Zhu2024].

Further progress After the parent lanthanum compound, the confirmation that superconductivity is possible at zero doping in ILs came almost at the same time for thin-films of $NdNiO_2$

[6] In fact, cuprates have already been synthesized at that time, but the chemists were looking for catalytic properties of oxygen-deficient compounds at elevated temperatures, and not for superconductivity [Bednorz1987].

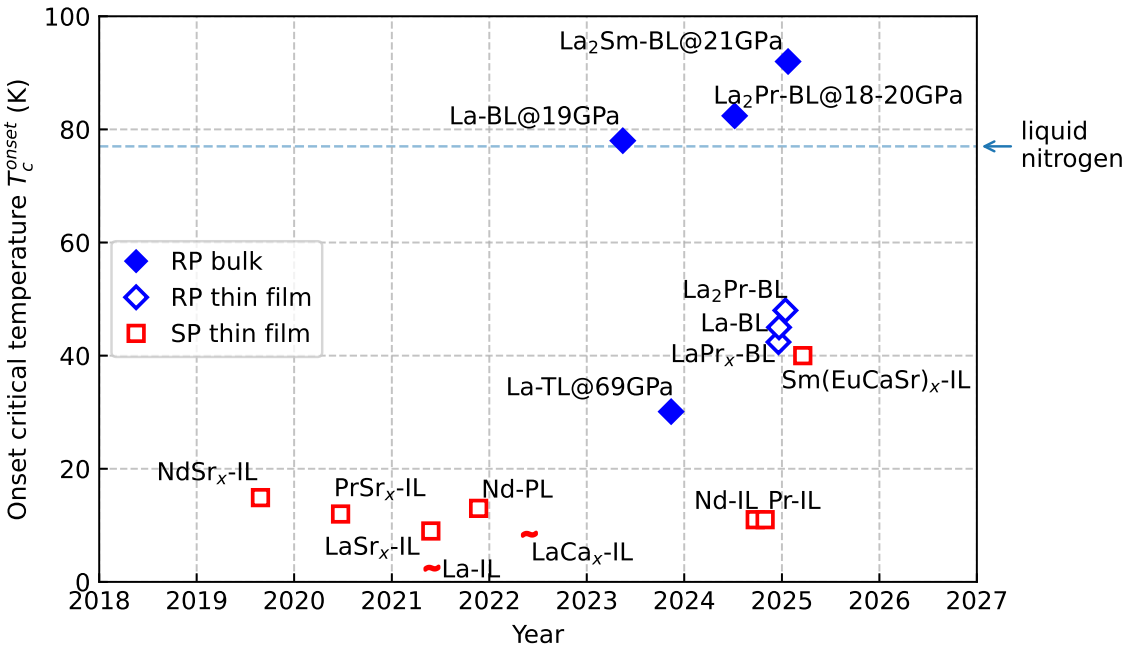

Figure 1.7: Timeline of the superconductivity discoveries in nickelates, with the corresponding *onset* critical temperatures. The abbreviation *R*-type@*P* for a compound is composed of: (1) the main rare-earth element *R* involved (or a combination of them, the potential doping element being indicated by the subscript *x*), (2) the type of structure and (3) the pressure potentially needed to achieve superconductivity. Tildes indicates results for which the onset T_c was not explicitly given. The dates correspond to the first apparition of the result online, and can therefore correspond to the first preprint published on arXiv. As an indication, this PhD thesis took place from march 2022 to december 2025.

and $PrNiO_2$, with similar T_c's of 11 K [Parzyck2025, Sahib2025]. After the bulk material, compressively strained thin-films of the lanthanum BL, either with or without praseodymium doping, were found superconducting with T_c's ranging from 42 to 48 K [Ko2025, Zhou2025, Liu2025]. Recently, a thin-film of a samarium-based IL with a complex doping of europium, calcium and strontium was measured superconducting at 40 K, being the first copper-free material isostructural to cuprates superconducting above 30 K at ambient pressure [Chow2025]. Research on nickelate is in constant progress, many possibilities to obtain superconductivity are explored in both square-planar and RP families. The various electronic configurations in these two nickelates families indicates a rich and complex physics, and likely two different superconducting mechanism. The discoveries being very recent, studies that further characterize the exact stoichiometry of these compounds (*e.g.* their oxygen rate), their gap symmetry and their experimental electronic structure measured by ARPES[7] are rare if not lacking, which generates many speculations.

1.3.3 Further comparison with cuprates

Further differences exists between nickelates and cuprates, which can help to single out the features relevant or not for superconductivity.

[7] Angle-resolved photoemission spectroscopy: an experimental technique allowing to probe the electronic structure of materials, in particular their Fermi surface. It will be the subject of Sec. 4.3.

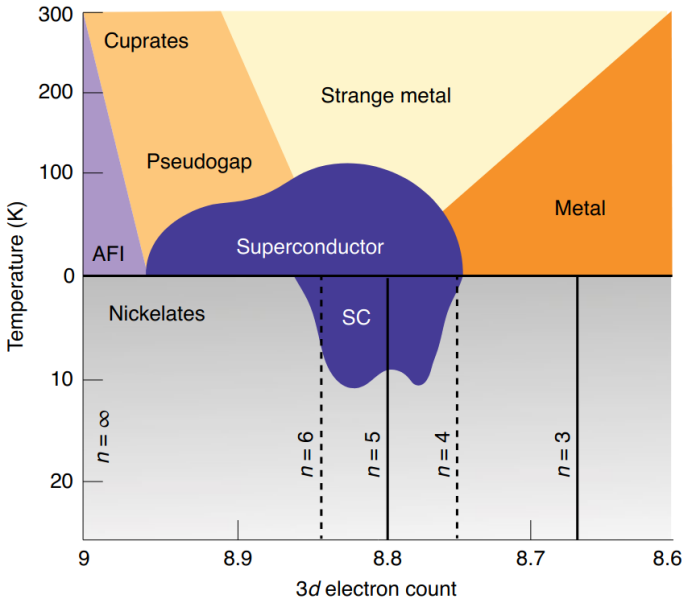

Figure 1.8: Schematic phase diagrams of cuprates (top) and of square-planar nickelates (bottom). The abscissa represent the filling of the d-shell, which depends only on chemical doping in cuprates and on chemical doping or on the number of layers in square-planar nickelates. One remarks the d^9 configuration on the left, corresponding to the parent phase of cuprates and of IL nickelates. AFI stands for antiferromagnetic insulator. From [Pan2022].

1.3.3.1 Phase diagram

The cuprates phase diagram, shown on the upper part of Fig. 1.8 in its temperature vs hole-doping version, is very complex already for the normal state and is still not completely understood despite the efforts made for almost forty years. In their parent phase, the cuprates are insulators and present a long-range antiferromagnetic order. At higher doping lies a mysterious pseudogap phase, where the metallicity emerges but with a truncated Fermi surface, made of the so-called Fermi arcs as it appears in ARPES experiments. As the doping increase, the holes acquire more mobility and the system goes more metallic, but shows some non-Fermi liquid behaviors[8], hence the name strange metal. In particular, the resistivity is linear instead of varying in T^2 (electron-electron interactions as described by the Fermi-liquid theory) and then in T^5 (electron-phonon interactions) like in a normal metal. Finally at high doping, a metallic phase well described by the Fermi-liquid theory is recovered. The superconducting dome ranges from about 5 to 25% of doping, the maximum T_c's being reached around 16%. Superconductivity in cuprates therefore emerges from a very rich normal state which himself keeps its part of mystery, and whose interplay with superconductivity is not understood yet.

The phase diagram of nickelates looks far simpler. Indeed, nickelates are almost all paramagnetic metals, even if the ILs present so-called "bad metal" or "weak insulator" phases, characterized by a metallic behavior of the resistivity with respect to temperature, but whose order of magnitude is typical of the one of insulators. As metals or bad metals, most of nickelates can be considered as simpler systems than cuprates, their normal state being well described by the Fermi liquid theory. A schematic phase diagram of both doped ILs and undoped square-planar compounds with a varying number of layer n is shown in the lower part of Fig. 1.8. The super-

[8]The Laudau Fermi-liquid theory (FL theory) describes the behavior of most metals and alloys at low temperature, by the mean of weakly interacting quasiparticles which behave like electrons but with renormalized properties (*e.g.* their mass).

conducting dome is centered at 20% of hole-doping which corresponds to a $d^{8.8}$ configuration, comparable with the one of superconducting cuprates. Only the single-layer is insulating and magnetic in its parent phase (which will be extensively discussed in Chap. 9). Interestingly, and contrary to the bilayer and trilayer, it has not been measured superconducting so far, which might be due to the bad interplay between magnetism and superconductivity often observed.

1.3.3.2 Multi-band character and self-doping

In cuprates, the only active orbital is Cu-3$d_{x^2-y^2}$, which is responsible for the typical four-leaflets Fermi surface. As already mentioned, in the RP nickelates (and not in the square-planar) both Ni-3$d_{x^2-y^2}$ and 3d_{z^2} states are involved at the Fermi level. It is therefore necessary to take these two bands into account to describe superconductivity, thus moving away from a "simple" single-band picture.

In both square-planar and RP nickelates, the rare-earth 5d manifold lies above the Fermi level by a few electron-volts, and one or several of these bands can even cross the Fermi level or at least be lowered down toward it, this effect being enhanced by the application of pressure. If a rare-earth band crosses the Fermi level, it induces self-doping, that is electrons from the active nickel bands are taken to fill rare-earth 5d states in the spacer. Thus, holes are left in the NiO_2 planes and the system is naturally away from half-filling (in a Hubbard model picture), and then from a Mott insulating configuration. In the square-planar nickelates, this self-doping effect is systematic and explains why these compounds are not antiferromagnetic insulators. It can be considered again as an intrinsic doping, but from a different origin than the one due to the tuning of the dimensionality with n. It is important to precise that the rare-earth states do not have to play an active role in the superconductivity mechanism, they can just act as a reservoir of charges (holes in this case) which dopes the NiO_2 planes where superconductivity occurs.

1.3.3.3 Debate on the gap symmetry of nickelates

Although it is not a completely solved problem, the symmetry of the superconducting gap in cuprates likely has a $d_{x^2-y^2}$ symmetry, as it can be probed by measuring the single-particle tunneling spectrum. In nickelates, which have been discovered very recently, these measures are very rare and even if some articles or preprints exist, they are not yet confirmed. The debate has then mainly be theoretical so far, with various types of gap symmetry proposed, including $d_{x^2-y^2}$, $s_{\pm}$ and d_{xy}. This debate is particularly strong for the BL compound, for which it has been shown that the gap symmetry is extremely sensible to details of the electronic structure [Xia2025], hence the necessity to describe the latter accurately (which is the purpose of the work presented in Chap. 8).

To summarize, superconducting nickelates share some similarities with cuprates, but also interesting differences. This is why they have triggered such an enthusiasm in 2019: they offer a new opportunity to address the mystery of unconventional superconductivity, on which condensed matter physicists hit a brick wall since forty years and the discovery of cuprates. Their electronic configurations ranging from d^9 to d^7 makes them versatile, and they do not form a unique block: on one hand the square-planar compounds seem analogous to cuprates, on the other hand the RP compounds are suspected to host a different superconductivity mechanism.

1.4 Motivation

Superconductivity emerges from an instability of the normal state triggered by an interaction between electrons. In order to understand superconducting materials, one proceeds in two steps: (i) describe their electronic structure in the normal state, (ii) include the physical ingredients which are known or suspected to mediate superconductivity, to describe the superconducting state.

In this thesis, we have addressed the first point from first-principles, i.e. with theories and methods *directly* based on fundamental laws and constants of quantum mechanics, using the least amount of approximations and adjustable parameters possible. We have naturally used density functional theory (DFT), one of the most standard *ab initio* method to address many-electrons systems. However, DFT suffers from limitations to describe the electronic structure of materials presenting strong electron-electron interactions. To go beyond, we have used many-body perturbation theory within the *GW* approximation, a more advanced theoretical framework designed to capture the many-body effects. As a perturbation theory, *GW* relies on a starting point which is often the solution of a DFT calculation. For the perturbation theory to work, the starting point must be close enough to the actual solution. It turns out that DFT incorrectly predict cuprates as metals, although they are antiferromagnetic insulators in their parent phase. Symptomatic of this fact, there is not much literature addressing cuprates by the *GW* approximation, and it has been shown than reproducing some aspects of their electronic structure requires the use of a cumbersome self-consistent *GW* approach [Jang2015]. On the contrary, DFT correctly predicts nickelates as metallic as they are measured experimentally. The starting point of the perturbation theory seems therefore more reliable than in cuprates. Additionally, most of nickelates are paramagnetic (except the single-layer), which greatly simplifies their *ab initio* treatment, without resorting on spin-polarized calculations that are very cumbersome to perform at the *GW* level. The *GW* method has been applied to these new superconductors only recently, by the supervisors of the present thesis prior to its start [Olevano2020]. The aim of this thesis was to use this more advanced theoretical framework to study and clarify the electronic structure of nickelates in their normal state, and to explore to which extent it can capture the many-body effects within these materials. A particular attention was given to the evolution of their electronic structure with respect to structural changes induced by pressure, epitaxial strain and chemical doping, parameters that are known to affect superconductivity.

Addressing step (ii) can be done either *ab initio*, for example using the Eliashberg theory for phonon-mediated superconductivity, or by models. So far, the latter are required to address unconventional superconductivity, whose coupling mechanism has not been yet understood. The aim of this thesis was originally not to address superconductivity itself, but rather to see how the *GW* description of the electronic structure can affect it, for example by modifying the parameters of the models. However, one specific result in the literature precisely based on *GW* calculations and challenging the unconventional nature of superconductivity in the infinite-layer nickelates [Li2024] drove us to directly investigate the electron-phonon coupling within these materials, using the Eliashberg theory.

1.5 Organization of the manuscript

The first part of this manuscript describes the theoretical framework used in this thesis. Chap. 2 is a general introduction to the quantum many-body problem. DFT is introduced in Chap. 3. Chapters 4 and 5 are dedicated to many-body perturbation theory and the *GW* approximation. Chap. 6 introduces the basics of the theoretical description of superconductivity, and in particular the Eliashberg theory.

The second part of this manuscript is dedicated to the results of our research work on nickelates. It consists first of three independent works that have been published or are in the peer-review process. Chap. 7 addresses the electron-phonon coupling in the infinite-layer nickelates, as mentioned in the previous section [Meier2024]. Chap. 8 addresses the lanthanum bilayer nickelate, which was discovered superconducting one year after the beginning of this thesis. As the T_c record holder, it triggered an avalanche of work and speculation about its superconducting mechanism, mainly based on models fitted on DFT electronic structures. We described the *GW* electronic structure of this material accurately and pointed out some key differences compared to the DFT result, which are crucial in the description of superconductivity [de Vaulx2025a]. Chap. 9 is the result of a long-standing investigation about the single-layers compound which last over the three and a half years of this PhD thesis. While we started to study the fluorine compound La_2NiO_3F, promising for superconductivity [Bernardini2021], we finally focused on the parent compound La_2NiO_4 and investigated its structural and singular magnetic behavior with respect to pressure and doping, mainly at the DFT level [de Vaulx2025b]. The concluding chapter Chap. 10 gathers observations from these three studies and highlights common aspects to the different compounds investigated. Having observed several intriguing features that have not yet been explored in depth, this final chapter outlines possible directions for future research.

References

The overview article [Goodge2025] provides a short and recent presentation of the quest of superconductivity in nickelates with its strategies and unsolved questions.

[Anisimov1999] V. I. Anisimov, D. Bukhvalov and T. M. Rice. *Electronic structure of possible nickelate analogs to the cuprates*. Physical Review B, vol. 59, no. 12, pages 7901–7906, March 1999. doi:10.1103/PhysRevB.59.7901.

[Averill2012] Bruce A. Averill and Patricia Eldredge. *Crystal Field Theory - Principles of General Chemistry*, December 2012. URL: `https://2012books.lardbucket.org/books/principles-of-general-chemistry-v1.0/s27-05-crystal-field-theory.html`.

[Bardeen1957a] J. Bardeen, L. N. Cooper and J. R. Schrieffer. *Microscopic Theory of Superconductivity*. Physical Review, vol. 106, no. 1, pages 162–164, April 1957. doi:10.1103/PhysRev.106.162.

[Bardeen1957b] J. Bardeen, L. N. Cooper and J. R. Schrieffer. *Theory of Superconductivity*. Physical Review, vol. 108, no. 5, pages 1175–1204, December 1957. doi:10.1103/PhysRev.108.1175.

[Bednorz1986] J. G. Bednorz and K. A. Müller. *Possible high T_c superconductivity in the Ba-La-Cu-O system*. Zeitschrift für Physik B - Condensed Matter, vol. 64, no. 2, pages 189–193, June 1986. doi:10.1007/BF01303701.

[Bednorz1987] J Georg Bednorz and K Alex Müller. *Perovskite-type oxides - The new approach to high-T_c superconductivity*, December 1987. Nobel lecture. URL: `https://www.nobelprize.org/prizes/physics/1987/bednorz/lecture/`.

[Bernardini2021] F. Bernardini, A. Demourgues and A. Cano. *Single-layer T'-type nickelates: Ni^{1+} is Ni^{1+}*. Physical Review Materials, vol. 5, no. 6, page L061801, June 2021. doi:10.1103/PhysRevMaterials.5.L061801.

[Chow2025] S. Lin Er Chow, Zhaoyang Luo and A. Ariando. *Bulk superconductivity near 40 K in hole-doped $SmNiO_2$ at ambient pressure*. Nature, vol. 642, no. 8066, pages 58–63, June 2025. doi:10.1038/s41586-025-08893-4.

[Cooper1956] Leon N. Cooper. *Bound Electron Pairs in a Degenerate Fermi Gas*. Physical Review, vol. 104, no. 4, pages 1189–1190, November 1956. doi:10.1103/PhysRev.104.1189.

[de Vaulx2025a] J.B. de Vaulx, Q.N. Meier, P. Toulemonde, A. Cano and V. Olevano. *Pressure and strain effects on the ab initio GW electronic structure of $La_3Ni_2O_7$*. Physical Review B, vol. 112, no. 8, page 085143, August 2025. doi:10.1103/q5ymhf5k.

[de Vaulx2025b] J. B. de Vaulx, F. Bernardini, V. Olevano, Q. N. Meier and A. Cano. *Pressure and doping effects on the electronic structure and magnetism of the single-layer nickelate La_2NiO_4*. Physical Review Materials, vol. 9, no. 11, page 114804, November 2025. doi:10.1103/94sd-ssbw.

[Eliashberg1960] GM Eliashberg. *Interactions between electrons and lattice vibrations in a superconductor*. Soviet Physics JETP, 1960.

[Garisto2023] Dan Garisto. *This month in physics history: April 1986*, March 2023. https://www.aps.org/apsnews/2023/03/bednorz-muller-high-temperature-superconductivity. URL: `https://www.aps.org/apsnews/2023/03/bednorz-muller-high-temperature-superconductivity`.

[Goodge2025] Berit H. Goodge and Michael R. Norman. *Nickelates provide answers about high-temperature superconductivity—and raise new questions*. Physics Today, vol. 78, no. 8, pages 28–33, August 2025. doi:10.1063/pt.sfmg.bbvg.

[Gor'Kov1959] L P Gor'Kov. *Microscopic derivation of the ginzburg-landau equations in the theory of superconductivity*. Soviet Physics JETP, page 4, June 1959.

[HTSCwiki] Wikipedia. *High-temperature superconductivity*, July 2025. URL: `https://en.wikipedia.org/w/index.php?title=High-temperature_superconductivity&oldid=1302988203`.

[Jang2015] Seung Woo Jang, Takao Kotani, Hiori Kino, Kazuhiko Kuroki and Myung Joon Han. *Quasiparticle self-consistent GW study of cuprates: electronic structure, model parameters and the two-band theory for Tc*. Scientific Reports, vol. 5, no. 1, page 12050, July 2015. doi:10.1038/srep12050.

[Kamerlingh Onnes1911] H. Kamerlingh Onnes. *Further experiments with Liquid Helium. D. On the change of Electrical Resistance of Pure Metals at very low Temperatures, etc. V. The Disappearance of the resistance of mercury*. Koninklijke Nederlandse Akademie van Wetenschappen Proceedings Series B Physical Sciences, vol. 14, pages 113–115, January 1911.

[Ko2025] Eun Kyo Ko, Yijun Yu, Yidi Liu, Lopa Bhatt, Jiarui Li, Vivek Thampy, Cheng-Tai Kuo, Bai Yang Wang, Yonghun Lee, Kyuho Lee, Jun-Sik Lee, Berit H. Goodge, David A. Muller and Harold Y. Hwang. *Signatures of ambient pressure superconductivity in thin film $La_3Ni_2O_7$*. Nature, vol. 638, no. 8052, pages 935–940, February 2025. doi:10.1038/s41586-024-08525-3.

[Li2019] Danfeng Li, Kyuho Lee, Bai Yang Wang, Motoki Osada, Samuel Crossley, Hye Ryoung Lee, Yi Cui, Yasuyuki Hikita and Harold Y. Hwang. *Superconductivity in an infinite-layer nickelate*. Nature, vol. 572, no. 7771, pages 624–627, August 2019. doi:10.1038/s41586-019-1496-5.

[Li2024] Zhenglu Li and Steven G. Louie. *Two-Gap Superconductivity and the Decisive Role of Rare-Earth d Electrons in Infinite-Layer Nickelates*. Physical Review Letters, vol. 133, no. 12, page 126401, September 2024. doi:10.1103/PhysRevLett.133.126401.

[Li2025] Feiyu Li, Di Peng, Jie Dou, Ning Guo, Liang Ma, Chao Liu, Lingzhen Wang, Yulin Zhang, Jun Luo, Jie Yang, Jian Zhang, Weizhao Cai, Jinguang Cheng, Qiang Zheng, Rui Zhou, Qiaoshi Zeng, Xutang Tao and Junjie Zhang. *Ambient pressure growth of bilayer nickelate single crystals with superconductivity over 90 K under high pressure*, January 2025. arXiv:2501.14584.

[Liu2025] Yidi Liu, Eun Kyo Ko, Yaoju Tarn, Lopa Bhatt, Jiarui Li, Vivek Thampy, Berit H. Goodge, David A. Muller, Srinivas Raghu, Yijun Yu and Harold Y. Hwang. *Superconductivity and normal-state transport in compressively strained $La_2PrNi_2O_7$ thin films*. Nature Materials, vol. 24, no. 8, pages 1221–1227, August 2025. doi:10.1038/s41563-025-02258-y.

[Meier2024] Q. N. Meier, J. B. de Vaulx, F. Bernardini, A. S. Botana, X. Blase, V. Olevano and A. Cano. *Preempted phonon-mediated superconductivity in the infinite-layer nickelates*. Physical Review B, vol. 109, no. 18, page 184505, May 2024. doi:10.1103/PhysRevB.109.184505.

[Meissner1933] W. Meissner and R. Ochsenfeld. *Ein neuer Effekt bei Eintritt der Supraleitfähigkeit*. Naturwissenschaften, vol. 21, no. 44, pages 787–788, November 1933. doi:10.1007/BF01504252.

[Meng2023] Ziang Meng, Han Yan, Peixin Qin, Xiaorong Zhou, Xiaoning Wang, Hongyu Chen, Li Liu and Zhiqi Liu. *Topotactic Transition: A Promising Opportunity for Creating New Oxides*. Advanced Functional Materials, vol. 33, no. 46, page 2305225, 2023. doi:10.1002/adfm.202305225.

[Olevano2020] Valerio Olevano, Fabio Bernardini, Xavier Blase and Andrés Cano. *Ab initio many-body GW correlations in the electronic structure of $LaNiO_2$*. Physical Review B, vol. 101, no. 16, page 161102, April 2020. doi:10.1103/PhysRevB.101.161102.

[Osada2020] Motoki Osada, Bai Yang Wang, Berit H. Goodge, Kyuho Lee, Hyeok Yoon, Keita Sakuma, Danfeng Li, Masashi Miura, Lena F. Kourkoutis and Harold Y. Hwang. *A Superconducting Praseodymium Nickelate with Infinite Layer Structure*. Nano Letters, vol. 20, no. 8, pages 5735–5740, August 2020. doi:10.1021/acs.nanolett.0c01392.

[Osada2021] Motoki Osada, Bai Yang Wang, Berit H. Goodge, Shannon P. Harvey, Kyuho Lee, Danfeng Li, Lena F. Kourkoutis and Harold Y. Hwang. *Nickelate Superconductivity without Rare-Earth Magnetism: (La,Sr)NiO_2*. Advanced Materials, vol. 33, no. 45, page 2104083, 2021. doi:10.1002/adma.202104083.

[Pan2022] Grace A. Pan, Dan Ferenc Segedin, Harrison LaBollita, Qi Song, Emilian M. Nica, Berit H. Goodge, Andrew T. Pierce, Spencer Doyle, Steve Novakov, Denisse Córdova Carrizales, Alpha T. N'Diaye, Padraic Shafer, Hanjong Paik, John T. Heron, Jarad A. Mason, Amir Yacoby, Lena F. Kourkoutis, Onur Erten, Charles M. Brooks, Antia S. Botana and Julia A. Mundy. *Superconductivity in a quintuple-layer square-planar nickelate*. Nature Materials, vol. 21, no. 2, pages 160–164, February 2022. doi:10.1038/s41563-021-01142-9.

[Parzyck2025] C. T. Parzyck, Y. Wu, L. Bhatt, M. Kang, Z. Arthur, T. M. Pedersen, R. Sutarto, S. Fan, J. Pelliciari, V. Bisogni, G. Herranz, A. B. Georgescu, D. G. Hawthorn, L. F. Kourkoutis, D. A. Muller, D. G. Schlom and K. M. Shen. *Superconductivity in the parent infinite-layer nickelate $NdNiO_2$*. Physical Review X, vol. 15, no. 2, page 021048, May 2025. doi:10.1103/PhysRevX.15.021048.

[Ray2016] Pia Jensen Ray. *Master's thesis: Structural investigation of $La_{2-x}Sr_xCuO_{4+y}$ - Following staging as a function of temperature*. February 2016. doi:10.6084/m9.figshare.2075680.v2.

[Sahib2025] Hoshang Sahib, Aravind Raji, Francesco Rosa, Giacomo Merzoni, Giacomo Ghiringhelli, Marco Salluzzo, Alexandre Gloter, Nathalie Viart and Daniele Preziosi. *Superconductivity in $PrNiO_2$ Infinite-Layer Nickelates*. Advanced Materials, vol. 37, no. 16, page 2416187, March 2025. doi:10.1002/adma.202416187.

[Sun2023] Hualei Sun, Mengwu Huo, Xunwu Hu, Jingyuan Li, Zengjia Liu, Yifeng Han, Lingyun Tang, Zhongquan Mao, Pengtao Yang, Bosen Wang, Jinguang Cheng, Dao-Xin Yao, Guang-Ming Zhang and Meng Wang. *Signatures of superconductivity near 80 K in a nickelate under high pressure*. Nature, vol. 621, no. 7979, pages 493–498, September 2023. doi:10.1038/s41586-023-06408-7.

[Wu1987] M. K. Wu, J. R. Ashburn, C. J. Torng, P. H. Hor, R. L. Meng, L. Gao, Z. J. Huang, Y. Q. Wang and C. W. Chu. *Superconductivity at 93 K in a new mixed-phase Y-Ba-Cu-O compound system at ambient pressure*. Physical Review Letters, vol. 58, no. 9, pages 908–910, March 1987. doi:10.1103/PhysRevLett.58.908.

[Xia2025] Chengliang Xia, Hongquan Liu, Shengjie Zhou and Hanghui Chen. *Sensitive dependence of pairing symmetry on Ni-eg crystal field splitting in the nickelate superconductor $La_3Ni_2O_7$*. Nature Communications, vol. 16, no. 1, page 1054, January 2025. doi:10.1038/s41467-025-56206-0.

[Xu2020] Xiaomin Xu, Yangli Pan, Yijun Zhong, Ran Ran and Zongping Shao. *Ruddlesden–Popper perovskites in electrocatalysis*. Materials Horizons, vol. 7, no. 10, pages 2519–2565, October 2020. doi:10.1039/D0MH00477D.

[Zhou2025] Guangdi Zhou, Wei Lv, Heng Wang, Zihao Nie, Yaqi Chen, Yueying Li, Haoliang Huang, Wei-Qiang Chen, Yu-Jie Sun, Qi-Kun Xue and Zhuoyu Chen. *Ambient-pressure superconductivity onset above 40 K in $(La,Pr)_3Ni_2O_7$ films*. Nature, vol. 640, no. 8059, pages 641–646, April 2025. doi:10.1038/s41586-025-08755-z.

[Zhu2024] Yinghao Zhu, Di Peng, Enkang Zhang, Bingying Pan, Xu Chen, Lixing Chen, Huifen Ren, Feiyang Liu, Yiqing Hao, Nana Li, Zhenfang Xing, Fujun Lan, Jiyuan Han, Junjie Wang, Donghan Jia, Hongliang Wo, Yiqing Gu, Yimeng Gu, Li Ji, Wenbin Wang, Huiyang Gou, Yao Shen, Tianping Ying, Xiaolong Chen, Wenge Yang, Huibo Cao, Changlin Zheng, Qiaoshi Zeng, Jian-gang Guo and Jun Zhao. *Superconductivity in pressurized trilayer $La_4Ni_3O_{10-\delta}$ single crystals*. Nature, vol. 631, no. 8021, pages 531–536, July 2024. doi:10.1038/s41586-024-07553-3.

Part I

Theoretical framework and methods

2

The quantum many-electron problem

Vous voyez ce que ça fait déjà un million Larmina ?

Hubert Bonisseur de La Bath in *OSS 117 : Le Caire, nid d'espions*

In classical mechanics and more precisely in astrophysics, the motion of N bodies interacting via the gravitational force has no general closed-form solution from $N = 3$, and requires numerical methods to be predicted. The quantum many-body problem, in our case the quantum many-electron problem, rather involves electrostatic interactions between electrons. These interactions are described by the Coulomb potential whose form in $1/r$ is the same than for the gravitational potential. But the formalism of quantum mechanics, based on a wavefunction defined in the entire space, makes the resolution of the quantum many-body problem even more difficult than its classical version.

In the first part of this chapter, I will define what I mean by quantum many-electron problem and explain the reason for which it is difficult to solve, if not impossible. Next, the historically first practical methods that have been used to address this problem will be described, being at the basis of the modern methods. Since this PhD thesis is about nickelates, the generality will sometimes be lost to focus on the particular case of crystals, i.e. infinite periodic systems. In this case, N corresponds to the number of electrons within the unit cell, which contains one or several atoms. Among the materials studied in this PhD thesis, the infinite-layer nickelate $LaNiO_2$ has the lowest N, which is already of 101 electrons per unit cell, 41 if restricted to valence electrons[1].

[1] Valence electrons are the ones in the outermost shell of atoms, by opposition to core electrons. They are the "active" electrons, and will therefore be the only ones considered in our calculations.

2.1 The many-body hamiltonian

In many cases of interest, solving a quantum-mechanical physical problem can be reduced to solving the time-intependent Schrodinger equation:

$$\hat{H}\,\Psi_i = E_i \Psi_i \tag{2.1}$$

with $\hat{H}$ the many-body hamiltonian and Ψ the many-body wavefunction. The subscript i indexes the many-body eigenstates and the associated total energies E_i. As we are interested in the description of particles constituting matter, the many-body hamiltonian should describe the energy of both electrons and nuclei. Because of their larger mass[2], the nuclei move way slower than the electrons, which are then supposed to adapt adiabatically to the movement of the nuclei. Using the Born-Oppenheimer approximation, we consider the nuclei as fixed and only focus on the electronic part of $\hat{H}$. Reduced to the essential physical ingredients needed to describe the problems that are addressed in the PhD thesis[3], this many-body hamiltonian reads in first quantization:

$$\hat{H} = -\frac{1}{2}\sum_{n=1}^{N} \nabla_n^2 + \sum_{n=1}^{N} V_{\text{ext}}(\mathbf{r}_n) + \frac{1}{2}\sum_{\substack{n,m=1 \\ m\neq n}}^{N} v(\mathbf{r}_n, \mathbf{r}_m) \tag{2.2}$$

where the n and m subscripts identifies the electrons. The first term accounts for the usual kinetic energy, the second for the interaction with the external potential and the last one for the interaction between electrons. The external potential is generated by the Coulomb interaction with the atomic nuclei of charge Z_a located at positions $\mathbf{R}_a$ (considered as fixed):

$$V_{\text{ext}}(\mathbf{r}_n) = \sum_a \frac{Z_a}{|\mathbf{r}_n - \mathbf{R}_a|} \tag{2.3}$$

This local external potential defines completely the system of interest[4], the kinetic and electron-electron interaction terms being universal since they read the same for every many-electron system. The two first terms in $\hat{H}$ can be grouped into a sum of non-interacting single-particle hamiltonians which read:

$$\hat{h}_n = -\frac{1}{2}\nabla_n^2 + V_{\text{ext}}(\mathbf{r}_n) \tag{2.4}$$

The electrostatic interaction between electrons is described by the non-local Coulomb potential[5]:

$$v(\mathbf{r}_n, \mathbf{r}_m) = \frac{1}{|\mathbf{r}_n - \mathbf{r}_m|} \tag{2.5}$$

All the complexity of the many-body problem is due to this electron-electron interaction term, which prevents the many-body wavefunction to factorize.

[2] $m_{\text{nucleon}}/m_{\text{e}} \approx 1836$

[3] That is without external electric or magnetic fields as well as no relativistic effects (including spin-orbit coupling)

[4] Bulk silicon or the nickel atom ($N = 28$ for both), a water or a DNA molecule, diamond, etc.

[5] The factor one half in front of the latter in $\hat{H}$ avoids double counting of the interactions.

2.2 The many-body wavefunction

Letting aside the time-dependence by considering eigenstates, the N-electron wavefunction written in position-spin representation is a function of N space-spin variables:

$$\Psi = \Psi(\mathbf{r}_1\sigma_1, \mathbf{r}_2\sigma_2, \mathbf{r}_3\sigma_3, ..., \mathbf{r}_N\sigma_N) = \Psi(q_1, q_2, q_3, ..., q_N) \tag{2.6}$$

where we introduce the notation $q_n = \mathbf{r}_n\sigma_n$. The squared modulus of this many-body wavefunction $|\Psi(q_1, q_2, q_3, ..., q_N)|^2$ corresponds the probability *density* to measure an electron of spin σ_1 in $\mathbf{r}_1$, another of spin σ_2 in $\mathbf{r}_2$, another of spin σ_3 in $\mathbf{r}_3$ etc. The integration over the entire space and over all spin configurations should give one by definition of a probability density, which defines the normalization of Ψ:

$$\int dq_1 \ ... \int dq_N \, |\Psi(q_1, ..., q_N)|^2 = 1 \tag{2.7}$$

where $\int dq_n = \int d\mathbf{r}_n \sum_{\sigma_n}$.

2.2.1 Antisymmetry condition for fermions

Electrons being indistinguishable particles, the probability density $|\Psi|^2$ should be invariant by exchange of two space-spin coordinates. Hence, the many-body wavefunction have to be either symmetric or antisymmetric by this exchange. The antisymmetric case is associated to fermions, which are particles of half-integer spin obeying the Pauli principle. This condition writes:

$$\Psi(... , q_n, ... , q_m, ...) = -\Psi(... , q_m, ... , q_n, ...) \tag{2.8}$$

By setting $q_m = q_n$ in the latter formula, one can see that it is impossible to find two electrons of the same spin at the same position since the wavefunction equals zero in this configuration.

2.2.2 Exponential wall

Each of the N space variables have to range over the entire space. As it is classic in numerical physics, one can discretize space on a mesh of M sites[6], which are labelled from s_1 to s_M. The value of the wavefunction when for example its first space-variable is at s_1 with a spin up, its second at s_3 with a spin down, etc. is represented by $\Psi_{s_1\uparrow s_3\downarrow...}$ with N space-spin subscripts. Now, if the first variable is at $s_5\uparrow$ and the second at $s_2\uparrow$, all the others remaining unchanged, the corresponding value writes $\Psi_{s_5\uparrow s_2\uparrow...}$. Since Ψ has to be evaluated for every configuration of its variables, the amount of (complex) numbers needed to store the wavefunction is

$$\mathcal{N} = (2M)^N$$

where the factor two is due to the spins. It is obvious that this number scales exponentially with N, which is known as the exponential wall. As there is a lot of redundancy in Ψ due to the antisymmetry requirement, one can reduce $\mathcal{N}$ in the following way. First of all, the wavefunction equals zero if two space-spin variables are equal, so one have to choose N different sites among the $2M$ ones of the space-spin mesh. Second, since every permutation of variables only changes the sign of the wavefunction, the order of the arguments does not matter. The number of ways to choose an unordered subset of size N from a larger set of size $2M$ is the binomial coefficient.

[6] $2M$ has to be larger or equal to N. Imagine a three-particle wavefunction sampled on a spacial mesh with only one site...the antisymmetry requirement can even not be written.

Hence, by using the Stirling approximation for the factorial[7], the amount of complex numbers to store reduces to:

$$\mathcal{N}' = \binom{2M}{N} = \frac{2M!}{(2M-N)!N!} \approx \frac{1}{\sqrt{2\pi}}\sqrt{\frac{2M}{(2M-N)N}}\left(\frac{2M}{2M-N}\right)^{2M}\left(\frac{2M-N}{N}\right)^{N}$$

where one see that the exponential behavior in N remains. The use of the space symmetries specific to the system we are considering can help to reduce M, but it cannot compensate the exponential wall. Fig. 2.1 shows the evolution of $\mathcal{N}$ and $\mathcal{N}'$ for a coarse 3D cubic mesh of $M = 10\times10\times10$ sites. The values of N associated to some physical systems given as examples are indicated by vertical dashed lines. If this mathematical object is impossible to store already for small values of N, it is *a fortiori* impossible to calculate and manipulate.

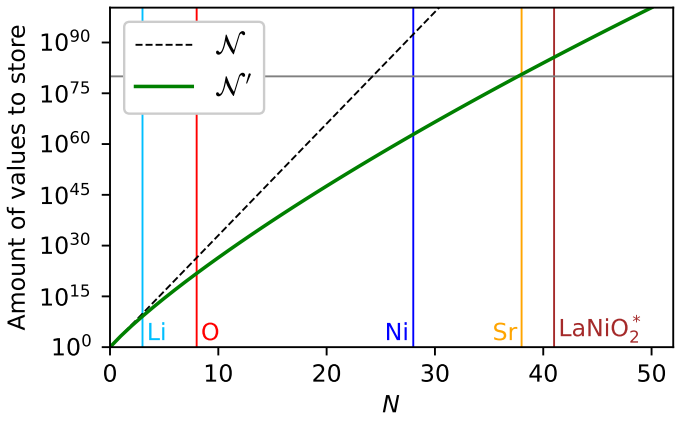

Figure 2.1: Amount of complex values necessary to store the wavefunction sampled on a spatial mesh of 10^3 sites, with respect to the number of electrons in the system. $\mathcal{N}$ corresponds to the full wavefunction storage while $\mathcal{N}'$ takes advantage of its antisymmetry. The lithium atom ($N=3$) is still tractable with one billion of numbers required. The oxygen atom ($N=8$) requires about 10^{21} values, the nickel atom ($N=28$) about 10^{62}, and the strontium atom ($N=38$) more than 10^{80}, which is the estimated number of baryons in the universe (gray line). $LaNiO_2$ is beyond this symbolic limit (the star indicates that $N^* = 41$ corresponds only to the number of *valence* electrons per unit cell). Lanthanum ($N=57$) and neodymium ($N=60$) atoms lie already outside of this plot, as well as the single-layer nickelate La_2NiO_4 ($N^*=64$) and the bilayer nickelate $La_3Ni_2O_7$ ($N^*=111$).

2.3 Methods

In principle, the knowledge of the many-body wavefunction would enable to calculate any physical observables as expectation values $\langle\Psi|\hat{\mathcal{O}}|\Psi\rangle$. In this way all the properties of matter could be explained and predicted from first-principle. In particular, if one was able to solve the many-body problem in materials where electron-electron interactions are important, exotic properties of matter like superconductivity could be directly described. But it turns out that this problem is impossible to solve via brut-force. In 1929 Dirac wrote *"The general theory of quantum mechanics is now almost complete [...] and the difficulty is only that the exact*

[7] The Stirling approximation is $n! = \sqrt{2\pi n}(n/e)^n$ and is valid even for small values of n (starting from 1 !) The approximation for $\mathcal{N}$ is then valid even for small values of $2M$, N and $(2M-N)$.

application of this laws leads to equations much too complicated to be soluble. It therefore becomes desirable that approximate practical methods of applying quantum mechanics should be developed [...]" [Dirac1929].

In the following we will introduce three of the firsts methods used historically enabling to find approximate solutions to the many-electron problem, by increasing order of complexity. They are important because they introduced physical objects (Hartree potential, Hartree-Fock exact exchange) and methods (self-consistent field procedure) that are the ingredients of the more complex modern methods. The idea of this section is also to understand the complexity of the wavefunction approach, in order to better appreciate the convenience of density functional theory.

2.3.1 Independent electrons

The crudest approximation consists of neglecting the interaction term, that is to consider only the single-particle hamiltonian $\hat{h}$. In our case (no spin-orbit coupling), it is sufficient to consider orbitals that are eigenfunctions of the spin operator $\hat{S}_z$ with spins $\sigma = \pm 1/2$ quantized along the z-axis. Then one spin-orbital is separable into a product of one spatial and one spin part: $\phi_n(q) = \psi_n(\mathbf{r})\chi_n(\sigma)$. We will focus on the spatial part, but whenever it is relevant, we will write $\psi_n^{\sigma_n}(\mathbf{r})$ to denote that the spatial part is associated to a spin-up or spin-down eigenfunction.

In a crystal described by a unit-cell periodic potential and Born-von Kármán periodic boundary conditions, the spatial-part of the single-particle eigenstates reads thanks to the Bloch theorem:

$$\psi_{n\mathbf{k}}(\mathbf{r}) = e^{i\mathbf{k}.\mathbf{r}} u_{n\mathbf{k}}(\mathbf{r}) \tag{2.9}$$

with n the band index and $\mathbf{k}$ the crystal momentum, which is chosen to belong to the first Brillouin zone (FBZ). The $u_{n\mathbf{k}}$ are periodic functions over the unit cell. The eigenenergies $\epsilon_{n\mathbf{k}} = \epsilon_n(\mathbf{k})$ form dispersion branches called bands. In metals, their intersection with the Fermi energy E_F defines the Fermi surface, central in the study of superconductors. In insulators or semi-conductors, the distance between the energies of the highest occupied state and the lowest unoccupied state define the bandgap, which is a key quantity for transport and optical phenomenon in solids. The calculation of the bandgap and the comparison with experimental values is a key criterium to evaluate the quality of the approximation employed to describe these systems (see Fig. 5.8). These quantities and the associated vocabulary (FBZ, bandplots and Fermi surfaces), although defined in an independent electrons picture, are still of great use in the many-body context.

The independent electrons approximation already enables to explain, at least qualitatively, many properties of solids. Nevertheless, for both precise quantitative results and the description of properties that this approximation cannot describe (e.g. finite bonding lengths in matter, magnetic orders), it is necessary to take into account the electron-electron interaction term.

2.3.2 Hartree approximation and self-consistent field

In 1928, Hartree developed a mean-field approach where the electrons interact with each other only in average, via their density $|\psi(\mathbf{r})|^2$ [Hartree1928]. In this approach, the non-local electron-electron interaction potential of the many-body hamiltonian is replaced by an effective *local* potential. A system of N coupled single-particle Schrödinger equations using this potential

needs to be solve:

$$\left[\hat{h}(\mathbf{r}) + \int d\mathbf{r}' \sum_{\substack{m \text{ occ} \\ m \neq n}} \frac{|\psi_m(\mathbf{r}')|^2}{|\mathbf{r} - \mathbf{r}'|}\right] \psi_n(\mathbf{r}) = \epsilon_n \psi_n(\mathbf{r}) \tag{2.10}$$

Notice that via this potential, the n-th electron interacts with all the other electrons, no matter their spin. To simplify the problem, one can include the $m = n$ term to show the total electronic density:

$$n(\mathbf{r}) = \sum_{m \text{ occ}} |\psi_m(\mathbf{r})|^2 \tag{2.11}$$

The modified effective potential then reads:

$$V_{\text{H}}(\mathbf{r}) = \int \frac{n(\mathbf{r}')}{|\mathbf{r} - \mathbf{r}'|} d\mathbf{r}' \tag{2.12}$$

and is called Hartree potential. It corresponds simply to the classical electrostatic potential generated by the averaged charge distribution of all the electrons. The potential becomes the same for all the electrons

$$\left[\hat{h}(\mathbf{r}) + V_{\text{H}}(\mathbf{r})\right] \psi_n(\mathbf{r}) = \epsilon_n \psi_n(\mathbf{r}) \tag{2.13}$$

Equations (2.11), (2.12) and (2.13) are known as the Hartree equations.

2.3.2.1 Self-interaction problem

The inclusion of the term $m = n$ into the Hartree potential introduces an unphysical interaction of the electron with itself. This self-interaction is negligible for a system with many electrons, but plays an important role if the number of electrons is small. Another key point is the degree of localization of the electrons. Since the Coulomb potential is in $1/r$, its effect is greater at short range than at long range. If the electron is strongly localized, it will therefore interacts mainly with itself. This artificial interaction is removed by the exchange term in the Hartree-Fock method (sec. 2.3.3), but remain an issue in Kohn-Sham DFT (sec. 3.4).

2.3.2.2 Self-consistent field (SCF) procedure

As the Schrödinger equation (2.13) requires, to construct n and then V_{H}, the knowledge of all the $\{\psi_n\}$ which are themselves solutions of this equation, the problem has to be solved by the self-consistent field method (SCF) proposed by Hartree himself. From an initial guess $\{\psi_n^0\}$, a first density and then a first Hartree potential is calculated. With this potential, the Schrödinger equation is solved a first time to obtain a new set $\{\psi_n^1\}$, from which the cycle starts again. The calculation stops whenever a convergence criterium is reached. The latter can be for example that the eigenenergy differences from one iteration to the other needs to pass below a certain threshold, or that the wavefunctions have to not change anymore[8]. This SCF procedure is completely general and will be used also in the Hartree-Fock method as well as in Kohn-Sham DFT.

2.3.2.3 Hartree ansatz

One can prove that equation (2.13) follows from a minimization of the total energy $\langle \Psi_H | \hat{H} | \Psi_H \rangle$ if the following ansatz is used for the many-body wavefunction:

$$\Psi_{\text{H}}(q_1, q_2, ..., q_N) = \phi_1(q_1)\,\phi_2(q_2) \ldots \phi_N(q_N) \tag{2.14}$$

[8] Of course this has to be carefully quantified, and the choice of convergence criteria is crucial to carry out calculations. The choice strongly depends on the type of observables we are interested in.

which a simple product of spin-orbitals. The demonstration is due to Slater and Gaunt and does not correspond to the Hartree original approach [Blinder1965]. In this approach, the Hartree energies ϵ_n^{H} correspond to Lagrange multipliers, ensuring the normalization of the single-particle wavefunctions. One remarks that this Hartree ansatz does not obey the antisymmetry requirement. It therefore misses the so-called exchange interaction, which will be introduced by the Hartree-Fock wavefunction.

2.3.3 Hartree-Fock approximation and exchange

The antisymmetry of the many-body wavefunction can be enforced via a Slater determinant of all the occupied spin-orbitals:

$$\Psi_{\mathrm{HF}}(q_1, q_2, ..., q_N) = \frac{1}{\sqrt{N!}} \begin{vmatrix} \phi_1(q_1) & \phi_2(q_1) & \cdots & \phi_N(q_1) \\ \phi_1(q_2) & \phi_2(q_2) & \cdots & \phi_N(q_2) \\ \vdots & \vdots & \ddots & \vdots \\ \phi_1(q_N) & \phi_2(q_N) & \cdots & \phi_N(q_N) \end{vmatrix} \tag{2.15}$$

which is known as the Hartree-Fock (HF) approximation. One see that the spin-orbitals used to construct this determinant have to be different from each other, otherwise the wavefunction will be identically zero. In this way, the Pauli principle is obeyed. If the total energy $E_{\mathrm{HF}} = \langle \Psi_{\mathrm{HF}} | \hat{H} | \Psi_{\mathrm{HF}} \rangle$ is minimized with respect to the set of the spin-orbitals via the same procedure than for the Hartree ansatz, the problem reduces to a set of single-particle Schrödinger equations to be solved:

$$\left[\hat{h}(\mathbf{r}) + V_{\mathrm{H}}(\mathbf{r}) + \hat{V}_{\mathrm{X}} \right] \psi_n^{\sigma_n}(\mathbf{r}) = \epsilon_n^{\mathrm{HF}} \psi_n^{\sigma_n}(\mathbf{r}) \tag{2.16}$$

which involves only the spatial part of the wavefunctions, but with the indication of the spin associated. The Hartree potential appears once again but together with a new non-local operator, called the exchange potential (also known as Fock operator or exact exchange operator). The latter is defined by its action on one state n of spin σ_n:

$$\hat{V}_{\mathrm{X}} \psi_n^{\sigma_n}(\mathbf{r}) = - \sum_{m \text{ occ}} \left\{ \int d\mathbf{r}' \, \frac{\psi_m^{\sigma_m *}(\mathbf{r}') \psi_n^{\sigma_n}(\mathbf{r}')}{|\mathbf{r} - \mathbf{r}'|} \delta_{\sigma_n \sigma_m} \right\} \psi_m^{\sigma_m}(\mathbf{r}) \tag{2.17}$$

where the minus sign is due to the antisymmetry of Ψ_{HF}. As its name suggests, this operator "exchanges" the original state n with all the other occupied states *of the same spin* (one says it is spin-diagonal). The coefficients of the linear combination are calculated as orbital overlaps over all space, weighted by the Coulomb potential. Contrary to the Hartree potential, it is non-local since it does not simply multiply the wavefunction $\psi_n^{\sigma_n}(\mathbf{r})$ by a scalar potential evaluated locally, that is at the same point $\mathbf{r}$. This non-locality is the key difference with the Hartree method.

Similarly to the Hartree method, the HF method requires the SCF procedure to find a converged solution. Thanks to the term $m = n$ and the minus sign in the exchange potential definition (2.17), the artificial self-interaction in the Hartree potential is removed.

2.3.3.1 Physical relevance of exchange

The exchange interaction comes from the action of the Coulomb operator on an antisymmetric wavefunction, and is therefore genuinely quantum contrary to the Hartree interaction. It is proven to be extremely important to understand properties of matter. For example, it is responsible for the existence of finite bounding lengths. Without it, the particles will only repel each others and will never form solids or molecules. It is also responsible for the existence of magnetic orders.

2.3.3.2 Definition of the correlation energy

The HF exchange defines the word "correlation" as used in the *ab initio* community. Indeed, the total correlation energy is defined [Löwdin1955, Wigner1934] as the difference between the "true" total energy one would obtain by solving the many-body Schrödinger equation, and the HF one:

$$E_c = \langle \Psi | \hat{H} | \Psi \rangle - \langle \Psi_{\text{HF}} | \hat{H} | \Psi_{\text{HF}} \rangle = E - E_{\text{HF}} \tag{2.18}$$

Therefore, the correlation energy includes all the effects which cannot be described by the HF wavefunction, in particular correlations between electrons of *opposite spins*. Its definition is purely conventional as it is not associated with a new physical interaction (it is due to the electron-electron term (2.5) in $\hat{H}$), but comes from the choice of the Hartree-Fock ansatz for the wavefunction. By definition, the correlation energy is unknown and one can only approach it via refining calculation methods.

2.3.3.3 Koopman's theorem

If one assume that the many-body wavefunction of the $(N-1)$-electron system in its i-th excited states can be written as the Slater determinant of all the spin-orbitals of the N-electron system except ϕ_i (i.e. the relaxation of the spin-orbitals after the electron removal is neglected), then the removal energy is formally equal to the HF eigenenergy corresponding to ϕ_i:

$$E_N - E_{N-1,i} = \langle \Psi_N | \hat{H} | \Psi_N \rangle - \langle \Psi_{N-1,i} | \hat{H} | \Psi_{N-1,i} \rangle = \epsilon_i^{\text{HF}} \tag{2.19}$$

Equivalently for the $(N+1)$-electron system for which an unoccupied ϕ_i is added in the Slater determinant one can write:

$$E_{N+1,i} - E_N = \langle \Psi_{N+1,i} | \hat{H} | \Psi_{N+1,i} \rangle - \langle \Psi_N | \hat{H} | \Psi_N \rangle = \epsilon_i^{\text{HF}} \tag{2.20}$$

Thus, in this so-called adiabatic approximation, the HF eigenenergies are not simple Lagrange multipliers but have a real physical interpretation as addition and removal energies of electrons, which are observables measured in photoemission experiments (see Sec. 4.3). However, it does not mean that the HF energies are always reliable, since correlations are missing. For example in semiconductors and insulators, HF has the tendency to strongly overestimate the gap.

2.3.3.4 Formulation in terms of self-energy

To pave the way for many-body perturbation theory (MBPT) and the *GW* approximation which will be introduced in the two next chapters, equation (2.16) can be alternatively written in this integral form [Martin2016]:

$$\left[\hat{h}(\mathbf{r}) + V_{\text{H}}(\mathbf{r})\right] \psi_n^{\sigma_n}(\mathbf{r}) + \int d\mathbf{r}' \, \Sigma_{\text{X}}^{\sigma_n}(\mathbf{r}, \mathbf{r}') \psi_n^{\sigma_n}(\mathbf{r}') = \epsilon_n^{\text{HF}} \psi_n^{\sigma_n}(\mathbf{r}) \tag{2.21}$$

with the non-local exchange self-energy defined as:

$$\Sigma_{\text{X}}^{\sigma_n}(\mathbf{r}, \mathbf{r}') = -\sum_{m}^{\text{occ}} \frac{\psi_m^{\sigma_m *}(\mathbf{r}') \psi_m^{\sigma_m}(\mathbf{r})}{|\mathbf{r} - \mathbf{r}'|} \delta_{\sigma_n \sigma_m} \tag{2.22}$$

which will be one of the two components of the *GW* self-energy (5.9). As in formula (2.17), the Kronecker delta ensures that ψ_n interacts via exchange only with orbitals ψ_m having the same spin, that is if $\sigma_m = \sigma_n$.

References

[Blinder1965] S. M. Blinder. *Basic Concepts of Self-Consistent-Field Theory*. American Journal of Physics, vol. 33, no. 6, pages 431–443, June 1965. doi:10.1119/1.1971665.

[Dirac1929] Paul Adrien Maurice Dirac. *Quantum Mechanics of Many-Electron Systems*. Proceedings of the Royal Society of London. Series A, Containing Papers of a Mathematical and Physical Character, vol. 123, no. 792, pages 714–733, 1929. URL: `https://www.jstor.org/stable/95222`.

[Hartree1928] D. R. Hartree. *The Wave Mechanics of an Atom with a Non-Coulomb Central Field. Part I. Theory and Methods*. Mathematical Proceedings of the Cambridge Philosophical Society, vol. 24, no. 1, pages 89–110, January 1928. doi:10.1017/S0305004100011919.

[Löwdin1955] Per-Olov Löwdin. *Quantum Theory of Many-Particle Systems. III. Extension of the Hartree-Fock Scheme to Include Degenerate Systems and Correlation Effects*. Physical Review, vol. 97, no. 6, pages 1509–1520, March 1955. doi:10.1103/PhysRev.97.1509.

[Martin2016] Richard M. Martin, Lucia Reining and David M. Ceperley. Interacting Electrons: Theory and Computational Approaches. Cambridge University Press, Cambridge, 2016. Exponential scaling: sec. 1.2, definition of the correlation energy: sec. 2.1, exchange self-energy: sec. 4.1. doi:10.1017/CBO9781139050807.

[Wigner1934] E. Wigner. *On the Interaction of Electrons in Metals*. Physical Review, vol. 46, no. 11, pages 1002–1011, December 1934. doi:10.1103/PhysRev.46.1002.

3
Density Functional Theory

When I find my model's unpredictive,
Walter Kohn just comes to me,
speaking words of wisdom,
DFTee...

DFT song by Volker Blum and Kieron Burk,
to the tune of *Let it be*[1]

3.1 General idea

In the previous chapter, we have seen that the many-body wavefunction is a tremendously complicated object and the resolution of the eigenvalue problem $\hat{H}\Psi = E\Psi$ is untractable already for a few electrons. As its name suggests, the idea of density functional theory (DFT) is to work with the total electronic density $n(\mathbf{r})$ instead of Ψ. The formal definition of the density reads as the integral of the many-body wavefunction over all space-variables *but one* times N:

$$n(\mathbf{r}) = N \int d\mathbf{r}_2 \cdots \int d\mathbf{r}_N \, |\Psi(\mathbf{r}, \mathbf{r}_2, \cdots, \mathbf{r}_N)|^2 \tag{3.1}$$

where we have supposed that the system is non-spin-polarized, so that Ψ designates only the spatial-part of the total wavefunction[2]. The density has the advantage to be a much simpler and compact mathematical object, depending on only one space-variable, thus requiring only M real positive numbers to be stored (if one takes the same mesh than in Sec. 2.2.2) and which can be easily visualized in 3D. Indeed, this object does not suffer from the exponential wall, as

[1] The full lyrics as well as a terrible version can be found in [Burk2017] at 24:15.

[2] If the hamiltonian does not contain terms coupling spin and orbital degrees of freedom, then Ψ can be factorized in separated orbital and spin parts (analogously to ϕ in the single-electron case). As the spin-part normalizes to one when summed over the spin-space $\sum_{\sigma\sigma_2\ldots\sigma_N}$, it disappears from the density formula.

its size does not depend on N. Moreover, it is a tangible physical quantity since it corresponds to the distribution of the negative charges in the system (i.e. the electronic cloud), which in principle can be probed experimentally.

3.2 Hohenberg-Kohn theorem

One wants to work with the density to study matter, predict its properties, calculate observables, etc., because it is a simple and handleable object. The validity and the usefulness of this approach is however not trivial at all. A key question is whether the density $n(\mathbf{r})$ completely characterized the system. The rigorous mathematical formulation of DFT is given by the Hohenberg-Kohn (HK) theorem.

3.2.1 One-to-one correspondence between $V_{\mathbf{ext}}$, Ψ and n

Let us consider a system at $T = 0$ K in its ground-state. We know that the external potential V_{ext} is the only term in the hamiltonian which is specific to the physical system of interest. Although not tractable, solving the many-body Schrödinger equation (MBSE) with this external potential would in principle enable to obtain the ground-state wavefunction Ψ, which is unique if the latter is non-degenerate[3]. One can easily understand that two different potentials (differing by more than a constant) cannot give the same ground-state wavefunction via the MBSE, otherwise two different physical systems would have the same ground-state[4]. That is, there is a one-to-one correspondence (i.e. a bijection) between V_{ext} and Ψ, that we write symbolically $V_{\text{ext}} \underset{\text{MBSE}}{\leftrightarrow} \Psi$.

From a given GS wavefunction Ψ (which correspond to a unique V_{ext}), one can calculate the associated ground-state density n via its explicit mathematical definition (3.1). Symbolically:

$$(V_{\text{ext}} \underset{\text{MBSE}}{\leftrightarrow} \Psi) \underset{\text{explicit}}{\longrightarrow} n \tag{3.2}$$

The Hohenberg-Kohn theorem states that the reciprocal is true, i.e. the ground-state density N of a many-electron system determines uniquely the external potential V_{ext}, modulo one noninfluent constant, and then also the ground-state wavefunction [Hohenberg1964].

$$(V_{\text{ext}} \underset{\text{MBSE}}{\leftrightarrow} \Psi) \underset{\text{HK}}{\longleftarrow} n \tag{3.3}$$

Hence, there is a one-to-one correspondence between V_{ext}, Ψ and n, which is illustrated in Fig. 3.1. The proof of the HK theorem proceed by a quite simple *reductio ad absurdum* and can be found in the seminal paper [Hohenberg1964].

Let us begin by a discussion about the bijection $\Psi \leftrightarrow n$. This is a very strong result: one could have thought that two different wavefunctions can give the same density via formula (3.1), by some symmetry or even by accident, since the integration can wash the differences out. But this is not the case and Ψ, despite its monstrous complexity, does not contain more information

[3] We suppose a non-degenerate ground-state for simplicity, but the HK theorem has also been proven for the case of degenerate ground-states.

[4] In fact, this statement can be more rigorously proven, see *Demonstration of the Hohenberg-Kohn theorem* in [Sottile2021], but it is not at the heart of the HK theorem.

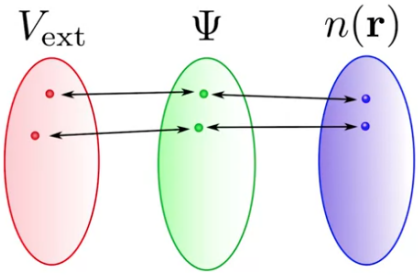

Figure 3.1: Illustration of the HK theorem: there is a one-to-one correspondence (i.e. a bijection) between the external potential, the GS many-electron wavefunction and the GS electronic density. From [Sottile2021].

than the density. On the other hand, the bijection $V_{\text{ext}} \leftrightarrow n$ tells us that the density also entirely characterized the system.

In order to describe the physical properties of matter, one would like to calculate observables. An observable $\mathcal{O}$ is formally defined as the expectation value of the corresponding operator $\hat{\mathcal{O}}$ sandwiched by the many-body state Ψ. Hence, any observable is an explicit functional of Ψ:

$$\mathcal{O} = \langle \Psi | \hat{\mathcal{O}} | \Psi \rangle \underset{\text{explicit}}{=} \mathcal{O}[\Psi] \tag{3.4}$$

As a consequence, the one-to-one correspondence of the HK theorem enables us to say that as a functional of Ψ, any observable can also be written as a functional of the density

$$\mathcal{O} \underset{\text{HK}}{=} \mathcal{O}[n] \tag{3.5}$$

which is unique but likely implicit. Therefore, the HK theorem rigorously validates the idea at the basis of DFT, that is to work with the density instead of the many-body wavefunction[5]. However, it does not tell us how to write these functionals explicitly.

3.2.2 Variational principle

Now, let us look at one very special observable which is ruling the system: the ground-state total energy E. By the HK theorem, it can in principle be written as a functional of the GS density:

$$E = E[n] \tag{3.6}$$

Let us choose a trial density $\tilde{n}$ instead of n and plug it into the energy functional, assuming we have an explicit expression for it. The well known variational principle tells us that if one minimizes $E[\tilde{n}]$ by optimizing $\tilde{n}$, one will find the actual GS total energy E corresponding to the actual GS density n:

$$E = \min_{\text{wrt } \tilde{n}} E[\tilde{n}] = E[\tilde{n}=n] \tag{3.7}$$

In other words, the variational principle gives us a method to find the GS total energy of a system with its associated density, assuming we know the energy functional. This is game-changing since the problem of minimizing a quantity with respect to a mathematical object of one space-variable (n) is far easier than doing the same for a N space-variables object (Ψ).

[5] Actually, the idea to use the density in physical equations is anterior to DFT and traces back to the Thomas-Fermi model, but this model was too limited to be successful (e.g. it did not lead to any chemical binding).

This result is sometimes called the 2nd part of the HK theorem or even the 2nd HK theorem, even though it is only a consequence of it and of the variational principle.

Structural relaxation An explicit total energy functional of the density enables to find the equilibrium structure of solids and molecules (i.e. lattice constants and atomic positions within the unit-cell, or bond lengths and angles), which is among the main goals of *ab initio* calculations. The procedure is the following: one starts with an initial guess for the geometry of the system, corresponding to an external potential V_{ext}^0. A first minimization of the energy functional with respect to $\tilde{n}$ is performed to obtain the initial total energy E^0. As it is not necessary the lowest total energy for the system, the atoms are moved corresponding to the forces exerted on them and the procedure is repeated, every time with a new V_{ext}, until E finds its minimum value. The last V_{ext} then corresponds to the equilibrium structure, at which the forces vanish, hence the term "relaxation". This procedure enables in particular to predict structural phase transition (e.g. with respect to pressure or doping). Via tiny displacement from the equilibrium position, one can calculate the forces on atoms and deduces the so-called frozen phonon spectrum.

But at this point, beyond the fact that one still do not know an expression for $E[n]$, it is anyway very difficult to perform a functional minimization with respect to n in practice. Actually, there are a very few methods which work in the way of the HK theorems. The vast majority of the DFT implementations uses the Kohn-Sham method.

3.3 The Kohn-Sham method

A common approach to study a very complex system is to isolate the effect of interest and to find an auxiliary system which produces the same effect than the real system. Of course, this auxiliary system cannot reproduce the other physical properties and behavior of the complete system correctly. Let us take an analogy inspired from [Sottile2021]. If one want to study the effects of life in space on the human body, but cannot send an astronaut for a space travel (because it is too expensive in terms of resources, money or whatever), one can at least *choose* to simulate only the effect of say, weightlessness, in an easier and more accessible way. The auxiliary system associated is the zero-G plane which will reproduce weightlessness for the passengers by taking a parabolic trajectory. Of course, all the other effects of life in space (e.g. radiation effects, disruption of the biological clock, etc.) are not described by this auxiliary system, but it is better than nothing as it can simulate at least one of these effects.

Coming back to our many-electron problem, the quantity one wants to reproduce is the *ground-state* electronic density n. As we know from the HK theorem, the GS total energy E is a functional of the density (for which we suppose we have an expression). So if the auxiliary system is able to reproduce the GS density of the real system, it will enable to calculate the corresponding GS total energy and perform structural relaxations for example. It will also enable in principle to calculate any observable, as they are all functionals of n.

The simplest auxiliary system one can work with is a system of N non-interacting electrons that somehow reproduces the total electronic density, which is the approach that Kohn and Sham proposed in 1965 [Kohn1965]. As these electrons are non-interacting, one can solve a single-particle Schrödinger-like equation with a local effective potential designed to take all the

interaction effects into account, in a mean-field approach. This equation reads:

$$\left[-\frac{1}{2}\nabla^2 + V_{\text{KS}}(\mathbf{r})\right]\psi^{\text{KS}}(\mathbf{r}) = \epsilon^{\text{KS}}\psi^{\text{KS}}(\mathbf{r}) \tag{3.8}$$

with V_{KS}, ψ^{KS} and ϵ^{KS} the Kohn-Sham (KS) potential, orbitals and eigenenergies, respectively. This equation has an infinity of solutions $\{\psi_i^{\text{KS}}, \epsilon_i^{\text{KS}}\}$, which have to be filled with two electrons per state by increasing energy to obey the Pauli principle. Similarly as in the Hartree and HF cases, the total electronic density is calculated as the sum of single-electron densites:

$$n(\mathbf{r}) = \sum_{i}^{N_{\text{occ}}} \left|\psi_i^{\text{KS}}(\mathbf{r})\right|^2 \tag{3.9}$$

All the difficulty lies in the construction of the KS potential. A natural way to address the problem is to decompose it in the following manner:

$$V_{\text{KS}}[n](\mathbf{r}) = V_{\text{ext}}(\mathbf{r}) + V_{\text{H}}[n](\mathbf{r}) + V_{\text{XC}}[n](\mathbf{r}) \tag{3.10}$$

The external potential is known and the Hartree potential can be explicitely calculated by formula (2.12) from which it is obvious that it is a functional of the density. The so-called exchange-correlation potential V_{XC} consists in all the rest, that is all the quantum effects due to the Coulomb interaction which are beyond the Hartree classical term[6]. This decomposition of the KS potential is particularly convenient if it ranges from the highest to the lowest magnitude term. Indeed, the Bloch single-particle hamiltonian $\hat{h} = -\frac{1}{2}\nabla^2 + V_{\text{ext}}(\mathbf{r})$ generally gives a good idea of the dispersion, hence it is the dominant term. The Hartree potential usually have relatively smaller variations in magnitude since the electron cloud is far more delocalized than the nuclei. Finally, V_{XC} is supposed to be smaller than these two first terms (which does not mean it is not crucial[7]). Since no explicit expression is known, one have to approximate it. Due to the relatively smaller magnitude of this term, the approximation is supposed to have a limited impact on the results. Approaches to write it as a functional of the density will be introduced in Sec. 3.4.

The KS equations (3.8), (3.9) and (3.10) are self-consistent and one should therefore use the same SCF method than in the Hartree and HF methods (see Sec. 2.3.2.2). The KS formulation is the key of the DFT success, as it transforms it from a difficult functional minimization problem into a tractable problem of solving a Schrödinger equation self-consistently. Indeed, as the exponential wall disappears, the simulation of very large systems with hundreds or even thousands of electrons becomes possible[8]. KS-DFT is the most widely used computational method in the physics and chemistry communities, in areas as diverse as condensed matter, molecular physics, astrophysics, biology, etc. Thanks to this success, Walter Kohn received the 1998 Nobel Prize in chemistry.

3.3.1 Interpretation of the Kohn-Sham eigenvalues

Here comes an important discussion, especially in the context of this PhD thesis, dedicated to the description of electronic structures within the *GW* approximation. As we have insisted on, the KS auxiliary system is designed to reproduce the "true" GS electronic density and the total energy associated, but no more. The KS orbitals ψ^{KS} and eigenenergies ϵ^{KS} correspond to a

[6] In fact, it should also account for corrections to the kinetic energy of the non-interacting KS system towards the kinetic energy of the real interacting system.

[7] Crucial for example to find equilibrium positions, which are sensible to slight variations of the total potential.

[8] The scaling of DFT is still in $O(N^3)$ because of the diagonalization of the KS equation.

fictitious system of non-interacting electrons. In fact, as in the Hartree and HF cases, the KS eigenvalues are only Lagrange multipliers. Contrary to Hartree-Fock, there is no Koopman's theorem (see Sec. 2.3.3.3) in KS-DFT[9]. Hence in principle, the latter cannot be formally interpreted as "real" single-particle energies.

However in practice, the dispersion of the KS electrons are often quite representative of the actual single-particle dispersion within the material[10]. A notable case in which it fails is the calculation of the bandgap of insulators and semiconductors, which is inaccurately reproduced. In metals, this eigenvalue problem is less important. In particular in nickelates, which are in most of the cases metals, the KS description of the electronic structure is just estimated to be satisfying relatively to cuprates, which are antiferromagnetic insulators.

The satisfying description of electronic structures by the KS eigenvalues can have two reasons: (i) the exchange-correlation term is weak enough in magnitude and/or (ii) its approximation works quite well for single-particle energies, even thought it has been designed in the first place to reproduce the total electronic density. However, they can completely fail to describe the electronic structure of more correlated materials, where the inaccurate exchange-correlation potential introduces too much error and/or where the mean-field approach fails to describe single-particle energies. These KS energies have then to be taken carefully.

But KS-DFT is often the most affordable and fastest method to address many-electron systems. The methods which go beyond DFT, more legitimate to provide single-particle quantities, are indeed way more cumbersome. It explains why KS eigenvalues are massively used as representing the "real" electronic structure, in order for example to fit tight-binding models.

KS orbitals and eigenvalues are nevertheless often a quite good starting point for methods formulated as perturbation theories, which will be introduced in the next chapter. In these methods, the "physicality" of the single-particle energies will be recovered as representing addition and removal energies of electrons, as measured in ARPES experiments (see Sec. 4.3).

3.4 Exchange-correlation functionals

The success or the failure of KS-DFT essentially relies on the appropriateness of the exchange-correlation potential. Let us first introduce the exchange-correlation energy functional E_{XC} which defines the potential of the same name as its functional derivative:

$$V_{\text{XC}}[n](\mathbf{r}) = \left.\frac{\delta E_{\text{XC}}[\tilde{n}]}{\delta \tilde{n}(\mathbf{r})}\right|_{\tilde{n}(\mathbf{r})=n(\mathbf{r})} \tag{3.11}$$

Actually, we could have introduced E_{XC} in the first place as it is done in many rigorous textbooks, but we have preferred to focus on the KS method where the potential is the central object. The goal is to get an expression for $E_{\text{XC}}[n]$, in order to derive the corresponding potential

[9] In fact, there is at least one KS eigenvalue that have a physical interpretation, but only in finite-size systems (i.e. molecules): the energy of the highest occupied state, whose magnitudes relative to the vacuum equals the ionization energy. This is a particular case of the Janak's theorem that holds in KS-DFT, which is a weaker version of the Koopman's theorem [Kümmel2008].

[10] One should rather speak about quasiparticle dispersion, but this concept will be introduced in the next chapter.

V_{XC} via formula (3.11). In the following subsections, three different approaches to write the exchange-correlation functional will be introduced. Beyond the fact that they illustrate well the increasing complexity of the exchange-correlation functional design, these three functionals have been used and compared between them in our work about the infinite-layer nickelates presented in Chap. 7.

3.4.1 Local density approximation (LDA)

There is one reference system for which an analytical expression for the exchange energy is known: the homogeneous electron gas (HEG) where the electronic density $\bar{n} = N/V$ is constant. The exchange energy *density* is in this case a *function* of $\bar{n}$ (and not a functional) and reads:

$$\varepsilon_X^{HEG}(\bar{n}) = \frac{E_X^{HEG}(\bar{n})}{V} = -\frac{(3\pi^2\bar{n})^{4/3}}{4\pi^3} \tag{3.12}$$

The correlation energy density ε_C^{HEG} has no analytical expression but it is possible to fit an almost exact formula on Monte-Carlo data [Ceperley1980]. The total exchange-correlation reads of course:

$$\varepsilon_{XC}^{HEG}(\bar{n}) = \varepsilon_X^{HEG}(\bar{n}) + \varepsilon_C^{HEG}(\bar{n}) \tag{3.13}$$

The idea of the so-called local density approximation (LDA) proposed in the same paper than the KS method [Kohn1965] is simply to consider that the exchange-correlation energy of an inhomogeneous electron cloud of density $n(\mathbf{r})$ can be calculated as

$$E_{XC}^{LDA}[n] = \int d\mathbf{r}\, \varepsilon_{XC}^{HEG}(n(\mathbf{r})) \tag{3.14}$$

This is exactly as if we have considered the density constant in an infinitesimal volume $d\mathbf{r}$ so that the HEG formula applies, and then summed all these local contributions over the entire volume.

LDA is extremely successful to predict some observables, for example lattice parameters of many solids (it typically gives it with a relative error of only 1 or 2%). One can think, in the case of metals, that this is due to the valence electrons which are sufficiently delocalized to form a relatively homogeneous electron gas with a slowly varying density, so that the LDA works well. But as the predictions of lattice parameters work also extremely well for insulators, there should be an averaging effect that makes the LDA work even for systems where the density is less homogeneous[11].

3.4.2 Generalized gradient approximation (GGA) and PBE

The hypothesis of an exchange-correlation functional depending only on the local density at $\mathbf{r}$ seems quite crude for systems with rapidly varying densities. The idea of the generalized gradient approximation (GGA) is to also take into account the local gradient of the density $\nabla n(\mathbf{r})$. Thus, it is called a semi-local functional since to numerically calculate the local gradient, one needs to know the density in the neighborhood of $\mathbf{r}$. The energy density is, like in the LDA, only a function but of these two local quantities, so that the GGA exchange-correlation energy reads:

$$E_{XC}^{GGA}[n] = \int d\mathbf{r}\, \varepsilon_{XC}^{GGA}(n(\mathbf{r}), \nabla n(\mathbf{r})) \tag{3.15}$$

The most widely used exchange-correlation functional is nowadays the PBE functional named after Perdew, Burke and Ernzerhof who designed it [Perdew1996]. It is a GGA functional

[11] This is due to the fact that LDA fulfill exact constraints, see [Sottile2021].

without empirical parameters[12], contrary to many others GGA functionals which are fitted to reproduce properties of a given class of systems. Although a bit less accurate than the latter for specific systems, PBE is more general and gives relatively satisfying results for a wider range of systems. PBE improves the LDA results for many properties and are not much more expansive, but still have failures, for example to describe weakly bonded systems (e.g. layered system with van der Waals bounds).

3.4.3 Hybrid functionals and HSE06

As we have already a lot insisted on, the local KS potential is not designed to reproduce single-particle energies but the total electronic density. Yet, we are still very interested in these energies, for example to calculate a bandgap. The idea is the following: if one gives more degree of freedom to the KS potential, for example allowing it to be non-local, the auxiliary system can reproduce more observables. The idea of hybrids is just to incorporate in the exchange-correlation functional a portion of HF exact exchange (2.17) evaluated with the KS orbitals ψ_i^{KS}. The KS scheme has then to be generalized: the effective potential involved in the KS equation (3.8) is now non-local. This idea turns out to work: the bandgaps calculated with hybrids are closer to experiment. In fact, it can be seen as an average between the underestimation of the gap by LDA and GGAs and its overestimation by HF.

The introduction of exact-exchange has the effect to remove part of the self-interaction, which is a known problem of usual local functionals when addressing systems with highly-localized electrons (such as *d* and *f*). But the hybrids have the drawbacks of their advantages, the exact-exchange being computationally expansive especially for solids treated with plane waves codes.

HSE functionals, named after Heyd, Scuseria and Ernzerhof [Heyd2003], are range-separated hybrids: they use a mixture of HF exchange and PBE exchange at short-range (sr), while only PBE exchange at long-range (lr). The correlation part is the one of PBE at any range. It reads:

$$E_{\text{XC}}^{\text{HSE}} = aE_{\text{X}}^{\text{HF,sr}}(\omega) + (1-a)E_{\text{X}}^{\text{PBE,sr}}(\omega) + E_{\text{X}}^{\text{PBE,lr}}(\omega) + E_{\text{C}}^{\text{PBE}} \tag{3.16}$$

where a is the mixing parameter and ω a parameter controlling the short-range/long-range separation. HSE06 corresponds to the special choice $a = 1/4$ and $\omega = 0.2$. The range separation allows an effective description of the screening, which decreases the range of the Coulomb interaction especially in metals. Thus, HSE incorporates a portion of exact-exchange with an effective static screening. This is in between HF and *GW* (which will be introduced in Chap. 5), the latter being described as a dynamically screened version of HF (see Sec. 5.3.2). Hence, the HSE functionals can be seen as approximations to *GW*.

3.4.4 Wrap-up on functionals

The initial success of KS-DFT is also due to the success of LDA, which works surprisingly well despite its simplicity. Further improvements led to GGAs and in particular PBE, which has been the default functional used in this PhD work to determine structural properties. If LDA and GGAs are good at predicting the structure of solids, they highly underestimate the bandgap (usually by ∼30-50%, see Fig. 5.8). It illustrates well the problem of the KS eigenvalues: the density and the total energy are well described, but not this important feature of the electronic structure. Further inclusion of exact exchange in the hybrids helps to reduce the bandgap

[12] PBE does not involve empirical parameters, but it still involves a choice of the exact constraints the functional fulfilled, as not all of them can be.

problem (although the density and the total energy are less accurately described than with LDA or GGAs, so it is not better from every angle). Of course, exchange-correlation functionals fails in general to describe the electronic structure of strongly correlated systems.

References

The MOOC *Density Functional Theory* by F. Sottile and L. Reining [Sottile2021] is a very pedagogical introduction to DFT, that covers the basic aspects of this theory as well as some really advanced ones. The paper *A bird's-eye view of density-functional theory* based on the lectures given by K. Capelle [Capelle2006] was also really helpfull to understand this theory. The Walter Kohn's Nobel lecture [Kohn1999] is interesting to read in a second time, when one have already understood the basics of DFT.

[Burk2017] Kieron Burk. *Concluding remarks and DFT song*, June 2017. Timecode: 24:15. For a pdf with the full lyrics: https://openscholar.huji.ac.il/sites/default/files/elikraisler/files/dft_song.pdf. URL: `https://www.youtube.com/watch?v=9kUSpd5F_44&t=1455s`.

[Capelle2006] Klaus Capelle. *A bird's-eye view of density-functional theory*. Brazilian Journal of Physics, vol. 36, pages 1318–1343, December 2006. doi:10.1590/S0103-97332006000700035.

[Ceperley1980] D. M. Ceperley and B. J. Alder. *Ground State of the Electron Gas by a Stochastic Method*. Physical Review Letters, vol. 45, no. 7, pages 566–569, August 1980. doi:10.1103/PhysRevLett.45.566.

[Heyd2003] Jochen Heyd, Gustavo E. Scuseria and Matthias Ernzerhof. *Hybrid functionals based on a screened Coulomb potential*. The Journal of Chemical Physics, vol. 118, no. 18, pages 8207–8215, May 2003. doi:10.1063/1.1564060.

[Hohenberg1964] P. Hohenberg and W. Kohn. *Inhomogeneous Electron Gas*. Physical Review, vol. 136, no. 3B, pages B864–B871, November 1964. doi:10.1103/PhysRev.136.B864.

[Kohn1965] W. Kohn and L. J. Sham. *Self-Consistent Equations Including Exchange and Correlation Effects*. Physical Review, vol. 140, no. 4A, pages A1133–A1138, November 1965. doi:10.1103/PhysRev.140.A1133.

[Kohn1999] W. Kohn. *Nobel Lecture: Electronic structure of matter—wave functions and density functionals*. Reviews of Modern Physics, vol. 71, no. 5, pages 1253–1266, October 1999. doi:10.1103/RevModPhys.71.1253.

[Kümmel2008] Stephan Kümmel and Leeor Kronik. *Orbital-dependent density functionals: Theory and applications*. Reviews of Modern Physics, vol. 80, no. 1, pages 3–60, January 2008. doi:10.1103/RevModPhys.80.3.

[Perdew1996] John P. Perdew, Kieron Burke and Matthias Ernzerhof. *Generalized Gradient Approximation Made Simple*. Physical Review Letters, vol. 77, no. 18, pages 3865–3868, October 1996. doi:10.1103/PhysRevLett.77.3865.

[Sottile2021] Francesco Sottile and Lucia Reining. *MOOC "Density Functional Theory"*, 2021. *Demonstration of the Hohenberg-Kohn theorem* in module 1, *Exact constraints and GGA* in module 3. URL: `https://www.coursera.org/learn/density-functional-theory`.

4

Many-body perturbation theory

Many bod-eee, not DFT,
Many bod-eee, no densitee,
this must be the answer,
on which we'll all agree!

DFT song by Volker Blum and Kieron Burk,
to the tune of *Let it be*

To go beyond Hartree-Fock and Kohn-Sham DFT, other methods are required to include some more many-body effects. Many-body perturbation theory (MBPT) is, as its name suggests, build by adding corrections on top of a mean-field solution. A key ingredient of MBPT is the Green's function formalism which is a powerful tool to treat perturbations. The notions of self-energy and quasiparticle are central and will be defined in this chapter. As in the DFT chapter, we consider a system at $T = 0$ and we suppose that there is no spin-polarization for simplification purpose.

4.1 Green's functions

A Green's function is a general mathematical object associated with a differential equation. In our case, it describes how the many-body system reacts to a local "excitation" (in space and time), that is how this perturbation propagates.

4.1.1 Definition

The object one has to consider is the single-particle Green's function, which is the probability amplitude for the propagation of one particle, but *through the many-body system*. We will work with the second quantization formalism, in the Heisenberg picture where operators depend on time while the states do not (which enables to use the T-product). Let us define first the

electron propagator as:

$$K^e(\mathbf{r}_1, t_1; \mathbf{r}_2, t_2) = \left\langle \Psi_0^N \middle| \hat{\psi}(\mathbf{r_1}, t_1)\hat{\psi}^\dagger(\mathbf{r_2}, t_2) \middle| \Psi_0^N \right\rangle \tag{4.1}$$

with $\hat{\psi}^\dagger$ and $\hat{\psi}$ the creation and annihilation field operators. This formula is interpreted as follows: at time t_2 an electron is added to the ground-state $\left|\Psi_0^N\right\rangle$ at a position $\mathbf{r}_2$. The system is now a $(N+1)$ electrons system in an excited state. As we then project it onto another state $\hat{\psi}^\dagger(\mathbf{r_1}, t_1)\left|\Psi_0^N\right\rangle$, this bracket measures the overlap between two excited states with $(N+1)$ electrons. In other words, it corresponds to the probability of finding an extra electron at $\mathbf{r_1}$ and t_1 knowing that it was added in $\mathbf{r_2}$ and t_2. For the propagation of a hole created by removing an electron from the ground-state, the propagator analogously reads:

$$K^h(\mathbf{r}_1, t_1; \mathbf{r}_2, t_2) = \left\langle \Psi_0^N \middle| \hat{\psi}^\dagger(\mathbf{r_1}, t_1)\hat{\psi}(\mathbf{r_2}, t_2) \middle| \Psi_0^N \right\rangle \tag{4.2}$$

These two mathematical objects are schematically depicted in Fig. 4.1. As we will see in section 4.3, they describe respectively the processes of inverse-photoemission and photoemission. In the rest of the manuscript we will use the short notation $1 = (\mathbf{r}_1, t_1, \sigma_1)$ for space-time-spin coordinates. The time-ordered Green's function, which is the one of interest in our case, is defined as

$$\begin{aligned} iG^T(1,2) &= \left\langle \Psi_0^N \middle| T\left\{\hat{\psi}(1)\hat{\psi}^\dagger(2)\right\} \middle| \Psi_0^N \right\rangle \\ &= \theta(t_1 - t_2)\left\langle \Psi_0^N \middle| \hat{\psi}(1)\hat{\psi}^\dagger(2) \middle| \Psi_0^N \right\rangle - \theta(t_2 - t_1)\left\langle \Psi_0^N \middle| \hat{\psi}^\dagger(2)\hat{\psi}(1) \middle| \Psi_0^N \right\rangle \\ &= \theta(t_1 - t_2)K^e(1,2) - \theta(t_2 - t_1)K^h(2,1) \end{aligned} \tag{4.3}$$

with $T\{..\}$ the T-product that sorts the operators by putting the earliest in time on the right and imposes causality with respect to this ordering (with the Heaviside θ functions). As in the second term one has to commute $\hat{\psi}(1)$ and $\hat{\psi}^\dagger(2)$ which are fermionic, a minus sign appears. If $t_1 > t_2$, it describes the propagation of an electron, if $t_1 < t_2$, it describes the propagation of a hole.

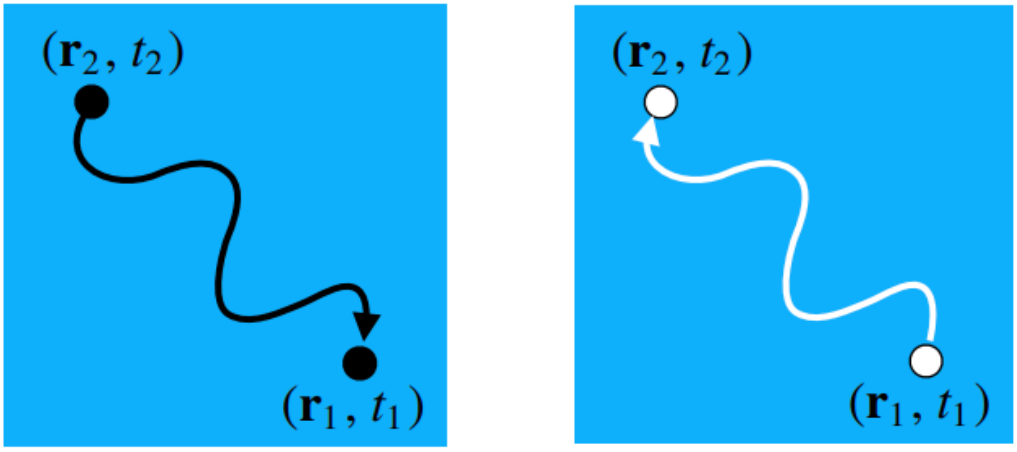

Figure 4.1: Illustration of the two terms involved in the time-ordered Green's function defined in eq. (4.3): the propagation of an electron from 2 to 1 (left), and the propagation of a hole from 1 to 2 (right) through the many-body system. From [Rignanese2014].

4.1.2 Lehmann representation in frequency domain

As the hamiltonian is time-independent, the only relevant time variable is the difference $t_1 - t_2$, hence the Fourier transform depends on a single frequency ω. But before moving to frequency

space, several quantities have to be defined. The total energy of the excited system where we added an electron is denoted E_i^{N+1}, and the total energy of the excited system where we removed an electron is denoted E_i^{N-1}. With respect to the ground-state energy E_0^N, we define the excitation energies:

$$\epsilon_i = E_i^{N+1} - E_0^N \tag{4.4}$$

and

$$\epsilon_i = E_0^N - E_i^{N-1} \tag{4.5}$$

which are respectively addition and removal energies of an electron as measured in photoemission spectroscopy. One has to notice that $E_i^{N\pm1}$ are the eigenenergies of the $(N\pm1)$ electrons system, which implies that they are real quantities, so are the excitation energies ϵ_i. The so-called Lehmann amplitudes are defined as the following:

$$f_i^{N+1}(\mathbf{r}) = \left\langle \Psi_0^N \middle| \hat{\psi}(\mathbf{r}) \middle| \Psi_i^{N+1} \right\rangle \tag{4.6}$$

and

$$f_i^{N-1}(\mathbf{r}) = \left\langle \Psi_i^{N-1} \middle| \hat{\psi}(\mathbf{r}) \middle| \Psi_0^N \right\rangle \tag{4.7}$$

where the eigenstates of the $(N\pm1)$ electrons system are expressed in the Heisenberg picture (time-independent) and the annihilation field operator in the Schrödinger picture (time-independent as well) [Blase2022]. These quantities are then both time-independent and will not be affected by the Fourier transformation. A case of particular interest for us is the non-interacting electron system, where the many-body wavefunction can be expressed (without approximation) as a Slater determinant of orbitals ψ_ℓ^0. In this situation, we simply have $f_\ell(\mathbf{r}) = \psi_\ell^0(\mathbf{r})$, i.e. the Lehmann amplitudes equal the single-particle wavefunctions.

Using closure relations on the $(N+1)$ and $(N-1)$-electrons systems eigenstates and introducing an infinitesimal energy η to make the Fourier transform convergent (with a sign depending on the occupation of the state i), one can show that at $T=0$ the time-ordered Green's function in frequency domain reads:

$$G^T(\mathbf{r}_1, \mathbf{r}_2, \omega) = \lim_{\eta\to0^+} \sum_i \frac{f_i(\mathbf{r}_1) f_i^*(\mathbf{r}_2)}{\omega - \epsilon_i + i\eta \mathrm{sgn}(\epsilon_i - \mu)} \tag{4.8}$$

with μ the chemical potential which at $T=0$ is simply the Fermi energy E_F. The expression that we choose for the f_i's between eq. (4.6) and (4.7) is determined by the sign of $\epsilon_i - \mu$ (hence we have dropped the $N\pm1$ superscripts), as well as the one we choose for the ϵ_i between eq. (4.4) and (4.5). This is the so-called Lehmann representation of the Green's function. We see that $G^T(\omega)$ has poles at addition and removal energies of the system but shifted from the real axis by an infinitesimal amount $i\eta$. In the rest of the manuscript the superscript T will be omitted as G will always refer to the time-ordered Green's function G^T.

4.2 Many-body perturbation theory

4.2.1 Self-energy and quasiparticles

As the many-body problem is untractable, it will be separated into two parts: a simplified one that is tractable exactly or at least numerically, and a complex one that includes the remaining degrees of freedom and requires approximations to be handled. For the physics to be correctly

described, the simple problem, embedded in the complete one, has to somehow "fill" it in an effective manner. This will be made possible by a dynamical[1] and non-local complex scalar field called the self-energy, central in MBPT, which acts as a potential. Contrary to the mean-field approaches where the static and local potentials are already approximations and miss physical effects, with such a self-energy all the physics is preserved. In other words, at this point it is an exact reformulation of the original many-body problem. However, we will have to use approximations to handle it. The name *self*-energy comes from the fact that the particle acts on its environment (i.e. all the other particles) and the environment gives a feedback. The action and then the feedback depends on the energy of the particle itself, hence the self-energy is energy-dependent[2]. This is not due to any time-dependence of the hamiltonian, which is static in our case. An enlightening explanation of the necessary energy-dependence of the self-energy is given in Chap. 7 of [Martin2016].

The properties of particles in this reduced problem will be renormalized or "dressed" by the many-body effects, resulting into so-called quasiparticles (QP). In our case, the quasiparticles are electrons or holes dressed by their environment, described as independent particles, which interact only in an effective manner via the self-energy. However, they do not correspond to eigenstates and have finite lifetimes, hence the name *quasi*-particles.

4.2.2 Dyson equation

We have seen that the object relevant to describe the propagation of quasiparticles is the single-particle Green's function G. Let G_0 be the one associated to the non-interacting system, which we choose as our reference system. The self-energy is defined as the most general correction from the non-interacting to the interacting inverse Green's function:

$$\Sigma(\mathbf{r}_1, \mathbf{r}_2, \omega) = G_0^{-1}(\mathbf{r}_1, \mathbf{r}_2, \omega) - G^{-1}(\mathbf{r}_1, \mathbf{r}_2, \omega) \tag{4.9}$$

and is of course unknown since G is unknown. Multiplying this equation by G_0 on the left and G on the right (in symbolic notation) and then re-arranging the terms gives:

$$G = G_0 + G_0 \Sigma G \tag{4.10}$$

which is the so-called Dyson equation for the self-energy. Plugging G into itself we can expand this expression to an arbitrary order:

$$\begin{aligned} G &= G_0 + G_0\Sigma(G_0 + G_0\Sigma G) \\ &= G_0 + G_0\Sigma G_0 + G_0\Sigma G_0\Sigma G \\ &= G_0 + G_0\Sigma G_0 + G_0\Sigma G_0\Sigma G_0 + \dots \end{aligned} \tag{4.11}$$

which is of practical interest since we can in principle truncate it whenever the required precision is reached. But since the higher is the order of perturbation, the more cumbersome are the calculations, we are more likely limited by our calculation capabilities.

One can understand the label many-body *perturbation theory* from this expression: the solution for G is G_0 but corrected by the self-energy. The closer is G_0 from G, the smaller is the self-energy (4.9) and the faster is the convergence of the Dyson serie (4.11). For the moment, our definition of the self-energy is self-consistent (since it depends on G, which we want to find

[1] Energy-dependant, time-dependent, frequency-dependant and dynamical are of course synonyms.

[2] Imagine one slow and one fast particle, i.e. with different kinetic energies: their action on their environment will be different, so their self-energies.

using Σ) and we cannot really use it. One exact expression will be designed in the next chapter, and then simplified by the use of the *GW* approximation. Let us assume for the moment that we get an expression for it.

4.2.3 Spectral function

A quantity of great interest in MBPT is the spectral function which is directly derived from the Green's function. Its definition is:

$$A(\mathbf{r}_1, \mathbf{r}_2, \omega) = \frac{1}{\pi} |\mathfrak{Im} G(\mathbf{r}_1, \mathbf{r}_2, \omega)| \tag{4.12}$$

From the Lehmann representation of G (4.8) and using the Sokhotski-Plemelj formula (for the real line):

$$\lim_{\eta \to 0^+} \frac{1}{x \pm i\eta} = \mathcal{P}\left(\frac{1}{x}\right) \mp i\pi\delta(x) \tag{4.13}$$

where $\mathcal{P}$ denotes the Cauchy principal value, we can derive this expression for the spectral function:

$$A(\mathbf{r}_1, \mathbf{r}_2, \omega) = \sum_i f_i(\mathbf{r}_1) f_i^*(\mathbf{r}_2) \delta(\omega - \epsilon_i) \tag{4.14}$$

which is a summation of Dirac δ-peaks lying at all the excitations energies of the system, weighted by the Lehmann amplitudes.

Matrix element in a single-particle orbitals basis set

Let us now express the spectral function in the orthonormal basis set $\{\psi_\ell^0\}$, corresponding to single-particle eigenstates of the non-interacting system. The matrix elements of the spectral function are defined as:

$$A_{\ell m}(\omega) = \int d\mathbf{r}_1 \int d\mathbf{r}_2 \, \psi_\ell^{0*}(\mathbf{r}_1) \psi_m^0(\mathbf{r}_2) A(\mathbf{r}_1, \mathbf{r}_2, \omega) \tag{4.15}$$

and they enable to write the spectral function as:

$$A(\mathbf{r}_1, \mathbf{r}_2, \omega) = \sum_{\ell m} \psi_\ell^0(\mathbf{r}_1) \psi_m^{0*}(\mathbf{r}_2) A_{\ell m}(\omega) \tag{4.16}$$

Thanks to this, we get rid of the double spatial dependence and it is particularly suitable to keep the single-particle picture, which is the idea of the quasiparticle approach. For the non-interacting system, A^0 is diagonal and matrix elements are just Dirac δ-peaks at the single-particle eigenenergies:

$$A^0_{\ell\ell}(\omega) \equiv A^0_\ell(\omega) = \delta(\omega - \epsilon^0_\ell) \tag{4.17}$$

which is consistent with equation (4.14) and (4.16) since $f_\ell = \psi^0_\ell$ for a non-interacting system. Now if we consider the interacting system, the diagonal matrix elements read:

$$A_\ell(\omega) = \sum_i \left| f_i^\ell \right|^2 \delta(\omega - \epsilon_i) \tag{4.18}$$

where we have defined

$$\begin{aligned} f_i^\ell &= \left\langle \Psi_0^N \middle| \hat{c}_\ell \middle| \Psi_i^{N+1} \right\rangle \quad \text{if } \epsilon_i - \mu > 0 \\ &= \left\langle \Psi_i^{N-1} \middle| \hat{c}_\ell \middle| \Psi_0^N \right\rangle \quad \text{if } \epsilon_i - \mu < 0 \end{aligned} \tag{4.19}$$

which corresponds to Lehmann amplitudes expressed in the chosen basis[3], and where the operator $\hat{c}_\ell$ annihilates the single-particle eigenstate $|\psi_\ell^0\rangle$. Since in an interacting system $\hat{c}_\ell|\Psi_i^{N+1}\rangle$ and $\hat{c}_\ell^\dagger|\Psi_i^{N-1}\rangle$ have no reason to be eigenstates of the many-body system with N particles, their projections f_i^ℓ onto $|\Psi_0^N\rangle$ have no reason to be zero. So we see in eq. (4.18) that the matrix element for the state ℓ is no longer a single δ-peak but rather a sum of δ-peaks located at excitation energies of the many-body system (the Lehmann energies $\epsilon_i \neq \epsilon_\ell^0$).

But if the non-interacting eigenstates are close enough to the actual quasiparticle states of the interacting-system, the main contribution in $A_\ell(\omega)$ will still be reminiscent of ϵ_ℓ^0 since it will contain a so-called quasiparticle peak at an energy ϵ_i close to ϵ_ℓ^0. This is one of the most important properties of a Fermi-liquid: there is a one-to-one correspondence between the non-interacting states and the quasiparticle states. Thanks to this continuity, it makes sense to assume that $\epsilon_i = \epsilon_\ell^{\text{QP}}$, blurring a bit the clear separation between single and many-body energies.

In other words, if the starting basis is a good approximation of the real system, the corrections to the energies $\epsilon_\ell^{\text{QP}} - \epsilon_\ell^0$ are small and the quasiparticle peaks are only slightly shifted from the original δ-peaks (see Fig. 4.3). The contributions coming from other states will be responsible for the appearance of so-called satellites at energies different from $\epsilon_\ell^{\text{QP}}$. For a finite system the spectrum of excitations is discrete but for an infinite system (like a crystal) it is continuous and the delta peaks in formula (4.18) will merge to form a continuum. These aspects are depicted in Fig. 4.2.

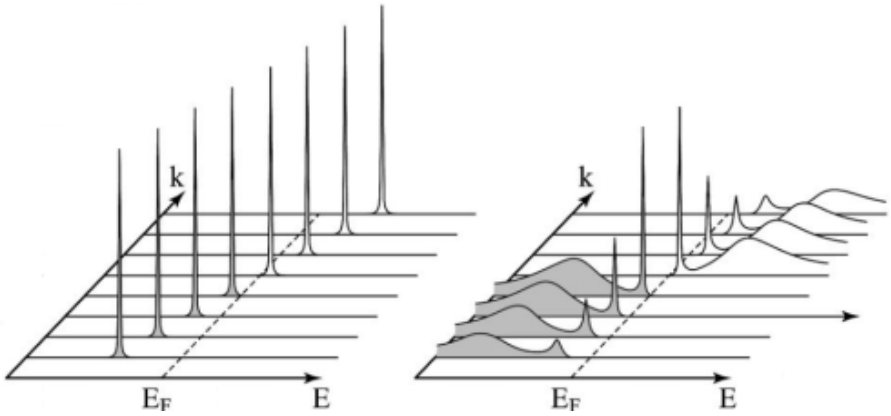

Figure 4.2: Illustration of the spectral function matrix elements $A_\ell(\omega)$ in the non-interacting case (left) and in the interacting case (right). On the right, we see the quasiparticle peaks reminiscent of the single-particle δ-peaks, as well as the appearance of satellites and a general broadening due to the infinite size of the system. One can notice the fact that the closer the quasiparticle peak is from E_F, the sharper it is, which is a general Fermi-liquid behavior (see Sec. 4.2.5). Adapted from [Damascelli2003].

As the Kohn-Sham orbitals $\{\psi^{\text{KS}}\}$ corresponds to an auxiliary system, we can use them as our basis. Of course, electron-electron interactions are taken into account in the KS system, but only in an effective way via the exchange-correlation potential V_{XC}. If we do not obtain a well-defined quasiparticle peak in $A_\ell(\omega)$, it can mean two things: either the quasiparticle picture is not good (because interactions are too strong) or the chosen basis is too far from the "true" QP wavefunctions (which can happen for d and f states for which KS orbitals are too spread).

[3] To obtain these expressions, we have used the expansion of the field operator in terms of single-orbitals: $\hat{\psi}(\mathbf{r}) = \sum_\ell \psi_\ell(\mathbf{r})\hat{c}_\ell$.

4.2.4 Quasiparticle energies

One would like to obtain the energies $\epsilon_i = \epsilon_\ell^{\mathrm{QP}}$ of these peaks. Let us first re-write the Green's function. Its diagonal matrix elements in the non-interacting basis should have new poles located at $\epsilon_\ell^{\mathrm{QP}}$. The corrections to the denominator which enable the shift of the poles are the diagonal matrix elements of the self-energy:

$$G_\ell(\omega) = \frac{1}{\omega - \epsilon_\ell^0 - \Sigma_\ell(\omega)} \tag{4.20}$$

The infinitesimal imaginary shift $i\eta$ in the denominator has been replaced by the self-energy, which is a finite complex quantity. It means that the positions of the poles have been shifted along the real axis (by $\mathfrak{Re}\Sigma_\ell$) but also *out* of it (by $\mathfrak{Im}\Sigma_\ell$). From (4.20), the diagonal matrix elements of the spectral function read:

$$A_\ell(\omega) = \frac{1}{\pi}\left|\mathfrak{Im}G_\ell(\omega)\right| = \frac{1}{\pi}\frac{\left|\mathfrak{Im}\Sigma_\ell(\omega)\right|}{\left[\omega - \epsilon_\ell^0 - \mathfrak{Re}\Sigma_\ell(\omega)\right]^2 + \left[\mathfrak{Im}\Sigma_\ell(\omega)\right]^2} \tag{4.21}$$

As a consequence, they do not present Dirac δ-peaks as in (4.17), but rather broadened peaks (and possibly satellites depending on the exact structure of $\Sigma_\ell(\omega)$), as it is shown in Fig. 4.3. Expressions (4.18) and (4.21) both describe the same object: one can see that the presence of a complex self-energy "generates" the many-body effects, but still in a single-particle picture, as it is designed for. The new peak is located at the energy where the left bracket of the denominator equals zero, which leads to:

$$\epsilon_\ell^{\mathrm{QP}} = \epsilon_\ell^0 + \mathfrak{Re}\Sigma_\ell(\omega = \epsilon_\ell^{\mathrm{QP}}) \tag{4.22}$$

which corrects the energies of the non-interacting system. It is a self-consistent (or non-linear) equation since the self-energy depends, by definition, on $\epsilon_\ell^{\mathrm{QP}}$ which is the solution to be found.

4.2.4.1 On-shell and off-shell approximations

Assuming that the correction $\epsilon_\ell^{\mathrm{QP}} - \epsilon_\ell^0$ is small, there are two options to deal with this self-consistency. The first one is to suppose that $\Sigma(\omega)$ is almost constant on this small interval and simply evaluate it at $\omega = \epsilon_\ell^0$ (which is known). This is the so-called *on-shell* approximation to the self-energy. A further approximation consists in linearizing the real part of the self-energy around ϵ_ℓ^0 with a Taylor expansion at first order:

$$\mathfrak{Re}\Sigma_\ell(\epsilon_\ell^{\mathrm{QP}}) = \mathfrak{Re}\Sigma_\ell(\epsilon_\ell^0) + \left.\frac{\partial\,\mathfrak{Re}\Sigma_\ell}{\partial\omega}\right|_{\epsilon_\ell^0}\left(\epsilon_\ell^{\mathrm{QP}} - \epsilon_\ell^0\right) \tag{4.23}$$

Remarking that $\mathfrak{Re}\Sigma_\ell(\epsilon_\ell^{\mathrm{QP}})$ is by definition equal to $(\epsilon_\ell^{\mathrm{QP}} - \epsilon_\ell^0)$ from eq. (4.22), we can re-arrange the terms to finally obtain:

$$\epsilon_\ell^{\mathrm{QP}} = \epsilon_\ell^0 + Z_\ell\,\mathfrak{Re}\Sigma_\ell(\omega = \epsilon_\ell^0) \tag{4.24}$$

where the renormalization factor is defined as:

$$Z_\ell = \frac{1}{1 - \left.\frac{\partial\mathfrak{Re}\Sigma_\ell}{\partial\omega}\right|_{\epsilon_\ell^0}} \tag{4.25}$$

Now we still need to evaluate the self-energy (and its derivative) at ϵ_ℓ^0, but the fact that the self-energy should be in principle evaluated at $\epsilon_\ell^{\mathrm{QP}}$ is taken into account. This is the so-called *off-shell* approximation. It is proved to be valid near the Fermi level in the limit of the homogeneous electron gas, where $\Sigma(\omega)$ is almost linear. The use of one or the other of these two approximations can be really important for quantitative results as we will demonstrate in Chap. 7.

4.2.4.2 Interpretation of the quasiparticle spectral weight Z

The definition of Z in eq. (4.25) is not very enlightening but this quantity has a deep physical meaning and is central in our formalism. Developing (4.21) around $\omega = \epsilon_\ell^{\mathrm{QP}}$, it can be shown that the quasiparticle peak in $A_\ell(\omega)$ can be fitted by a normalized lorentzian L_Γ centered on $\epsilon_\ell^{\mathrm{QP}}$ and multiplied by Z_ℓ:

$$A_\ell(\omega) \underset{\omega \to \epsilon_\ell^{\mathrm{QP}}}{\simeq} Z_\ell \, L_\Gamma(\omega - \epsilon_\ell^{\mathrm{QP}}) \tag{4.26}$$

with $\Gamma = 2Z_\ell |\mathfrak{Im}\Sigma_\ell(\epsilon_\ell^{\mathrm{QP}})|$ the full width at half maximum. This is why Z is called the quasiparticle spectral weight: it measures the fraction of the spectral function integral located under the main quasiparticle peak, as it is depicted in Fig. 4.3. Note that as $A_\ell(\omega)$ is a single-particle quantity, its integral over the frequency axis is equal to one, therefore Z ranges from 0 to 1. The remaining part of the spectral weight $1-Z$ is located under the satellite features. Hence, Z quantifies the importance of the quasiparticle peak compare to the rest of the spectral function. The higher Z is, the best is the quasiparticle picture. Conversely, the lower Z is, the more the system can be qualified as "correlated".

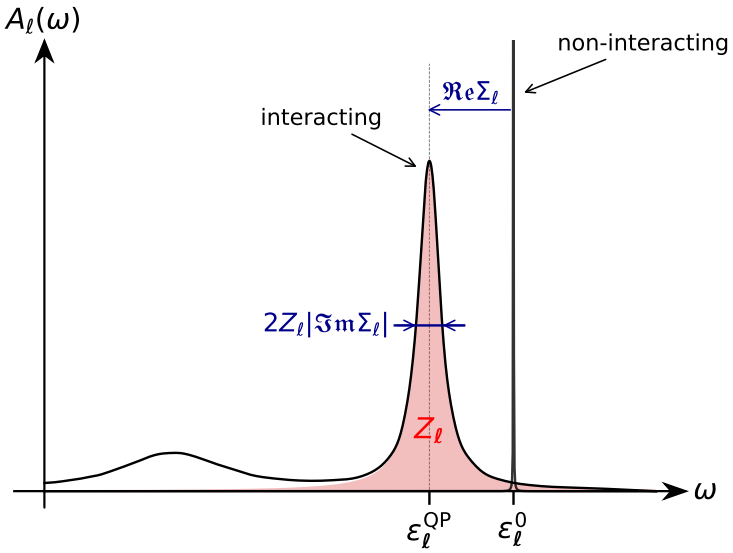

Figure 4.3: Diagonal matrix element $A_\ell(\omega)$ of the spectral function for a non-interacting and an interacting electron system. The area in red indicates the surface under the main quasiparticle peak, corresponding to Z_ℓ. Here, Σ_ℓ designates $\Sigma_\ell(\epsilon_\ell^{\mathrm{QP}})$. Inspired from [Bruneval2005] and [Gatti2012].

Notice that in this first-order perturbation theory, the only quantities one will obtain at the end of the calculation are $\epsilon_\ell^{\mathrm{QP}}$ and Z_ℓ (the spectral function with its frequency dependence is not calculated, as well as the wavefunctions associated to quasiparticles (see Sec. 4.2.6)). It is interesting to compare the spectral weight Z obtained in *ab initio* MBPT with the one obtained via other methods, for example dynamical mean-field theory (DMFT) which uses the Hubbard model. If the Hubbard U is sufficiently large relatively to the other characteristic energies of the system, the Z can drop to zero so that the quasiparticle peak disappears. In this case, all the spectral weight goes under two satellite features called lower and upper Hubbard bands.

4.2.5 Quasiparticle lifetime

Instead of real quasiparticle energies, one can define their complex version which includes the imaginary part of the self-energy:

$$\widetilde{\epsilon}_\ell^{\mathrm{QP}} = \epsilon_\ell^{\mathrm{QP}} + i\,\mathfrak{Im}\Sigma_\ell(\epsilon_\ell^{\mathrm{QP}}) \tag{4.27}$$

The real part triggers the usual phase rotation when applying the time-evolution operator $\exp(-i\hat{H}t)$ on the quasiparticle state, but the imaginary part makes this state decay in time. Hence, quasi-particles are not eigenstates of the many-body system and propagates only for a given time. This lifetime τ_ℓ is inversely proportional to the width of the quasiparticle peak:

$$\frac{1}{\tau_\ell} = \left|\mathfrak{Im}\widetilde{\epsilon}_\ell^{\mathrm{QP}}\right| \propto \Gamma \tag{4.28}$$

In Landau's Fermi-liquid theory, the lifetime is also inversely proportional to the square of the distance with respect to the Fermi level:

$$\frac{1}{\tau_\ell} \underset{FL}{\propto} \left(\epsilon_\ell^{\mathrm{QP}} - E_F\right)^2 \tag{4.29}$$

This ideal behavior is not rigorously observed in real materials which have a more complex behavior than the Fermi-liquid, but the global trend to decrease while going away from E_F is verified in many materials, that are said to have a "Fermi-liquid character". In these cases, the closer we are from the Fermi level, the sharper and higher are the quasiparticle peaks (as depicted in Fig. 4.2) and the longer are the lifetimes of quasiparticles. In other words, for states near the Fermi level the quasiparticle peaks are often well-defined so the quasiparticle picture is valid. An analysis of the spectral weights will be carried out in Sec. 8.3.1.4 and 10.2, precisely in order to discuss the Fermi-liquid character of nickelates.

4.2.6 Quasiparticle equation

In order to obtain the quasiparticle wavefunctions ψ^{QP}, one can use the so-called quasiparticle equation in which the self-energy acts as a non-local potential:

$$\left[\hat{h}(\mathbf{r}) + V_{\mathrm{H}}(\mathbf{r})\right]\psi_n^{\mathrm{QP}}(\mathbf{r}) + \int d\mathbf{r}'\,\Sigma(\mathbf{r},\mathbf{r}',\omega=\epsilon_n^{\mathrm{QP}})\,\psi_n^{\mathrm{QP}}(\mathbf{r}') = \epsilon_n^{\mathrm{QP}}\psi_n^{\mathrm{QP}}(\mathbf{r}) \tag{4.30}$$

Although not used in this PhD thesis, this equation is interesting to compare with equations of the similar form (2.21) and (3.8) used in Hartree-Fock and Kohn-Sham DFT, respectively. Indeed, it can be considered as an "exactification" of these mean-field theories.

4.3 Photoemission and inverse photoemission

The addition and removal energies of electrons belonging to a solid are directly measurable by direct and inverse photoemission experiments, thanks to the photoelectric effect. In direct photoemission, an incident photon of kinetic energy E_{kin} will remove an electron from the system (if its energy is higher than the binding energy of the electron). Energy conservation enables to write:

$$h\nu + E_0^N = E_i^{N-1} + E_{\mathrm{kin}} \tag{4.31}$$

In inverse photoemission, an electron is added to the system and a photon emitted. The energy balance reads:

$$E_0^N + E_{\text{kin}} = E_i^{N+1} + h\nu \tag{4.32}$$

These two processes are illustrated in Fig. 4.4, where we see that direct photoemission concerns occupied levels, and inverse photoemission unoccupied levels. From equations (4.4) and (4.5), one can identify the addition and removal excitation energies which read in both cases:

$$\epsilon_i = E_{\text{kin}} - h\nu \tag{4.33}$$

That is, we have a direct manner to measure quasiparticle energies $\epsilon_\ell^{\text{QP}} = \epsilon_i$ as calculated in MBPT.

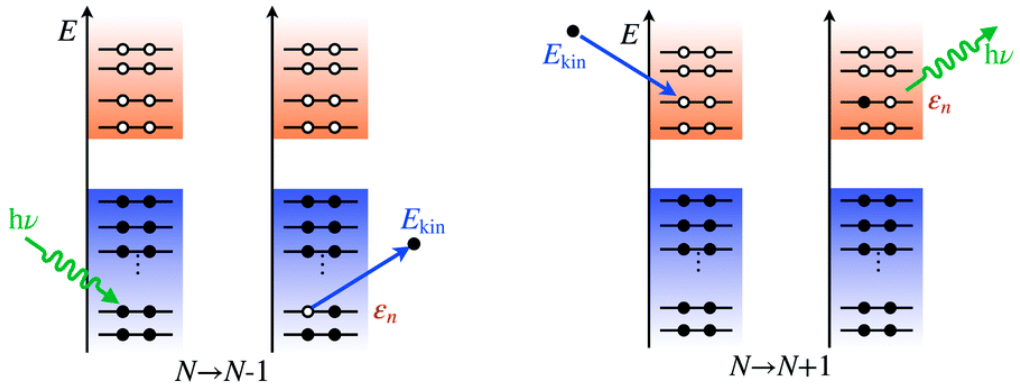

Figure 4.4: Principle of direct (left) and inverse (right) photoemission experiments. From Gian-Marco Rignanese.

As its name suggest, angle-resolved photoemission spectroscopy (ARPES) enables to measure the electronic energy levels for specific wave-vectors $\mathbf{k}$, and then provides a direct measurement of the electronic structure in reciprocal space. To be precise, what is measured in ARPES is the spectral function $A_{\mathbf{k}}(\omega)$, so in addition to the main quasiparticle peak, it also provides the potential satellites. Fermi surfaces and bandplots (close to E_F) can be directly probed experimentally and compared with the theoretical ones obtained via MBPT (see the comparison between the experimental and calculated Fermi surfaces of the bilayer nickelate $La_3Ni_2O_7$ in Sec. 8.3.1.1).

References

The reading of *Interacting electrons* by R. Martin, L. Reining and D. Ceperley [Martin2016], especially its chapters 5 and 7, has been really helpful in order to (start to) understand MBPT. Various presentations given during schools were also of great use, for example from X. Blase and G.M. Rignanese [Blase2022, Rignanese2014].

[Blase2022] Xavier Blase. *An introduction to Green's function in many-body condensed-matter quantum systems*. International summer School in electronic structure Theory: electron correlation in Physics and Chemistry (ISTPC). Centre Européen de Calcul Atomique et Moléculaire (CECAM). Aussois. June 2022. URL: `http://perso.neel.cnrs.fr/xavier.blase/LECTURES/greens2022.pdf`.

[Bruneval2005] Fabien Bruneval. *Exchange and Correlation in the Electronic Structure of Solids, from Silicon to Cuprous Oxide: GW Approximation and beyond*. PhD thesis, Palaiseau, Ecole polytechnique, October 2005. URL: `https://theses.fr/2005EPXX0037`.

[Damascelli2003] Andrea Damascelli, Zahid Hussain and Zhi-Xun Shen. *Angle-resolved photoemission studies of the cuprate superconductors*. Reviews of Modern Physics, vol. 75, no. 2, pages 473–541, April 2003. doi:10.1103/RevModPhys.75.473.

[Gatti2012] Matteo Gatti. *The one-particle Green's function and the GW approximation*. 5th School on Time-Dependent Density-Functional Theory. Centre Européen de Calcul Atomique et Moléculaire (CECAM). Center of Science Pedro Pascual, Benasque, Spain. January 2012. URL: `https://benasque.org/2012tddft/talks_contr/049_12benasque_gw.pdf`.

[Martin2016] Richard M. Martin, Lucia Reining and David M. Ceperley. Interacting Electrons: Theory and Computational Approaches. Cambridge University Press, Cambridge, 2016. Chap. 5 and 7. For the demonstration of the lorentzian of weight Z: section 7.5. doi:10.1017/CBO9781139050807.

[Rignanese2014] Gian-Marco Rignanese. *Many-Body Perturbation Theory: the GW method*. International summer school on Computational Methods for Quantum Materials. Université de Sherbrooke. Sherbrooke, Québec, Canada. June 2014. URL: `https://pitp.phas.ubc.ca/confs/sherbrooke2014/archives/MBPT_GW_Gian-Marco_Rignanese.pdf`.

5

The *GW* approximation

For though the band gap may be parted,
there's a chance that you will see:
GW is the answer,
thank you, Rex Godbee!

DFT song by Volker Blum and Kieron Burk,
to the tune of *Let it be*

The objective of this chapter is to explain how the self-energy needed in the framework of many-body perturbation theory (MBPT) is designed via a reformulation of the problem in terms of the screened Coulomb interaction W, and then simplified via the so-called *GW* approximation.

5.1 On the importance of screening

In a solid the outermost valence electrons are more or less delocalized, depending whether it is a metal or an insulator, forming a gas of electron, or more precisely, a Fermi liquid of interacting electrons. If an external charged particle is added to the system, the electron gas adapts to this change, either being attracted by the particle (if it is a hole) or being repelled (if it is an electron). A so-called polarization cloud forms around the particle, which *screens* the charge of the latter. Therefore, the total charge of the ensemble {particle + polarization cloud} is lowered down. If the density of the electron gas is high enough to generate a strong screening, this ensemble interacts weaklier with other charges, and can be considered as an almost independent particle: i.e. a quasiparticle. This screening effect is taken into account by the introduction of an effective screened Coulomb potential W which renormalizes the bare Coulomb potential $v(r) = 1/r$. Thus, W describes the electrostatic interaction of the quasiparticle with its environment and the other quasiparticles, as illustrated on Fig. 5.1. Close to the charge, the bare and the screened Coulomb potentials are the same, but at long range

the charge is screened and then $W(r)$ decays faster with distance, typically exponentially in metals.

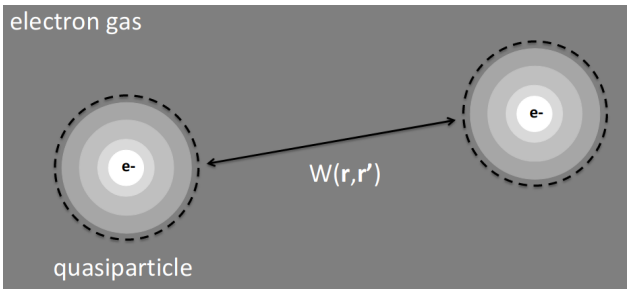

Figure 5.1: Polarization cloud around two electrons, which can then considered as quasiparticles interacting weaklier via the screened Coulomb potential W. From [Blase2021].

5.2 Hedin's equations

As the screened Coulomb potential is weaker than the bare one, a perturbation theory in W will converge faster than a perturbation theory in v. This is the main idea behind the *GW* approach, as formulated by Hedin in 1965 [Hedin1965]. In systems where the screening is weak, for example small molecules with only a few electrons, this approach might not be adapted. But it is completely relevant in solids, especially in metals and semiconductors, and explains its success. It consists in five self-consistent equations which are an exact reformulation of the many-electron problem. Their derivation can be found in the original paper, as well as in [Strinati1988] and in many-body textbooks, i.e. [Martin2016].

Dyson equation for the interacting Green's function

In MBPT, the interacting Green's function is related to the non-interacting one by the self-energy, via a Dyson equation (see Sec. 4.2.2). Written with the full spatio-temporal dependence, it reads as an integral equation:

$$G(1,2) = G_0(1,2) + \iint d34\, G_0(1,3)\Sigma_{\text{XC}}(3,4)G(4,2) \tag{5.1}$$

where $i = (\mathbf{r}_i, t_i, \sigma_i)$. In the *GW* framework, G_0 designates the Green's function of a system interacting only via the Hartree potential V_{H}, i.e. independent electrons evolving in a mean-field generated by the averaged electronic density. Hence, the self-energy contains all the exchange-correlation effects beyond the Hartree term, and is denoted Σ_{XC}, by analogy with the decomposition of the Kohn-Sham potential (3.10).

Vertex function

Roughly speaking, the vertex function describes how particles interact. It is defined by the following self-consistent equation:

$$\Gamma(1,2;3) = \delta(1,2)\delta(1,3) + \iiint d4567 \frac{\delta\Sigma_{\text{XC}}(1,2)}{\delta G(4,5)} G(4,6)G(7,5)\Gamma(6,7;3) \tag{5.2}$$

Irreducible polarizability

The *reducible* polarizability describes, as in classical physics, how a charged system reacts to a perturbation of its external potential. Without entering in too much details, in the Hedin's equations one rather use an *irreducible* polarizability[1] which reads:

$$P(1,2) = -i \iint d34\, G(1,3)G(4,1)\Gamma(3,4,2) \tag{5.3}$$

Dyson equation for the screened Coulomb interaction

The irreducible polarizability is the kernel of the Dyson equation defining the screened Coulomb interaction:

$$W(1,2) = v(1,2) + \iint d34\, v(1,3)P(3,4)W(4,2) \tag{5.4}$$

Thus, the effective screened interaction is equal to the bare one but corrected by polarization effects. One can see this equation as the "construction" of the quasiparticle.

Self-energy

From the beginning, our aim was to design an expression for the self-energy, that we can use to correct the quasiparticle energies (see Sec. 4.2.4). Within the Hedin's formulation in terms of screened interactions, one finally obtains the following expression for this self-energy:

$$\Sigma_{\text{XC}}(1,2) = i \iint d34\, G(1,4)W(1^+,3)\Gamma(4,2;3) \tag{5.5}$$

where $1^+ = (\mathbf{r}_1, t_1 + \eta, \sigma_1)$ for an infinitesimal positive time η. As mentioned in Sec. 4.2.1, the self-energy can be seen as a non-local dynamical potential which corrects the mean-field Hartree hamiltonian to a fully interacting one by adding exchange and correlation effects, and can be seen as the "turning on" of the interactions between electrons, beyond Hartree. In other words, this is the exact "mean-field" which governs the motion of quasiparticle.

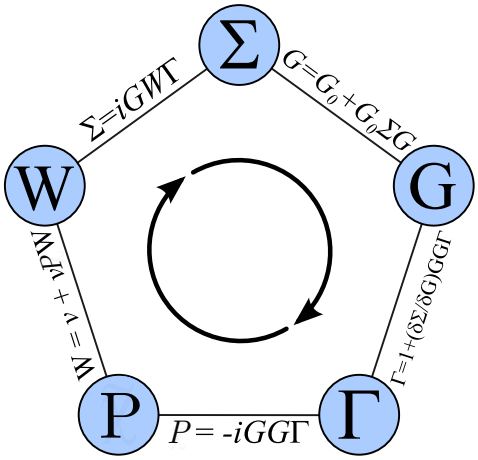

Figure 5.2: Hedin's pentagon representing the self-consistent cycle to carry out to obtain the five basic quantities of the theory, connected by the Hedin's equations. From [AbinitWebpage].

[1] The reducible and irreducible polarizabilities are mathematically connected by a Dyson equation.

Hedin's pentagon

In principle, these five equations have to be solved self-consistently, which is depicted by the so-called Hedin's pentagon in Fig. 5.2. It is an exact reformulation of the original many-electron problem, but in practice the full self-consistency is out of reach, especially because of the vertex function Γ. Some concessions are therefore required.

5.3 RPA-*GW* approximation

It turns out that the second term in the vertex function (5.2) – called vertex correction – produces terms of at least second order in W when plugged into the self-energy (5.5). The so-called *GW* approximation, introduced by Hedin himself in 1965, can be seen as the lowest order approximation in W and consists of neglecting the vertex correction:

$$\Gamma(1,2;3) \approx \delta(1,2)\delta(1,3) \tag{5.6}$$

The formulas for the polarizability and the self-energy are then simplified, and the Hedin's pentagon reduces to a quadrilateral, as illustrated in Fig. 5.3. These two simplifications, although looking similar, have to be interpreted independently.

5.3.1 Random-phase approximation to the polarizability

Neglecting the vertex correction, the irreducible polarizability (5.3) reduces to:

$$P^{\text{RPA}}(1,2) = -iG(1,2^+)G(2,1^+) \tag{5.7}$$

where RPA stands for random-phase approximation. This approximation, introduced by Bohm and Pines in the 50's, is anterior to Hedin's work. Their aim was to calculate the polarizability of the homogeneous electron gas (HEG) in order to include the effect of screening. In their calculations they encountered a sum over plane waves which was averaging to zero because of "random phases", hence the name. But this approximation can be valid for other systems than the HEG, where its name is not illuminating, and the RPA needs to be more generally interpreted. In this approximation, the polarizability is only due to the formation of independent electron-hole pairs (see the two counter-propagating Green's function in (5.7)), on top of the Fermi sea. These pairs are independent since they do not interact between them explicitly, and they are quasiparticles in the sense that they are dressed by all the electrons of the system. P being the kernel of the Dyson equation for W (5.4)[2], the quality of the screening description relies on the validity of the RPA in the system considered.

5.3.2 *GW* approximation to the self-energy

Independently, neglecting the vertex correction in the self-energy formula (5.5) gives:

$$\Sigma_{\text{XC}}^{GW}(1,2) = iG(1,2)W(1^+,2) \tag{5.8}$$

hence the name "*GW* approximation". Formally, this name only designates the latter approximation to the self-energy, but often it also implicitly includes the random-phase approximation to P and then to W, and hence refers rigorously to $\Sigma_{\text{XC}}^{\text{RPA-}GW} = iGW^{\text{RPA}}$. The neglect of the

[2] A Dyson equation intrinsically contains all orders of perturbation, even if the kernel is of low order.

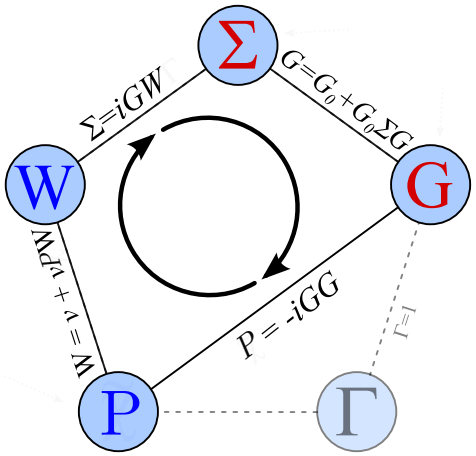

Figure 5.3: Depiction of the RPA-*GW* approximation as a simplification of the Hedin's pentagon, with the vertex correction in Γ neglected (in both *P and* Σ). The two different colors indicates the quantities connected by two different Dyson equations. From [AbinitWebpage].

vertex correction in the *GW* self-energy corresponds to the neglect of direct interactions of the added particle with both the electrons and the holes of the excited pairs. This self-energy can be decomposed into a static exchange term and a dynamical correlation term (here symbolically in frequency space):

$$\Sigma_{\mathrm{XC}}^{GW}(\omega) = iG\,W(\omega) = iGv + iG(W(\omega) - v) = \Sigma_{\mathrm{X}} + \Sigma_{\mathrm{C}}(\omega) \tag{5.9}$$

where the first term corresponds to the Hartree-Fock self-energy $\Sigma_{\mathrm{X}}^{\mathrm{HF}} = iGv$[3]. This separation is consistent with our definition of correlations (2.3.3.2), as all the effects that are beyond Hartree-Fock. One can see that Hartree-Fock and *GW* self-energies have the same structure, but the former uses the bare Coulomb potential while the second the screened one. Due to this similarity, *GW* is frequently described has a "dynamically screened version of Hartree-Fock". Exactly like in the Hartree-Fock cases (see eq. (2.22)), the *GW* self-energy is spin-diagonal and correlations between electrons of opposite spins are still not considered[4]. It turns out that the latter interaction is negligible in most cases, and what makes the success of *GW* compare to Hartree-Fock is the use of the screened Coulomb potential, with its dynamical dependence. The two terms in (5.9) do not have the same structure and are evaluated separately by different algorithms in practical calculations.

To summarize, within the RPA-*GW* approximation, the added electrons or holes propagating in the quantum many-body system (as described in MBPT) are screened or "dressed" by the excitations of correlated electron-hole pairs, but are not directly interacting with the electrons and the holes of these pairs (due to the neglect of the vertex correction). This is depicted on the right-hand side of Fig. 5.4.

[3] This is consistent with formula (2.22), once the latter has been Fourier transformed to frequency space, and the Lehmann representation of the Green's function identified.

[4] This is true for standard *GW* calculations, in particular as used in this thesis, but spin-polarized *GW* calculations are possible.

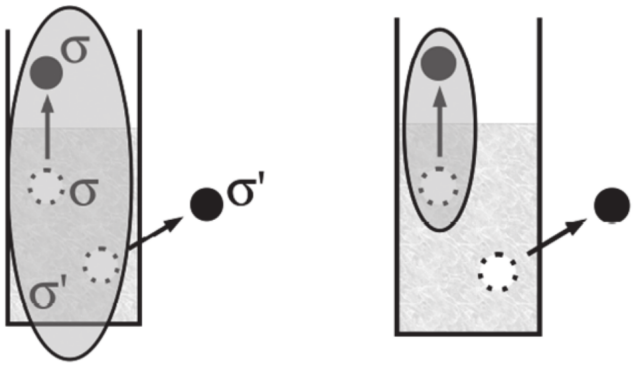

Figure 5.4: Schematic comparison between the original many-body problem of electron removal (left), and the same problem as seen by the RPA-*GW* approximation (right). The gray ellipses designate the particles which are explicitly interacting. From [Martin2016].

5.4 One-shot G_0W_0

The convergence of the self-consistent cycle is supposed to be fast thanks to the use of the screened Coulomb potential W rather than the bare one v. Therefore, one can do only one iteration of the *GW* cycle, starting from $G = G_0$, as illustrated on Fig. 5.5. The self-energy Σ_0 obtained after this first iteration contains first-order corrections to the single-particle energies (see eq. 4.22), and the use of the off-shell approximation provides the spectral weights (4.25). This one-shot calculation is of course less cumbersome than the fully self-consistent resolution, but to stop after only one iteration also has deeper physical reasons. *GW* remains an approximation, and looping over an approximation can have damaging effects, at least for some properties. Indeed, it has been demonstrated that fully self-consistent *GW* improves the total energy but worsen spectral properties, in particular because self-consistency in P^{RPA} destroys the plasmon structure in the spectral function [von Barth1996, Holm1998].

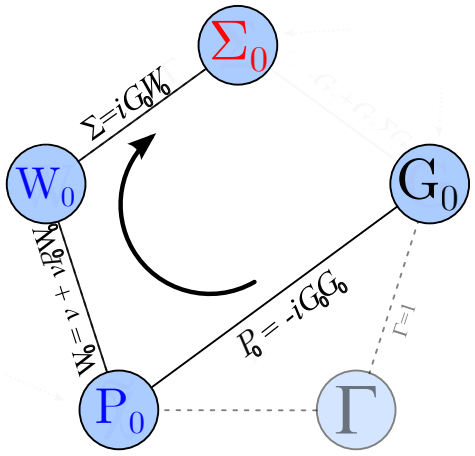

Figure 5.5: One-shot G_0W_0 corresponds to the first iteration of the *GW* cycle of Fig. 5.3, starting from a non-interacting G_0. Adapted from [AbinitWebpage].

Adler-Weiser formula for the RPA-polarizability

At the first iteration, the RPA-polarizability reads $P^{\text{RPA}} = -iG_0G_0$. Therefore, using the Lehmann representation of the Green's function (4.8) with the fact that for a non-interacting system the Lehmann amplitudes reduce to single-particle wavefunctions $\psi_i^0(\mathbf{r})$, one obtains the

Adler-Weiser formula [Adler1962, Wiser1963]:

$$P_0^{\text{RPA}}(\mathbf{r}_1, \mathbf{r}_2, \omega) = \sum_{\ell,m} (f_\ell - f_m) \frac{\psi_\ell^0(\mathbf{r}_1)\psi_m^{0*}(\mathbf{r}_1)\psi_\ell^{0*}(\mathbf{r}_2)\psi_m^{0*}(\mathbf{r}_2)}{\omega - (\epsilon_\ell^0 - \epsilon_m^0)} \tag{5.10}$$

where the infinitesimal shift $i\eta$ in the denominator of the Green's function has been dropped for simplicity. The f_ℓ are the occupation numbers (equal to 0 or 1 at $T = 0$), hence the term between parenthesis is non-zero only if one state is occupied and the other is not. It means that the polarizability includes all the possible transitions from occupied to unoccupied states and vice-versa: the picture in terms of excited electron-hole pairs is recovered. The reciprocal space version of this formula expressed in the Bloch state basis $\ell = (n, \mathbf{k})$ is directly implemented in the ABINIT code.

5.5 *GW* in practice

Using the *GW* approximation, even in its one-shot version, is still cumbersome and further approximations or tricks are required to ensure the tractability and the efficiency of the method.

5.5.1 Starting point

To enter the *GW* cycle one needs a first guess for G_0. The closer the starting point is from the self-consistent G, the faster the convergence will be, which is of course crucial for one-shot G_0W_0. Even if in original MBPT G_0 is the Green's function of the non-interacting system, one can include some effective interaction into it. As already mentioned in Sec. 5.2, in Hedin's equations G_0 contains the Hartree interaction. In practice however, Kohn-Sham or Hartree-Fock solutions provides better starting points. Here these methods are grouped under the generic name "mean-field" (MF) and the associated potential with the interactions beyond Hartree is denoted V^{MF} (which can be the non-local exchange V_{X} of Hartree-Fock or the local V_{XC} of KS-DFT). In this case, the first-order corrections to the energies are the differences between the diagonal matrix elements of the Hedin's self-energy (5.5) and the mean-field potential:

$$\begin{aligned} \epsilon_\ell^{GW} &= \epsilon_\ell^{\text{MF}} + \left\langle \psi_\ell^{\text{MF}} \middle| \mathfrak{Re}\hat{\Sigma}^{GW}(\omega) - \hat{V}^{\text{MF}} \middle| \psi_\ell^{\text{MF}} \right\rangle \\ &= \epsilon_\ell^{\text{MF}} + \left(\mathfrak{Re}\Sigma_\ell^{GW}(\epsilon_\ell^{GW}) - \hat{V}_\ell^{\text{MF}} \right) \end{aligned} \tag{5.11}$$

which is a modified version of equation (4.22). In the first line, a self-energy *operator* have been introduced. The spectral weights Z_ℓ are still directly calculated by formula (4.25), since $\hat{V}^{\text{MF}}$ is not frequency-dependent.

5.5.2 Frequency dependence of W

In frequency space, the self-energy (5.8) is evaluated by the convolution:

$$\Sigma_{\text{XC}}^{GW}(\mathbf{r}_1, \mathbf{r}_2, \omega) = \frac{i}{2\pi} \int_{-\infty}^{+\infty} d\omega' \, G(\mathbf{r}_1, \mathbf{r}_2, \omega + \omega') W(\mathbf{r}_1, \mathbf{r}_2, \omega') \tag{5.12}$$

While the frequency dependence of G is straightforward and comes directly from the Lehmann representation (4.8), it is far more complex for W. Let us first reformulate the problem in terms of the dielectric function ε and its inverse. As in classical electromagnetics, the dielectric

function (or permittivity) describes how a material polarizes when an external electric field is applied. It is related to the irreducible polarizability defined in (5.3) via the following formula:

$$\varepsilon(1,2) = \delta(1,2) - \int d3\, v(1,3)P(3,2) \tag{5.13}$$

which in frequency space and expressed on the plane-wave basis simplifies to a product:

$$\varepsilon_{\mathbf{G}\mathbf{G}'}(\mathbf{q},\omega) = \delta_{\mathbf{G}\mathbf{G}'} - v(\mathbf{q},\mathbf{G})P_{\mathbf{G}\mathbf{G}'}(\mathbf{q},\omega) \tag{5.14}$$

The *inverse* dielectric function directly relates the screened and bare Coulomb potentials:

$$W(1,2) = \int d3\, \varepsilon^{-1}(1,3)v(3,2) \tag{5.15}$$

to compare with equation (5.4). In frequency and reciprocal space, this formula reads:

$$W_{\mathbf{G}\mathbf{G}'}(\mathbf{q},\omega) = \varepsilon^{-1}_{\mathbf{G}\mathbf{G}'}(\mathbf{q},\omega)v(\mathbf{q}+\mathbf{G}) \tag{5.16}$$

Therefore, calculating the screening for a *given* frequency ω requires first to calculate the polarizability matrix using the Adler-Weiser formula (5.10), from which the dielectric matrix $\varepsilon_{\mathbf{G}\mathbf{G}'}$ is obtained via (5.14). To be used in (5.16), the dielectric matrix needs to be inverted, which represents a major computational effort, especially if the procedure has to be done many times for a fine mesh of frequencies.

5.5.2.1 Plasmon pole models

Since in the convolution (5.12) the details of the frequency dependence are integrated out, a simple model for the screening might capture the essential physics. The ω-dependence of ε^{-1} can be approximated via so-called plasmon-pole models (PPM) which rely only on a few parameters fitted from exact calculations. In this thesis we have used the Godby-Needs (GN) and the Hybertsen-Louie (HL) plasmon-pole models, the former being the standard one. Both of them have the same analytical form:

$$\begin{aligned}\varepsilon^{-1}_{\mathrm{PPM},\mathbf{G}\mathbf{G}'}(\mathbf{q},\omega) = \delta_{\mathbf{G}\mathbf{G}'} + \frac{\Omega^2_{\mathbf{G}\mathbf{G}'}(\mathbf{q})}{\omega^2 - \tilde{\omega}^2_{\mathbf{G}\mathbf{G}'}(\mathbf{q})} \\ + iA_{\mathbf{G}\mathbf{G}'}(\mathbf{q})\Big[\delta\big(\omega - \tilde{\omega}_{\mathbf{G}\mathbf{G}'}(\mathbf{q})\big) - \delta\big(\omega + \tilde{\omega}_{\mathbf{G}\mathbf{G}'}(\mathbf{q})\big)\Big]\end{aligned} \tag{5.17}$$

and only differ in the way the parameters Ω, A and $\tilde{\omega}$ are fitted. For a given $\mathbf{q}$-point in the Brillouin zone and a given couple of $\mathbf{G}$ and $\mathbf{G}'$ reciprocal space vectors, the inverse dielectric function contains only one (positive) pole at $\tilde{\omega}_{\mathbf{G}\mathbf{G}'}(\mathbf{q})$, so does $W_{\mathbf{G}\mathbf{G}'}$ via formula (5.16). It is then straightforward to calculate the self-energy (5.12) by integrating this unique pole.

Godby-Needs In the GN PPM [Godby1989], the calculation of $P_{\mathbf{G}\mathbf{G}'}(\mathbf{q},\omega)$ is done only for two frequencies $\omega = 0$ and the imaginary plasma frequency $\omega = i\omega_p$[5]. The parameters of $\varepsilon^{-1}_{\mathrm{PPM}}$ are then fitted to reproduce the exact ε^{-1} at these two frequencies (see the center panel of Fig. 5.6).

[5] The plasma frequency is defined as $\omega_p = \sqrt{\frac{\bar{n}e^2}{\varepsilon_0 m}}$ with $\bar{n}$ the averaged electronic density.

Hybertsen-Louie In the HL PPM [Hybertsen1986], the first condition is also to reproduce ε^{-1} at $\omega = 0$ but the second condition is to fulfill the so-called f-sum rule [Johnson1974]:

$$\int_0^\infty d\omega\, \omega\, \Im\mathrm{m}\left[\varepsilon^{-1}_{\mathrm{PPM},\mathbf{G}\mathbf{G}'}(\mathbf{q},\omega)\right] = 2\pi^2 \frac{(\mathbf{q}+\mathbf{G})(\mathbf{q}+\mathbf{G}')}{|\mathbf{q}+\mathbf{G}|^2} n_{\mathbf{G}-\mathbf{G}'} \tag{5.18}$$

with $n_{\mathbf{G}}$ the Fourier coefficients of the density. In other words, the integral of the imaginary part of the inverse dielectric function times ω is constrained. A major issue with the HL PPM is the slower convergence of the results with respect to the number of unoccupied bands considered in the self-energy calculation (as well as with respect to the plane-wave cutoff), as it has been shown in [Stankovski2011].

Fig. 5.6 shows a comparison of these two plasmon-pole models with the exact calculated inverse dielectric function and indicates the fitting points, in the case of the infinite-layer nickelate $Nd_{0.8}Sr_{0.2}NiO_2$ (see Chap. 7). One can see that the approximation is crude, modeling the complex structure of $\varepsilon^{-1}(\omega)$ by a single plasmon. Nevertheless, the self-energy calculated using these plasmon-pole models reproduces quite well the exact result obtained via the contour deformation method (introduced in the next section), which validates their use.

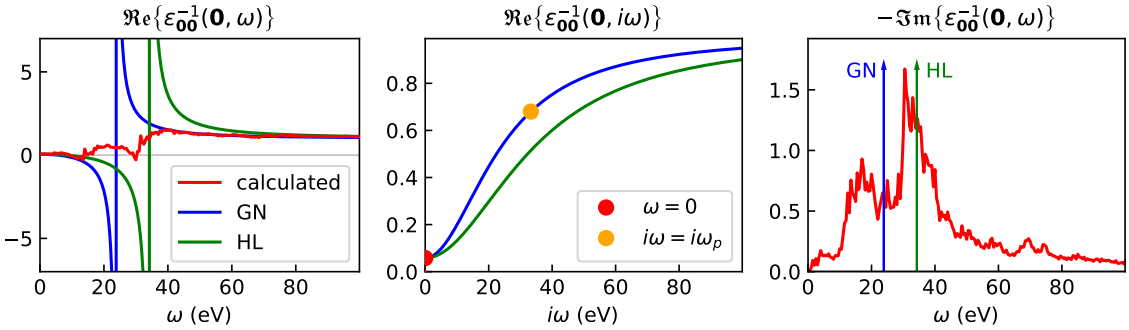

Figure 5.6: Comparison between the calculated inverse dielectric function (for $\mathbf{G} = \mathbf{G}' = \mathbf{0}$ and $\mathbf{q} \to \mathbf{0}$) and the GN and HL plasmon-pole models, in the case the infinite-layer nickelate $Nd_{0.8}Sr_{0.2}NiO_2$. On the right, $-\Im\mathrm{m}\left\{\varepsilon^{-1}_{\mathbf{00}}(\mathbf{0},\omega)\right\}$ is nothing else than the electron-energy loss function (EELF), which can be probed experimentally. The plasma frequency in this system is $\omega_p = 33.3$ eV.

5.5.2.2 Contour deformation method

Without a plasmon-pole model, the integral (5.12) has in principle to be evaluated on a fine mesh of frequencies on the real axis, where the integrand behavior is ragged due to the proximity of the poles. Taking advantage of the residual theorem and the fact that the integrand behavior is smoother on the imaginary axis and then requires less sampling to be numerically integrated, the integral over the real axis is transformed into an integral over the imaginary axis. A deformed contour shown on Fig. 5.7 is used, enclosing only poles of the Green's function whose frequency dependence is known, which eases the evaluation of the associated residuals. The value of the integral on the real axis finally equals:

$$\Sigma^{GW}_{\mathrm{XC}}(\omega) = \frac{i}{2\pi}\left\{2\pi i \sum_{z_p} \lim_{z\to z_p} G(\omega+z)W(z)(z-z_p) - \int_{+i\infty}^{-i\infty} dz\, G(\omega+z)W(z)\right\} \tag{5.19}$$

with z a complex variable and z_p the poles enclosed inside the contour. The space variables have been omitted. The sum over residuals is the left-hand side term. Despite this trick, this method is still very cumbersome and has only been used to check the results of the two aforementioned plasmon-pole models.

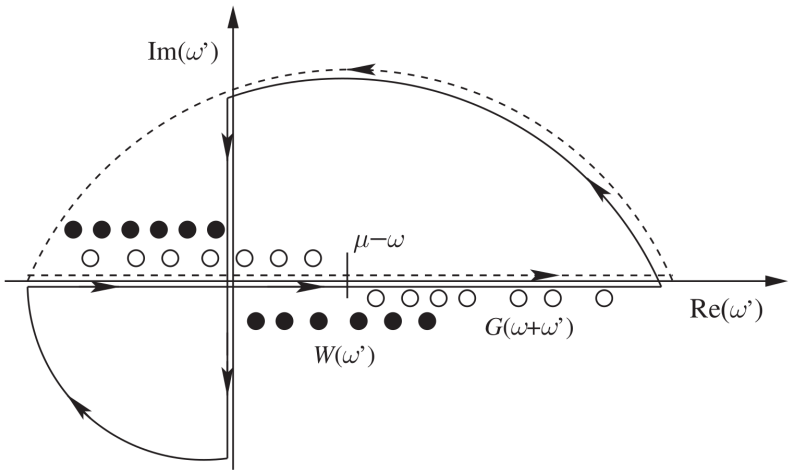

Figure 5.7: Integration paths to calculate the self-energy using the residual theorem. Poles of G and W are empty and filled circles, respectively. The dashed line indicates the simplest contour, while the continuous line indicates the deformed contour enclosing only poles of G located in the top right quadrant. From [Martin2016].

5.6 Discussions

The Hedin's equations have been designed to address situations where the screening is important, such as in solids and in particular in metals. In fact, this approach turns out to be relevant also for insulators and molecules. One of the key successes of the *GW* approach is indeed the calculation of bandgaps, which are well reproduced compared to Hartree-Fock overestimated values and DFT underestimated values (see Fig. 5.8 for the case of solids). The simplification of the vertex function (5.6) turns out to be valid in many cases, and further considerations of vertex corrections are tedious and do not improve results dramatically. Hence, some people do not hesitate to speak about the "*GW* miracle": an approximation that makes the calculations tractable, but which contains the necessary physical ingredients to perform well [Bruneval2021]. The quality of the result obtained in the perturbative approach, *a fortiori* in the case of one-shot G_0W_0, relies of course on the mean-field starting point, but the *GW* corrections converge rapidly towards a final answer (relatively) independent of the starting point, as it will be evidenced in our work about infinite-layer nickelates (see Sec. 7.6).

We have extensively discussed the validity of the Kohn-Sham eigenvalues in the preceding chapters. The idea of calculating first order *GW* corrections on top of DFT is to describe more accurately single-particle energies in the framework of MBPT where the latter recover a clear physical interpretation as addition and removal energies of electrons, measurable by ARPES experiments. The magnitude of these corrections can be considered as an indication of the exchange and correlation effects in the system. One generally estimates the *numerical* accuracy of *GW* quasiparticle energies not to exceed 0.1 eV: this is also the value to which is set the $i\eta$ parameter to be used in the denominator of Green's functions and polarizabilities to avoid poles. Therefore, it is unnecessary to converge a *GW* result under this value.

Although far more cumbersome than DFT calculations, one-shot G_0W_0 calculations with plasmon-pole models can be carried out in a reasonable amount of time. Taking the example of the electronic structure calculation of the single-layer nickelate $Nd_{0.8}Sr_{0.2}NiO_2$ parallelized on 32 processors, the DFT first step took no more than 15 mn, the screening part a bit more than one hour and finally the self-energy part a bit less than 20 hours (using the contour deformation technique, the latter part took two weeks).

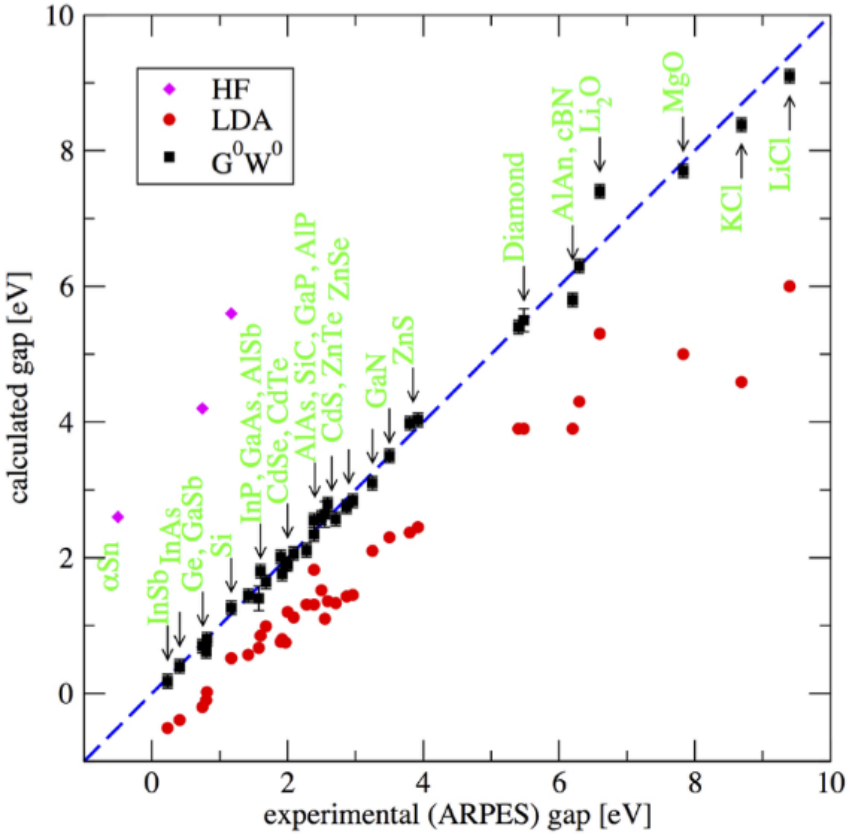

Figure 5.8: Comparison between the experimental bandgaps of some solids measured by ARPES, and theoretical values obtained within Hartree-Fock, DFT-LDA and G_0W_0 on top of LDA. The closer the values are from the diagonal, the more accurate they are. From Valerio Olevano.

References

Chapters 5, 11, 12 and 13 of *Interacting electrons* [Martin2016] addresses the *GW* approximation in a clear and pedagogical way. The first part of the review article [Golze2019] gives another pedagogical entry into the *GW* world.

[AbinitWebpage] Matteo Giantomassi. *Many-Body Perturbation Theory*. Abinit webpage. URL: `https://docs.abinit.org/theory/mbt/`.

[Adler1962] Stephen L. Adler. *Quantum Theory of the Dielectric Constant in Real Solids*. Physical Review, vol. 126, no. 2, pages 413–420, April 1962. doi:10.1103/PhysRev.126.413.

[Blase2021] Xavier Blase. *An introduction to the GW formalism*. International summer School in electronic structure Theory: electron correlation in Physics and Chemistry (ISTPC). Centre Européen de Calcul Atomique et Moléculaire (CECAM). Online. June 2021. URL: `http://perso.neel.cnrs.fr/xavier.blase/LECTURES/gw2021.pdf`.

[Bruneval2021] Fabien Bruneval, Nike Dattani and Michiel J. van Setten. *The GW Miracle in Many-Body Perturbation Theory for the Ionization Potential of Molecules*. Frontiers in Chemistry, vol. 9, December 2021. doi:10.3389/fchem.2021.749779.

[Godby1989] R. W. Godby and R. J. Needs. *Metal-insulator transition in Kohn-Sham theory and quasiparticle theory*. Physical Review Letters, vol. 62, no. 10, pages 1169–1172, March 1989. doi:10.1103/PhysRevLett.62.1169.

[Golze2019] Dorothea Golze, Marc Dvorak and Patrick Rinke. *The GW Compendium: A Practical Guide to Theoretical Photoemission Spectroscopy*. Frontiers in Chemistry, vol. 7, July 2019. doi:10.3389/fchem.2019.00377.

[Hedin1965] Lars Hedin. *New Method for Calculating the One-Particle Green's Function with Application to the Electron-Gas Problem*. Physical Review, vol. 139, no. 3A, pages A796–A823, August 1965. doi:10.1103/PhysRev.139.A796.

[Holm1998] B. Holm and U. von Barth. *Fully self-consistent GW self-energy of the electron gas*. Physical Review B, vol. 57, no. 4, pages 2108–2117, January 1998. doi:10.1103/PhysRevB.57.2108.

[Hybertsen1986] Mark S. Hybertsen and Steven G. Louie. *Electron correlation in semiconductors and insulators: Band gaps and quasiparticle energies*. Physical Review B, vol. 34, no. 8, pages 5390–5413, October 1986. doi:10.1103/PhysRevB.34.5390.

[Johnson1974] David Linton Johnson. *Local field effects and the dielectric response matrix of insulators: A model*. Physical Review B, vol. 9, no. 10, pages 4475–4484, May 1974. doi:10.1103/PhysRevB.9.4475.

[Martin2016] Richard M. Martin, Lucia Reining and David M. Ceperley. Interacting Electrons: Theory and Computational Approaches. Cambridge University Press, Cambridge, 2016. Chapters 11, 12 and 13. Hedin's equations: Sec. 11.1. Inverse dielectric function: Sec. 5.5. Schematic representation of the RPA-*GW* approximation: section 15.1. doi:10.1017/CBO9781139050807.

[Stankovski2011] M. Stankovski, G. Antonius, D. Waroquiers, A. Miglio, H. Dixit, K. Sankaran, M. Giantomassi, X. Gonze, M. Côté and G.-M. Rignanese. *G_0W_0 band gap of ZnO: Effects of plasmon-pole models*. Physical Review B, vol. 84, no. 24, page 241201, December 2011. doi:10.1103/PhysRevB.84.241201.

[Strinati1988] G. Strinati. *Application of the Green's functions method to the study of the optical properties of semiconductors*. Rivista del Nuovo Cimento, vol. 11, no. 12, pages 1–86, December 1988. doi:10.1007/BF02725962.

[von Barth1996] Ulf von Barth and Bengt Holm. *Self-consistent GW_0 results for the electron gas: Fixed screened potential W_0 within the random-phase approximation*. Physical Review B, vol. 54, no. 12, pages 8411–8419, September 1996. doi:10.1103/PhysRevB.54.8411.

[Wiser1963] Nathan Wiser. *Dielectric Constant with Local Field Effects Included*. Physical Review, vol. 129, no. 1, pages 62–69, January 1963. doi:10.1103/PhysRev.129.62.

6

Theories and methods for superconductivity

So far, the methods presented were dedicated to electronic structure calculations in the *normal* state, and the physical ingredients known or suspected to mediate superconductivity are not yet considered (phonons in the case of conventional superconductivity, spin fluctuations for example in the case of unconventional superconductivity). The hamiltonian describing the many-electron system will be therefore split into two parts:

$$\hat{H} = \hat{H}_0 + \hat{V} \tag{6.1}$$

where $\hat{H}_0$ accounts for the electronic dispersion in the normal state and $\hat{V}$ for the physical interactions responsible for superconductivity. The normal state, described by $\hat{H}_0$, can be unstable with respect to the term $\hat{V}$. If so, the system transitions to its superconducting state. $\hat{H}_0$ is typically written in second quantification as the sum of independent-particle energies corresponding to Bloch states of band index n and wavevector $\mathbf{k}$:

$$\hat{H}_0 = \sum_{n\mathbf{k}} \epsilon_{n\mathbf{k}} \hat{c}^{\dagger}_{n\mathbf{k}} \hat{c}_{n\mathbf{k}} \tag{6.2}$$

as if the system was non-interacting. However, the Coulomb interaction between electrons can be effectively taken into account in this hamiltonian, for example by considering the Kohn-Sham energies, which is standard, or the *GW* energies. In both cases, the single-particle or quasiparticle picture must be valid. In the so-called weak coupling limit, the term $\hat{V}$ has a smaller magnitude than $\hat{H}_0$.

6.1 BCS theory

The BCS theory was the first consistent microscopic theory of superconductivity, and at the time of its development it described successfully all the conventional superconductors (see Sec. 1.2). As such, it introduced key notions and vocabulary, still relevant in more modern theories addressing unconventional superconductivity.

The first brick of the theory is the existence of Cooper pairs made of two electrons of opposite momenta and spins ($\mathbf{k}\uparrow, -\mathbf{k}\downarrow$) where for the moment, we include the band index n into the

wavevector $\mathbf{k}$. The formation of these pairs results from a generic attractive interaction between electrons, which can be arbitrarily small [Cooper1956], and can be of any physical origin, which makes the BCS theory general. The BCS hamiltonian reads [Bardeen1957a, Bardeen1957b]:

$$\hat{H}_{\text{BCS}} = \sum_{\mathbf{k}\sigma} (\epsilon_{\mathbf{k}} - \mu) \hat{c}^{\dagger}_{\mathbf{k}\sigma} \hat{c}_{\mathbf{k}} + \sum_{\mathbf{k}\mathbf{k}'} V_{\mathbf{k}\mathbf{k}'} \hat{c}^{\dagger}_{\mathbf{k}'\uparrow} \hat{c}^{\dagger}_{-\mathbf{k}'\downarrow} \hat{c}_{-\mathbf{k}\downarrow} \hat{c}_{\mathbf{k}\uparrow} \tag{6.3}$$

The first term is the single-particle dispersion corresponding to $\hat{H}_0$, and the second to an effective interaction between electrons. The latter scatters a Cooper pair from a state $(\mathbf{k}\uparrow, -\mathbf{k}\downarrow)$ to a state $(\mathbf{k}'\uparrow, -\mathbf{k}'\downarrow)$ with an associated energy $V_{\mathbf{k}\mathbf{k}'}$. Cooper demonstrated that these matrix elements are non-negligible only for electrons close to the Fermi surface, i.e. whose energies lie within a $\pm\hbar\omega_c$ interval around E_F, with the maximal cutoff frequency ω_c of the order of the Debye frequency. Based on this fact, Cooper made the approximation of a constant and isotropic interaction V for electrons near the Fermi surface, and zero elsewhere. It translates into:

$$V_{\mathbf{k}\mathbf{k}'} = \begin{cases} -V & \text{if } |\epsilon_{\mathbf{k}} - E_F| \text{ and } |\epsilon_{\mathbf{k}'} - E_F| < \hbar\omega_c \\ 0 & \text{otherwise} \end{cases} \tag{6.4}$$

The electrons which form Cooper pairs are then only those near the Fermi surface. Therefore, the electronic dispersion is unchanged except near E_F, where a so-called superconducting gap opens, due to the absence of the paired electrons which have lowered their energies. The existence of Cooper pairs explains why a superconductor has zero resistivity: the scattering of one of the electron of the pair onto any defect from $\mathbf{k}$ to $\mathbf{k}+\mathbf{q}$ is automatically compensated by the other one, scattered back from $-\mathbf{k}$ to $-\mathbf{k}-\mathbf{q}$ so to conserve the total momentum. Therefore, the total current flowing through the material is not affected by the scattering events. It is important to note that the ground-state of the BCS theory is not the usual Fermi sea at zero temperature, but rather the condensate of an undetermined number of Cooper pairs. This superconducting ground-state is resulting from the instability of the normal state Fermi sea, induced by the attractive interaction bounding the Cooper pairs. It was understood in the 50s' that this interaction involved in conventional superconductivity, was mediated by vibrations of the crystal lattice: the so-called phonons.

The BCS theory introduces a complex gap function $\Delta(\mathbf{k})$, playing the role of the superconducting order parameter. It is solution of a gap equation and is non-trivial in the general case due to the $\mathbf{k}$-dependence, but the approximation (6.4) simplifies the problem and enables to obtain the following relations:

$$\Delta_0 = 1.764\, k_B T_c = 2\hbar\omega_c \exp\left(-\frac{1}{\lambda}\right) \quad ; \quad \lambda = N_F V \tag{6.5}$$

with Δ_0 the gap at $T = 0$, T_c the critical temperature of the superconducting transition, N_F the density of states (DOS) at the Fermi level, and λ the standard notation for the electron-phonon coupling constant. These relations are relatively well verified in conventional superconductors. It is important to note that they are obtained in the weak-coupling limit $\lambda \ll 1$. In the strong coupling limit, more complex formulas such as the McMillan one are necessary. It is nevertheless interesting to interpret the relations (6.5): an increase in the density of states N_F or in the coupling strength V, or in both, results in an increase in Δ_0 and T_c, promoting superconductivity. The evolution of N_F and V when the GW correlations are taken into account is the key of our work about the electron-phonon coupling in the infinite-layer nickelates (see Chap. 7).

Now, if the interaction $V_{\mathbf{k}\mathbf{k}'}$ is not anymore assumed isotropic, the gap remains $\mathbf{k}$-dependent, and its symmetry characterize the Cooper pair symmetry, and therefore give indication on the

superconducting mechanism. Indeed, one can define a Cooper pair wavefunction[1], which have the same symmetry that of the gap function[2]. Since the spin part of the wavefunction is antisymmetric (in our spin-singlet case where Cooper pair are formed of electrons of opposite spins), the spatial part has to be symmetric. By analogy with the atomic orbitals, one label the allowed symmetries *s*-wave and *d*-wave (see Fig. 6.1). Simple conventional superconductors often have a *s*-wave gap function, while there are strong evidences that high-T_c cuprates present a *d*-wave gap function. Other cases are possible, for example the $s_\pm$ symmetry which is one of the possible gap symmetries in the bilayer nickelate (see Fig. 8.1). Experimentally, the symmetry of the gap function can be deducted from the local DOS obtained by scanning tunneling microscopy, a typical U-shape with respect to the bias voltage indicating a *s*-wave gap, while a V-shape indicates a *d*-wave gap.

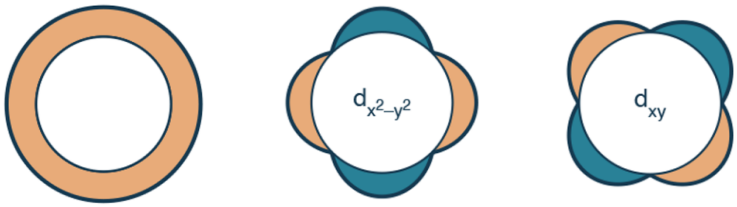

Figure 6.1: Gap functions $\Delta(\mathbf{k})$ with symmetry *s*, $d_{x^2-y^2}$ and d_{xy}, with the color indicating the sign. From [von Rohr2023].

6.2 Eliashberg theory

The BCS theory remains based on a model hamiltonian, with an effective electron-electron interaction $V_{\mathbf{k}\mathbf{k}'}$. The Eliashberg theory corresponds the fully *ab initio* treatment of phonon-mediated superconductivity [Eliashberg1960]. It is written in the language of field theory, considering the electronic and phonon[3] fields, as well as their interaction. In its complete version, an anisotropic gap equation needs to be numerically solved in order to obtain the gap function, as in the BCS theory. In the lighter version presented below, one first calculates the e-ph coupling λ at $T = 0$ and then uses the semi-empirical McMillan–Allen-Dynes formula to estimate the critical temperature.

6.2.1 Electron-phonon coupling

The Eliashberg theory is based on the Fröhlich hamiltonian, which reads:

$$\hat{H} = \sum_{n\mathbf{k}\sigma}(\epsilon_{n\mathbf{k}} - \mu)\hat{c}^\dagger_{n\mathbf{k}\sigma}\hat{c}_{n\mathbf{k}\sigma} + \sum_{\nu\mathbf{q}}\hbar\omega_{\nu\mathbf{q}}(\hat{a}^\dagger_{\nu\mathbf{q}}\hat{a}_{\nu\mathbf{q}} + 1/2) + \frac{1}{\sqrt{N_{\mathrm{BvK}}}}\sum_{\substack{nm\mathbf{k}\sigma\\ \nu\mathbf{q}}} g^\nu_{mn}(\mathbf{k},\mathbf{q})(\hat{a}_{\nu\mathbf{q}} + \hat{a}^\dagger_{\nu\text{-}\mathbf{q}})\hat{c}^\dagger_{m\mathbf{k}+\mathbf{q}\sigma}\hat{c}_{n\mathbf{k}\sigma} \quad (6.6)$$

[1] A two-body wavefunction of indistinguishable particles !

[2] It can be mathematically seen in the BCS formula $\Psi_{\mathrm{CP}}(\mathbf{k}) = \frac{\Delta_\mathbf{k}}{2E_\mathbf{k}}$ where $E_\mathbf{k} = \sqrt{\Delta^2_\mathbf{k} + (\epsilon_\mathbf{k} - \epsilon_F)^2}$

[3] Similarly to the BCS theory, the phonon field can in fact be replaced by another bosonic field, so that the Eliashberg theory can be generalized to address unconventional superconductivity also.

where $\hat{c}^\dagger$ and $\hat{c}$ are the electronic creation and annihilation operators, while $\hat{a}^\dagger$ and $\hat{a}$ are their phonon counterparts. N_{BvK} is the number of unit-cells in the Born–von-Kármán supercell and $g^\nu_{mn}(\mathbf{k},\mathbf{q})$ denotes the e-ph matrix elements. The coupling term can be understood as follows: an electron in the Bloch state $n\mathbf{k}$ with energy $\epsilon_{n\mathbf{k}}$ absorbs or creates a phonon of branch index ν, wavevector $\mathbf{q}$ and frequency $\omega_{\nu\mathbf{q}}$, which has the effect to changes its momentum to $\mathbf{k}'=\mathbf{k}+\mathbf{q}$ and potentially its band index to m, without affecting its spin. The e-ph matrix elements, which describe the energy of the interactions, are defined in the DFT framework as:

$$g^\nu_{mn}(\mathbf{k},\mathbf{q}) = \left\langle \psi^{\text{KS}}_{m\mathbf{k}+\mathbf{q}} \middle| \Delta_{\nu\mathbf{q}} V^{\text{KS}} \middle| \psi^{\text{KS}}_{n\mathbf{k}} \right\rangle \tag{6.7}$$

where V^{KS} is the Kohn-Sham potential. The notation $\Delta_{\nu\mathbf{q}}$ designates the linear change in the potential generated by the displacement associated to a phonon $\nu\mathbf{q}$. If the state $|\psi_{n\mathbf{k}}\rangle$ diffused by this operator overlaps strongly with $|\psi_{m\mathbf{k}+\mathbf{q}}\rangle$, it gives a strong coupling. In other words, high e-ph matrix elements mean that the lattice distortions modify strongly the energy of the electrons. These matrix elements are calculated using density functional perturbation theory (DFPT), a refinement of DFT which enables to calculate response functions. The so-called anisotropic Eliashberg spectral function is defined as a sum of Dirac δ-peaks at the phonon-energies, weighted by the e-ph matrix elements:

$$\alpha^2F(n\mathbf{k},m\mathbf{k}',\omega) = N_F \sum_\nu \left|g^\nu_{mn}(\mathbf{k},\mathbf{k}-\mathbf{k}')\right|^2 \delta(\omega-\omega_{\nu\mathbf{k}-\mathbf{k}'}) \tag{6.8}$$

from which one can define a Fermi surface-averaged spectral function:

$$\alpha^2F(\omega) = \frac{1}{2N_F^2}\int_{\text{BZ}} \frac{d\mathbf{k}}{(2\pi)^3}\frac{d\mathbf{k}'}{(2\pi)^3} \sum_{nm} \alpha^2F(n\mathbf{k},m\mathbf{k}',\omega)\delta(\varepsilon_{n\mathbf{k}}-E_F)\delta(\varepsilon_{m\mathbf{k}'}-E_F) \tag{6.9}$$

where the two Dirac δ-peaks ensure that $\mathbf{k}$ and $\mathbf{k}'$ belong to the Fermi surface. This weird notation for the spectral function is due to historical reasons, and is reminiscent of its definition (6.8): the squared coupling weights of the possible diffusions by phonons, multiplied by the phonon DOS. Notice that it has the same form than the single-particle spectral function (4.18) defined in the MBPT framework. Finally, the isotropic electron-phonon coupling is defined as:

$$\lambda = 2\int_0^\infty d\omega\, \frac{\alpha^2F(\omega)}{\omega} \tag{6.10}$$

One can also define the anisotropic e-ph coupling matrix elements:

$$\lambda_{\mathbf{k}\mathbf{k}'} = \frac{1}{N_F}\sum_{nm,\nu}\int_0^\infty d\omega\, \frac{|g^\nu_{mn}(\mathbf{k},\mathbf{k}-\mathbf{k}')|^2}{\omega}\delta(\varepsilon_{n\mathbf{k}}-E_F)\delta(\varepsilon_{m\mathbf{k}'}-E_F)\delta(\omega-\omega_{\nu\mathbf{k}-\mathbf{k}'}) \tag{6.11}$$

without integrating on the Brillouin zone. This quantity is interesting since it tells us between which part of the Fermi surface the coupling is stronger. Indeed, in a multiband system like nickelates, the coupling can come from different sheets of the Fermi surface with different values of $\lambda_{\mathbf{k}\mathbf{k}'}$ (see for example Fig. 7.9c). One can notice that in the Eliashberg theory, the frequency dependence is considered. Hence, contrary to the BCS theory in which the interaction between electrons is supposed instantaneous, here the dynamics and more specifically the retardation effects are taken into account.

6.2.2 McMillan–Allen-Dynes formula

From λ, an estimate of the critical temperature can be obtained via the McMillan-Allen-Dynes formula [McMillan1968, Allen1975], which is an analytical approximation of the Eliashberg solution:

$$T_c = \frac{\hbar\omega_{\log}}{1.2k_B}\exp\left(\frac{-1.04(1+\lambda)}{\lambda-\mu^*(1+0.62\lambda)}\right) \tag{6.12}$$

In this formula, the logarithmic average of the phonon frequency $\omega_{\log}$ is obtained from the Eliashberg spectral function as

$$\omega_{\log} = \exp\left(\frac{2}{\lambda}\int d\omega \frac{\log\omega}{\omega}\alpha^2 F(\omega)\right) \tag{6.13}$$

while the quantity μ^* is the so-called effective Coulomb pseudopotential (whose value typically ranges between 0.04 and 0.16). The McMillan formula is valid for stronger electron-phonon coupling. One notice that an hardening of the phonons, resulting in a increase in ω_{log}, will enhance the superconducting T_c.

To summarize: the phonons determine the peaks position of the Eliashberg spectral function, and the e-ph matrix elements their amplitude. The integration of this spectral function over the frequency axis gives the e-ph coupling constant λ. The higher the latter is, the higher is the T_c calculated via the McMillan–Allen-Dynes formula. Hence, from plots of the spectral function like the one shown in Fig. 7.9, one can identify which are the most important phonons in the coupling mechanism.

6.3 Unconventional superconductivity

So far, there are no fully *ab initio* methods enabling to tackle unconventional superconductivity, therefore addressed by models. Most of the time, these models are a refinement of the Hubbard model fitted on electronic structures calculated *ab initio*. In the context of the bilayer nickelate $La_3Ni_2O_7$, see for example [Zhang2024, Xia2025] which details their models and the way to solve the associated gap equation.

References

A full derivation of the BCS theory can be found in Chap. III of the Bible [Tinkham1996]. The reviews [Marsiglio2020] and [Giustino2017] (Sec. XI), and the articles [Margine2013] and [Poncé2016] presenting the EPW code were also really helpful to get a bird's-eye view of the Eliashberg theory. Finally, parts of the text of this section were taken from our article [Meier2024].

[Allen1975] P. B. Allen and R. C. Dynes. *Transition temperature of strong-coupled superconductors reanalyzed*. Physical Review B, vol. 12, no. 3, pages 905–922, August 1975. doi:10.1103/PhysRevB.12.905.

[Bardeen1957a] J. Bardeen, L. N. Cooper and J. R. Schrieffer. *Microscopic Theory of Superconductivity*. Physical Review, vol. 106, no. 1, pages 162–164, April 1957. doi:10.1103/PhysRev.106.162.

[Bardeen1957b] J. Bardeen, L. N. Cooper and J. R. Schrieffer. *Theory of Superconductivity*. Physical Review, vol. 108, no. 5, pages 1175–1204, December 1957. doi:10.1103/PhysRev.108.1175.

[Cooper1956] Leon N. Cooper. *Bound Electron Pairs in a Degenerate Fermi Gas*. Physical Review, vol. 104, no. 4, pages 1189–1190, November 1956. doi:10.1103/PhysRev.104.1189.

[Eliashberg1960] GM Eliashberg. *Interactions between electrons and lattice vibrations in a superconductor*. Soviet Physics JETP, 1960.

[Giustino2017] Feliciano Giustino. *Electron-phonon interactions from first principles*. Reviews of Modern Physics, vol. 89, no. 1, page 015003, February 2017. doi:10.1103/RevModPhys.89.015003.

[Margine2013] E. R. Margine and F. Giustino. *Anisotropic Migdal-Eliashberg theory using Wannier functions*. Physical Review B, vol. 87, no. 2, page 024505, January 2013. doi:10.1103/PhysRevB.87.024505.

[Marsiglio2020] F. Marsiglio. *Eliashberg theory: A short review*. Annals of Physics, vol. 417, page 168102, June 2020. doi:10.1016/j.aop.2020.168102.

[McMillan1968] W. L. McMillan. *Transition Temperature of Strong-Coupled Superconductors*. Physical Review, vol. 167, no. 2, pages 331–344, March 1968. doi:10.1103/PhysRev.167.331.

[Meier2024] Q. N. Meier, J. B. de Vaulx, F. Bernardini, A. S. Botana, X. Blase, V. Olevano and A. Cano. *Preempted phonon-mediated superconductivity in the infinite-layer nickelates*. Physical Review B, vol. 109, no. 18, page 184505, May 2024. doi:10.1103/PhysRevB.109.184505.

[Poncé2016] S. Poncé, E. R. Margine, C. Verdi and F. Giustino. *EPW: Electron–phonon coupling, transport and superconducting properties using maximally localized Wannier functions*. Computer Physics Communications, vol. 209, pages 116–133, December 2016. doi:10.1016/j.cpc.2016.07.028.

[Tinkham1996] Michael Tinkham. Introduction to superconductivity. McGraw-Gill, 2nd edition edition, 1996.

[von Rohr2023] Fabian O. von Rohr. *Chemical Principles of Intrinsic Topological Superconductors*. Chemistry of Materials, vol. 35, no. 22, pages 9455–9472, November 2023. doi:10.1021/acs.chemmater.3c00760.

[Xia2025] Chengliang Xia, Hongquan Liu, Shengjie Zhou and Hanghui Chen. *Sensitive dependence of pairing symmetry on Ni-eg crystal field splitting in the nickelate superconductor $La_3Ni_2O_7$*. Nature Communications, vol. 16, no. 1, page 1054, January 2025. doi:10.1038/s41467-025-56206-0.

[Zhang2024] Yang Zhang, Ling-Fang Lin, Adriana Moreo, Thomas A. Maier and Elbio Dagotto. *Structural phase transition, s±-wave pairing, and magnetic stripe order in bilayered superconductor $La_3Ni_2O_7$ under pressure*. Nature Communications, vol. 15, no. 1, page 2470, March 2024. doi:10.1038/s41467-024-46622-z.

Part II

Research work on nickelates

7

Electron-phonon coupling in the infinite-layer nickelates $R\mathrm{NiO}_2$

« To be, or not to be phonon-mediated, that is the question. »

Freely adapted from *Hamlet*, Shakespeare

This chapter addresses the possibility of phonon-mediated superconductivity in the infinite-layer nickelates, using *GW* electronic structures. The majority of the work detailed here has been published in Q. N. Meier, J.B. de Vaulx, et al. *"Preempted phonon-mediated superconductivity in the infinite-layer nickelates"*, Physical Review B, May 2024 [Meier2024] and parts of the text of this article have been re-used. However, the introduction has been re-written differently to insist on the reasons we have worked on this subject and some sections have been further developed in order to describe what I did myself (electronic structures, comparisons of the different plasmon-pole models and of the different DFT functionals). On the other hand, the parts of the work mainly carried out by Quintin Meier (phonon and electron-phonon calculations) have been shortened.

7.1 Introduction

At the end of 2022, only square-planar nickelates in thin films were measured superconducting (see Sec. 1.3.2), namely several types of doped infinite-layers (IL) with different rare-earths as well as an undoped neodymium pentalayer (PL). The observed onset critical temperatures, not exceeding 15 K, were comparable with the ones of conventional superconductors. Hence, wondering about the conventional or unconventional nature of superconductivity in these square-planar nickelates was legitimate. However, these materials have been investigated in the first place because they present the same electronic configuration than cuprates, the

most iconic unconventional superconductors (d^9 for parent ILs, $d^{8.8}$ for doped ILs and the PL). The enthusiasm about nickelates was just based on this similarity: they were offering a new perspective to tackle the problem of unconventional superconductivity. Moreover, early electron-phonon coupling calculations based on DFT electronic structures ruled out the possibility of phonon-mediated superconductivity in these compounds [Nomura2019] as well as for hydrogen-intercalated systems [Di Cataldo2023].

In this context, Li and Louie released in october 2022 a preprint on arXiv that was reconsidering the possibility of phonon-mediated superconductivity in the specific case of the infinite-layer $Nd_{0.8}Sr_{0.2}NiO_2$ [Li2022]. In this work, where both the electronic structure and the e-ph matrix elements were treated at the GW level, they obtained T_cs comparable with experiment, challenging the unconventional nature of these nickelates. Quite surprising and unexpected, this conclusion was to take seriously, and we decided to cross-check it.

Electronic structure

At the density-functional-theory (DFT) level, the Fermi surface of these systems resembles the one of the cuprates and is similarly dominated by Ni-3$d_{x^2-y^2}$ states (see Fig. 7.1). However, in contrast to the cuprates, there is a so-called self-doping effect by rare-earth derived 5d states which results in the appearance of two additional electron pockets around Γ and A (see the bandplot with orbital characters in Fig. 7.2). Introducing hole doping as in $Nd_{0.8}Sr_{0.2}NiO_2$ reduces these pockets and eventually promotes superconductivity with maximal T_c around 20 K.

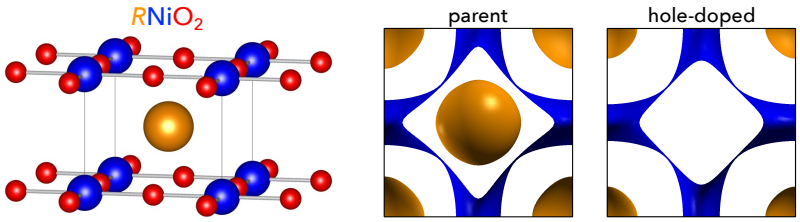

Figure 7.1: (Left panel) Crystal structure of the infinite-layer nickelates RNiO$_2$ (R=Nd,La) with nickel atoms in blue, oxygens in red, and rare-earth in orange. (Middle and right panels) Top view of the characteristic Fermi surface of these systems with the main Ni-3$d_{x^2-y^2}$ sheet in blue and the additional rare-earth derived sheets (self-doping) in orange.

7.2 Inconsistency of electronic structures with respect to literature

In a first place, we tried to reproduce Li and Louie's bandstructure for $Nd_{0.8}Sr_{0.2}NiO_2$, using ABINIT. As we found discrepancies with our preliminary calculations, we digged further in order to identify why, even to use the BERKELEYGW code they have used. We managed to clearly identify two main elements which explains their bandplot.

7.2.1 Slow convergence of the self-energy with the HL PPM

One of the specificity of the Li and Louie's work was the use of the Hybertsen-Louie (HL) plasmon-pole model (PPM) in the dynamical screening W, and not the more common Godby-Needs (GN) PPM (see Sec. 5.5.2.1). The slow convergence of the self-energy $\Sigma = GW$ with respect to the number of bands n_b taken into account in its calculation, when the HL PPM is

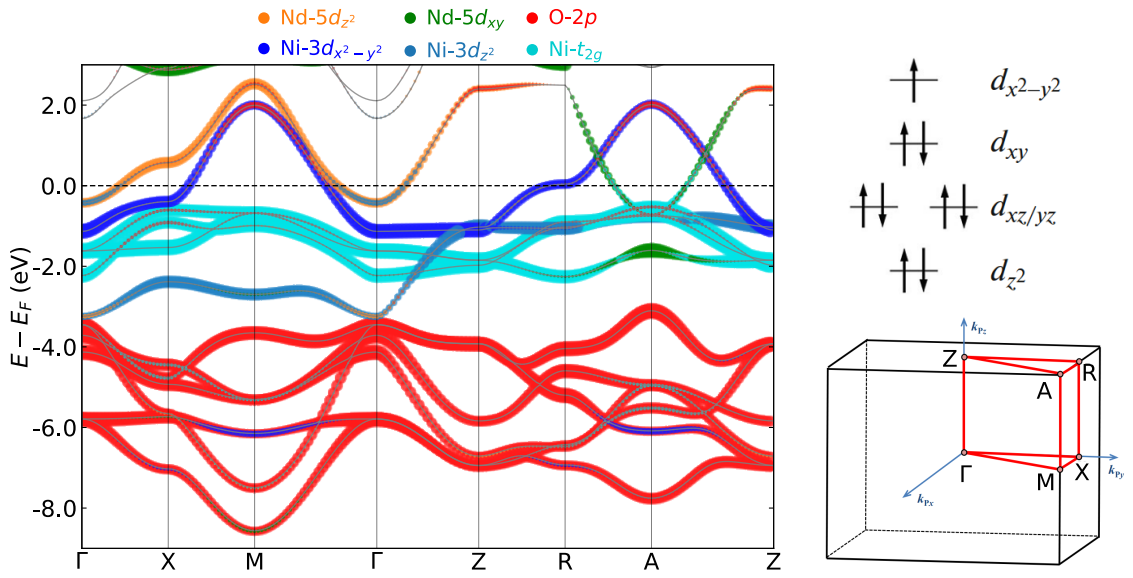

Figure 7.2: (left) DFT bandplot of the IL parent $NdNiO_2$ with orbital character projections. (bottom right) Associated **k**-path, from [Hinuma2017]. (top right) Nominal d^9 electronic configuration of the Ni^{1+} ion, from [Botana2021]. The Fermi surface is made of the main Ni-3$d_{x^2-y^2}$ sheet (blue) plus two self-doping electron pockets: one around Γ due to the Nd-5d_{z^2} band (orange) and another one around A originating from a band of mixed Nd-5d_{xy}/Ni-t_{2g} character (green/cyan).

used for W, has already been pointed out in [Stankovski2011].

As it is standard in GW calculations, we performed a convergence study for this parameter n_b. The screening W was calculated with plane-wave cutoffs of 40 and 15 Ha for the wavefunctions and the dielectric matrix, respectively, as well as 170 bands. For the self-energy stage, we chose three **k**-points and the two bands around E_F, namely the Ni-3$d_{x^2-y^2}$ and the rare-earth 5d bands, for which we calculated the GW self-energy. These bands are the relevant ones since the e-ph coupling is a low energy phenomenon which takes place in a small region around E_F. The point $\mathbf{k}_{\Gamma\text{-}Z}$ at 1/3 of the Γ-Z segment was chosen since we observed a big difference on this segment between our preliminary calculation and Li and Louie's ones (see Fig. 7.4).

Fig. 7.3 shows the result of this study for $\mathbf{k}_{\Gamma\text{-}Z}$ (results were similar for the two other **k**-points). The HL PPM requires more than 1200 bands to converge whithin a window of ±0.1 eV (considered as the GW uncertainty) around the most converged value. To account for the margin of error, we considered 1400 bands as a reliable value to perform calculations with the HL PPM, which is way higher than the 200 bands used in [Li2024b][1]. Fig. 7.4 compare the bandplots and DOSs in the low and high convergence cases. In the former, the two bands are overlapping on the Γ-X-M-Γ path and hence the DOS at the Fermi level N_F is higher, as shown in the inset. It is likely to give a higher e-ph coupling, as one can guess from the BCS formula $\lambda = N_F V$ (see Sec. 6.1). Increasing n_b has the effect to increase $\Delta\epsilon$, i.e. the two bands move from the Fermi level in opposite directions. Our convergence study then shows that this higher DOS at E_F is an artifact of the low convergence of the HL PPM.

[1] In the supplemental material of their article, Li and Louie shows a HL calculation using 1000 bands (see their Fig. S3(b)) which confirms the convergence difficulties with the HL PPM: to include more bands strongly modifies the position of the rare-earth band by shifting it up.

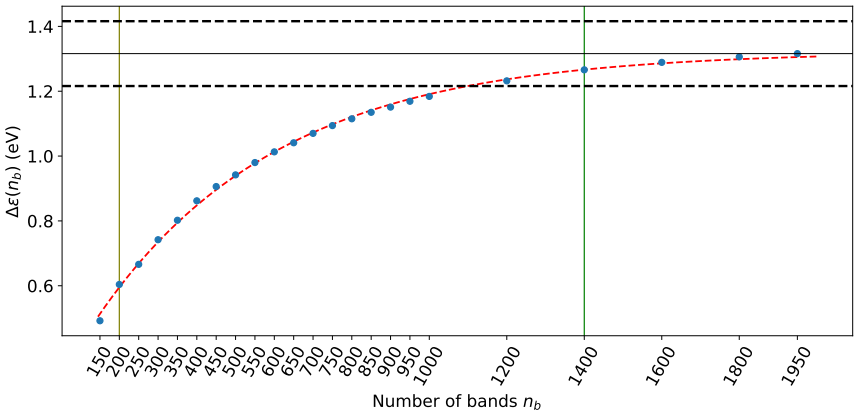

Figure 7.3: Slow convergence of the self-energy with respect to the number of bands n_b when the HL PPM is used for W, in the case of $Nd_{0.8}Sr_{0.2}NiO_2$. $\Delta\epsilon$ is the QP difference at $\mathbf{k}_{\Gamma\text{-}Z}$ between the Ni-3$d_{x^2-y^2}$ and Nd-5d_{z^2} bands. The black dashed lines indicate a ± 0.1 eV window around the most converged value. The red dashed line is a fit of the form $f(n_b) = ae^{-bn_b} + c$. The olive and green vertical lines indicate the number of bands used in Li and Louie's work and ours, respectively.

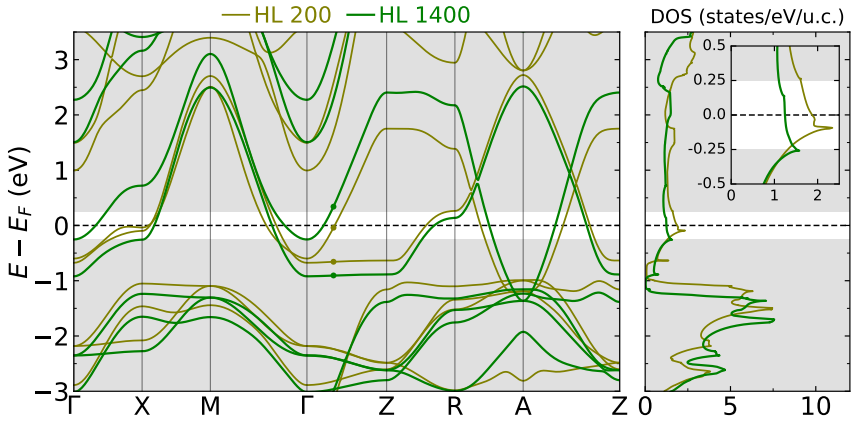

Figure 7.4: Comparison of the HL-GW bandplots and DOSs of $Nd_{0.8}Sr_{0.2}NiO_2$ with 200 and 1400 bands taken into account in the self-energy calculation. The dots indicates the GW energies at $\mathbf{k}_{\Gamma\text{-}Z}$ for the two bands of interests. The white window of ± 250 meV corresponds to the states taken into account for the e-ph coupling. The singularity in the DOS is due to the shoulder of the Ni-3$d_{x^2-y^2}$ band close to X.

7.2.2 On and off-shell approximations

The low convergence when using the HL PPM does not explain on its own the bandplot in [Li2024b]. Using BerkeleyGW and performing many tests, we managed to find a fundamental reason for it. Fig. 7.5 compares the bandplots calculated with BerkeleyGW using both off-shell (a) and on-shell approximations (b). Although considerably better convergence is obtained with $n_b = 1400$ for the HL PPM as described in the previous section, in this calculation we used $n_b = 200$ as in [Li2024b]. The bandplot in blue is given as a reference and corresponds to the Abinit calculation for which we used the same parameters than in [Li2024b] (HL PPM, lattice parameters, convergence parameters). Since there are fundamental differences between the two codes (e.g. the treatment of the screening at the $\mathbf{q} \to 0$ limit) it does not exactly reproduce the BerkeleyGW bandplot. However, the problem we want to point out lies elsewhere. The on-shell calculation in (b) reproduces in a satisfactory manner the bandplot reported in [Li2024b] and shown in (c). The conclusion is the following: the on-shell approximation for the self-energy was used in this paper, and not the more common and recommended off-shell (see Sec. 4.2.4.1). In other words, the quasiparticle renormalization factor Z has been neglected.

It was latter confirmed by the authors in their subsequent arXiv release. Further, considering the electronic structures in Fig. 7.5(a), we later found that the corresponding e-ph coupling constant λ is 0.31 (ABINIT) and 0.36 (BERKELEYGW) while considering the BERKELEYGW one in (b) λ becomes 0.41 (and hence explains the larger value reported in [Li2024b]). With 1400 bands for the HL PPM as described in the previous section, $\lambda = 0.163$ is obtained with ABINIT (see Tab. 7.1).

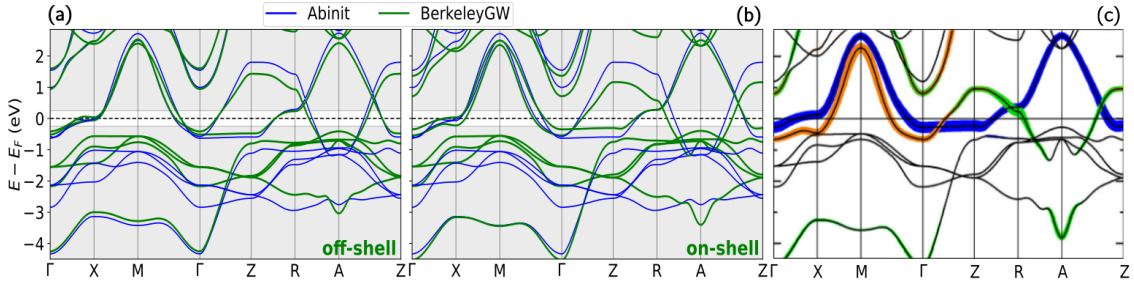

Figure 7.5: (a and b) *GW* bandplots for $Nd_{0.8}Sr_{0.2}NiO_2$ obtained with ABINIT (blue) and BERKELEYGW (green) using the HL PPM. The white window indicates ±250 meV around E_F. The ABINIT results in the two panels are the same and correspond to the off-shell solution (same curve as "HL 200" of Fig. 7.4). The BERKELEYGW results in a and b correspond to the off-shell and on-shell solutions, respectively. (c) Li and Louie's *GW* bandplot using the on-sell approximation in BERKELEYGW [Li2024b], which is well reproduced by the green curve in the b.

7.3 Methodology for electron-phonon coupling calculations

The findings presented in the previous section encouraged us to perform our own e-ph coupling calculations. This section present the general methodology which has been used for the studies presented in sections 7.4, 7.5 and 7.6. To begin with, G_0W_0 electronic structures were calculated for the compounds of interest using ABINIT, as well as the phonons spectra using QUANTUM ESPRESSO. Putting together the results of these two independent calculations, the e-ph couplings (isotropic and anisotropic) were calculated using EPW. Finally, the corresponding T_cs were calculated using either the McMillan formula or the more cumbersome fully anisotropic Eliashberg theory. Fig. 7.6 synthesizes the procedure. For the doped compound $Nd_{0.8}Sr_{0.2}NiO_2$, the Nd substitution with Sr was included via the virtual crystal approximation (VCA) [Bellaiche2000]. The relevance of VCA has been carefully addressed in the context of these ILs in [Li2024b]. All the technical details, calculations parameters and cutoffs are in App. 7.A.

We used the *GW* electronic structure combined with the e-ph matrix elements obtained from DFT and DFPT, a procedure that we denote (ϵ^{GW}, g^{DFT}). In fact, it amounts to consider the *GW* Fermi surface and DOS to calculate the Eliashberg spectral function (6.9), instead of the DFT ones. Our description of the electronic structures at the *GW* level considers dynamical correlation effects compared to such calculations in the literature which are most of the time carried out at the DFT level only. On the other hand, Li and Louie used an advanced methodology they developed to calculate the e-ph matrix elements at the *GW* level [Li2019b,Li2024a], using an in-house modified version of the EPW code that they did not release yet. In one word, they replaced the exchange-correlation potential of DFT by the non-local *GW* self-energy in formula (6.7), that is $g^{GW}_{mn\nu}(\mathbf{k},\mathbf{q}) = g^{\mathrm{DFT}}_{mn\nu}(\mathbf{k},\mathbf{q}) - \langle\psi_{m\mathbf{k}+\mathbf{q}}|\Delta_{\nu\mathbf{q}}V_{\mathrm{XC}}|\psi_{n\mathbf{k}}\rangle +$

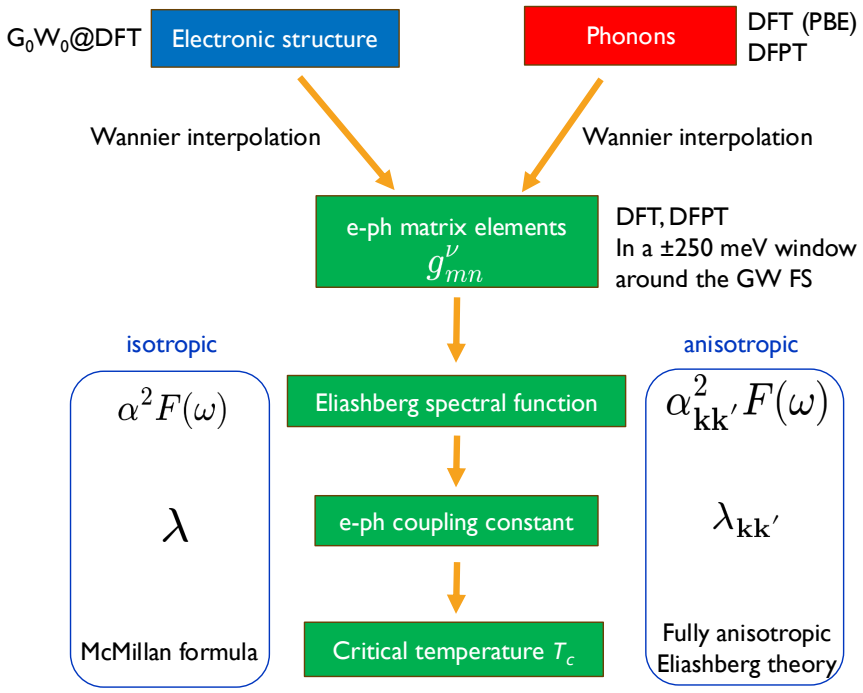

Figure 7.6: Scheme of the general electron-phonon coupling calculation procedure, in its isotropic and anisotropic versions.

$\langle\psi_{m\mathbf{k}+\mathbf{q}}|\Delta_{\nu\mathbf{q}}\Sigma_{GW}|\psi_{n\mathbf{k}}\rangle$. Hence, their procedure corresponds to (ϵ^{GW}, g^{GW}), but they also compared this result with other combinations of DFT and *GW* quantities, as shown in Fig. 7.7. One can see that the *GW* corrections in the electronic structure or in the e-ph matrix elements independently enhance λ. We can then anticipate that our quantitative results will miss the *GW*-induced enhancement in the e-ph matrix elements, but the fact we want to point out is that the enhancement of λ when using ϵ^{GW} has been overestimated in [Li2024b], where the coupling is multiplied by almost a factor of four (from 0.13 to 0.48).

7.4 Study for different plasmon-pole models

The plasmon-pole model is a key ingredient of a *GW* calculation and influences the result. The GN PPM is more standard than the HL one, and it has been proven to give closer results from the exact contour deformation (CD) method (see Sec. 5.5.2.1) [Stankovski2011]. To clearly determine to which extent the results depend on the PPM, we carried out a comparative study using these three different manners to treat the dynamical screening: GN and HL PPMs as well as the CD method. This study was carried out at ambient pressure for different infinite-layers: the doped Nd$_{0.8}$Sr$_{0.2}$NiO$_2$ as well as the parent compounds NdNiO$_2$ and LaNiO$_2$.

7.4.1 Hole-doped Nd$_{0.8}$Sr$_{0.2}$NiO$_2$

We started our investigation on the hole-doped Nd$_{0.8}$Sr$_{0.2}$NiO$_2$ which was the first superconducting nickelate and reaches its maximal superconducting T_c near 20% doping [Li2019a]. This is also the compound studied in [Li2024b].

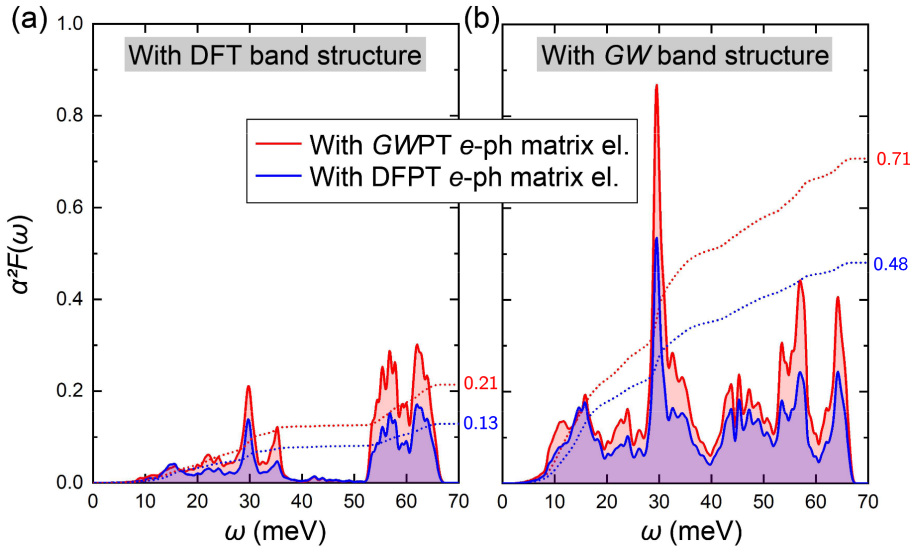

Figure 7.7: Comparison between the Eliashberg spectral functions corresponding to four different cases: on the left $(\epsilon^{DFT}, g^{DFT})$ and (ϵ^{DFT}, g^{GW}), on the right (ϵ^{GW}, g^{DFT}) and (ϵ^{GW}, g^{GW}). From the Supplemental Material of [Li2024b].

7.4.1.1 Electronic structure

Fig. 7.8 shows the computed band structure of this system at the DFT and *GW* level for different treatments of the screening. At the DFT level, there is no self-doping at the Γ point but an important one around A. However, from the *GW* results, we confirm a general enhancement of the self-doping due to electronic correlations which tends to create the electron pocket at Γ. This is accompanied by a decrease in the bandwidth of the bands crossing the Fermi level, which further translates into a significant increase in the density of states (DOS) at the Fermi level. At the same time, we find differences in these changes depending on how the screened Coulomb interaction is described in practice. *GW*-CD yields a low-energy electronic structure that is the most similar to DFT, while both GN and HL PPMs seem to slightly overestimate the many-body corrections and the self-doping effect, although GN is in better overall agreement with the CD result in this case. Compared with the numerically exact CD method, the plasmon-pole models tend to overestimate the self-doping effect (i.e. the dipping of the rare-earth band down the Fermi level at Γ and A).

7.4.1.2 Electron-phonon coupling

Next, we address the influence of correlations on the e-ph coupling and its implications for superconductivity in $Nd_{0.8}Sr_{0.2}NiO_2$. To do this, we start by calculating the phonons, whose DOS is shown in Fig. 7.9a. The lightest O atoms dominate the phonon DOS above 40 meV and produce the main feature at 30 meV. The Ni atom and the VCA atom $Nd_{0.8}Sr_{0.2}$ related modes are softer and contribute to the phonon DOS only below 40 meV and 30 meV respectively.

Estimation of T_c with the McMillan formula In order to quantify the e-ph coupling and to identify possible phonon-mediated superconducting instabilities, we calculate the isotropic Eliashberg spectral function $\alpha^2F(\omega)$ and the total e-ph coupling constant λ (see Sec. 6.2.1). These quantities are shown in Fig. 7.9b. From the comparison with the phonon DOS, we find that the main contributions to λ mainly come from the hard O modes with a subdominant

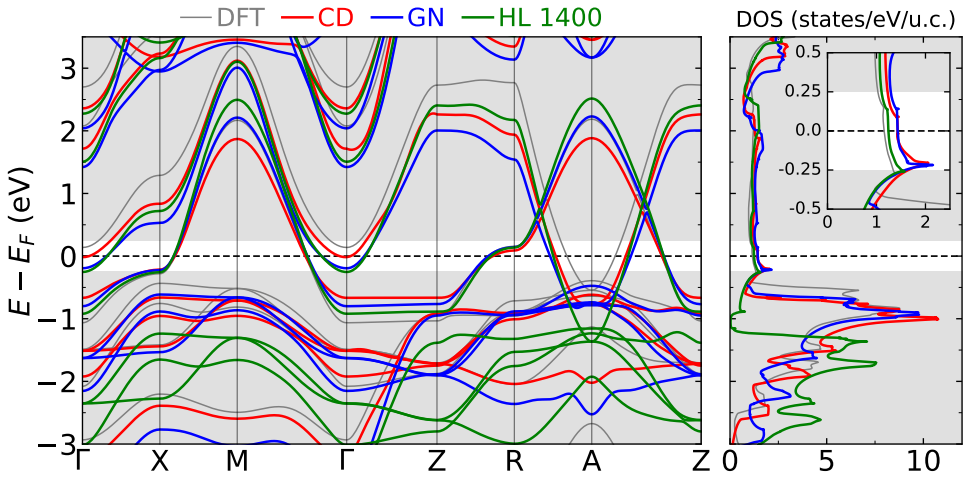

Figure 7.8: DFT and *GW* band structures of $Nd_{0.8}Sr_{0.2}NiO_2$ near the Fermi level. The different colors correspond to the different treatments of the screening, namely via the CD technique (red), the GN PPM (blue) and the HL one (green). The DFT result is in gray.

contribution from the softer Ni modes[2]. In general, the renormalization of the energies due to *GW* correlations tends to enhance the e-ph coupling compared to DFT values as it has been shown in several works [Faber2011, Yin2013, Li2019b]. This enhancement, however, turns out to be marginal in $Nd_{0.8}Sr_{0.2}NiO_2$ with λ increasing from 0.136 to just 0.183 in the numerically exact *GW*-CD case, while the plasmon-pole models yield 0.163 (HL) and 0.204 (GN). From λ, an estimate of the critical temperature for phonon-mediated superconductivity can be obtained according to the McMillan-Allen-Dynes formula (see Sec. 6.2.2). In this formula, the characteristic phonon frequency $\omega_{\log}$ is directly obtained from the Eliashberg spectral function, while μ^* is the so-called Coulomb pseudopotential and has to be chosen (with a value that typically ranges from 0.04 to 0.16). The electron-phonon coupling values and the resulting T_c's are summarized in Tab. 7.1. Even for a Coulomb pseudopotential as small[3] as $\mu^* = 0.05$, the correlation-enhanced calculated T_c's, not exceeding 0.05 K in the case of $Nd_{0.8}Sr_{0.2}NiO_2$, seems to be hardly compatible with the one experimentally reported of about 20 K [Li2019a].

Anisotropic Eliashberg theory The McMillan-Allen-Dynes considerations, however, miss the possibility of having superconductivity with different energy gaps in different parts of the Fermi surface. Consequently, the calculations described above may underestimate the corresponding T_c if such an anisotropy becomes relevant. Given the distinct multiband features of infinite-layer nickelates (see Fig. 7.2), then it is more appropriate to analyze the possible emergence of superconductivity in these systems in terms of the full Eliashberg theory. To this end, we first calculate the distribution of coupling strength $\lambda_{\mathbf{k}\mathbf{k}'}$ over the Fermi surface. The *GW* results are compared with DFT calculations in Fig. 7.9c. This comparison confirms that there is a slight overall enhancement of the e-ph coupling due to correlations. Further, the *GW* distributions feature a main peak at $\lambda_{\mathbf{k}\mathbf{k}'} \sim 0.1$, a second peak at ~ 0.27, and then a broader feature extending up to 1. This suggests that the gap function can be different in different parts of the Fermi surface, so that the actual T_c may be higher than that obtained from the McMillan-Allen-Dynes formula. This is confirmed from the solution of the anisotropic Eliashberg equations from which, in the *GW*-GN case, we obtain $T_c \sim 1$ K (and hence an increase of the effective λ from 0.2 to 0.3 due to the multiband features of the system). This T_c, however, still fails to explain

[2] Hard means at high frequency, as opposed to soft.
[3] The parameter μ^* is taken small to not risk to underestimate T_c.

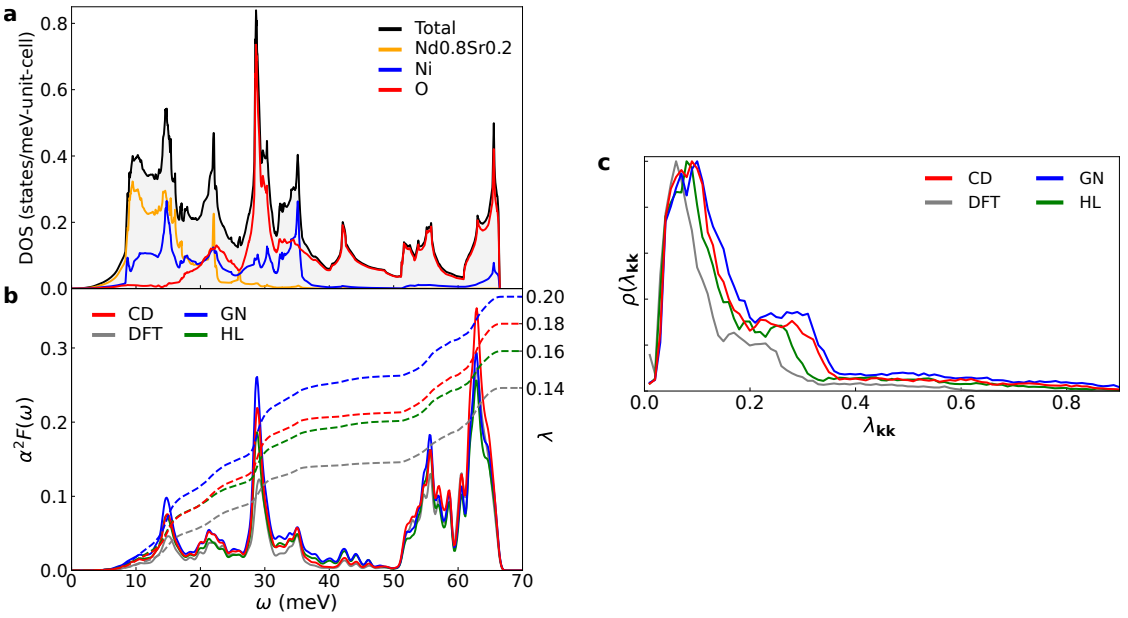

Figure 7.9: (a) Total and site-resolved phonon density of states and (b) Eliashberg spectral functions $\alpha^2F(\omega)$ (solid lines) with corresponding cumulative coupling constants $\lambda(\omega) = \int_0^\omega d\omega' \alpha^2F(\omega')/\omega'$ (dashed lines) calculated for $Nd_{0.8}Sr_{0.2}NiO_2$. (c) Distribution of e-ph coupling strength $\lambda_{\mathbf{kk}'}$ for the four different calculations. This is an histogram counting the number of $\lambda_{\mathbf{kk}'}$ within a small interval.

the experimentally measured one.

7.4.2 Parent compounds $NdNiO_2$ and $LaNiO_2$

From the previous analysis of the effect of correlations on the e-ph coupling in $Nd_{0.8}Sr_{0.2}NiO_2$, we can conclude that the electron pockets at Γ and A both provide additional states relevant for e-ph interactions. The amount of self-doping then effectively plays an important role with the size of these electron pockets being an indicator of the eventual coupling strength. To further investigate this point, we shift our focus to the parent compounds $NdNiO_2$ and $LaNiO_2$ where the self-doping effect is more pronounced. We find that, compared to $Nd_{0.8}Sr_{0.2}NiO_2$, the recovery of the electron pocket at Γ in $NdNiO_2$ leads to the increase of λ from 0.136 to 0.181 at the DFT level already. Then, as illustrated in Fig. 7.10, the incorporation of further electronic correlations at the *GW* level increases the eventual amount of self-doping. This translates into the additional increase of the e-ph coupling constant λ from 0.181 to 0.270 in $NdNiO_2$ and from 0.180 to 0.221 and $LaNiO_2$ respectively (see Tab. 7.1). This increase further gives a non-zero superconducting T_c of 0.5 K and 0.1 K according to McMillan-Allen-Dynes formula assuming a Coulomb pseudopotential $\mu^* = 0.05$. These results shows that the e-ph superconducting instability is higher in the parent compounds than in the doped one, although still very weak. It is nevertheless interesting since some indications of superconductivity have been found in $LaNiO_2$ in 2021 [Osada2021], and $NdNiO_2$ has been measured superconducting at the end of 2024 with $T_c^{\text{onset}} = 11$ [Parzyck2025].

We have also seen that the HL PPM does not give wrong results, but since it is harder to converge and as the GN PPM has proven to be an accurate approximation to the numerically exact CD method, we stick to the GN PPM for the rest of this work.

	Method		λ	$\omega_{\log}$ (meV)	T_c (K)
$Nd_{0.8}Sr_{0.2}NiO_2$	DFT		0.136	32.3	0.00
	GW	CD	0.183	30.5	0.02
		GN	0.204	28.1	0.05
		HL	0.163	29.0	0.00
$NdNiO_2$	DFT		0.181	27.7	0.02
	GW	CD	0.270	25.8	0.48
		GN	0.344	23.8	1.67
		HL	0.250	24.3	0.27
$LaNiO_2$	DFT		0.180	28.0	0.01
	GW	CD	0.221	28.0	0.12
		GN	0.244	26.0	0.25

Table 7.1: Electron-phonon coupling constants λ and $\omega_{\log}$ computed within DFT and *GW*, and corresponding superconducting transition temperature T_c according to the McMillan-Allen-Dynes formula with $\mu^* = 0.05$.

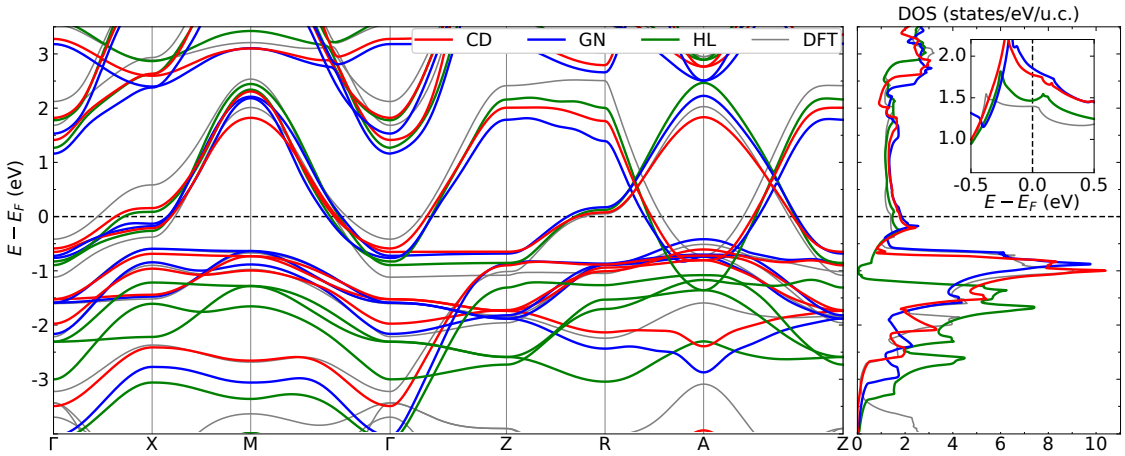

Figure 7.10: DFT and *GW* band structures of $NdNiO_2$, with the associated DOS.

7.5 Evolution with respect to pressure

For all the tested methods as well as the different compounds investigated, the T_cs we have obtained were very weak, if not zero. As our methodology was lacking the calculation of the e-ph coupling at the *GW* level, which can make us underestimate the T_cs, we needed another manner to confirm that superconductivity in ILs cannot be explained by an e-ph mechanism. The previous analysis confirms that one of the underlying factors that could enable e-ph superconductivity in the infinite-layer nickelates manifests through the enhancement of the self-doping effect. Such a self-doping traces back to the atomic-orbital overlaps along the out-of-plane direction so that, in principle, it can be tuned by means of applied pressure. To explore this possibility, we performed additional calculations as a function of pressure. This study was also motivated by an experimental article published in July 2022 [Wang2022], in which a monotonic enhancement of T_c with pressure was observed in the strontium-doped IL

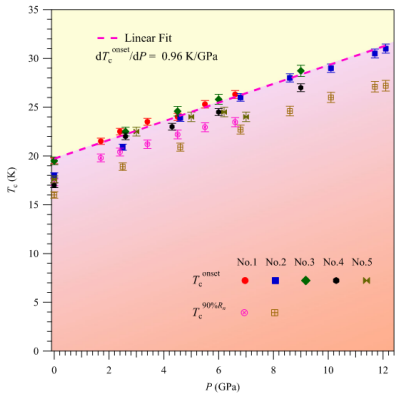

Figure 7.11: Experimental evolution of the T_c with respect to pressure in the IL thin-film $Pr_{0.82}Sr_{0.18}NiO_2$ from [Wang2022]. This monotonic increase is not consistent with the evolution of our calculated e-ph T_c's.

$PrNiO_2$[4] (see Fig. 7.11).

7.5.1 Hole-doped $Nd_{0.8}Sr_{0.2}NiO_2$

As in the previous section, we first consider the doped compound $Nd_{0.8}Sr_{0.2}NiO_2$. Fig. 7.12 illustrates the changes obtained its electronic structure due to hydrostatic pressure. There is an overall increase of the bandwidths so that the DOS at the Fermi level N_F is reduced accordingly. Further, while the self-doping of the Fermi surface remains practically unchanged at A, it increases at Γ with pressure.

When it comes to the phonons, we find a general hardening of all phonon modes. Assuming that the coupling constant λ remains unchanged, this would imply an increase of T_c according to McMillan-Allen-Dynes formula. At the same time, the reduction of the DOS at the Fermi level should reduce the coupling constant since $\lambda = V_{\text{e-ph}} N_F$ (see inset in Fig. 7.12a). In reality, N_F is reduced by $\sim$7.6% while the calculated λ is further lowered by $\sim$10% between 0 and 24 GPa (see Fig. 7.12b). Consequently, the overall change in λ is mostly due to a decrease in the DOS.

The computed distribution of the matrix elements $\lambda_{\mathbf{k}\mathbf{k}'}$ shows a small but visible shift towards lower values (see Fig 7.12c). We further obtain a saturation and then a slight increase in the e-ph coupling constant for pressures above 24 GPa. However, if the superconductivity was phonon mediated, then the superconducting T_c should initially decrease under the application of pressure, rather than increase like experimentally [Wang2022]. Even without agreeing quantitatively with the experimental T_c's, if the calculated e-ph coupling was increasing with pressure, it would have been an argument in favor of the phonon-mediated scenario. However, we have found exactly the opposite trend, which tends to rule out this scenario, at least as the main one responsible for the superconductivity mechanism.

7.5.2 Parent compounds $NdNiO_2$ and $LaNiO_2$

Finally, we consider the parent compounds under pressure, whose electronic structures are shown in Fig. 7.13. Similarly to the previous hole-doped case, the DOS at the Fermi level is reduced.

[4] Praseodymium is not neodymium neither lanthanum (the two elements we have taken into account in our calculations), but it is another common rare-earth used in the synthesis of nickelates, sharing similar properties with its neighbors in the periodic table. There are good reasons to think that a behavior observed in the Pr-based compound occurs also in its Nd and La counterparts.

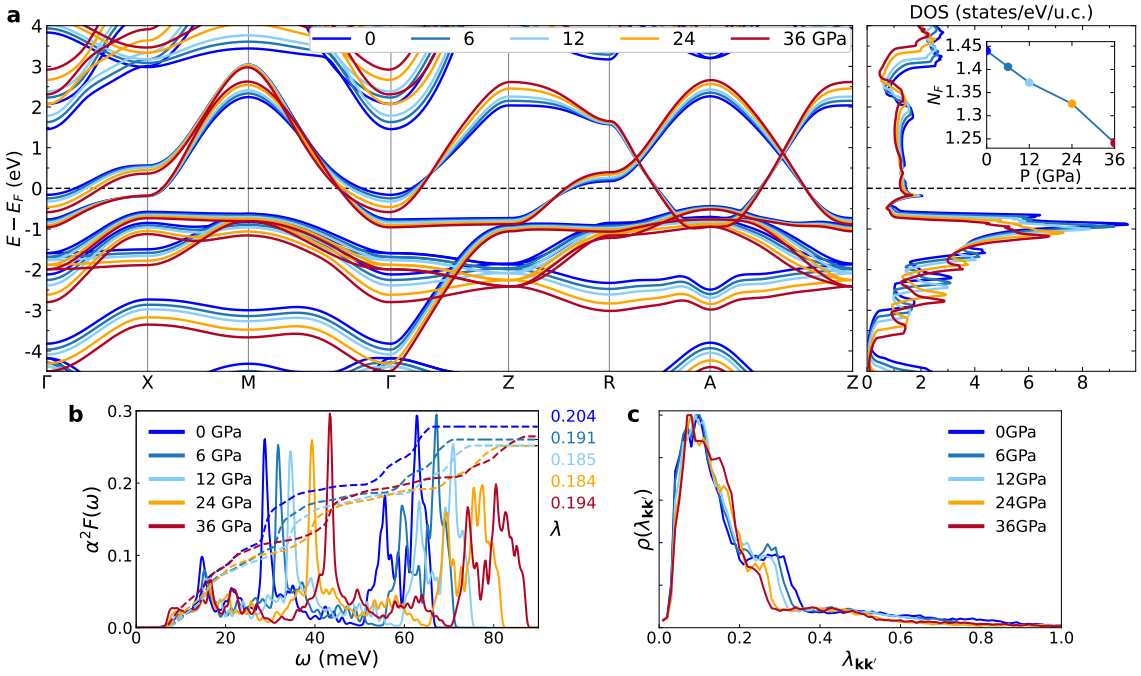

Figure 7.12: (a) Computed *GW* band structure and DOS of $Nd_{0.8}Sr_{0.2}NiO_2$ as a function of pressure. (b) Eliashberg function $\alpha^2F(\omega)$ and e-ph coupling constant λ and (c) distribution of e-ph coupling strength $\lambda_{\mathbf{kk'}}$ associated with the electronic structures in (a).

As a result, we find a decrease of the e-ph coupling constant λ as well as a narrowing of the distribution of e-ph coupling strength $\lambda_{\mathbf{kk'}}$ (not shown). The phonon-mediated superconducting instability obtained for the parent compounds is therefore expected to be suppressed by pressure too.

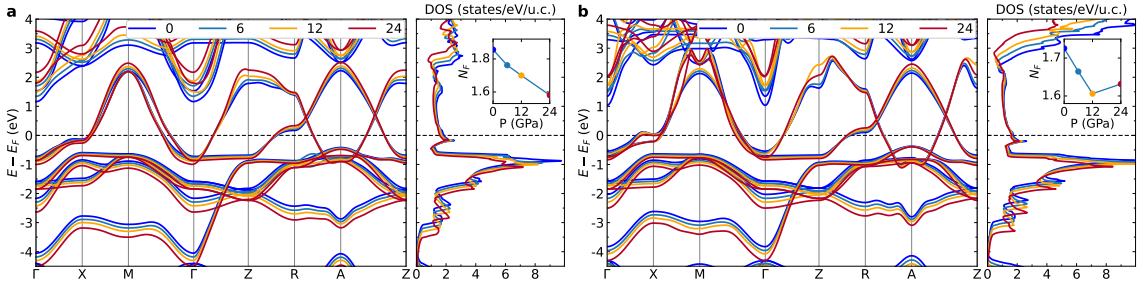

Figure 7.13: Computed *GW* band structure and DOS of $NdNiO_2$ (a) and $LaNiO_2$ (b) as a function of pressure. The initial self-doping of the Fermi surface is further enhanced at Γ with pressure resulting in the swapping of the Ni-3$d_{x^2-y^2}$ and R-3d_{z^2} bands along the Γ-X-M-Γ path. At A, in contrast, the self-doping remains essentially the same. In addition, there is a concomitant increase in the bandwidths that further results into a decrease of the DOS at the Fermi level.

7.6 Variation with respect to the starting DFT functional

These results, however, may still depend on the starting DFT functional. All our calculations were so far carried out using PBE. In this section, we analyze this possible dependence by testing the LDA and the hybrid HSE06 functionals. We focus here on the parent compound $LaNiO_2$.

This choice of La instead of Nd or $Nd_{0.8}Sr_{0.2}$ is representative from the *ab initio* perspective since it avoids limitations related to the modeling of doping by VCA as well as to the treatment of the 4*f* states, which are frozen into the core in the Nd pseudopotential.

7.6.1 Electronic structure

We first analyze the influence of the DFT functional choice on the electronic structure itself. To consider different starting points for *GW*, we performed electronic-structure calculations using LDA and the hybrid HSE06. In all these calculations, we considered the same PBE lattice parameters to single out purely electronic effects. The results are illustrated in Fig. 7.14. This figure shows that the initial DFT result can indeed be quite different. However, within the *GW* accuracy, the subsequent *GW* calculation tends to converge towards a common electronic structure and thereby correct possible drawbacks of the initial assumption. This is in fact quite spectacular, in the sense that the Ni-3*d* derived states are renormalized differently compared with the O-2*p* ones depending on initial DFT functional: with LDA and PBE the Ni-3*d* vs O-2*p* manifolds undergo modest vs substantial shifts respectively, while with HSE06 it is the

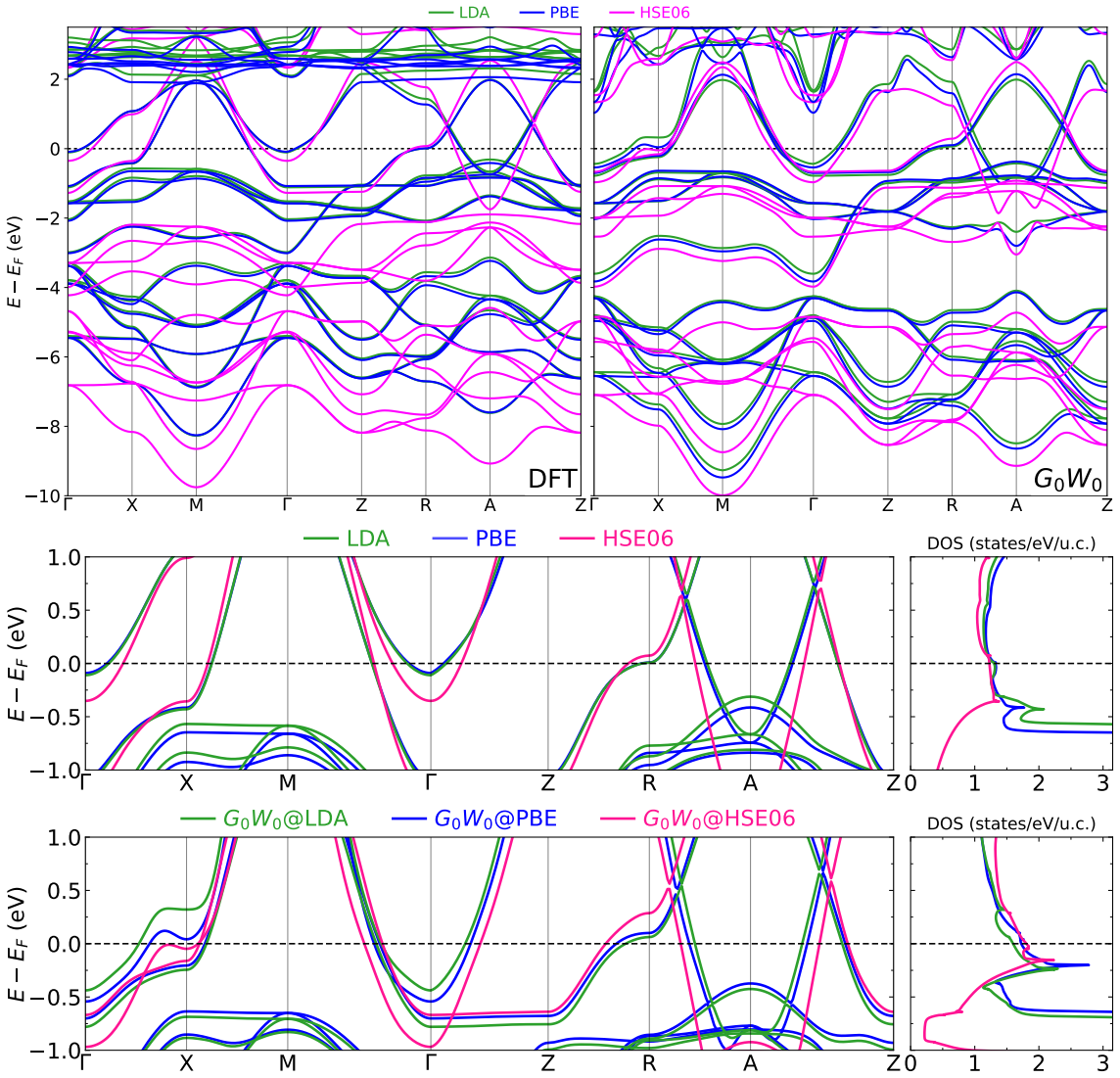

Figure 7.14: Comparison between the electronic band structure of $LaNiO_2$ computed at the DFT level using LDA, PBE and HSE06 for the exchange-correlation functional and subsequently within the *GW* approximation using the GN plasmon-pole model.

other way around (see Fig. 7.14). Also, while performing self-consistent *GW* calculations is out of the scope of this work, the above observation suggests that the one-shot *GW* results should be quite comparable to those obtained after reaching self-consistency in the energies.

The consistency between these results is also remarkably obtained near the Fermi level, which is the most important region for superconductivity. At the DFT level, LDA and PBE yield essentially the same result near the Fermi level with some differences. HSE06, however, introduces significant changes everywhere, including for the Ni-3*d* and La-4*d* bands crossing the Fermi level. Despite these differences, the subsequent *GW*-GN calculation tends to give the same result, again within the *GW* accuracy. It is at least converging towards the same —presumably the ideal nonperturbative self-consistent— structure, and confirms the reliable behavior of the *GW* corrections, no matter the starting point used for the perturbation theory. To further quantify this, we recalculated the e-ph coupling constant λ combining all the above *GW* results with the PBE phonons. The result is illustrated in Fig. 7.15a. This gives a direct measure of the possible spread with respect to the initial DFT functional used for the subsequent *GW* calculations, from which we obtain $\lambda = 0.24 \pm 0.04$.

7.6.2 Phonons

The choice of DFT functional also impacts the calculated phonons and e-ph matrix elements, and this impact may propagate to the final e-ph coupling. We scrutinize this possibility by comparing the results obtained with LDA and PBE phonons (LDA mostly underestimates the *a* lattice parameter while PBE overestimates *c*). Specifically, we performed additional calculations in which the LDA phonons are calculated with the lattice parameters optimized with both LDA and PBE functionals. The resulting phonons are quite different, with frequency changes of ~ 5 meV or even more. However, when it comes to the e-ph coupling constant, these differences are surprisingly washed out and the above values are recovered as illustrated in 7.15b.

In conclusion, we find that our results are remarkably robust with respect to the choice of the DFT functional.

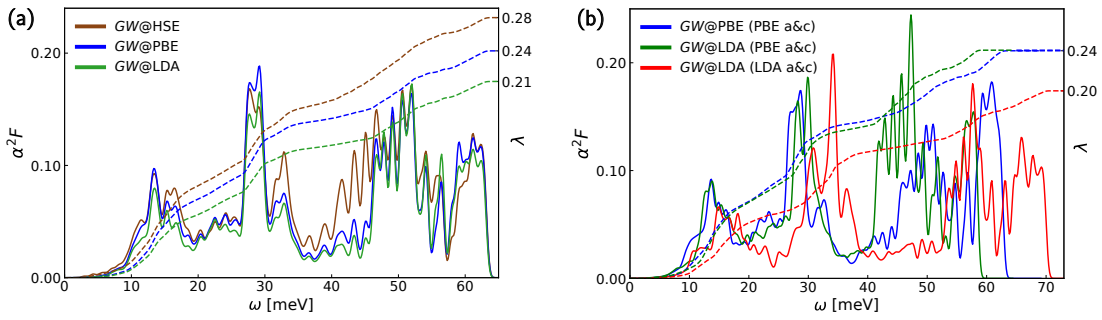

Figure 7.15: (a) Comparison between Eliashberg function $\alpha^2F(\omega)$ and cumulative coupling constant λ computed for LaNiO$_2$ from *GW* calculations using the GN plasmon pole model with different initial electronic structures (LDA, PBE and HSE06). (b) Comparison between Eliashberg function $\alpha^2F(\omega)$ and cumulative coupling constant λ computed for LaNiO$_2$ from *GW* calculations using different phonons: LDA with LDA optimized lattice parameters, LDA with PBE optimized lattice parameters and PBE with PBE optimized lattice parameters.

7.7 Conclusion

Our results confirm that, compared to DFT calculations, the e-ph coupling in the infinite-layer nickelates is enhanced due to correlations as included in the *GW* approximation. We have shown that this enhancement is robust with respect to important aspects of the *GW* methodology, such as the starting DFT functional and the subsequent modelling of the screening. In doing so, the computed enhancement of λ yields superconducting instabilities in these systems. Interestingly, we find that the above enhancement results in higher phonon-mediated superconducting instabilities in the parent $NdNiO_2$ and $LaNiO_2$ compounds than in the hole-doped compound $Nd_{0.8}Sr_{0.2}NiO_2$. However, the estimated T_c's remain way too small compared with the experimental ones, and gets further reduced with pressure, so that phonon-mediated superconductivity is visibly preempted by another unconventional mechanism in these systems.

References

[Bellaiche2000] L. Bellaiche and David Vanderbilt. *Virtual crystal approximation revisited: Application to dielectric and piezoelectric properties of perovskites*. Physical Review B, vol. 61, no. 12, pages 7877–7882, March 2000. doi:10.1103/PhysRevB.61.7877.

[Bernardini2022] F. Bernardini, A. Bosin and A. Cano. *Geometric effects in the infinite-layer nickelates*. Physical Review Materials, vol. 6, page 044807, April 2022. doi:10.1103/PhysRevMaterials.6.044807.

[Botana2021] A. S. Botana, F. Bernardini and A. Cano. *Nickelate Superconductors: An Ongoing Dialog between Theory and Experiments*. Journal of Experimental and Theoretical Physics, vol. 132, no. 4, pages 618–627, April 2021. doi:10.1134/S1063776121040026.

[Di Cataldo2023] Simone Di Cataldo, Paul Worm, Liang Si and Karsten Held. *Absence of electron-phonon-mediated superconductivity in hydrogen-intercalated nickelates*. Physical Review B, vol. 108, no. 17, page 174512, November 2023. doi:10.1103/PhysRevB.108.174512.

[Faber2011] Carina Faber, Jonathan Laflamme Janssen, Michel Côté, E. Runge and X. Blase. *Electron-phonon coupling in the C_{60} fullerene within the many-body GW approach*. Physical Review B, vol. 84, no. 15, page 155104, October 2011. doi:10.1103/PhysRevB.84.155104.

[Giannozzi2009] Paolo Giannozzi, Stefano Baroni, Nicola Bonini, Matteo Calandra, Roberto Car, Carlo Cavazzoni, Davide Ceresoli, Guido L. Chiarotti, Matteo Cococcioni, Ismaila Dabo, Andrea Dal Corso, Stefano de Gironcoli, Stefano Fabris, Guido Fratesi, Ralph Gebauer, Uwe Gerstmann, Christos Gougoussis, Anton Kokalj, Michele Lazzeri, Layla Martin-Samos, Nicola Marzari, Francesco Mauri, Riccardo Mazzarello, Stefano Paolini, Alfredo Pasquarello, Lorenzo Paulatto, Carlo Sbraccia, Sandro Scandolo, Gabriele Sclauzero, Ari P. Seitsonen, Alexander Smogunov, Paolo Umari and Renata M. Wentzcovitch. *QUANTUM ESPRESSO: a modular and open-source software project for quantum simulations of materials*. Journal of Physics: Condensed Matter, vol. 21, no. 39, page 395502, September 2009. doi:10.1088/0953-8984/21/39/395502.

[Giannozzi2017] P Giannozzi, O Andreussi, T Brumme, O Bunau, M Buongiorno Nardelli, M Calandra, R Car, C Cavazzoni, D Ceresoli, M Cococcioni, N Colonna, I Carnimeo, A Dal Corso, S de Gironcoli, P Delugas, R A DiStasio, A Ferretti, A Floris, G Fratesi, G Fugallo, R Gebauer, U Gerstmann, F Giustino, T Gorni, J Jia, M Kawamura, H-Y Ko, A Kokalj, E Küçükbenli, M Lazzeri, M Marsili, N Marzari, F Mauri, N L Nguyen, H-V Nguyen, A Otero-de-la Roza, L Paulatto, S Poncé, D Rocca, R Sabatini, B Santra, M Schlipf, A P Seitsonen, A Smogunov, I Timrov, T Thonhauser, P Umari, N Vast, X Wu and S Baroni. *Advanced capabilities for materials modelling with Quantum ESPRESSO*. Journal of Physics: Condensed Matter, vol. 29, no. 46, page 465901, October 2017. doi:10.1088/1361-648X/aa8f79.

[Giustino2007] Feliciano Giustino, Marvin L. Cohen and Steven G. Louie. *Electron-phonon interaction using Wannier functions*. Physical Review B, vol. 76, no. 16, page 165108, October 2007. doi:10.1103/PhysRevB.76.165108.

[Hinuma2017] Yoyo Hinuma, Giovanni Pizzi, Yu Kumagai, Fumiyasu Oba and Isao Tanaka. *Band structure diagram paths based on crystallography*. Computational Materials Science, vol. 128, pages 140–184, February 2017. doi:10.1016/j.commatsci.2016.10.015.

[Li2019a] Danfeng Li, Kyuho Lee, Bai Yang Wang, Motoki Osada, Samuel Crossley, Hye Ryoung Lee, Yi Cui, Yasuyuki Hikita and Harold Y. Hwang. *Superconductivity in an infinite-layer nickelate*. Nature, vol. 572, no. 7771, pages 624–627, August 2019. doi:10.1038/s41586-019-1496-5.

[Li2019b] Zhenglu Li, Gabriel Antonius, Meng Wu, Felipe H. da Jornada and Steven G. Louie. *Electron-Phonon Coupling from Ab Initio Linear-Response Theory within the GW Method: Correlation-Enhanced Interactions and Superconductivity in $Ba_xLa_{1-x}BiO_3$*. Physical Review Letters, vol. 122, no. 18, page 186402, May 2019. doi:10.1103/PhysRevLett.122.186402.

[Li2022] Zhenglu Li and Steven G. Louie. *Two-gap superconductivity and decisive role of rare-earth d electrons in infinite-layer nickelates*, October 2022. arXiv:2210.12819.

[Li2024a] Zhenglu Li, Gabriel Antonius, Yang-Hao Chan and Steven G. Louie. *Electron-phonon coupling from GW perturbation theory: Practical workflow combining BerkeleyGW, ABINIT, and EPW*. Computer Physics Communications, vol. 295, page 109003, February 2024. doi:10.1016/j.cpc.2023.109003.

[Li2024b] Zhenglu Li and Steven G. Louie. *Two-Gap Superconductivity and the Decisive Role of Rare-Earth d Electrons in Infinite-Layer Nickelates*. Physical Review Letters, vol. 133, no. 12, page 126401, September 2024. doi:10.1103/PhysRevLett.133.126401.

[Margine2013] E. R. Margine and F. Giustino. *Anisotropic Migdal-Eliashberg theory using Wannier functions*. Physical Review B, vol. 87, no. 2, page 024505, January 2013. doi:10.1103/PhysRevB.87.024505.

[Meier2024] Q. N. Meier, J. B. de Vaulx, F. Bernardini, A. S. Botana, X. Blase, V. Olevano and A. Cano. *Preempted phonon-mediated superconductivity in the infinite-layer nickelates*. Physical Review B, vol. 109, no. 18, page 184505, May 2024. doi:10.1103/PhysRevB.109.184505.

[Mostofi2014] A. A. Mostofi, J. R. Yates, G. Pizzi, Y. S. Lee, I. Souza, D. Vanderbilt and N. Marzari. *An updated version of wannier90: A tool for obtaining maximally-localised Wannier functions*. Computer Physics Communications, vol. 185, page 2309, 2014.

[Nomura2019] Yusuke Nomura, Motoaki Hirayama, Terumasa Tadano, Yoshihide Yoshimoto, Kazuma Nakamura and Ryotaro Arita. *Formation of a two-dimensional single-component correlated electron system and band engineering in the nickelate superconductor $NdNiO_2$*. Physical Review B, vol. 100, no. 20, page 205138, November 2019. doi:10.1103/PhysRevB.100.205138.

[Osada2021] Motoki Osada, Bai Yang Wang, Berit H. Goodge, Shannon P. Harvey, Kyuho Lee, Danfeng Li, Lena F. Kourkoutis and Harold Y. Hwang. *Nickelate Superconductivity without Rare-Earth Magnetism: $(La,Sr)NiO_2$*. Advanced Materials, vol. 33, no. 45, page 2104083, 2021. doi:10.1002/adma.202104083.

[Parzyck2025] C. T. Parzyck, Y. Wu, L. Bhatt, M. Kang, Z. Arthur, T. M. Pedersen, R. Sutarto, S. Fan, J. Pelliciari, V. Bisogni, G. Herranz, A. B. Georgescu, D. G. Hawthorn, L. F. Kourkoutis, D. A. Muller, D. G. Schlom and K. M. Shen. *Superconductivity in the parent infinite-layer nickelate $NdNiO_2$*. Physical Review X, vol. 15, no. 2, page 021048, May 2025. doi:10.1103/PhysRevX.15.021048.

[Poncé2016] S. Poncé, E. R. Margine, C. Verdi and F. Giustino. *EPW: Electron–phonon coupling, transport and superconducting properties using maximally localized Wannier functions*. Computer Physics Communications, vol. 209, pages 116–133, December 2016. doi:10.1016/j.cpc.2016.07.028.

[Stankovski2011] M. Stankovski, G. Antonius, D. Waroquiers, A. Miglio, H. Dixit, K. Sankaran, M. Giantomassi, X. Gonze, M. Côté and G.-M. Rignanese. *G_0W_0 band gap of ZnO: Effects of plasmon-pole models*. Physical Review B, vol. 84, no. 24, page 241201, December 2011. doi:10.1103/PhysRevB.84.241201.

[van Setten2018] M. J. van Setten, M. Giantomassi, E. Bousquet, M. J. Verstraete, D. R. Hamann, X. Gonze and G. M. Rignanese. *The PseudoDojo: Training and grading a 85 element optimized norm-conserving pseudopotential table*. Computer Physics Communications, vol. 226, pages 39–54, May 2018. doi:10.1016/j.cpc.2018.01.012.

[Wang2022] N. N. Wang, M. W. Yang, Z. Yang, K. Y. Chen, H. Zhang, Q. H. Zhang, Z. H. Zhu, Y. Uwatoko, L. Gu, X. L. Dong, J. P. Sun, K. J. Jin and J.-G. Cheng. *Pressure-induced monotonic enhancement of Tc to over 30 K in superconducting $Pr_{0.82}Sr_{0.18}NiO_2$ thin films*. Nature Communications, vol. 13, no. 1, page 4367, July 2022. doi:10.1038/s41467-022-32065-x.

[Yin2013] Z. P. Yin, A. Kutepov and G. Kotliar. *Correlation-Enhanced Electron-Phonon Coupling: Applications of GW and Screened Hybrid Functional to Bismuthates, Chloronitrides, and Other High-T_c Superconductors*. Physical Review X, vol. 3, no. 2, page 021011, May 2013. doi:10.1103/PhysRevX.3.021011.

Appendix

7.A Technical details

DFT The DFT calculations performed with ABINIT were converged with a 12×12×14 Monkhorst-Pack **k**-mesh with a 100 Ha cutoff for the wavefunctions and a 0.01 Ha smearing. For the calculations at different pressures, the lattice parameters were optimized using a convergence threshold of 0.001 kbar.

GW One-shot G_0W_0 calculations were performed with ABINIT using an unshifted 6×6×6 **k**-mesh. The screening was calculated using a wavefunction cutoff of 40 Ha, a dielectric matrix with 939 plane-waves (15 Ha), and summing over 170 bands. The subsequent convergence on the *GW* self-energy was obtained with a cutoff of 40 Ha and 15 Ha on the exchange and correlation parts, respectively, and summing over 200 bands when using the contour-deformation (CD) integration technique and the Godby-Needs (GN) plasmon-pole model and 1400 bands in the case of the Hybertsen-Louie (HL) plasmon-pole model. The CD integration was performed using 30 frequencies on a logarithmic mesh along the imaginary axis, and 200 on the real axis to evaluate the pole residuals. Thus, the *GW* quasiparticle corrections were calculated for 29 bands around the Fermi level starting from the bottom of the O-2p manifold (in DFT, these 29 bands are within the energy interval $[-8, 10]$ eV around the Fermi level).

Wannier interpolation Both the DFT eigenvalues and the *GW* energies were interpolated with Wannier90 [Mostofi2014]. Specifically, we used 17 Wannier functions associated with the O-2p, Ni-3d, and R-5d states and one additional interstitial-s state as in [Li2024b]. For the La compound we used 7 additional Wannier functions associated with La-4f states.

Phonons Phonon calculations were performed using the QUANTUM ESPRESSO package [Giannozzi2009, Giannozzi2017], also using norm-conserving pseudopotentials from the PseudoDojo repository [van Setten2018]. We used a **k**-mesh of 18×18×18 with a planewave cutoff of 125 Ry (= 62.5 Ha) for the corresponding DFT calculations. In these calculations, we stick to PBE for the exchange-correlation functional as this is a reliable choice for the structural properties of interest (see e.g. [Bernardini2022]). Phonon spectra and displacement potentials were calculated on a 6×6×6 **q**-mesh using density functional perturbation theory.

Electron-phonon coupling For the calculations of electron-phonon coupling matrices and Eliashberg equations we use the wannier-interpolation method as implemented in EPW package [Giustino2007, Poncé2016, Margine2013]. Specifically, we used the *GW* electronic structure combined with the phonon frequencies and electron-phonon matrix elements obtained from DFT. A coarse 6×6×6 mesh was used for both the electronic structure and the phonons, with interpolated 36×36×36 and 18×18×18 meshes for the electronic and phononic parts respectively. The presented Eliashberg spectral function $\alpha^2F(\omega)$ is computed as in eq. (6.9), and the anisotropic e-ph coupling matrix elements $\lambda_{\mathbf{k}\mathbf{k}'}$ as in eq. (6.11). In these calculations, we considered an energy window of 0.5 eV (= 13.6 Ha) centered at the Fermi level, with an electronic smearing of 0.05 eV (= 1.36 Ha) and phonon smearing of 0.5 meV (= 13.6 mHa).

8

GW electronic structure of the bilayer nickelate $La_3Ni_2O_7$

The results detailed in this chapter have been published in J.B. de Vaulx, Q.N. Meier, P. Toulemonde, A. Cano, et V. Olevano, *"Pressure and strain effects on the ab initio GW electronic structure of $La_3Ni_2O_7$"*, Physical Review B, August 2025 [de Vaulx2025a].

8.1 Introduction

In 2023, superconductivity has been observed in bulk samples of the bilayer $La_3Ni_2O_7$ under high pressure [Sun2023], with the superconducting phase forming a right-triangular region spanning 14 to 80 GPa, and reaching a maximum onset critical temperature T_c of approximately 80 K at 18 GPa [Li2025a]. More recently, superconductivity has also been reported at $T_c \sim$ 40 K in $La_3Ni_2O_7$ thin films under epitaxial compressive strain at ambient pressure [Ko2025, Zhou2025]. While the superconducting mechanism is still debated in infinite-layer RNiO$_2$ nickelates (see Chap. 7), the high critical temperature observed in $La_3Ni_2O_7$ is difficult to reconcile with a BCS electron-phonon pairing mechanism [Ouyang2024, You2025], thus pointing to unconventional superconductivity. The unconventional superconducting mechanism is likely different in cuprates and RP nickelates, as explained in Chap. 1.

Interestingly, unconventional superconductivity was theoretically anticipated in $La_3Ni_2O_7$ by invoking finite-energy spin fluctuations as pairing glue [Nakata2017]. Then many other different model theoretical pictures [Zhang2024a, Luo2023, Gu2023, Yang2023, Lechermann2023, Sakakibara2024, Christiansson2023] have been proposed to explain the superconductivity in the bilayer. The respective role of the two Ni-3d e_g orbitals in the superconducting mechanism is still under discussion [Lechermann2024]. With respect to spin fluctuations, the gap between the two upper and lower Ni-3d_{z^2} bands, originating from the interlayer hopping, seems to be relevant [Sakakibara2024]. The presence or absence of the so-called γ hole pocket in the Fermi surface, that should arise from the lower Ni-3d_{z^2} band, is still unclear both in theoretical calculations [Christiansson2023, Wang2024, Ryee2024] and in experimental angle-resolved photoemission spectroscopy (ARPES) measurements [Yang2024, Li2025b]. The symmetry of

the superconducting gap remains unclear as subsequent studies have indicated the possibility of not only $s_\pm$-wave, but also d-wave pairing states including d_{xy}-wave, depending on specific details of the electronic structure [Sakakibara2024, Zhang2024b, Xia2025]. In these works, the idea is to determine the gap symmetry of the leading superconducting instability, from models fitted on DFT electronic structures (see the example given in Fig. 8.1). All the previous points then require a correct description of the electronic structure, including electronic correlations.

In this work we study the electronic structure of bulk $La_3Ni_2O_7$ at the G_0W_0 level, with respect to pressure, as well as in presence of in-plane constraints that simulate a thin film grown on a substrate. Our purpose is to highlight aspects which might be relevant to explain superconductivity that in this system is induced by pressure without doping. The focus is at the Fermi level but also at higher energy features which are less affected by the estimated 0.1 eV best *GW* absolute accuracy, and which might be relevant in the competition between different pairing symmetries according to some proposed superconducting mechanisms. The weight of correlation effects and their importance in this system is revealed by a comparison between the G_0W_0 electronic structure and the DFT band plot.

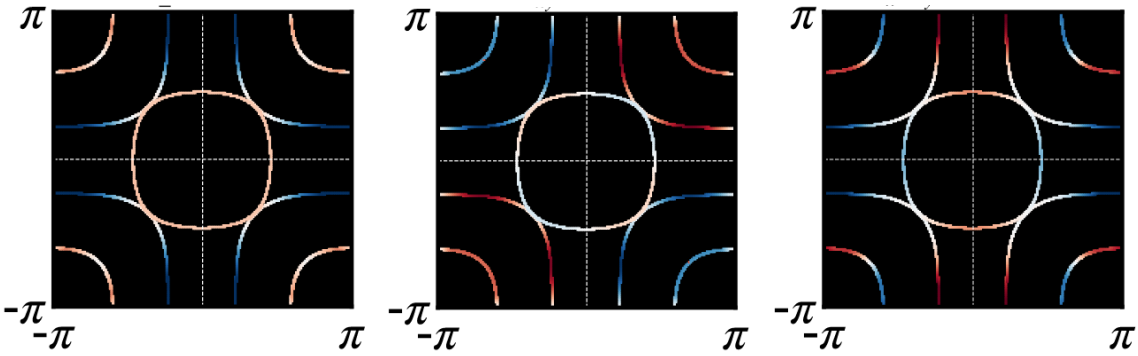

Figure 8.1: Examples of possible gap symmetries for the bilayer $La_3Ni_2O_7$, from left to right: $s_\pm$, d_{xy} and $d_{x^2-y^2}$. The color indicates the sign of the gap and its magnitude. The leading instability between these three possibilities is determined by the resolution of a gap equation at the superconducting transition, and is highly sensitive to the details of the electronic structure (in this case, on the so-called e_g-splitting between $d_{x^2-y^2}$ and d_{z^2} orbitals). The gap equation is derived from a model whose parameters are fitted on a DFT electronic structure. From [Xia2025].

8.2 Calculation details

8.2.1 Numerical methods

Our methodology relies as a first step on DFT calculations with the PBE functional, subsequently corrected by *GW* calculations, both stages using the plane waves code ABINIT [Gonze2020]. We use norm-conserving pseudo-potentials from the PseudoDojo table library [van Setten2018]. The La pseudo-potential takes $4f$ electrons in conduction and does not freeze them in the core. We have used a $16\times16\times16$ standard sampling of the Brillouin zone (BZ) and a plane waves (PW) cutoff of 65 Ha for the DFT-PBE starting calculation, as well as a Gaussian smearing of 0.01 Hartree. In the subsequent *GW* calculations, the BZ sampling has been reduced to $6\times6\times6$, whereas the PW cutoffs have been reduced to 40 Ha for the representation of the wave functions and for the exchange self-energy, and further down to 15 Ha for the correlation self-energy and the screening. We included 187 bands for the calculation of the

screening and 225 for the self-energy (see App. 8.A for convergence studies). We have carried just only one *GW* iteration (i.e. G_0W_0) on top of PBE, using a Godby-Needs plasmon-pole model [Godby1989] and a shift of 0.1 eV to avoid poles/divergences.

The final *GW* band plots, total and projected density of states (DOS and PDOS), as well as Fermi surfaces, were interpolated from the 6×6×6 to a denser *k*-mesh by the WANNIER90 code using a set of 67 projected Wannier functions (PWFs) with the closest possible character to atomic orbitals, namely O-2*p*, Ni-3*d*, La-5*d* and La-4*f*. The band orbital characters and PDOS identified by these PWFs are almost coincident with what one would obtain by projecting Bloch wave functions directly onto real (pseudo) atomic orbitals, as we have checked using the QUANTUM ESPRESSO code with equivalent parameters, which is not the case when selecting a set of maximally-localized Wannier functions (MLWFs) (see App. 8.B). In the bandplots showing projected orbital character, the width of the dots is proportional to the orbital contribution.

All calculations have been done with a Gaussian smearing temperature T_s of 0.01 Ha to ease self-consistency convergence and optical absorption onset stability (which in any case has little relevance on main plasmons, energy-loss and screening *W*). For the most critical case at $P = 29.5$ GPa we have checked that a calculation with T_s enforced at 10^{-4} Ha in both DFT and *GW* calculations provides the same physical picture, and in particular the same Fermi surface as in Fig. 8.2b, with only minor adjustments of less than 10 meV on band positions, mostly due to the fact that the chemical potential μ at larger temperature is a less accurate estimate for the Fermi energy (see App. 8.C).

8.2.2 Crystal structure and Brillouin zone

To determine the crystal structure of $La_3Ni_2O_7$ at ambient pressure, and then in the superconducting range at 14, 29.5 and 40 GPa, we have performed DFT PBE structural relaxations which provided the *I4/mmm* space group as the lowest energy structure at all considered pressures, except at 0 GPa where the *Amam* structure is more stable. Nevertheless, our *GW* calculations have all referred to the *I4/mmm* structure even at ambient pressure to ease the comparison and better follow the evolution of the electronic structure with pressure, from the superconducting range down to 0 GPa. For all the cases we have used the relaxed lattice parameters and the internal atomic position out of our PBE relaxations, except for the case at 29.5 GPa which we treated separately.

Indeed, 29.5 GPa is the most studied case in the theoretical literature, so that we use it as a benchmark case to compare with previous calculations. Thus, for the sake of comparison, we decided to stick to the lattice parameters and atomic positions used in most of previous works [Christiansson2023, Sakakibara2024]. Therefore, we consider a tetragonal $I4/mmm$ structure with $a = 3.715$ Å and $c = 19.734$ Å as Sakakibara et al. Further, in [Christiansson2023], it was noticed that the electronic structure of $La_3Ni_2O_7$ at 29.5 GPa is extremely sensitive to internal atomic positions and that the experimental ones reported by Sun et al. from the X-ray diffraction [Sun2023] likely yield artifacts at the Fermi level. This question will be further addressed in Sec. 10.1.

To simulate epitaxial strain, we enforced the tetragonal *a* lattice parameter to the experimentally observed value of 3.77 Å [Ko2025] and let the system relax in the *z* direction, which provided $c = 20.293$ Å. This crystal structure corresponds to a bulk non-hydrostatic planar stressed system, or equivalently a system pulled along the *c* axis, that we will use to simulate an epitaxially strained thin film. All our crystal structures are detailed in App. 8.D.

All our electronic structures are reported in the $I4/mmm$ body-centered tetragonal (BCT) Brillouin zone (BZ) which we report in Fig. 8.2c by black lines, while the blue line shows the path followed in our band plots with *k*-point labels using the convention of [Hinuma2017]. Notice that in this convention, the X and M *k*-points do not correspond to the canonical ones used in the 2D BZ of the square lattice widely used in the model literature: X is at

the BZ corner in the nodal direction and M lies in the $k_z = 2\pi/c$ plane. We also indicate in gray the BZ corresponding to the conventional cell, namely simple tetragonal, which ease the comparison with 2D BZs. In the same Fig. 8.2c, we report also the simple orthorhombic BZ and associated k-path to compare with the ARPES experiment [Yang2024] which referred to the tilted *Amam* structure needing a $\sqrt{2}\times\sqrt{2}\times 2$ supercell compared to ours; and finally the face-centered orthorhombic BZ (and associated k-path) to compare with the calculation of [Christiansson2023] who referred to the *Fmmm* crystal structure.

8.3 Results

8.3.1 Electronic structure at 29.5 GPa

We start discussing the electronic structure of $La_3Ni_2O_7$ at the pressure of 29.5 GPa over which most of previous theoretical calculations have been performed. Our PBE and *GW* Fermi surfaces are shown in Fig. 8.2a and 8.2b, while Fig. 8.2d shows the corresponding band structures. In the latter, selected orbital character contributions are plotted on the *GW* band structure, as well as the projected densities of states (PDOS) and the total density of states (DOS).

8.3.1.1 Ni e_g Fermi surface sheets

The Fermi level is dominated by bands with Ni-3d e_g character. The DFT PBE Fermi surface consists of three sheets, labeled α, β, and γ in previous literature [Luo2023]. The α sheet is a large cylindrical sheet centered around Γ; β is the sheet with the characteristic shape of the cuprate Fermi surface; and γ is a small hole pocket located at the Brillouin zone (BZ) corners which is highly dispersive along k_z. The α and β sheets are primarily of $d_{x^2-y^2}$ character, though they show significant hybridization with d_{z^2} orbitals in the anti-nodal direction, as well as with O-2p states (see Fig. 8.3b). In contrast, the γ pocket has an almost pure d_{z^2} character and is consistently present in PBE (or LDA) calculations.

The *GW* Fermi surface, in contrast, has no γ hole-pockets, as shown in Fig. 8.2b. This result is totally consistent with experimental ARPES data [Yang2024], with respect to which we provide a detailed comparison in Sec. 8.3.2 below, since it was performed at ambient pressure. This difference between DFT and *GW* is due to a slight downward shift (70∼80 meV) of the lower Ni-3d_{z^2} band along the XP direction (see Fig. 8.2d). The absence of the γ pocket in experiment has been discussed also in the literature, and several semi-empirical corrections have been shown to reconcile theoretical calculations with the ARPES experiment. These methods either include the use of a weighted Fock exchange operator, as by HSE [Wang2024]; or place more strength on correlation by introducing a Hubbard repulsion term of $U > 3.5$ eV on Ni-3d_{z^2} electrons, like it was done in the calculation of Yang et al., with the effect to lower this band [Yang2024]. On the basis of this fact, Yang et al. concluded that $La_3Ni_2O_7$ is a strongly correlated system. Here we show that, a calculation using physical quasiparticle energies out of a many-body self-energy, even in a non self-consistent *GW* approximation, is enough to get rid of the γ sheet at the Fermi level and achieve good agreement with the experiment. Our results are in line with the findings of [Ryee2024] who excluded both a transition to a Mott insulator or bad metal scenario.

The disappearance of the γ hole pocket has also been reported in a previous *GW* work [Christiansson2023] (see Fig. 8.2c for k-point correspondence). They performed a G_0W_0 calculation based on a reduced four-orbital tight-binding model restricted to the Ni-e_g manifold. This model does not include the La-5$d_{x^2-y^2}$ band, which, as we will discuss in the next section,

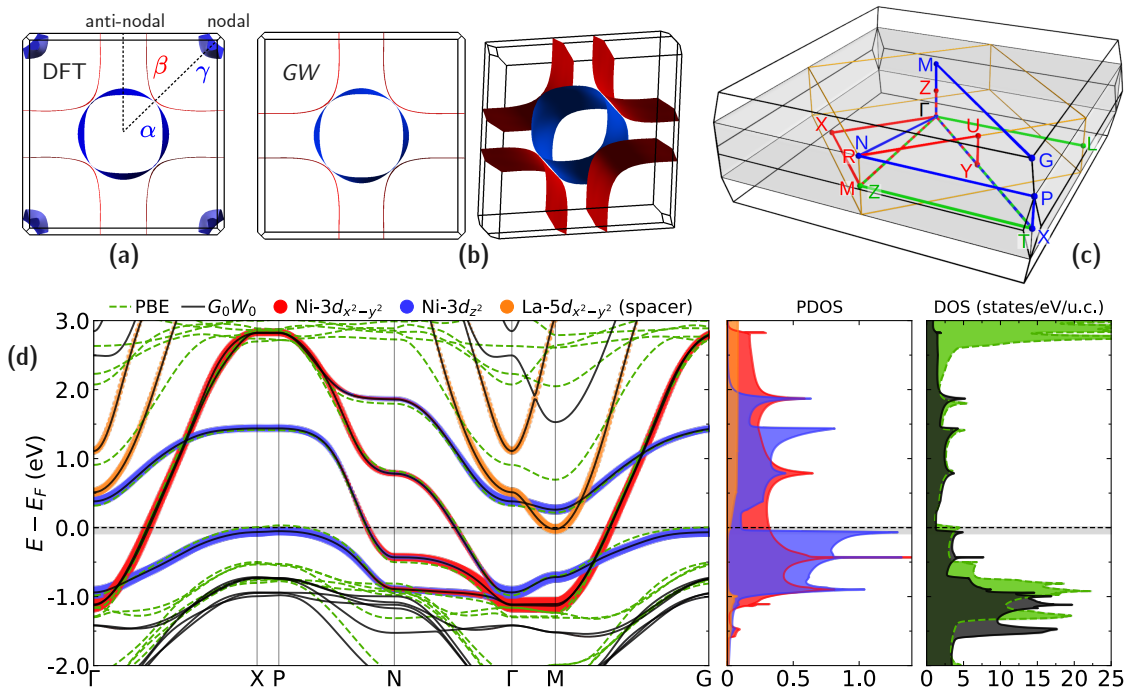

Figure 8.2: Fermi surfaces of $La_3Ni_2O_7$ at 29.5 GPa within the body-centered tetragonal (BCT) Brillouin zone (BZ) calculated for the DFT-PBE **(a)** and the *GW* **(b)** approximation. The Fermi sheets α and β are shown in blue and red, respectively. The blue sheets at the BZ corners are the Ni-3d_{z^2} hole pockets, labeled γ. **(c)** Comparison between different BZs and k-paths: the primitive BCT (black lines) and k-path [Hinuma2017] (blue line) corresponding to the *I4/mmm* structure used in this work; the simple tetragonal BZ (gray box) associated with the conventional cell; the simple orthorhombic BZ (orange lines) and k-path (red line) referred by the ARPES work [Yang2024] in which they referred to the tilted *Amam* structure requiring an $\sqrt{2} \times \sqrt{2} \times 2$ supercell with respect to our cell; and finally the k-path of [Christiansson2023] (green) in the simple orthorhombic BZ corresponding to the *Fmmm* structure. All orthorhombic BZs have been tetragonalized to ease the visualization. **(d)** PBE (dashed green) and G_0W_0 (black) band plots of $La_3Ni_2O_7$ at 29.5 GPa in the BCT Brillouin zone and along the k-path already indicated on (c). Relevant orbital character projections are plotted for G_0W_0, namely Ni-3$d_{x^2-y^2}$, Ni-3d_{z^2} and La-5$d_{x^2-y^2}$ (restricted to atoms of the spacer for the latter). The corresponding DOS and PDOS are shown on the right. The gray stripe shows the estimated uncertainty interval of 100 meV for the Fermi level, and the thin black dashed line the E_F value calculated by ABINIT, chosen as the origin of the energy axis (see App. 8.C).

plays a non-negligible role in the low energy spectrum. Their model also employs an effective screening that is renormalized to account for the missing degrees of freedom.

Despite these significant methodological differences, our results are in remarkable agreement with theirs regarding the absence of the γ pocket. However, Christiansson et al. do not further comment on this disappearance in their G_0W_0 calculation, because their subsequent EDMFT simulations—performed on top of both DFT and G_0W_0—reintroduce and even enhance the spectral weight of the lower Ni-3d_{z^2} band at the Fermi level. On this basis, they conclude that "the dominance of the d_{z^2} orbital distinguishes $La_3Ni_2O_7$ from the infinite-layer nickelates or the cuprates," which are instead dominated by $d_{x^2-y^2}$ character. This interpretation is not supported by our *GW* results (see Sec. 8.3.1.4 for the spectral weights), which show a predominantly $d_{x^2-y^2}$ character at low energy. Our findings rather align with the recent G_0W_0 calculations of You et al. [You2025].

Interestingly, Ryee et al. [Ryee2024] found the γ pocket in both DFT and dynamical mean-field theory (DMFT) calculations, but not in cluster-DMFT (CDMFT) which is therefore more in agreement with the *GW* finding. This is an indication that non-local correlations, as provided

by a CDMFT or a *GW* k-dependent self-energy, are important to describe such modification of the Fermi surface topology. However, CDMFT also find an important modification to the cuprate-shape β sheet which loses most of its 1D character (see below). On this point *GW* is more in agreement with DFT and local DMFT rather than with CDMFT.

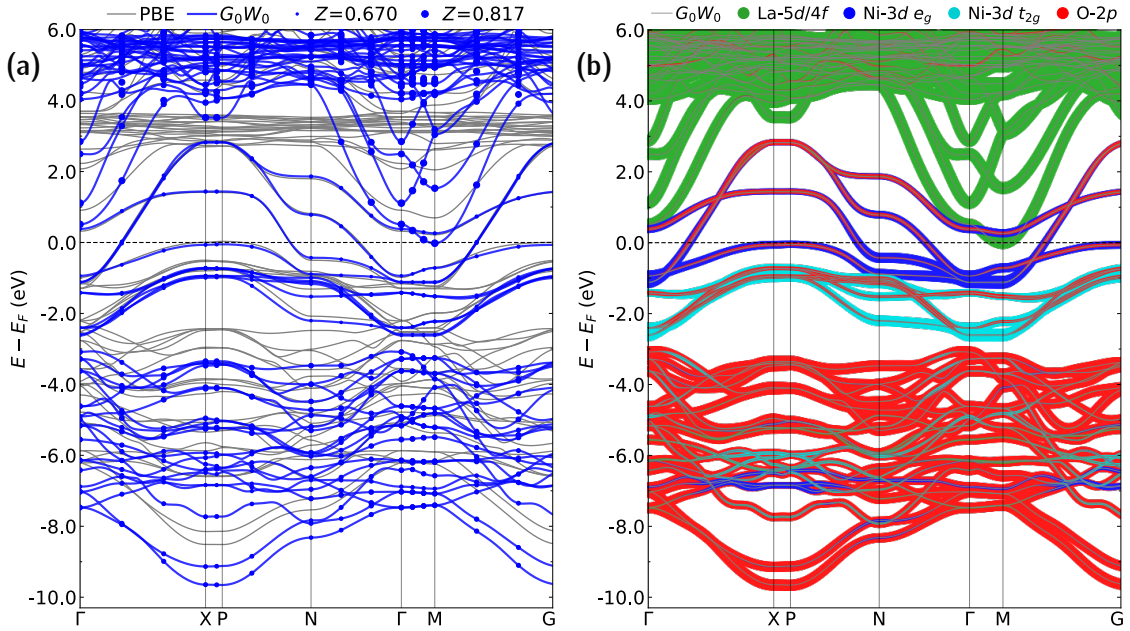

Figure 8.3: **(a)** *GW* quasiparticle spectral weight Z for $La_3Ni_2O_7$ at 29.5 GPa. The blue dots area on the *GW* bandplot (blue lines) indicates the QP weight Z with a specific scaling that ranges from minimum to maximum values (on the full BZ), indicated by the dots size in the legend. For reference, we show also the PBE band plot (gray lines). **(b)** *GW* band plot reporting the PWF orbital characters by the width of the lines with different colors. We remark that, like it was already found in infinite-layer nickelates, *GW* correlations shift 2 eV up the flat bands with predominant La-4f character, moving them further away from the Fermi level and out of the low-energy region, and shift 1 eV down the O-2p manifold, leading to an increased ionic charge-transfer energy between Ni-3d and O-2p states. These aspects were previously detailed [Olevano2020] and will not be again discussed here where we focus on the low-energy region.

8.3.1.2 La-5$d_{x^2-y^2}$ band lowering and self-doping

Beside this important qualitative modification of the Fermi surface, *GW* correlation corrections induce an even more evident and quantitative change in the bandwidth of the 5$d_{x^2-y^2}$ band contributed by the two La spacer atoms only (i.e., with no contribution by the La inner atom lying in between the NiO planes). This La-5$d_{x^2-y^2}$ band, which in DFT-PBE is well above the Ni-3d_{z^2} one, is lowered by *GW* corrections, as it can be seen at Γ in Fig. 8.2d. At the M point, which is often overlooked in 2D calculations restricted to the $k_z = 0$ plane only, the lowering in *GW* is so large (∼0.7 eV) that the La-5$d_{x^2-y^2}$ crosses the Ni-3d_{z^2} band and becomes the lowest lying conduction band at M. Due to this large *GW* correction, the bottom of conduction (BOC) of the La-5$d_{x^2-y^2}$ band at M is situated just only 30 meV above the top of valence (TOV) of the Ni-3d_{z^2} band at P (in the following, we will refer to this TOV-BOC distance of 30 meV as the *indirect gap*). As a consequence, the *GW* Fermi level results from a delicate equilibrium between these two *incipient bands*: the Ni-3d_{z^2} band, which tends to open a γ pocket of holes at the BZ corners; and the La-5$d_{x^2-y^2}$ one, which tends to open a pocket of electrons at M, hereafter labeled λ. In the latter case, states located on the La atoms of the spacer start to be occupied instead of Ni e_g states. This results in an effective *self-doping* (SD) by holes of the NiO_2 planes. Note that a possible role of rare-earth self-doping

was suggested [Christiansson2023] as responsible for the suppression of charge order, thereby possibly favoring superconductivity.

We can expect that any tiny perturbation of the system, e.g. doping, vacancies or defects, can drive the system to a qualitatively different electronic structure and Fermi surface, and therefore affect the superconductivity. Note that even computationally, these low-energy features are highly sensitive to the uncertainty of the integration method to calculate the Fermi level, which is discussed in further detail in App. 8.C. We mention two recent works which pointed out the shift of the La-5$d_{x^2-y^2}$ band due to correlations [You2025] and highlight the importance of this band on the screening which affects correlations on the Ni-e_g bands [Verraes2025]. The latter work remarked in particular some coincidences between the lowering trend of the La-5$d_{x^2-y^2}$ band with pressure and the shape of the superconducting region. In our *GW* calculation this band reaches the Fermi level at lower pressures and crosses the Fermi level already at 30 GPa at the M point, in comparison to 80 GPa at the Γ point in Verraes et al.

8.3.1.3 Upper-lower Ni-3d_{z^2} energy gap

A feature of the electronic structure that is considered of particular interest in relation to the emergence of superconductivity in $La_3Ni_2O_7$ is the energy difference between the upper and lower Ni-3d_{z^2} bands. In the literature they are labeled as bonding- and anti-bonding (as we explain in App. 8.E, we find that this labeling is not appropriate). This energy difference is related to the Ni interlayer hopping. According to the scenario proposed in [Sakakibara2024], a superconductivity gap would open on these two Ni-3d_{z^2} bands even though they can be as far as 1 eV away from the Fermi level, while the SC gap would be almost zero for the more Ni-3$d_{x^2-y^2}$ character bands crossing the Fermi level. In this scenario, a key parameter is precisely this Ni-3d_{z^2} interlayer hopping. As it can be seen in Fig. 8.2d, the two Ni-3d_{z^2} are practically unaffected by *GW* corrections, as their band width and separation remain essentially the same as in the DFT calculation. On this point our calculation is in disagreement both with the *GW* calculation in [Christiansson2023], which found a negative downward shift of the upper band of ~ -0.25 eV at the BZ corner, and with the calculation in [You2025], which in contrast found a positive upward shift of ~ 0.30 eV. Accordingly, our results leave practically unaffected the scenario proposed [Sakakibara2024], while it would be boosted or disrupted in the two other cases.

8.3.1.4 *GW* quasiparticle spectral weight and 1D character

A *GW* calculation can also provide the quasiparticle spectral weight Z which represents a measure of the degree of correlation of the system. In Fig. 8.3a we show the interpolated *GW* bandplot of $La_3Ni_2O_7$ at 29.5 GPa, with the dots corresponding to the *GW* energies sampled on the 6×6×6 k-mesh. The relative size of the dots indicates the corresponding value of Z. In Fig. 8.3b we show the general orbital character of the *GW* bands. These plots are complemented with Fig. 8.4 which illustrates the behavior of Z as a function of the energy.

We note that La-5d bands, followed by the 4f, present the maximum QP weight culminating at $Z = 0.82$. This is already quite remarkable, in particular for the most localized f flat bands. Some of the La bands, in particular the previously discussed La-5$d_{x^2-y^2}$ which almost achieved the Fermi level, bring these high spectral weights lower in energy than the main La manifold located around 5 eV. For La-5d states above 5 eV, the QP weight is slightly decreasing. On the other side of the Fermi level, we also observe for the O-2p manifold below -3 eV a reduced Z with increasing distance from E_F with values ranging from 0.75 to 0.70. This is surprisingly lower than for La-5d and 4f states. However, the most remarkable fact is that the Ni-3d bands, with no difference between e_g and t_{2g}, present the lowest weight of all quasiparticle states. For these states we observe a non-negligible Z drop of up to 0.15 when compared in particular with

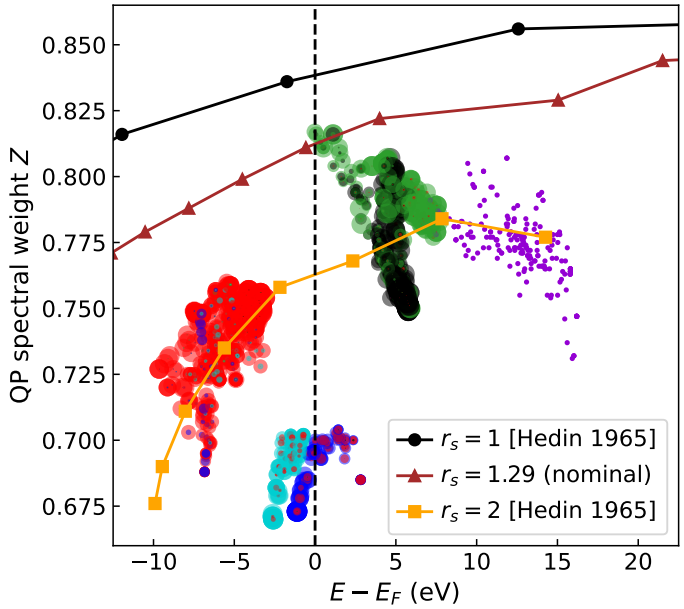

Figure 8.4: QP spectral weights Z with respect to *GW* quasiparticle energies with orbital characters corresponding to the ones of Fig. 8.3b, except for the La-4*f* which are separated from the La-5*d* and plotted in black. Points for which the orbital character projection was not calculated are shown in purple. We observe an overall Fermi liquid behavior, though at a higher correlation level with respect to the nominal density ($r_s = 2$ vs 1.29), and also its departure for the Ni-3*d* bands close to E_F.

the La-5$d_{x^2-y^2}$ which at M is situated at the same Fermi level as the Ni-3*d*. This fact points to a larger weight of the non-coherent part of the spectrum for the Ni-3*d* states.

For comparison, in Fig. 8.4 we also report the Z of the jellium model as in the Hedin *GW* calculation at $r_s = 1$ and 2 [Hedin1965], as well as at the $La_3Ni_2O_7$ nominal average density of $r_s = 1.29$ at 29.5 GPa ($r_s = \sqrt[3]{3V/4\pi N^*}$ with $V = 997$ a.u., the unit cell volume, and $N^* = 111$ the number of correlated electrons entering into the self-energy from the chosen pseudo-potentials). The *GW* general trend for a Fermi liquid is a reduction of the quasiparticle weight when going from the Fermi level to lower energies (see Fig. 4.2). Indeed, when going to the lowest energy quasiparticle states, the non-coherent part of spectra due to, e.g. plasmon losses, should increase, and correspondingly Z decreases. The same happens in the other higher energies direction, although not monotonically at the beginning (for $r_s = 1$ and 1.29, this decrease of Z occurs outside the plot range). From this, we can conclude that already with the correlations introduced by a non-self-consistent G_0W_0 approximation, $La_3Ni_2O_7$ show a Fermi liquid trend for all quasiparticle states. We can associate the O-2*p* and even the La-5*d* and La-4*f* quasiparticle weights to the $r_s = 2$ curve, that is to a higher level of correlation with respect to the system nominal density. On their side, the Ni-3*d* states show a departure from this Fermi liquid trend and so a even higher degree of correlation, although the minimal value of $Z = 0.67$ is still large enough not to configure a full breakdown of the Fermi liquid towards a strongly-correlated picture. Of course, this is the picture emerging from a *GW* calculation which could be confuted by future experimental measures of the Z. Should a Fermi liquid breakdown be measured, we will have a failure of the *GW* approximation pointing to the need to go beyond it.

As shown in Figs. 8.2a and b, the Fermi surface of $La_3Ni_2O_7$ exhibits negligible dispersion along the k_z direction, highlighting the pronounced 2D character of its electronic structure. We note that, while this situation is similar to what is found in most of the cuprates, it differs from the infinite-layer nickelates case that presents large k_z dispersion which introduces 3D features in their Fermi surface [Olevano2020]. Moreover, we note that the dispersion of the

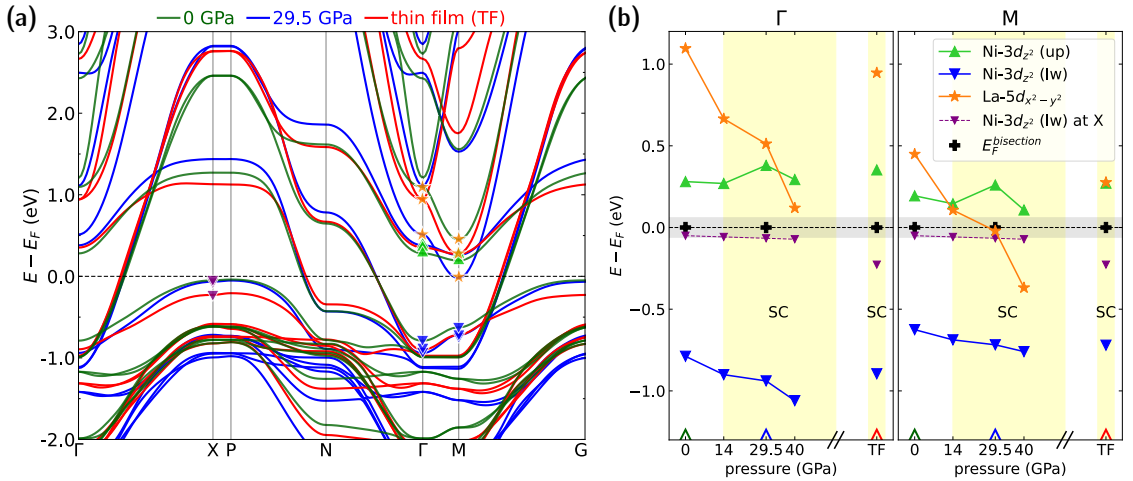

Figure 8.5: **(a)** G_0W_0 Wannier interpolated band plot for $La_3Ni_2O_7$ at ambient pressure (green), at 29.5 GPa (blue) and under substrate strain which simulate a thin film (TF, red). **(b)** Evolution with pressure of selected features, identified with corresponding markers on panel (a). Upper and lower d_{z^2} bands are designated by up and lw, respectively. For the calculations at 14 and 40 GPa where the Fermi level was not calculated (because *GW* energies where not sampled on the full BZ), E_F has been estimated by a linear interpolation on the difference $E(3d_{z^2}^{\text{lower}}(\text{X})) - E_F^{\text{bisection}}$ (purple) from the calculations where E_F was available (black plus signs).

Fermi surface of $La_3Ni_2O_7$ along k_x and k_y is also very weak. In fact, the α and β Fermi surface sheets can effectively be seen as a superposition of two sets of parallel planes along k_x and k_y, respectively. That is, as the superposition of 1D Fermi surfaces. These effectively 1D Fermi surfaces is an important difference with respect to cuprates. In particular, the emergence of $(\pi, 0)$ or $(0, \pi)$ spin-density-wave orders—as opposed to the (π, π) antiferromagnetic order characteristic of the cuprates—can be related to their nesting properties [Zhang2024b].

In the cuprates, ARPES experiments have revealed the emergence of so-called "Fermi arcs". Specifically, the quasiparticle spectral weight Z is found to be locally suppressed at points along the Fermi surface that would coincide with the 1D Fermi surface segments. Unfortunately, to check whether a similar phenomenon takes place in $La_3Ni_2O_7$, the $6\times6\times6$ k-sampling we have used in our *GW* calculation is not precise enough. Nevertheless, any experimental indication along this direction might provide a clue to understand superconductivity in both nickelates and cuprates.

8.3.2 Evolution with pressure

In order to gain further insight on the key aspects that might be relevant for superconductivity in $La_3Ni_2O_7$, we also analyze the evolution of its electronic structure with pressure. We remind that $La_3Ni_2O_7$ enters into a superconducting phase at an experimentally measured pressure of 14 GPa without doping [Sun2023].

To explore the largest range, we have included in our study a *fictitious* zero pressure phase of $La_3Ni_2O_7$ enforced in the tetragonal *I4/mmm* crystal structure, which in reality at 0 GPa should be unstable towards the orthorhombic *Amam* phase with tilted octahedra. Of course, at the present knowledge we cannot exclude that the structural transition occurs at the same critical pressure as the transition to superconductivity, so that it is an important ingredient to explain the superconductivity in this system. In this case, our calculation of the tetragonal phase at 0 GPa would be probably inadequate to study the normal-superconducting phase transition. But beyond the fact that a *GW* calculation is less cumbersome in systems with more symmetries, our choice is motivated by the fact that the comparison of electronic structures is

difficult between different crystal structures. Topological variations in the Fermi surface might trigger the superconducting phase transition (and maybe also the structural one): the approach proposed in this section focus on them.

In Fig. 8.5 we compare the *GW* electronic structure of $La_3Ni_2O_7$ at ambient pressure and at 29.5 GPa (in the same figure we also report the band plot of a biaxial strained $La_3Ni_2O_7$ which will be discussed in the next section). The most remarkable difference between the two pressures is in the La-5$d_{x^2-y^2}$ band at the point M which, at ambient pressure, lies $\sim$ 0.25 eV above the upper Ni-3d_{z^2} band in a very similar way to what already seen but at the DFT-PBE level in the 29.5 GPa case (see Fig. 8.2d), though in the latter the effect is much larger (0.5 eV). That is, correlations and pressure act in the same direction towards the emergence of the La-5$d_{x^2-y^2}$ band at the lowest energies. For a more complete discussion on this point, see Sec. 10.1. At ambient pressure the La-5$d_{x^2-y^2}$ band is not present in the low energy region, and therefore the delicate balance between the two incipient self-doping bands is lost.

The electronic structure of $La_3Ni_2O_7$ at ambient pressure has been measured by an ARPES experiment [Yang2024] whose main results are reproduced in Fig. 8.6, which we can now compare with our *GW* calculation at zero GPa. The γ hole pocket, which is found in the DFT PBE Fermi surface as due to the lower Ni-3d_{z^2} band, is absent in the ARPES experiment, exactly like in *GW*. ARPES spectra situate the top of this band at the BZ corners and 50 meV below the Fermi level. Our *GW* calculation at zero GPa (see Fig. 8.5), found the top of this band $\sim$50 meV below the Fermi level at the X *k*-point (corresponding to $\bar{\Gamma}'$ in Yang et al. [Yang2024], see Fig. 8.2c for *k*-points correspondence). In contrast to the La-5$d_{x^2-y^2}$ band, this lower Ni-3d_{z^2} band is almost unaffected by hydrostatic pressure: in the *GW* results at 29.5 GPa it just only shifts down $\sim$ 65 meV, which validates the comparison of the latter case with the ARPES, even if not performed at the same pressure.

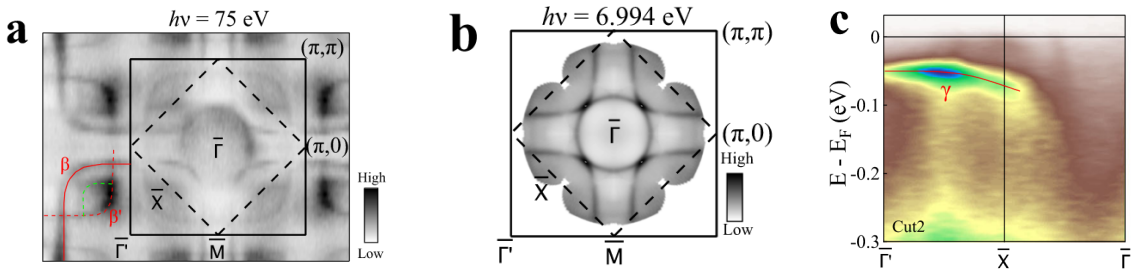

Figure 8.6: ARPES measures on the bilayer nickelate $La_3Ni_2O_7$ at ambient pressure [Yang2024]. **(a)** Fermi surface mapping measured by using synchrotron-based ARPES, and **(b)** by using laser-based ARPES. Two main Fermi surface sheets (α and β) are clearly observed, while the γ pocket is not. The solid line frame represents the first Brillouin zone from the conventional unit cell of the high symmetry $I4/mmm$ structure, while the dashed line frame represents the first Brillouin zone from the conventional unit cell of the real low symmetry structure at 0 GPa with tilted octahedra. **(c)** Measure of the γ band $\sim$50 meV below E_F, on a **k**-path corresponding to our Γ-X direction (see Fig. 8.2c).

In Fig. 8.5b, we report a graph presenting the top-of-valence (TOV) and bottom-of-conduction (BOC) positions of the most relevant bands for different hydrostatic pressures. We report extra calculations done at 14 and at 40 GPa, covering the range of superconductivity as measured experimentally in Sun et al. [Sun2023]. The indirect gap is at its minimum around 29.5 GPa, and the La-5$d_{x^2-y^2}$ band is clearly self-doping beyond. From the same figure we can also remark that the same La-5$d_{x^2-y^2}$ band crosses the Ni-3d_{z^2} upper band precisely at 14 GPa, which is precisely the onset of the superconducting region measured by Sun et al. [Sun2023]. This might be just only a coincidence or have deeper implications. In support to the latter, we cite a very recent work [Verraes2025] which also found a correlation between the position of the La-5$d_{x^2-y^2}$ band with respect to the Fermi level, and the shape of the superconducting region. Their calculation is at the DFT level, so that they missed the earlier coincidence in

pressure of the La-5$d_{x^2-y^2}$ with the Ni-3d_{z^2} band precisely at the onset of superconductivity at 14 GPa, but the relevance of the La-5$d_{x^2-y^2}$ for superconductivity has been remarked. We can more carefully conclude that both correlations and pressure are fundamental to describe the electronic structure of $La_3Ni_2O_7$ in its superconducting phase. In the next section we will see that xy-plane strain plays a similar role to correlations and pressure.

8.3.3 $La_3Ni_2O_7$ under epitaxial strain

Recent works [Ko2025, Zhou2025] have reported superconductivity at $T_c > 40$ K in $La_3Ni_2O_7$ thin films under compressive strain at ambient pressure. Here we present the electronic structure of a bulk $La_3Ni_2O_7$ with a 1.8% strained $a = 3.77$ Å and a relaxed c, which we use to simulate the experimental thin film. The corresponding PBE and GW band plots, PDOS and DOS are shown in Fig. 8.7. In comparison to the previously discussed case at ambient and 29.5 GPa (see also Fig. 8.5), the electronic structure retains most of its features. The Fermi level crossing is practically the same in the three different cases. In particular, the β cuprate-like sheet has exactly the same shape (refer to Fig. 8.2). The lower Ni-3d_{z^2} band is significantly further from E_F in the thin film case (~ -0.2 eV). However, we observe two important differences. First, the γ hole pocket is already absent at the DFT level, that is the lower Ni-3d_{z^2} band does not cross E_F any longer, an effect that is further enhanced by GW. Second, the La-5$d_{x^2-y^2}$ band at M, which also undergoes a large negative GW correction of almost 1 eV, now stays above the Fermi level by ~ 0.3 eV. In fact, it only reaches the upper Ni-3d_{z^2} band without crossing it. We can see that, with respect to the band positions at M, the epitaxial strained configuration is intermediate between 29.5 GPa and ambient pressure. Although our biaxial strain simulation implements a non-hydrostatic realization, we can compare it to the hydrostatic pressure case where the La-5$d_{x^2-y^2}$ BOC is degenerate with Ni-3d_{z^2} BOC at M. Following this analogy, from Fig. 8.5b, where we have also reported the band positions for the thin film, we can tentatively attribute our epitaxial strain simulation as equivalent to the 14 GPa hydrostatic pressure case, that is precisely at the superconducting onset. This could be an indication that the relative position and overlap of BOC at M, might play a role as a triggering mechanism of superconductivity.

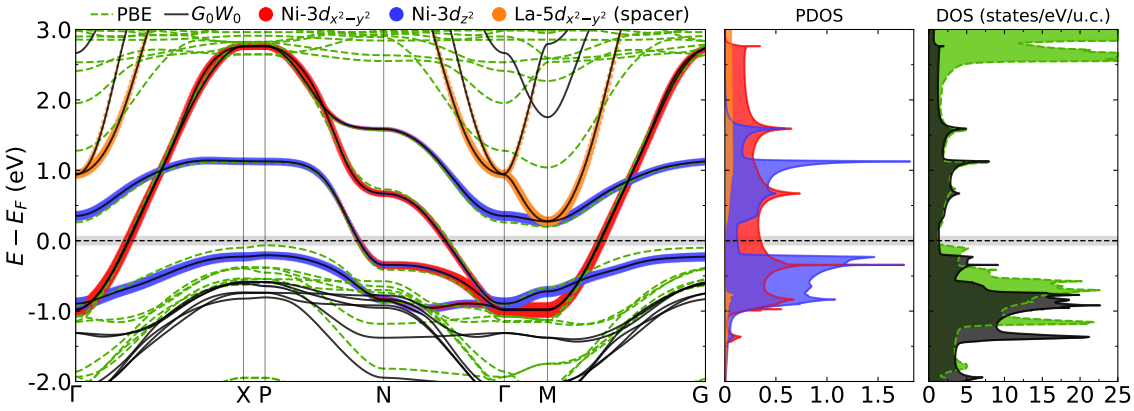

Figure 8.7: PBE (dashed green) and G_0W_0 (black) band plots, DOS, and PDOS of $La_3Ni_2O_7$ thin film under substrate constraint.

ARPES spectra have been measured on 1, 2 and 3 unit-cell epitaxial $La_{2.85}Pr_{0.15}Ni_2O_7$ films grown on $SrLaAlO_4$ substrates [Li2025b]. It is claimed that, in addition to the α and β sheets, the γ pocket is also present at the Fermi level. In another more recent ARPES experiment on a $La_2PrNi_2O_7$ thin film [Wang2025], the γ pocket is absent from the Fermi level and the Ni-3d_{z^2} band is found 70 meV below the Fermi energy, which compares more favorably with our GW result of -200 meV. In any case, the comparison with our GW electronic structure

is difficult because they considered a Pr doped system. From our side, we did not include the neighborhood effect of the substrate which is certainly affecting the electronic structure of such thin films. Our results should then be considered as an *ab initio* prediction of the electronic structure which could be measured for a $La_3Ni_2O_7$ thin film of enough large thickness. Or, possibly, for a non-hydrostatic planar strain applied on a bulk sample that can be realized experimentally by applying a tensile strain to the c axis, which will induce a biaxial compressive strain of the ab plane by Poisson law.

We can conclude that our *GW* calculation on the epitaxial strained case presents an electronic structure very similar to the bulk at 14 GPa pressure. Correlation effects are very important on both the lower Ni-3d_{z^2} band, causing the disappearance of the γ pocket, and on the increased relevance of the La-5$d_{x^2-y^2}$ band at low energy.

8.4 Conclusions

In conclusion, we have studied pressure and biaxial strain effects on the electronic structure of $La_3Ni_2O_7$, taking into account correlation effects within the *ab initio GW* approximation to the self-energy. We confirm that the electronic structure of $La_3Ni_2O_7$ is extremely sensitive to the internal atomic positions of its crystal structure. *GW* correlation effects shift downward the lower Ni-3d_{z^2} band, so to remove the γ hole pocket from the Fermi level without introducing any adjustable parameter. Therefore, the *GW* Fermi surface is composed only of the cuprate-shape sheet β plus the nickelate-specific cylinder α, both showing an effective 1D character, and is in good agreement with ARPES experiments [Yang2024] which did not find any γ pocket. Additionally, we observe a non-negligible drop in the *GW* quasiparticle spectral weight on the Ni-3d states, both e_g and t_{2g}, so to configure a little departure from a Fermi liquid behavior. Finally, we have shown that not only correlations, but also pressure or biaxial strain play a crucial role in pulling down the La-5$d_{x^2-y^2}$ band at Γ and M towards the Fermi level, which may induce self-doping. In any case, at pressures and strains of interest of superconductivity, this band might play an important role at low energy, a fact which is often overlooked in effective-model studies.

References

[Christiansson2023] Viktor Christiansson, Francesco Petocchi and Philipp Werner. *Correlated Electronic Structure of $La_3Ni_2O_7$ under Pressure*. Physical Review Letters, vol. 131, no. 20, page 206501, November 2023. doi:10.1103/PhysRevLett.131.206501.

[de Vaulx2025a] J.B. de Vaulx, Q.N. Meier, P. Toulemonde, A. Cano and V. Olevano. *Pressure and strain effects on the ab initio GW electronic structure of $La_3Ni_2O_7$*. Physical Review B, vol. 112, no. 8, page 085143, August 2025. doi:10.1103/q5ym-hf5k.

[Godby1989] R. W. Godby and R. J. Needs. *Metal-insulator transition in Kohn-Sham theory and quasiparticle theory*. Physical Review Letters, vol. 62, pages 1169–1172, March 1989. doi:10.1103/PhysRevLett.62.1169.

[Gonze2020] Xavier Gonze, Bernard Amadon, Gabriel Antonius, Frédéric Arnardi, Lucas Baguet, Jean-Michel Beuken, Jordan Bieder, François Bottin, Johann Bouchet, Eric Bousquet, Nils Brouwer, Fabien Bruneval, Guillaume Brunin, Théo Cavignac, Jean-Baptiste Charraud, Wei Chen, Michel Côté, Stefaan Cottenier, Jules Denier, Grégory Geneste, Philippe Ghosez, Matteo Giantomassi, Yannick Gillet, Olivier Gingras, Donald R. Hamann, Geoffroy Hautier, Xu He, Nicole Helbig, Natalie Holzwarth, Yongchao Jia, François Jollet, William Lafargue-Dit-Hauret, Kurt Lejaeghere, Miguel A. L. Marques, Alexandre Martin, Cyril Martins, Henrique P. C. Miranda, Francesco Naccarato, Kristin Persson, Guido Petretto, Valentin Planes, Yann Pouillon, Sergei Prokhorenko, Fabio Ricci, Gian-Marco Rignanese, Aldo H. Romero, Michael Marcus Schmitt, Marc Torrent, Michiel J. van Setten, Benoit Van Troeye, Matthieu J. Verstraete, Gilles Zérah and Josef W. Zwanziger. *The Abinit project: Impact, environment and recent developments*. Computer Physics Communications, vol. 248, page 107042, March 2020. doi:10.1016/j.cpc.2019.107042.

[Gu2023] Yuhao Gu, Congcong Le, Zhesen Yang, Xianxin Wu and Jiangping Hu. *Effective model and pairing tendency in bilayer Ni-based superconductor $La_3Ni_2O_7$*, August 2023. arXiv:2306.07275.

[Hedin1965] Lars Hedin. *New Method for Calculating the One-Particle Green's Function with Application to the Electron-Gas Problem*. Physical Review, vol. 139, no. 3A, pages A796–A823, August 1965. doi:10.1103/PhysRev.139.A796.

[Hinuma2017] Yoyo Hinuma, Giovanni Pizzi, Yu Kumagai, Fumiyasu Oba and Isao Tanaka. *Band structure diagram paths based on crystallography*. Computational Materials Science, vol. 128, pages 140–184, February 2017. doi:10.1016/j.commatsci.2016.10.015.

[Ko2025] Eun Kyo Ko, Yijun Yu, Yidi Liu, Lopa Bhatt, Jiarui Li, Vivek Thampy, Cheng-Tai Kuo, Bai Yang Wang, Yonghun Lee, Kyuho Lee, Jun-Sik Lee, Berit H. Goodge, David A. Muller and Harold Y. Hwang. *Signatures of ambient pressure superconductivity in thin film $La_3Ni_2O_7$*. Nature, vol. 638, no. 8052, pages 935–940, February 2025. doi:10.1038/s41586-024-08525-3.

[Lechermann2023] Frank Lechermann, Jannik Gondolf, Steffen Bötzel and Ilya M. Eremin. *Electronic correlations and superconducting instability in $La_3Ni_2O_7$ under high pressure*. Physical Review B, vol. 108, no. 20, page L201121, November 2023. doi:10.1103/PhysRevB.108.L201121.

[Lechermann2024] Frank Lechermann, Steffen Bötzel and Ilya M. Eremin. *Electronic instability, layer selectivity, and Fermi arcs in $La_3Ni_2O_7$*. Physical Review Materials, vol. 8, no. 7, page 074802, July 2024. doi:10.1103/PhysRevMaterials.8.074802.

[Li2025a] Jingyuan Li, Di Peng, Peiyue Ma, Hengyuan Zhang, Zhenfang Xing, Xing Huang, Chaoxin Huang, Mengwu Huo, Deyuan Hu, Zixian Dong, Xiang Chen, Tao Xie, Hongliang Dong, Hualei Sun, Qiaoshi Zeng, Ho-kwang Mao and Meng Wang.

Identification of the superconductivity in bilayer nickelate $La_3Ni_2O_7$ upon 100 GPa, February 2025. arXiv:2404.11369.

[Li2025b] Peng Li, Guangdi Zhou, Wei Lv, Yueying Li, Changming Yue, Haoliang Huang, Lizhi Xu, Jianchang Shen, Yu Miao, Wenhua Song, Zihao Nie, Yaqi Chen, Heng Wang, Weiqiang Chen, Yaobo Huang, Zhen-Hua Chen, Tian Qian, Junhao Lin, Junfeng He, Yu-Jie Sun, Zhuoyu Chen and Qi-Kun Xue. *Angle-resolved photoemission spectroscopy of superconducting $(La,Pr)_3Ni_2O_7/SrLaAlO_4$ heterostructures*. National Science Review, vol. 12, no. 10, page nwaf205, October 2025. doi:10.1093/nsr/nwaf205.

[Luo2023] Zhihui Luo, Xunwu Hu, Meng Wang, Wéi Wú and Dao-Xin Yao. *Bilayer Two-Orbital Model of $La_3Ni_2O_7$ under Pressure*. Physical Review Letters, vol. 131, no. 12, page 126001, September 2023. doi:10.1103/PhysRevLett.131.126001.

[Löwdin1950] Per-Olov Löwdin. *On the Non-Orthogonality Problem Connected with the Use of Atomic Wave Functions in the Theory of Molecules and Crystals*. The Journal of Chemical Physics, vol. 18, no. 3, pages 365–375, March 1950. doi:10.1063/1.1747632.

[Nakata2017] Masahiro Nakata, Daisuke Ogura, Hidetomo Usui and Kazuhiko Kuroki. *Finite-energy spin fluctuations as a pairing glue in systems with coexisting electron and hole bands*. Physical Review B, vol. 95, no. 21, page 214509, June 2017. doi:10.1103/PhysRevB.95.214509.

[Olevano2020] Valerio Olevano, Fabio Bernardini, Xavier Blase and Andrés Cano. *Ab initio many-body GW correlations in the electronic structure of $LaNiO_2$*. Physical Review B, vol. 101, no. 16, page 161102, April 2020. doi:10.1103/PhysRevB.101.161102.

[Ouyang2024] Zhenfeng Ouyang, Miao Gao and Zhong-Yi Lu. *Absence of electron-phonon coupling superconductivity in the bilayer phase of $La_3Ni_2O_7$ under pressure*. npj Quantum Materials, vol. 9, no. 1, pages 1–6, October 2024. doi:10.1038/s41535-024-00689-5.

[Ryee2024] Siheon Ryee, Niklas Witt and Tim O. Wehling. *Quenched Pair Breaking by Interlayer Correlations as a Key to Superconductivity in $La_3Ni_2O_7$*. Physical Review Letters, vol. 133, no. 9, page 096002, August 2024. doi:10.1103/PhysRevLett.133.096002.

[Sakakibara2024] Hirofumi Sakakibara, Naoya Kitamine, Masayuki Ochi and Kazuhiko Kuroki. *Possible High T_c Superconductivity in $La_3Ni_2O_7$ under High Pressure through Manifestation of a Nearly Half-Filled Bilayer Hubbard Model*. Physical Review Letters, vol. 132, no. 10, page 106002, March 2024. doi:10.1103/PhysRevLett.132.106002.

[Souza2001] Ivo Souza, Nicola Marzari and David Vanderbilt. *Maximally localized Wannier functions for entangled energy bands*. Physical Review B, vol. 65, no. 3, page 035109, December 2001. doi:10.1103/PhysRevB.65.035109.

[Sun2023] Hualei Sun, Mengwu Huo, Xunwu Hu, Jingyuan Li, Zengjia Liu, Yifeng Han, Lingyun Tang, Zhongquan Mao, Pengtao Yang, Bosen Wang, Jinguang Cheng, Dao-Xin Yao, Guang-Ming Zhang and Meng Wang. *Signatures of superconductivity near 80 K in a nickelate under high pressure*. Nature, vol. 621, no. 7979, pages 493–498, September 2023. doi:10.1038/s41586-023-06408-7.

[van Setten2018] M.J. van Setten, M. Giantomassi, E. Bousquet, M.J. Verstraete, D.R. Hamann, X. Gonze and G.-M. Rignanese. *The PseudoDojo: Training and grading a 85 element optimized norm-conserving pseudopotential table*. Computer Physics Communications, vol. 226, pages 39–54, 2018. doi:https://doi.org/10.1016/j.cpc.2018.01.012.

[Verraes2025] Daan Verraes, Tom Braeckevelt, Nick Bultinck and Veronique Van Speybroeck. *Evidence for strongly correlated superconductivity in $La_3Ni_2O_7$ from first principles*, February 2025. arXiv:2502.19501.

[Wang2024] Yuxin Wang, Kun Jiang, Ziqiang Wang, Fu-Chun Zhang and Jiangping Hu. *Electronic and magnetic structures of bilayer $La_3Ni_2O_7$ at ambient pressure*. Physical Review B, vol. 110, no. 20, page 205122, November 2024. doi:10.1103/PhysRevB.110.205122.

[Wang2025] Bai Yang Wang, Yong Zhong, Sebastien Abadi, Yidi Liu, Yijun Yu, Xiaoliang Zhang, Yi-Ming Wu, Ruohan Wang, Jiarui Li, Yaoju Tarn, Eun Kyo Ko, Vivek Thampy, Makoto Hashimoto, Donghui Lu, Young S. Lee, Thomas P. Devereaux, Chunjing Jia, Harold Y. Hwang and Zhi-Xun Shen. *Electronic structure of compressively strained thin film $La_3Ni_2O_7$*, April 2025. arXiv:2504.16372.

[Xia2025] Chengliang Xia, Hongquan Liu, Shengjie Zhou and Hanghui Chen. *Sensitive dependence of pairing symmetry on Ni-eg crystal field splitting in the nickelate superconductor $La_3Ni_2O_7$*. Nature Communications, vol. 16, no. 1, page 1054, January 2025. doi:10.1038/s41467-025-56206-0.

[Yang2023] Qing-Geng Yang, Da Wang and Qiang-Hua Wang. *Possible $s_\pm$-wave superconductivity in $La_3Ni_2O_7$*. Physical Review B, vol. 108, no. 14, page L140505, October 2023. doi:10.1103/PhysRevB.108.L140505.

[Yang2024] Jiangang Yang, Hualei Sun, Xunwu Hu, Yuyang Xie, Taimin Miao, Hailan Luo, Hao Chen, Bo Liang, Wenpei Zhu, Gexing Qu, Cui-Qun Chen, Mengwu Huo, Yaobo Huang, Shenjin Zhang, Fengfeng Zhang, Feng Yang, Zhimin Wang, Qinjun Peng, Hanqing Mao, Guodong Liu, Zuyan Xu, Tian Qian, Dao-Xin Yao, Meng Wang, Lin Zhao and X. J. Zhou. *Orbital-dependent electron correlation in double-layer nickelate $La_3Ni_2O_7$*. Nature Communications, vol. 15, no. 1, page 4373, May 2024. doi:10.1038/s41467-024-48701-7.

[You2025] Jing-Yang You, Zien Zhu, Mauro Del Ben, Wei Chen and Zhenglu Li. *Unlikelihood of a phonon mechanism for the high-temperature superconductivity in $La_3Ni_2O_7$*. npj Computational Materials, vol. 11, no. 1, pages 1–8, January 2025. doi:10.1038/s41524-024-01483-4.

[Zhang2024a] Yang Zhang, Ling-Fang Lin, Adriana Moreo, Thomas A. Maier and Elbio Dagotto. *Electronic structure, self-doping, and superconducting instability in the alternating single-layer trilayer stacking nickelates $La_3Ni_2O_7$*. Physical Review B, vol. 110, no. 6, page L060510, August 2024. doi:10.1103/PhysRevB.110.L060510.

[Zhang2024b] Yang Zhang, Ling-Fang Lin, Adriana Moreo, Thomas A. Maier and Elbio Dagotto. *Structural phase transition, s±-wave pairing, and magnetic stripe order in bilayered superconductor $La_3Ni_2O_7$ under pressure*. Nature Communications, vol. 15, no. 1, page 2470, March 2024. doi:10.1038/s41467-024-46622-z.

[Zhou2025] Guangdi Zhou, Wei Lv, Heng Wang, Zihao Nie, Yaqi Chen, Yueying Li, Haoliang Huang, Wei-Qiang Chen, Yu-Jie Sun, Qi-Kun Xue and Zhuoyu Chen. *Ambient-pressure superconductivity onset above 40 K in $(La,Pr)_3Ni_2O_7$ films*. Nature, vol. 640, no. 8059, pages 641–646, April 2025. doi:10.1038/s41586-025-08755-z.

Appendix

8.A Convergence in the number of bands

In a *GW* calculation, the number of bands taken into account in the calculation of the self-energy is critical. A convergence study is therefore needed. Moreover, this study is motivated by the discrepancy on the Ni-3d_{z^2} upper and lower bands which we have found between our results and the results of [Christiansson2023] from one side, and of [You2025] from another, especially regarding the shift the latter obtained on the upper Ni-3d_{z^2} band from DFT to *GW*. In our original calculation, we used 225 bands. For this test we rise up to 300 for the calculation of *GW* energies of three bands around the Fermi level. The *GW* energies obtained are plotted on top of the original calculation in Fig. 8.8. As we can see, the original calculation is already enough converged, the maximal difference for the set of checked bands being of $\sim$ 16 meV, validating the electronic structure presented in Fig. 8.2.

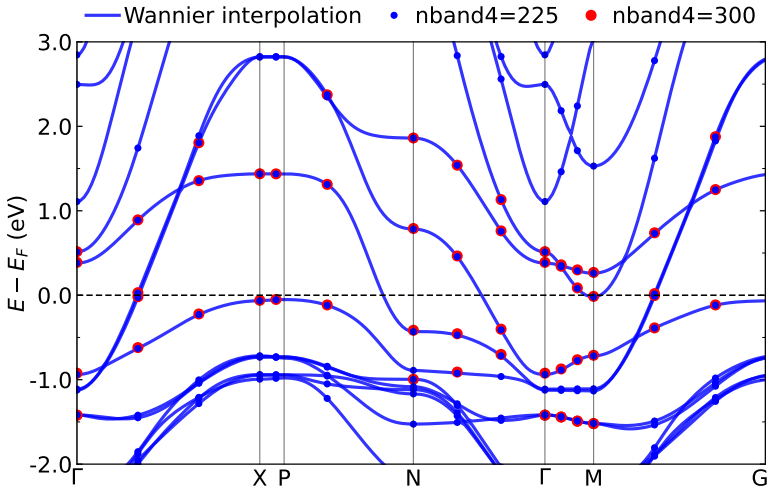

Figure 8.8: Convergence test on the number of bands included in the calculation of the *GW* self-energy: 225 bands (blue) and 300 bands (red).

8.B Orbital character projection: pure atomic orbitals vs Wannier functions

Fig. 8.9 shows three DFT PBE band character plots of $La_3Ni_2O_7$ at 29.5 GPa: the first one using projections on (pseudo) atomic orbitals calculated with QUANTUM ESPRESSO, which we will consider as the reference; and the two others with WANNIER90 but using different WF sets, namely projected Wannier functions (PWF) and maximally-localized Wannier functions (MLWF). PWF are the WANNIER90 first guess and correspond to WF with imposed well defined orbital character (in the input file), though not purely hydrogenoid atomic orbitals [Souza2001, Löwdin1950] (see below). Therefore, PWF is the set of WF one obtains from WANNIER90 by setting to zero the number of iterations in the Wannierisation procedure (not in the disentanglement one). PWF might not be the set best suited to a smooth interpolation of bands. However, in this case we used 67 WF, which is a set large enough to allows an already smooth interpolation. On the other hand, MLWF are obtained after a number of

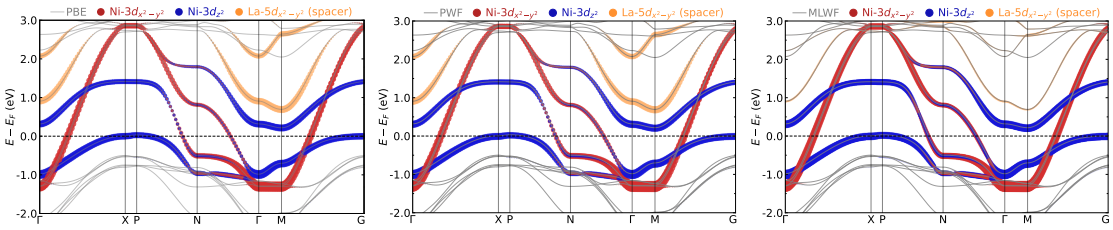

Figure 8.9: DFT PBE band character plots of $La_3Ni_2O_7$ at 29.5 GPa calculated with QUANTUM ESPRESSO (left) and with WANNIER90 using projected PWF (center) or MLWF (right). The PWF orbital character is much closer than the MLWF to the QUANTUM ESPRESSO projection scheme for the La-5$d_{x^2-y^2}$ band.

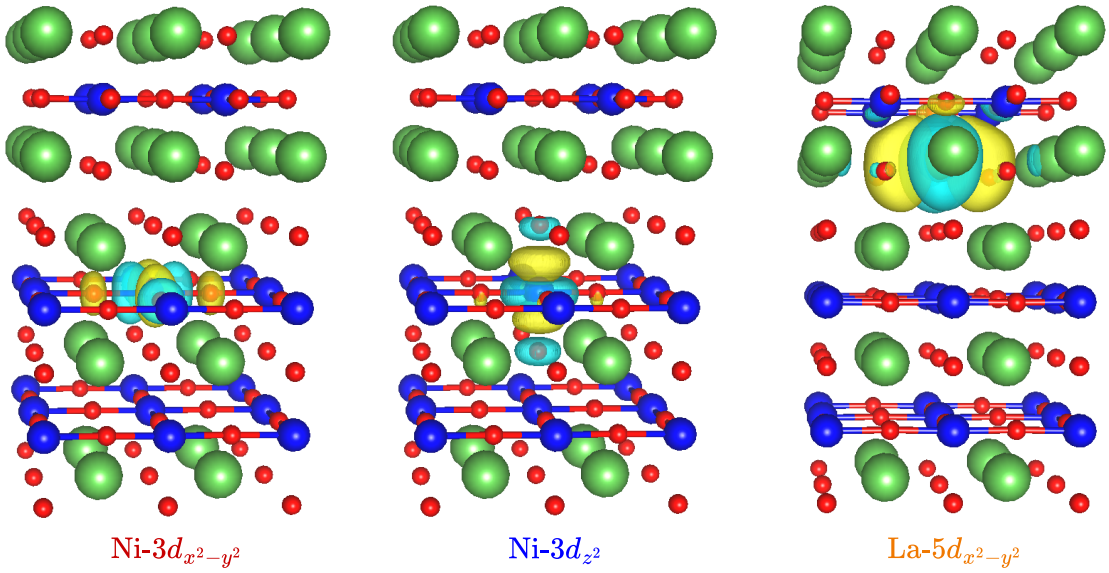

Figure 8.10: PWF plotted in real space for the three selected orbital characters. We remark extra lobes which make them different from real atomic orbitals.

Wannierisation iterations sufficient to minimize the Marzari-Vanderbilt functional towards the global or a local minimum, which correspond to a maximum in the localization of the WF. MLWF can loose their original orbital character, and they can even localize outside atoms and in the interstitial, if the target is to have the most localized WF.

The QUANTUM ESPRESSO and the PWF band plot characters are very consistent between themselves, whereas the MLWF shows important discrepancies for the La-5$d_{x^2-y^2}$ orbital character which lose weight on the band of interest and is more hybridized with the 4f manifold. It must be kept into account that the projection onto MLWF, beyond to strongly depend on the chosen set of MLWF (e.g. localized on atoms, on bonds, or on anti-bonding positions), is different from the projection onto atomic wave functions. But there is large arbitrariness also for atomic wave functions. For example whether projecting onto all-electron wave functions (as in all-electron codes), or pseudo-atomic wave functions (e.g. QUANTUM ESPRESSO and ABINIT, with some minor differences between them), or spherical harmonics (e.g. VASP). In conclusion, projections can be a convenient label to identify bands, establishing a convention. However, any physics argument built on them is always risky.

The comparison done here at the DFT level validates the use of PWF to show the orbital characters on the band character plots at the *GW* level (Fig. 8.2d and 8.7), for which a dense orbital character projection on bands is not possible because the energies are only sampled on a $6 \times 6 \times 6$ grid. Note that this orbital character comparison between QUANTUM ESPRESSO

and WANNIER90 has been done for the PDOS as well, providing the same conclusion.

One can remark on Fig. 8.10 that PWF do not correspond to real atomic orbitals, showing extra lobes and adaptation to neighboring atoms. This is due to the projection onto Bloch states and to the Löwdin orthogonalization procedure [Löwdin1950] as described in [Souza2001].

8.C Fermi energy calculation: standard bisection vs DOS integration

The indirect gap of 30 meV between the two incipient bands found in the calculation done at 29.5 GPa is beyond the accuracy by which the Fermi level can be calculated. This is already a consequence of the finite smearing temperature used to calculated metals, of the order of 10^{-3} Ha $\simeq$ 30 meV and up to 10^{-2} Ha $\simeq$ 300 meV (the ABINIT default is 10^{-2} Ha, while it is half that in QUANTUM ESPRESSO). We must also keep in mind that any change in the parameters used to generate the pseudo-potentials can affect DFT Kohn-Sham energies by even 100$\sim$200 meV. This is also the reason why the *GW* quasiparticle energy convergence is never pushed beyond 100 meV. A further indetermination of the Fermi energy arise in particular from the choice of the method used to calculate it. In this section we present the comparison between two of them: the classical method using a bisection algorithm, as implemented in ABINIT or QUANTUM ESPRESSO; and the integration of the WANNIER90 total DOS done with our own PYTHON code using the Simpson method. The WANNIER90 DOS is calculated from

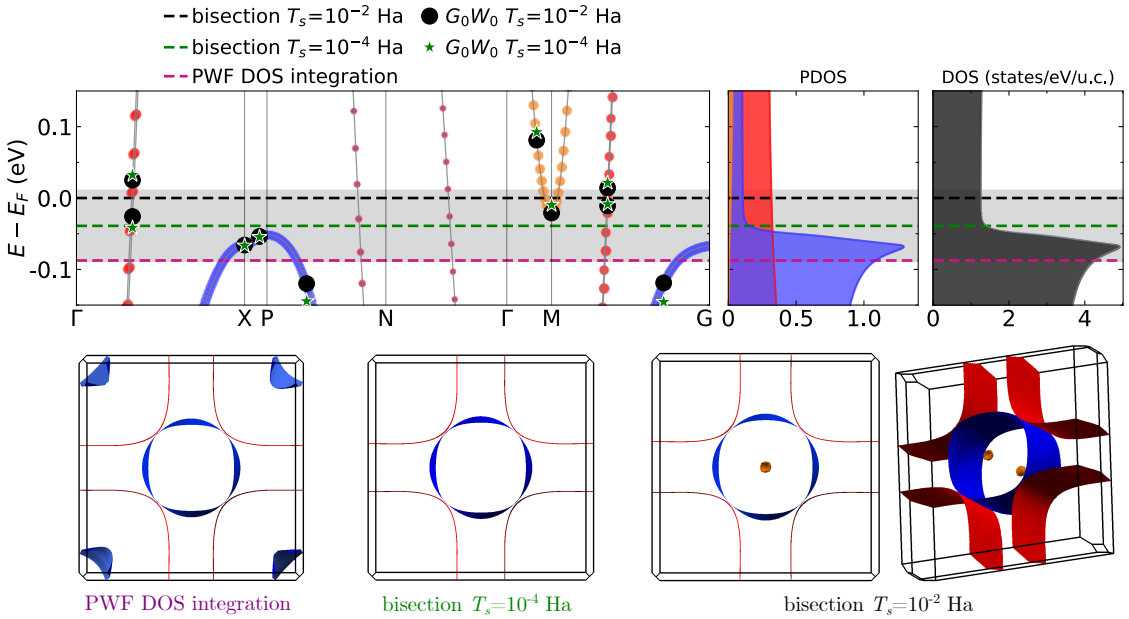

Figure 8.11: $La_3Ni_2O_7$@29.5GPa at the *GW* level: (top) bandplot zoomed on the Fermi level region with the different E_F values. (bottom) Fermi surfaces corresponding to the different Fermi levels. For the one corresponding to the $T_s = 10^{-2}$ Ha calculation, we also plot a three-quarter view to better see the appearance of the λ pocket around the M k-point. Note that we aligned the G_0W_0 energies of the $T_s = 10^{-2}$ (black dots) and 10^{-4} Ha (green stars) calculations at the k-point lying between X and P. The choice which has been made for the *GW* Fermi surface in Fig. 8.2b is $E_F(T_s = 10^{-4}$ Ha), while we kept the E_F calculated at $T_s = 10^{-2}$ Ha as the origin of the energy axis for the bandplot (Fig. 8.2d). The gray stripe shows the $\sim \pm 50$ meV uncertainty between our three E_F calculations, centered around the most precise value.

the PWF-interpolation bands, on a $48\times48\times48$ grid.

In this section we show how critical the calculation of the Fermi energy can be on the electronic structure and the Fermi surface of this system. For this reason, we take the most critical case of 29.5 GPa and we check the two methods here above described (for short labeled the *bisection* and *DOS* methods), keeping as close as possible to their defaults when there is matter of choice. In Fig. 8.11 we show a zoom around the Fermi level of the *GW* bandplot calculated using a smearing temperature T_s of 10^{-2} Ha, as in Fig. 8.2d, but reporting the different Fermi energies calculated and the associated Fermi surfaces below. First of all, one can remark the robustness of the α and β sheets with respect to a large variation of E_F (100 meV), which is due to the more dispersive character of the corresponding bands compared with to two incipient ones.

With the bisection method (E_F traced by a black line and set as the origin), a pocket of electrons (λ) appears around the M point in the $k_z = 2\pi/c$ plane (see BZ scheme on Fig. 8.2c), due to the La-5$d_{x^2-y^2}$ band crossing. On the other hand, with the DOS method and using the least arbitrary Wannier functions set among all possible sets, the PWF one, the Fermi energy is 87 meV (purple line) lower. In this case, there is no pocket of electrons at M and, in contrast, a pocket of holes is opened in the XP direction in the *GW* calculation, and the Fermi surface becomes again very similar to the DFT-PBE one, i.e. with the reappearance of the γ pocket in the BZ corners. As it can be seen, different methods provide qualitatively different Fermi surfaces leading to different low energy physics.

In order to improve our estimate on the Fermi energy, we have performed a full DFT+*GW* calculation reducing the smearing temperature T_s to 10^{-4} Ha $\simeq$ 3 meV. The corresponding *GW* quasiparticle energies are indicated by green stars and the associated E_F by the green dashed line in Fig. 8.11. As we can see, now the Fermi level situated more or less in the middle of the *indirect* band gap, at -39 meV compare to the E_F calculated with $T_s = 10^{-2}$ Ha. As a consequence both the electron pocket λ and the hole pocket γ are suppressed. And this is the Fermi level we have used to plot the *GW* Fermi surface in Fig. 8.2b.

In practice, in a system with such a delicate balance, any defect, vacancy ($La_3Ni_2O_7$ is usually oxygen deficient) or impurity, introduces a tiny perturbation in the Fermi energy which will open the electron or the hole pocket. In any case, the Fermi surface showed on Fig. 8.2b corresponds to a theoretical *ideal* situation. Therefore, we expect that a real experiment will probably not measure the ideal situation, and we leave a margin of error of 100 meV on the Fermi level to keep into account both experimental and theoretical uncertainties.

Notice that 29.5 GPa is a really critical pressure for the $La_3Ni_2O_7$ electronic structure. Indeed, at ambient pressure the La-5$d_{x^2-y^2}$ band is almost 0.5 eV above its position at 29.5 GPa (see Fig. 8.5b), and the bisection method set the *GW* Fermi energy well below the bottom of this band, with no possibility of an electron pocket opened at M. Consequently, the Fermi surface would be exactly that in Fig. 8.2b, with the stable α and β sheets and no γ or λ pockets at all, from ambient pressure on, and without any relevant modification up to 29.5 GPa.

8.D Crystal structures

Tab. 8.1 reports the crystal structures in the conventional cell used for the calculation at 29.5 GPa and for the in-plane strained system. In these two cases the parameters were chosen with a trade off between the values from the literature and obtained via a structural optimization. Tab. 8.2 reports the crystal structures used for the extra pressure calculations, all obtained via structural optimizations.

	29.5 GPa [Sun2023, Sakakibara2024]			epitaxial strained (thin film at 0 GPa) [Ko2025]		
	a=3.7148 ; c=19.7340			a=3.77 ; c=20.6927		
	x	*y*	*z*	*x*	*y*	*z*
Ni	0	0	0.096	0	0	0.095
La1	0	0	0.321	0	0	0.321
La2	0	0	0.5	0	0	0.5
O1	0	0.5	0.095	0	0.5	0.096
O2	0	0	0.204	0	0	0.205
O3	0	0	0	0	0	0

Table 8.1: Lattice parameters (LP) and atomic positions (AP) for $La_3Ni_2O_7$ at 29.5 GPa (left), with the theoretical AP taken from [Sakakibara2024], and the experimental LP from [Sun2023] and artificially tetragonalized as in [Sakakibara2024]. For the thin film (right), using the LP *a* from [Ko2025] and the rest from a structural relaxation performed with the ABINIT code.

	0 GPa			14 GPa			40 GPa		
	a=3.8408 ; c=20.2929			a=3.7533 ; c=19.7621			a=3.6378 ; c=19.1413		
	x	*y*	*z*	*x*	*y*	*z*	*x*	*y*	*z*
Ni	0	0	0.097	0	0	0.098	0	0	0.098
La1	0	0	0.321	0	0	0.321	0	0	0.321
La2	0	0	0.5	0	0	0.5	0	0	0.5
O1	0	0.5	0.096	0	0.5	0.096	0	0.5	0.095
O2	0	0	0.204	0	0	0.204	0	0	0.204
O3	0	0	0	0	0	0	0	0	0

Table 8.2: LP and AP used for the extra pressure calculations. They are all obtained by an ABINIT structural optimization enforcing the *I4/mmm* space group also at ambient pressure.

8.D.1 Influence of the tilt: *Amam* vs $I4/mmm$ bandplots

In this section we report the band plot for the *Amam* crystal structure relaxed at $P = 0$ GPa, shown in its *oS* base-centered orthorhombic BZ (Fig. 8.12 red lines). For comparison we also show the band plot for the 0 GPa relaxed system but constrained within the *I4/mmm* crystal structure and folded within the same *oS* BZ (blue lines) from its original *tI* body-centered tetragonal (BCT) BZ. Of course, the two BZ have different topology and even after the folding they do not overlap. High symmetry points of the *tI* may not correspond to any high symmetry point of the *oS*. And even in case of one-to-one correspondence between high symmetry points, they might be located at slightly different positions due to the different BZ shape determined by the *a* to *b* (and to *c*) ratios which of course differ.

We remark some differences, especially in the conduction states which however are not ob-

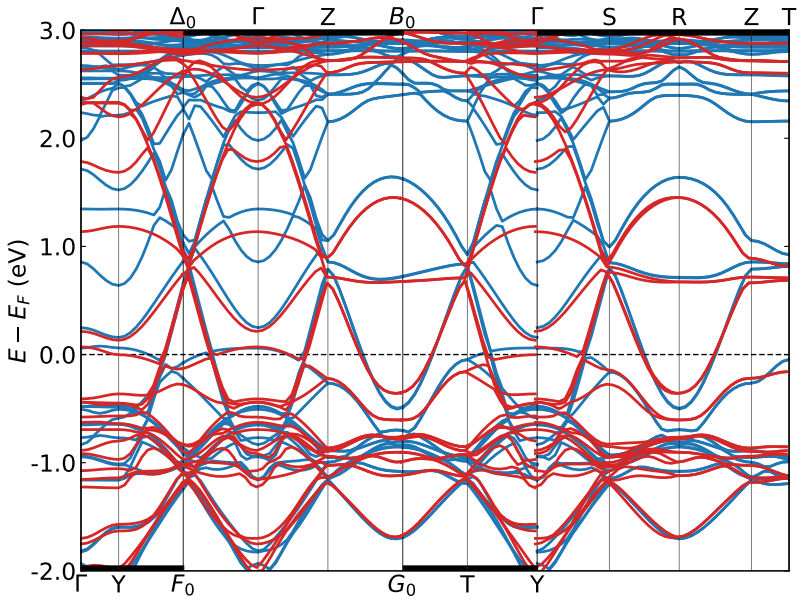

Figure 8.12: Ambient pressure $La_3Ni_2O_7$ band plots comparison within the *oS* base-centered orthorhombic Brillouin zone: freely relaxed at $P = 0$ in the *Amam* crystal structure (red); $P = 0$ constrained relaxation within the *I4/mmm* crystal structure (blue). The *I4/mmm* band plot is folded from its original *tI* body-centered tetragonal Brillouin zone into the same *oS* base-centered orthorhombic BZ. Some distortions cannot be avoided in such a folding between so different Brillouin zones. Since the two BZ have different topology and even after folding they do not overlap, this comparison implies a compromise between the two with unavoidable distortions.

served by direct ARPES photoemission, due to the reduction of symmetry induced by the tilting of NiO_6 octahedra and by the introduced orthorhombicity which are both at their maximum at 0 GPa. Nevertheless, the two plots are very similar at the Fermi level. In particular the presence of the γ hole pocket is confirmed also in the DFT PBE *Amam* structure: only folded from the X-P segment of the BCT Brillouin zone, into the (initial part of the) Γ-Y segment of the *oS* BZ. The only noticeable difference is, in the *Amam* structure, a slightly larger dispersion of the γ band along the z axis than in the *I4/mmm* where it is almost undispersive. The *Amam* γ band is either at the same level (in Γ) or shifted ~ 50 meV downward (in Y) compared to the *I4/mmm* one. We know that the general tendency of the *GW* corrections is to shift down this band by $70 \sim 80$ meV with respect to DFT PBE. Therefore the γ pocket should disappear also in a *GW* calculation of the *Amam* structure.

Finally, outside the Fermi region we remark that the La-5$d_{x^2-y^2}$ band is further shifted up in the *Amam* crystal structure with respect to the *I4/mmm* where, as discussed in Sec. 8.3.1.2, it is found a little below 1 eV at the M point (corresponding to the Y point of the *oS*). Therefore this band is further outside the low-energy region for the combined effect of pressure and symmetry reduction, and enters into play at the pressure of 14 GPa (at the *GW* level), as illustrated in Fig. 8.5.

This comparison indicates that the main *GW* conclusions of this work, and in particular about the topology of the Fermi surface and the disappearance of the γ hole pocket, should also hold for the case of the *Amam* crystal structure at ambient pressure as measured by ARPES.

8.E Bloch state plots

In this section we show some selected Bloch states that are interesting to visualize in real space. Notice that these Bloch states are calculated in DFT PBE, as our one-shot G_0W_0 first order perturbation theory calculation does not recalculate the wavefunctions, but only corrects the energies. The lower and upper Ni-3d_{z^2} bands are sometimes respectively labeled as bonding and anti-bonding, according to a chemical convention. For these two states we plot in Fig. 10.2 (left and center) the iso-surfaces of the Bloch wave functions at the X k-point which lies in the corner of the BZ. As we can see, these names are not appropriated, the upper state being more "bonding" than the lower one, with more weight on p_z orbitals of inner oxygen atoms lying in between NiO_2 planes. Another Bloch state worth to be shown is the one corresponding to the La-5$d_{x^2-y^2}$ band, which is the most sensitive to pressure, and in particular at the M point where it reaches its minimum. In Fig. 10.2 (right) we see that these electrons are delocalized in the spacer, which explain the highly dispersive shape of the corresponding band. From 0 to 29.5 GPa, this state is not occupied. It starts to be occupied beyond 29.5 GPa, inducing self-doping of the NiO_2 planes.

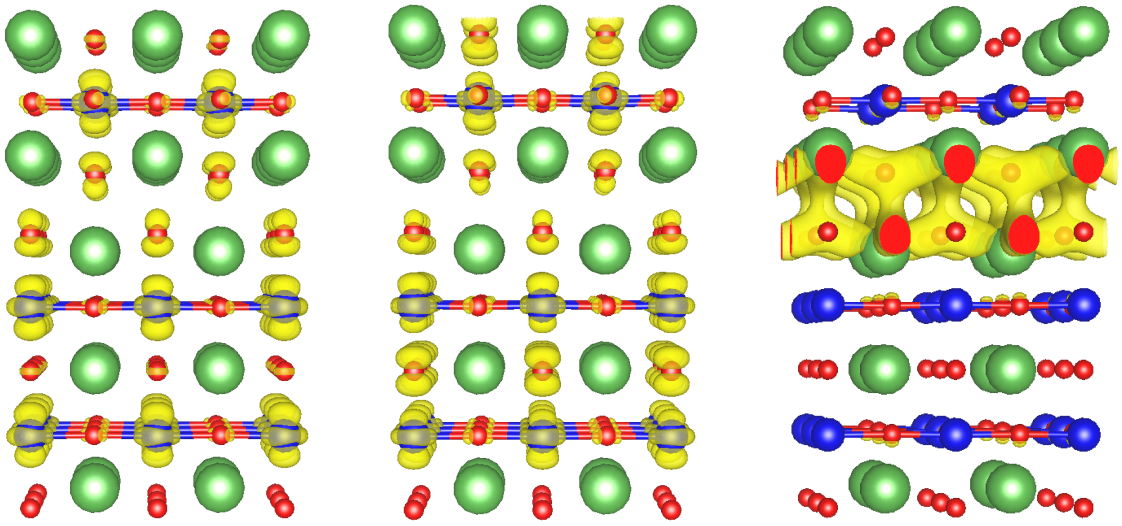

Figure 8.13: Iso-surface of the probability density $|\psi_{n\mathbf{k}}(\mathbf{r})|^2$ for the Bloch wave functions corresponding to the lower (left) and upper (center) Ni-3d_{z^2} bands at the X k-point, as well as for the Bloch wave functions corresponding to the La-5$d_{x^2-y^2}$ band at the M k-point.

8.F Additional orbital character projections

On Fig. 8.15 we provide more precise band character plots than on Fig. 8.3b, giving details on the specific orbitals involved in the Bloch states. We distinguish the two spacer La atoms from the inner one lying in between the two NiO_2 planes; as well as the planar O atoms lying in the NiO_2 planes, and the apical O atoms of the spacer (ap. sp.) or of the inner layer (ap. inner). See Fig. 8.14 which shows the atoms labeling on the VESTA structure. For O-2p, we also distinguish p_z and $p_{x/y}$ orbitals. We remark that there is a non-negligible La-4f orbital character on the lowered La-5$d_{x^2-y^2}$ band which almost reaches the Fermi level. We also remark that in-plane O-2$p_{x/y}$ orbitals have a strong contribution on what we label Ni-3$d_{x^2-y^2}$ bands, especially above the Fermi level.

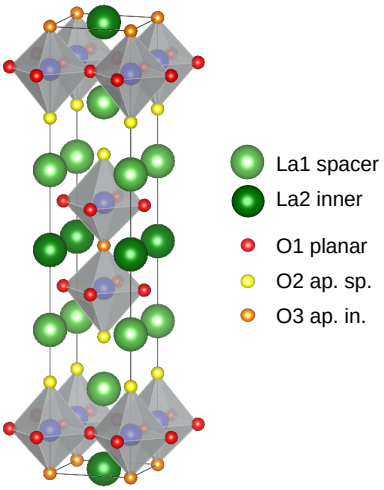

Figure 8.14: Definition of the La and O atom site labels used in projections of Fig. 8.15, with site indices corresponding to the ones in Tab. 8.1.

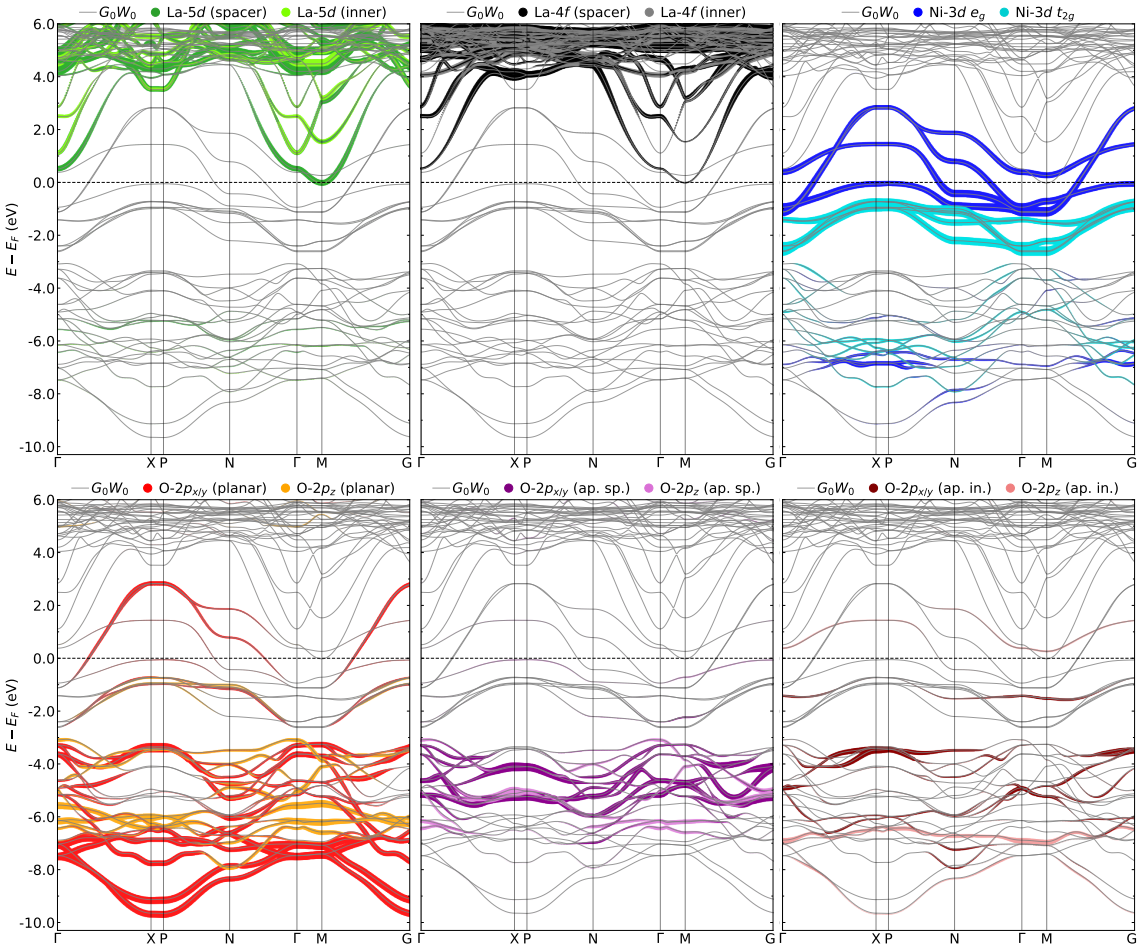

Figure 8.15: Detailed PWF orbital characters on top of *GW* Wannier interpolated bands, for the structure at 29.5 GPa. See Fig. 8.14 for the definition of the atom labels.

9

Pressure, doping and magnetism in the single-layer nickelate La_2NiO_4

The results detailed in this chapter have been published in J.B. de Vaulx, F. Bernardini, V. Olevano, Q. N. Meier, et A. Cano., *"Pressure and doping effects on the electronic structure and magnetism of the single-layer nickelate La_2NiO_4"*, Physical Review Materials, vol. 9, no. 11, page 114804, November 2025 [de Vaulx2025b]. In this work, I performed the non-spin polarized structural relaxations and electronic structure calculations. A. Cano did the spin-polarized structural relaxations, while the DFT+U calculations were performed by F. Bernardini.

9.1 Introduction

Among the Ruddlesden-Popper nickelates, the bilayer and trilayer compounds draw attention due to their superconducting nature (see Sec. 1.3.2 and Chap. 8), and their electronic structures have been extensively investigated. Progress in the field, however, requires a broader consideration of the entire family, including their magnetic properties. Early magnetic susceptibility measurements on nominal $La_3Ni_2O_7$ samples, for example, indicated very low superconducting volume fractions [Zhou2023], raising concerns about secondary phases and structural polymorphs arising from intergrowth. Partial substitution of La with Pr or Sm has been shown to stabilize a nearly pure bilayer phase [Wang2024, Zhang2024], yet completely eliminating intergrowth with other members of the series remains an experimental challenge. Furthermore, neutron scattering measurements have recently revealed long-range magnetic order in both $La_3Ni_2O_7$ and $La_2PrNi_2O_7$ at ambient pressure [Plokhikh2025]. In this context, the single-layer ($n = 1$) nickelates warrant renewed attention, not only to address synthesis and phase-purity issues, but also to serve as a reference point for a comprehensive understanding the electronic and magnetic properties across the Ruddlesden-Popper nickelate series.

In this work, we investigate the properties of the single-layer nickelates as a function of pressure and composition. Specifically, we use density-functional theory (DFT) to compute the structural phase diagram of La_2NiO_4 (see Fig. 9.1). Our calculations show that its crystal structure can be driven to a high-symmetry tetragonal phase by the application of pressure, which can be either physical, "chemical" or both. As an illustration, we consider partial substitution of

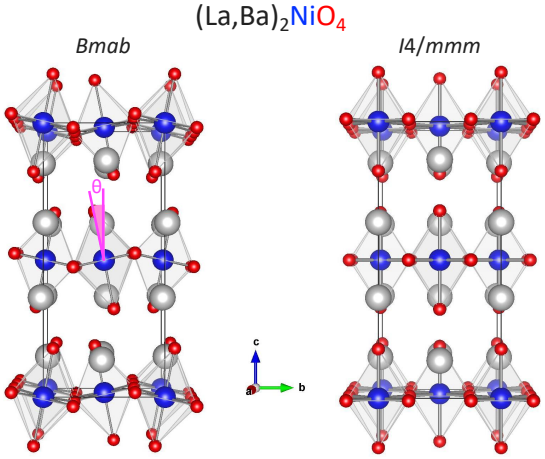

Figure 9.1: (a) Ball-and-stick model of the single-layer nickelates illustrating the orthorhombic ($Bmab$) and tetragonal ($I4/mmm$) structures—with and without NiO_6 octahedra tilts—characteristic of these systems.

La with Ba, which not only stabilizes the tetragonal phase but also formally dopes the system toward the $d^{7.5}$ configuration of the superconducting bilayer $La_3Ni_2O_7$. Further, we study the electronic structure and magnetic tendencies of $(La,Ba)_2NiO_4$, revealing both analogies and differences compared to the superconducting members of the Ruddlesden-Popper series. These results underscore the single-layer case as a valuable reference system for clarifying not only the emergence of magnetic order, but also the possible competition among distinct superconducting instabilities in the nickelates.

9.2 Methods

The structural optimizations and non-spin polarized DFT calculations were performed using Quantum Espresso. In these calculations, we considered the PBE exchange-correlation functional with PseudoDojo pseudopotentials. The calculations were converged using a $16\times16\times16$ k-point mesh for the $I4/mmm$ structure and a $12\times12\times12$ for the $Bmab$ one, with a 100 (400) Ry cutoff for wavefunction (density) and a Gaussian smearing of 0.01 Ry. For the spin-polarized calculations, we considered the previously optimized crystal structures and used the all-electron code WIEN2k with the LDA+U exchange-correlation functional [Liechtenstein1995]. In these calculations, we used muffin-tin radii of 2.5, 2.0, and 1.60 a.u. for the La, Ni, and O atoms, respectively, and a plane-wave cutoff $R_{\mathrm{MT}}K_{\mathrm{max}} = 6.0$. The integration over the Brillouin zone was done using a Monkhorst-Pack mesh of $10\times10\times10$ and tetrahedron method [Blöchl1994] for the primitive cell and equivalent ones for the supercells when computing the magnetically ordered structures. Additional structural optimizations were performed for the G-type antiferromagnetic (G-AFM) configuration using the corresponding primitive cell and a $10\times10\times10$ Monkhorst-Pack k-mesh with a 125 (500) Ry cutoff for the wavefunction (density) and a Gaussian smearing of 0.01 Ry.

To address compositional effects, we focused on the La $\rightarrow$ Ba substitution and employed the virtual crystal approximation (VCA) [Bellaiche2000]. From the methodological point of view, this approach is particularly appropriate since i) the relevant electronic shells in La^{3+} and Ba^{2+} are the same [Bernardini2020] and ii) they are treated on the same footing using Quantum Espresso and the PeudoDojo. In addition, to the best of our knowledge, there is

no experimental evidence of positional La/Ba ordering (see e.g. [Austin1989, Alonso1990, Zakharchuk2023, Schilling2008]), further justifying the use of VCA. For $La_{1.5}Ba_{0.5}NiO_4$ in particular, we thus obtain $a = 3.887$ Å and $c = 12.78$ Å in the non-spin polarized case, in close agreement with the experimental values $a = 3.842$ Å and $c = 12.86$ Å [Austin1989]. The reliability of VCA is further corroborated by the relaxed structure of $LaBaNiO_4$, for which VCA yields the lattice parameters $a = 3.942$ Å and $c = 12.69$ Å, essentially identical to the explicit La $\rightarrow$ Ba substitution in the primitive $I4/mmm$ ($a = 3.942$ Å and $c = 12.61$ Å).

9.3 Pressure and compositional effects

9.3.1 Pressure

We begin by examining the structural phase diagram of La_2NiO_4 under pressure. At ambient pressure, La_2NiO_4 adopts an orthorhombic structure with space group $Bmab$, characterized by tilted NiO_6 octahedra, as illustrated in Fig. 9.1 [Rodriguez-Carvajal1991]. Symmetry-wise, this phase is a subgroup of the high-symmetry tetragonal $I4/mmm$ one also illustrated in Fig. 9.1 (where the octahedral tilting is directly related to the X_3^+ irreducible representation of the latter). Our non-spin polarized calculations reveal that applying pressure gradually suppresses the octahedral tilts as shown in Fig. 9.2 (empty circles). According to these results, there should be a continuous pressure-induced $Bmab \leftrightarrow I4/mmm$ phase transition in La_2NiO_4 at 8 GPa.

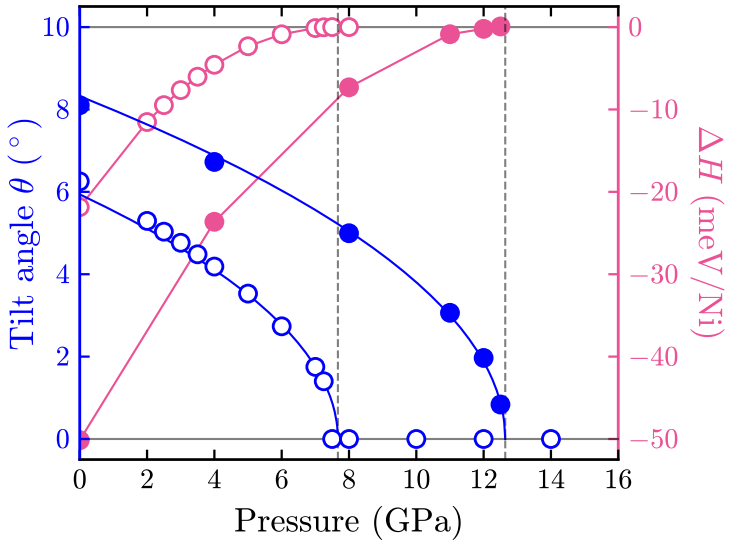

Figure 9.2: Calculated tilt angle θ and enthalpy $\Delta H = H_{Bmab} - H_{I4/mmm}$ as a function of pressure in La_2NiO_4. Empty and filled circles correspond to non-spin polarized calculations and G-AFM order respectively. In both cases, the suppression of the tilt as a function of pressure scales as $\theta \propto |P - P_c|^{1/2}$ as indicated by the lines. A negative ΔH indicates that the $Bmab$ phase is more favorable than the $I4/mmm$ one.

However, additional spin-polarized calculations for the experimental G-AFM configuration reveal a significant magnetostructural coupling in La_2NiO_4. In particular, the calculated lattice parameters at ambient pressure change from $(a, b, c) = (5.328, 5.465, 13.02)$ Å in the non-spin polarized case to $(a, b, c) = (5.459, 5.649, 12.46)$ Å in the presence of G-AFM order. The latter values are in better agreement with the experimental data (see e.g. [Rodriguez-Carvajal1991]). Furthermore, the presence of magnetic order produces a hardening effect that

shifts the calculated critical pressure of the structural transition to $\sim$ 12.5 GPa (filled circles in Fig. 9.2). Apart from this shift, we find that the overall behavior remains unchanged, in the sense that non-spin polarized and spin-polarized calculations cases both yield the Landau-theory scaling relation $\theta \propto |P - P_c|^{1/2}$ for the tilt angle. Interestingly, we find that the Ni magnetic moment does not vanish at P_c (although it decreases slightly from 1.32 μ_B at ambient pressure to 1.23 μ_B).

Further, the calculated Ni-O bond lengths show no significant change under pressure. Specifically, in the G-AFM configuration, the apical distance changes from 2.24 to 2.17 Å only between ambient pressure and 12.5 GPa. The equatorial bond, in its turn, decreases from 1.97 to 1.89 Å. To the best of our knowledge, experimental data are only available for non-stoichiometric $La_2NiO_{4+\delta}$ and $Pr_2NiO_{4+\delta}$ [Bull2020], where excess oxygen likely distorts the octahedra, precluding direct comparison. Nevertheless, both calculated and reported changes are small, indicating that the quasi-2D layered character is preserved across the pressure-driven structural transition.

9.3.2 Chemical pressure via Ba substitution

We now turn to chemical pressure effects by considering the substitution of La with Ba, whose larger ionic radius mimics the action of pressure. We find that Ba substitution in fact reproduces the effect hydrostatic pressure on the crystal structure, in the sense that it leads to the gradual suppression of the octahedral tilts according to a Landau-theory scaling $\theta \propto |x - x_{c,\theta}|^{1/2}$ with $x_{c,\theta} \sim 0.25$. This behavior is shown in the top panel of Figure 9.3, which correspond to spin-polarized calculations in the G-AFM configuration (blue circles and blue solid line for the $\theta \propto |x - x_{c,\theta}|^{1/2}$ scaling).

In addition, we find that Ba substitution leads to the subsequent suppression of the Ni magnetic moment in the *G*-AFM configuration, which eventually vanishes following a similar scaling $\mu_{Ni} \propto |x - x_{c,\mu_{Ni}}|^{1/2}$ with $x_{c,\mu_{Ni}} \sim 0.75$. As under pressure, we thus find a composition range in which the system becomes tetragonal yet retaining *G*-AFM order (opposite to the temperature-driven behavior, where the tilts persist in the absence of magnetic order [Rodriguez-Carvajal1991]). This demonstrates that, despite the presence of sizable magnetostructural coupling, the structural and magnetic instabilities are fundamentally distinct and can be tuned independently. This further implies that, in the general temperature-pressure-composition phase space, there should be a point in which both these transitions coincide, giving rise to multiferroic critical behavior [Narayan2019].

Further insight into the magnetostructural coupling is provided by the calculated lattice parameters as a function of Ba content (Fig. 9.3, bottom panel). These exhibit a non-monotonic behavior, deviating from Vegard's law[1], that is in remarkable agreement with the experimental data (see [Austin1989], as well as [Zakharchuk2023] and the references therein). By comparison with the tilt angle and the Ni magnetic moment, we find that this unusual trend is directly correlated with the structural and magnetic transitions.

To understand this correlation, it is convenient to take $LaBaNiO_4$ as the parent compound ($x = 1$ in Fig. 9.3). Thus, for decreasing Ba content, Vegard's law is initially obeyed in the absence of both octahedral tilts and magnetic order. This means that the free energy can be written as $F_0 = g_1 x'(u_{xx} + u_{yy}) + g_3 x' u_{zz} + \frac{K}{2} u_{ii}^2$, where $x' = 1 - x$ and u_{ij} is the strain tensor expressed in the orthorhombic axes (K is the bulk modulus and g_i are constants). The diagonal components of u_{ij} embody the relative variation of the lattice parameters which, in equilibrium, will then scale linearly with x' (Vegard's law). However, additional couplings of the strain to

[1] The empirical Vegard's law establishes a linear relation between the lattice parameters and the doping coefficient x.

the magnetic and structural order parameters L and Q are also allowed by symmetry:

$$F_L = g_{1,L} L^2 (u_{xx} + u_{yy}) + g_{3,L} L^2 u_{zz}, \tag{9.1}$$

$$F_Q = g_{1,Q} Q^2 (u_{xx} - u_{yy}) + g_{3,Q} Q^2 u_{zz}. \tag{9.2}$$

Thus, below the corresponding critical concentrations, where $L \propto |x' - x'_{c,L}|^{1/2}$ and $Q \propto |x' - x'_{c,Q}|^{1/2}$, the emergence of these orders modify Vegard's law producing the slope changes that can be seen in Fig. 9.3 (bottom panel). Remarkably, the strength of the purely structural and magnetostructural couplings, $g_{i,Q}$ and $g_{i,L}$ respectively, turn out to be comparable in $La_{2-x}Ba_xNiO_4$.

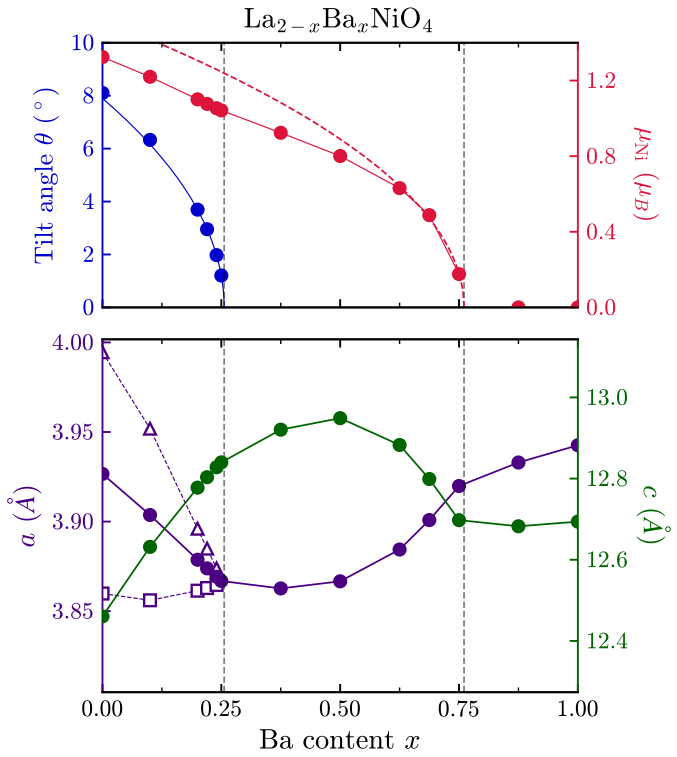

Figure 9.3: (Top panel) Calculated tilt angle θ and Ni magnetic moment μ_{Ni} as a function of the Ba content x in $La_{2-x}Ba_xNiO_4$ (G-AFM configuration). Both the suppression of the tilt angle and the quenching of the Ni magnetic moment scale as $|x - x_c|^{1/2}$ (blue line for θ and red dashed line for μ_{Ni}). (Bottom panel) Calculated lattice parameters as a function of the Ba content x in $La_{2-x}Ba_xNiO_4$. Circles represent "pseudo-tetragonal" or tetragonal lattice parameters ($a_{\text{pseudo-t}} = \sqrt{ab/2}$ or a and c). Squares and triangles correspond to the orthorhombic $a/\sqrt{2}$ and $b/\sqrt{2}$ respectively, whose difference correlates with the emergence of the tilt.

9.4 Electronic structure

Next, we discuss the evolution of the electronic structure of these systems.

9.4.1 Parent compound La_2NiO_4

The parent compound La_2NiO_4 is formally associated with a Ni d^8 configuration. In overall, the calculated electronic structure shows only moderate modifications as a function of pressure,

with rather small changes associated with the "tetragonalization" itself. Thus, we consider the tetragonal $I4/mmm$ structure at ambient pressure to illustrate the main features of the electronic structure of La_2NiO_4 in the non-spin polarized case. The calculated electronic structure is shown in Fig. 9.4 (see Fig. 9.5 for the electronic structure at 8 GPa). The Ni-3d derived states can be separated according to their projections into $e_g = d_{x^2-y^2/z^2}$ and $t_{2g} = d_{xy/xz/yz}$ states, which are partially filled and completely occupied respectively. Further, the bandwidth of the Ni-$d_{x^2-y^2}$ states is $\sim$ 3.5 eV, while the Ni-d_{z^2} ones produce a flat-band feature that dominates the DOS at the Fermi level. From the projected DOS, we find the occupancies $n_{d_{x^2-y^2}} = 1.03$, $n_{d_{z^2}} = 1.60$ and $n_{t_{2g}} = 5.84$. The difference from the nominal d^8 configuration can be ascribed to the hybridization with the O-2p states. In fact, the charge transfer energy is $\sim$ 3 eV, which is a typical cuprate-like value similar to that of the superconducting bilayer and trilayer nickelates. When it comes to the Fermi surface, it is formed of two sheets of hybridized Ni-e_g states. However, compared to the bilayer and trilayer cases, the d_{z^2} sheet is considerably more dispersive along k_z. Also, including electronic correlations at the GW level results in a self-doping effect from a La-5d state (see Fig. 10.1). We note that, although its detailed analysis is beyond the scope of the present work, a similar situation takes place in the bilayer and infinite-layer cases [Olevano2020, de Vaulx2025a]. This effect will be further discussed in Sec. 10.1.

9.4.2 Doped compound $La_{1.5}Ba_{0.5}NiO_4$

We now turn to the electronic structure of $La_{1.5}Ba_{0.5}NiO_4$, where the nominal electronic configuration changes to $d^{7.5}$. The calculated electronic structure is illustrated in Fig. 9.4 (see Fig. 9.6 for a comparison with La_2NiO_4 using the $Bmab$ structure of the latter). As we see, hole doping with Ba is mainly absorbed by the Ni-e_g manifold, which does not occur in a simple rigid-band-shift fashion. Specifically, the Ni-3$d_{x^2-y^2}$ bandwidth decreases while the Ni-

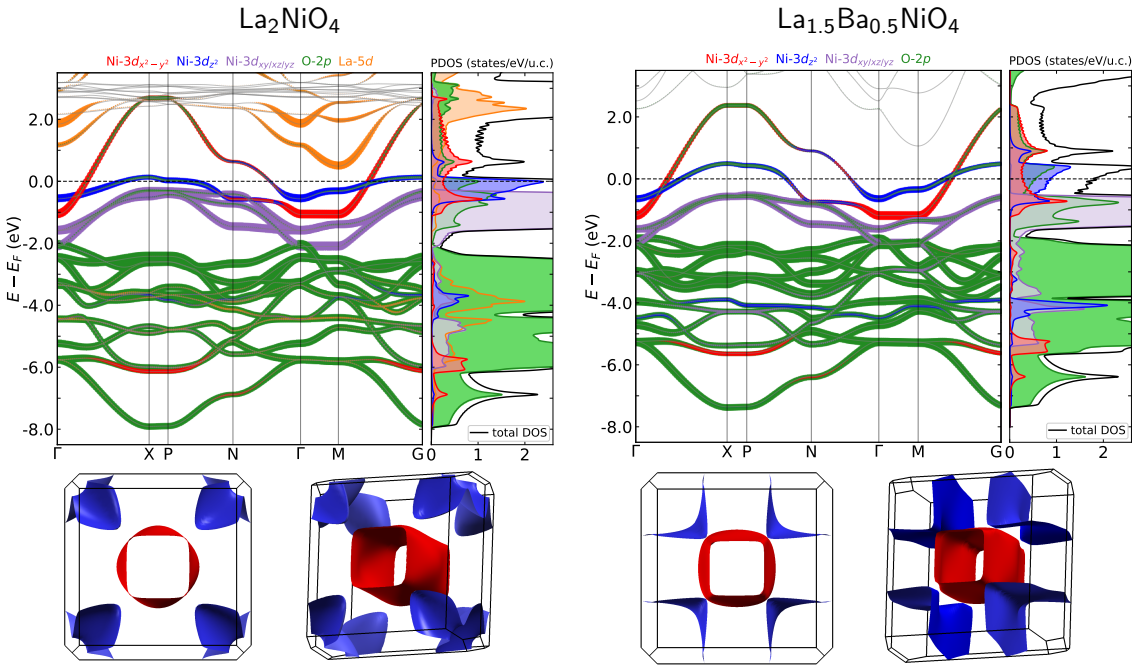

Figure 9.4: Electronic structures and Fermi surfaces of La_2NiO_4 in its $I4/mmm$ phase (left) and $La_{1.5}Ba_{0.5}NiO_4$ (right), both at ambient pressure. Note that, while the blue d_{z^2} flat bands yield the blue Fermi surface sheets, there is a k-dependent mixing between the $d_{x^2-y^2}$ and d_{z^2} states that yield the red Fermi surface sheet. In other words, there is no 100% correspondence between the colors of the Fermi-surface sheets and their orbital character.

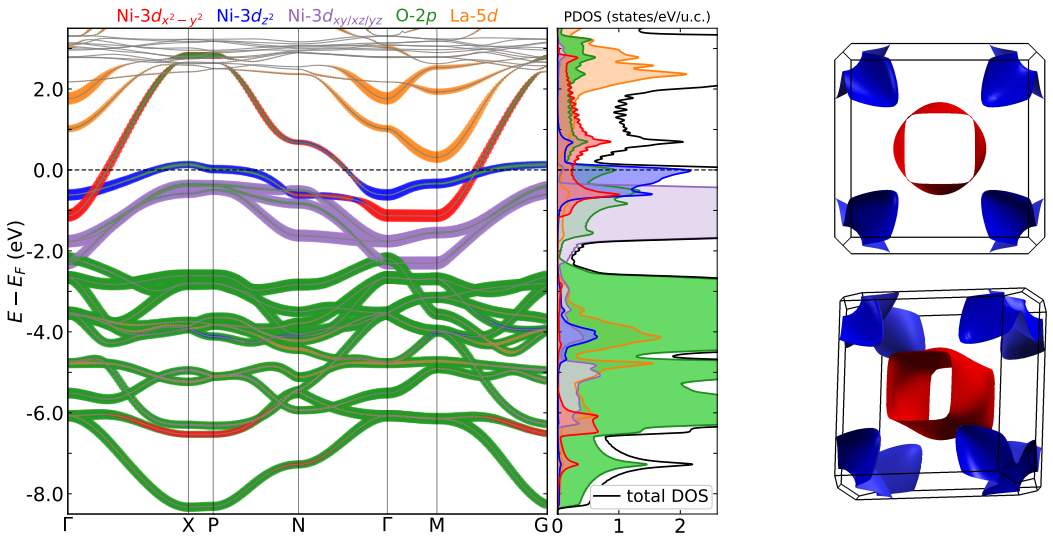

Figure 9.5: Electronic structure, PDOS and Fermi surface of La_2NiO_4 at 8 GPa, to compare with Fig. 9.4 which is at ambient pressure. The main difference is only in the dispersion which slightly increases, while the Fermi surface is almost unaffected.

$3d_{z^2}$ one increases. The occupancies of the different Ni-3d orbitals become $n_{d_{x^2-y^2}} = 1.17$, $n_{d_{z^2}} = 1.27$ and $n_{t_{2g}} = 5.91$. Further, we find that the Ni-3d_{z^2} states still yield the main contribution to the DOS at the Fermi level, followed by the O-2p and the Ni-3$d_{x^2-y^2}$ ones. In fact, the mixing between Ni-e_g and O-2p states increases as the charge-transfer energy reduces to ~ 1.8 eV. Further, Fermi surface retains its topology and main qualitative features. Specifically, the Fermi-surface sheet associated with the Ni-3d_{z^2} flatband remains present and, despite the larger size of the Ba atom, there is no self-doping effect from the La/Ba-5d states.

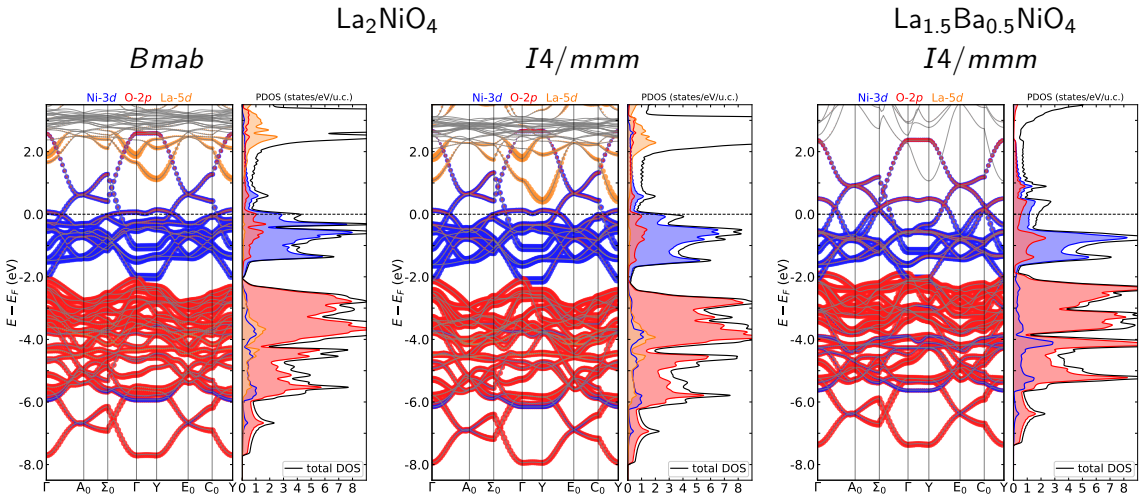

Figure 9.6: Comparison between the non-spin polarized band plot and DOS of the parent compound La_2NiO_4 in its $Bmab$ and $I4/mmm$ phases and $La_{1.5}Ba_{0.5}NiO_4$ (using analogous $Bmab$ supercells for the band plots).

9.5 Magnetism

We now analyze in more detail the tendency towards magnetic order of these single-layer compounds by performing LDA+U calculations. For this, we consider the following configurations: ferromagnetic (FM), A-type antiferromagnetic (A-AFM) where the first-neighbor Ni spins are parallel in-plane and anti-parallel out-of-plane, and G-type antiferromagnetic (AFM) with antiparallel first-neighbor Ni spins. Note that C-AFM with antiparallel first-neighbor Ni-spins in-plane and parallel out-of-plane is equivalent to G-AFM in the tetragonal $I4/mmm$ Ruddlesden-Popper structure which we will consider hereafter (see Fig. 9.7). In addition, we considered in-plane $(0, \pi)$- stripe AFM order but we were unable to find stable solutions for this configuration.

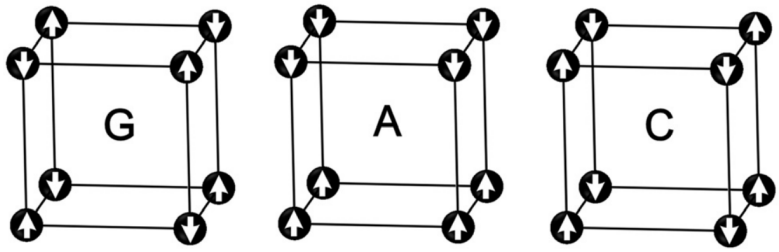

Figure 9.7: Labels of the generic antiferromagnetic orders. Notice that due to the ($a/2$, $b/2$) shift of the stacked perovskite blocks, G and C-AFM orders are equivalent in the single-layer. From [Hu2014].

9.5.1 Parent compound La_2NiO_4

We start with La_2NiO_4 as the reference compound. In this case, the G-AFM state minimizes the energy compared to non-spin polarized state as well as to the A-AFM and FM configurations. The energy difference depends on the value of the Hubbard U parameter. For $U = 0$ and ambient pressure, the system remains metallic and the calculated magnetic moment of the Ni atom in the G-AFM state is significantly lower than its experimental value (specifically, 0.64 μ_B vs. 1.68 μ_B

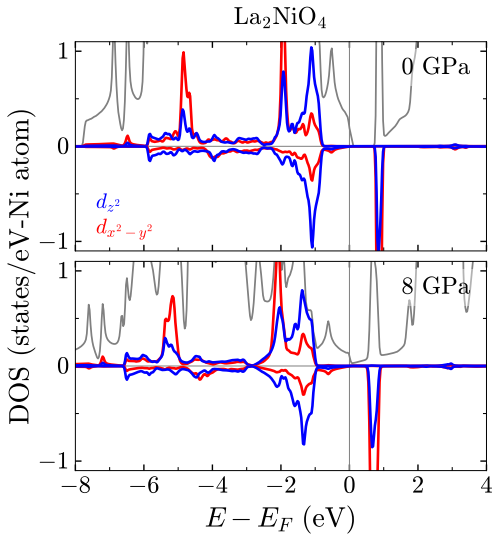

Figure 9.8: Density of states (DOS) projected on the Ni-d_{z^2} (blue) and Ni-$d_{x^2-y^2}$ (red) orbitals in the G-AFM ground state of La_2NiO_4 at ambient pressure and 8 GPa ($U = 3.5$ eV). Spin up/down states are indicated with positive/negative values respectively. The gray curves correspond to the total DOS, which reveals the insulator to metal transition when increasing pressure.

[Rodriguez-Carvajal1991]). For $U \geq 1$ eV and the G-AFM configuration, a gap opens in the DOS at the Fermi level thus yielding insulating behavior as in the experiments. Further, the results of constrained RPA calculations for the bilayer case suggest that $U \simeq 3.5$ eV [Christiansson2023] is a realistic value for these systems. In fact, with $U = 3.5$ eV the Ni moment increases to 1.4 μ_B, which better matches the experimentally observed value [Rodriguez-Carvajal1991] (see also [Bernardini2025] for additional calculations in the experimental *Bmab* structure). At the same time, we observe that the calculated moment varies for the different magnetic configurations. This difference suggests an intermediate situation between fully localized spins and itinerant magnetism, signalling that a mapping to a Heisenberg model could be problematic. In fact, unlike the G-AFM state in which a gap opens, the A-AFM and FM states remain metallic for all considered U values.

Under pressure, in the range from 0 to 8 GPa, we find that the tendency towards magnetic order of La_2NiO_4 remains strong, with just a slight decrease in overall magnetization energy and small changes in the relative energy of the studied magnetic configurations. Furthermore, for $U = 3.5$ eV, we find an insulator-to-metal transition for the G-AFM state at ~ 4 GPa (below the orthorhombic-to-tetragonal structural transition). This circumstance is illustrated in Fig. 9.8, which shows the corresponding DOS at 0 GPa and 8 GPa.

9.5.2 Doped compound $La_{1.5}Ba_{0.5}NiO_4$

Finally, we consider $La_{1.5}Ba_{0.5}NiO_4$. In this case, we obtain reduced magnetization energies together with an intriguing competition between the different magnetic configurations as illustrated in Fig. 9.9. Notably, we find that the FM and A-AFM solutions are essentially degenerate. This is a manifestation of the enhanced low-dimensional character of the system—also reflected in the shape of the Fermi surface—implying an effective decoupling in the out-of-plane direction even under pressure. Moreover, the relative energy with respect to the G-AFM configuration turns out to be significantly reduced also, as we find it always below ~ 50 meV/Ni (see Fig. 9.9).

Interestingly, this competition remains as a function of both U and pressure. For $U \lesssim 3.5$ eV, the configuration that minimizes the energy corresponds to the G-AFM state. This can be seen as reminiscent of the parent compound. For $U \gtrsim 3.5$ eV, however, the situation is reversed, in the sense that the energy is minimized by FM/A-AFM configurations. In addition, for $U \gtrsim 3.5$ eV, we find an intriguing crossover from FM/A-AFM to G-AFM as a function of pressure, which is illustrated in Fig. 9.9. This crossover implies a drop in the magnetic moment of the Ni atom of 0.5 μ_B.

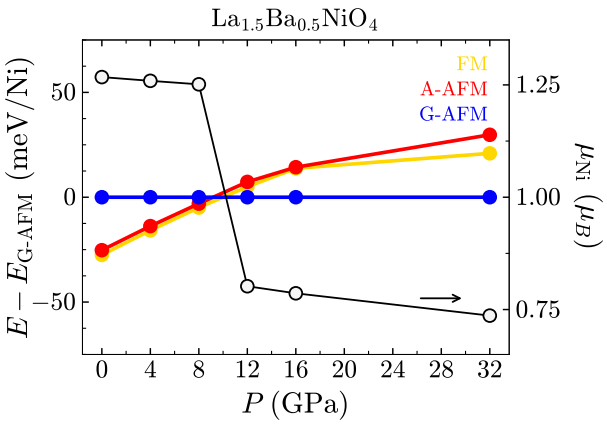

Figure 9.9: Relative energy and Ni magnetic moment as a function of pressure calculated for $La_{1.5}Ba_{0.5}NiO_4$ ($U = 3.5$ eV).

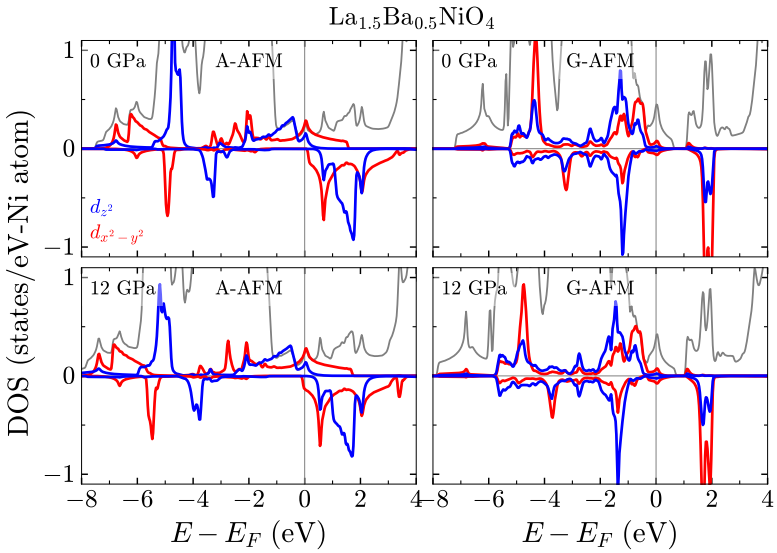

Figure 9.10: Density of states (DOS) projected on the Ni-d_{z^2} (blue) and Ni-$d_{x^2-y^2}$ (red) orbitals in the A-AFM and G-AFM configurations of $La_{1.5}Ba_{0.5}NiO_4$ at ambient pressure and 12 GPa ($U = 3.5$ eV). Spin up/down states are indicated with positive/negative values respectively. The gray curves correspond to the total DOS.

9.6 Discussion

We now turn to the implications of our results, beginning with the magnetostructural behavior. Our calculations have revealed a substantial interplay between the octahedral tilts, magnetic order and strain in $(La,Ba)_2NiO_4$. This interplay is a key factor in setting the critical pressure at which La_2NiO_4 becomes tetragonal, and further explains the unusual evolution of the lattice parameters with composition observed experimentally, which deviates from Vegard's law.

Further, the comparison between La_2NiO_4 and $La_{1.5}Ba_{0.5}NiO_4$ reveals the emergence of an intriguing competition between different magnetic configurations. This can lead to magnetic frustration and, consequently, to a paramagnetic-like disordered state. This scenario is in fact consistent with the glass-like behavior reported experimentally when the La:Ba ratio is 1:1 [Schilling2008].

Moreover, if the correlations are sufficiently strong, this competition can appear as a crossover from FM/A-AFM to G-AFM order that, at first glance, resembles the one obtained for the bilayer $La_3Ni_2O_7$ [LaBollita2024]. However, a closer inspection of the electronic structure reveals a redistribution of both $d_{x^2-y^2}$ and d_{z^2} states in the case of $La_{1.5}Ba_{0.5}NiO_4$ (see Fig. 9.10), pointing to a distinct microscopic origin of this crossover. Furthermore, the observation that La_2NiO_4 becomes metallic under either physical or chemical pressure suggests a possible modification of the magnetic-coupling mechanisms, evolving from superexchange toward direct exchange.

Regarding superconductivity, early theoretical studies emphasized the crucial role of the multilayer structure for superconductivity in the Ruddlesden-Popper nickelates, drawing direct analogies with the bilayer Hubbard model where $s_{\pm}$-wave pairing arises near half-filling for sufficiently large interlayer coupling (see, e.g., [Nakata2017, Sakakibara2024]). Subsequent works have also suggested the possibility of d-wave superconductivity in these systems, with multiband effects playing a different role [Lu2024, Xia2025, Lechermann2023, Sakakibara2024, Heier2024, Zhang2024, Xu2025]. Our results demonstrate that several key ingredients of this broader picture are present in the single-layer systems and can be tuned through pressure and doping. In particular, Ba substitution in La_2NiO_4 promotes a metallic fermiology

with partial analogies to the superconducting multilayers, alongside a similar tendency toward magnetism where different orders may compete. Notably, the Ni-d_{z^2} flatband supplemented with Ni-$d_{x^2-y^2}$ states can form a strongly two-dimensional Fermi surface, which could potentially support d-wave superconducting instabilities. At the same time, $(La,Ba)_2NiO_4$ lacks the multiband features necessary for multilayer-Hubbard-model-like $s_{\pm}$-wave superconductivity, making it an interesting case-study system to isolate the fundamental ingredients behind the competition of different superconducting instabilities proposed for the multilayer nickelates (see also [Kitamine2020] for a theoretical consideration of superconductivity in La_2NiO_4).

9.7 Conclusions

We have investigated the effects of pressure and doping on the crystal and electronic structure of the reference single-layer nickelate La_2NiO_4. We have found that the suppression of oxygen-octahedral tilts, driving a structural change to a high-symmetry tetragonal $I4/mmm$ phase, occurs at similar pressures in La_2NiO_4 compared to its bilayer and trilayer superconducting counterparts. Remarkably, this structural change can also be achieved at ambient pressure through partial substitution of La with Ba. In this case, we have uncovered a distinct magnetostructural interplay that explains the deviation from Vegard's law observed experimentally. Beyond stabilizing the tetragonal structure and eventually suppressing magnetism, we have also shown that Ba doping induces subtle but consequential modifications to the electronic structure, shifting it toward a nominal $d^{7.5}$ configuration similar to the superconducting bilayer compounds, as a result of which the two-dimensional character of the Ni-d_{z^2} Fermi-surface sheet is enhanced and there appears an intriguing competition between different magnetic configurations.

Our results thus position divalent-atom substituted single-layer nickelates like $(La,Ba)_2NiO_4$ as valuable model systems, not only for probing strong magnetostructural interplays, but also for mirroring key electronic features of the superconducting Ruddlesden-Popper nickelates, while lacking the full multiband character of the bi- and trilayer compounds. Precisely because of this latter simplification, they offer a valuable platform for disentangling the respective roles of structural symmetry, dimensionality, and electronic configuration. Our findings thus clarify essential aspects of La_2NiO_4 and provide a foundation for future studies aimed at isolating the key ingredients behind superconductivity in the nickelates.

References

[Alonso1990] J.A. Alonso, J. Amador, E. Gutiérrez-Puebla, M.A. Monge, I. Rasines, C. Ruíz-Valero and J.A. Campá. *Persistence of the La2NiO4 crystal structure in $La_{2-x}Ba_xNiO_4$ samples with high Ba contents ($x \leq 1$)*. Solid State Communications, vol. 76, no. 12, pages 1327–1331, December 1990. doi:https://doi.org/10.1016/0038-1098(90)90379-P.

[Austin1989] Amy B. Austin, Louis G. Carreiro and James V. Marzik. *Structural, magnetic, and electrical properties of La2-xBaxNiO4*. Materials Research Bulletin, vol. 24, no. 5, pages 639–646, May 1989. doi:10.1016/0025-5408(89)90113-X.

[Bellaiche2000] L. Bellaiche and David Vanderbilt. *Virtual crystal approximation revisited: Application to dielectric and piezoelectric properties of perovskites*. Physical Review B, vol. 61, no. 12, pages 7877–7882, March 2000. doi:10.1103/PhysRevB.61.7877.

[Bernardini2020] F. Bernardini, V. Olevano and A. Cano. *Magnetic penetration depth and T_c in superconducting nickelates*. Physical Review Research, vol. 2, page 013219, February 2020. doi:10.1103/PhysRevResearch.2.013219.

[Bernardini2025] Fabio Bernardini, Manfred Fiebig and Andrés Cano. *Ruddlesden–Popper and perovskite phases as a material platform for altermagnetism*. Journal of Applied Physics, vol. 137, no. 10, page 103903, March 2025. doi:10.1063/5.0252836.

[Blöchl1994] Peter E. Blöchl, O. Jepsen and O. K. Andersen. *Improved tetrahedron method for Brillouin-zone integrations*. Physical Review B, vol. 49, pages 16223–16233, June 1994. doi:10.1103/PhysRevB.49.16223.

[Bull2020] Craig L. Bull, Christopher J. Ridley and Helen Y. Playford. *Using applied pressure to guide materials design: a neutron diffraction study of $La_2NiO_{4+\delta}$ and $Pr_2NiO_{4+\delta}$*. Dalton Transactions, vol. 49, pages 10631–10637, 2020. doi:10.1039/D0DT02155E.

[Christiansson2023] Viktor Christiansson, Francesco Petocchi and Philipp Werner. *Correlated Electronic Structure of $La_3Ni_2O_7$ under Pressure*. Physical Review Letters, vol. 131, no. 20, page 206501, November 2023. doi:10.1103/PhysRevLett.131.206501.

[de Vaulx2025a] J.B. de Vaulx, Q.N. Meier, P. Toulemonde, A. Cano and V. Olevano. *Pressure and strain effects on the ab initio GW electronic structure of $La_3Ni_2O_7$*. Physical Review B, vol. 112, no. 8, page 085143, August 2025. doi:10.1103/q5ymhf5k.

[de Vaulx2025b] J. B. de Vaulx, F. Bernardini, V. Olevano, Q. N. Meier and A. Cano. *Pressure and doping effects on the electronic structure and magnetism of the single-layer nickelate La_2NiO_4*. Physical Review Materials, vol. 9, no. 11, page 114804, November 2025. doi:10.1103/94sd-ssbw.

[Heier2024] Griffin Heier, Kyungwha Park and Sergey Y. Savrasov. *Competing d_{xy} and $s_{\pm}$ pairing symmetries in superconducting* $La_3Ni_2O_7$*: LDA + FLEX calculations*. Physical Review B, vol. 109, page 104508, March 2024. doi:10.1103/PhysRevB.109.104508.

[Hu2014] Ai-Yuan Hu and Huai-Yu Wang. *The exchange interaction values of perovskite-type materials $EuTiO_3$ and $EuZrO_3$*. Journal of Applied Physics, vol. 116, no. 19, page 193903, November 2014. doi:10.1063/1.4902167.

[Kitamine2020] Naoya Kitamine, Masayuki Ochi and Kazuhiko Kuroki. *Designing nickelate superconductors with d^8 configuration exploiting mixed-anion strategy*. Physical Review Research, vol. 2, page 042032, November 2020. doi:10.1103/PhysRevResearch.2.042032.

[LaBollita2024] Harrison LaBollita, Victor Pardo, Michael R. Norman and Antia S. Botana. *Electronic structure and magnetic properties of $La_3Ni_2O_7$ under pressure: active role of the Ni-$d_{x^2-y^2}$ orbitals*, March 2024. arXiv:2309.17279.

[Lechermann2023] Frank Lechermann, Jannik Gondolf, Steffen Bötzel and Ilya M. Eremin. *Electronic correlations and superconducting instability in $La_3Ni_2O_7$ under high pressure*. Physical Review B, vol. 108, page L201121, November 2023. doi:10.1103/PhysRevB.108.L201121.

[Liechtenstein1995] A. I. Liechtenstein, V. I. Anisimov and J. Zaanen. *Density-functional theory and strong interactions: Orbital ordering in Mott-Hubbard insulators*. Physical Review B, vol. 52, pages R5467–R5470, August 1995. doi:10.1103/PhysRevB.52.R5467.

[Lu2024] Chen Lu, Zhiming Pan, Fan Yang and Congjun Wu. *Interlayer-Coupling-Driven High-Temperature Superconductivity in $La_3Ni_2O_7$ under Pressure*. Physical Review Letters, vol. 132, page 146002, April 2024. doi:10.1103/PhysRevLett.132.146002.

[Nakata2017] Masahiro Nakata, Daisuke Ogura, Hidetomo Usui and Kazuhiko Kuroki. *Finite-energy spin fluctuations as a pairing glue in systems with coexisting electron and hole bands*. Physical Review B, vol. 95, page 214509, June 2017. doi:10.1103/PhysRevB.95.214509.

[Narayan2019] Awadhesh Narayan, Andrés Cano, Alexander V. Balatsky and Nicola A. Spaldin. *Multiferroic quantum criticality*. Nature Materials, vol. 18, no. 3, pages 223–228, March 2019. doi:10.1038/s41563-018-0255-6.

[Olevano2020] Valerio Olevano, Fabio Bernardini, Xavier Blase and Andrés Cano. *Ab initio many-body GW correlations in the electronic structure of $LaNiO_2$*. Physical Review B, vol. 101, page 161102, April 2020. doi:10.1103/PhysRevB.101.161102.

[Plokhikh2025] Igor Plokhikh, Thomas J. Hicken, Lukas Keller, Vladimir Pomjakushin, Samuel H. Moody, Pascale Foury-Leylekian, Jonas J. Krieger, Hubertus Luetkens, Zurab Guguchia, Rustem Khasanov and Dariusz Jakub Gawryluk. *Unraveling Spin Density Wave Order in Layered Nickelates $La_3Ni_2O_7$ and $La_2PrNi_2O_7$ via Neutron Diffraction*. March 2025. arXiv:2503.05287.

[Rodriguez-Carvajal1991] J Rodriguez-Carvajal, M T Fernandez-Diaz and J L Martínez. *Neutron diffraction study on structural and magnetic properties of La_2NiO_4*. Journal of Physics: Condensed Matter, vol. 3, no. 19, page 3215, May 1991. doi:10.1088/0953-8984/3/19/002.

[Sakakibara2024] Hirofumi Sakakibara, Naoya Kitamine, Masayuki Ochi and Kazuhiko Kuroki. *Possible High T_c Superconductivity in $La_3Ni_2O_7$ under High Pressure through Manifestation of a Nearly Half-Filled Bilayer Hubbard Model*. Physical Review Letters, vol. 132, page 106002, March 2024. doi:10.1103/PhysRevLett.132.106002.

[Schilling2008] A Schilling, R Dell'Amore, J Karpinski, Z Bukowski, M Medarde, E Pomjakushina and K A Müller. *$LaBaNiO_4$: a Fermi glass*. Journal of Physics: Condensed Matter, vol. 21, no. 1, page 015701, December 2008. doi:10.1088/0953-8984/21/1/015701.

[Wang2024] Ningning Wang, Gang Wang, Xiaoling Shen, Jun Hou, Jun Luo, Xiaoping Ma, Huaixin Yang, Lifen Shi, Jie Dou, Jie Feng, Jie Yang, Yunqing Shi, Zhian Ren, Hanming Ma, Pengtao Yang, Ziyi Liu, Yue Liu, Hua Zhang, Xiaoli Dong, Yuxin Wang, Kun Jiang, Jiangping Hu, Shoko Nagasaki, Kentaro Kitagawa, Stuart Calder, Jiaqiang Yan, Jianping Sun, Bosen Wang, Rui Zhou, Yoshiya Uwatoko and Jinguang Cheng. *Bulk high-temperature superconductivity in pressurized tetragonal $La_2PrNi_2O_7$*. Nature, vol. 634, no. 8034, pages 579–584, October 2024. doi:10.1038/s41586-024-07996-8.

[Xia2025] Chengliang Xia, Hongquan Liu, Shengjie Zhou and Hanghui Chen. *Sensitive dependence of pairing symmetry on Ni-eg crystal field splitting in the nickelate superconductor $La_3Ni_2O_7$*. Nature Communications, vol. 16, no. 1, page 1054, January 2025. doi:10.1038/s41467-025-56206-0.

[Xu2025] Han-Xiang Xu, Yue Xie, Daniel Guterding and Zhijun Wang. *Competition of superconducting pairing symmetries in $La_3Ni_2O_7$*, January 2025. arXiv:2501.05254.

[Zakharchuk2023] Kiryl Zakharchuk, Andrei Kovalevsky and Aleksey Yaremchenko. *Characterization of Ruddlesden-Popper $La_{2-x}Ba_xNiO_{4\pm\delta}$ Nickelates as Potential Electrocatalysts for Solid Oxide Cells*. Materials, vol. 16, no. 4, February 2023. doi:10.3390/ma16041755.

[Zhang2024] Yang Zhang, Ling-Fang Lin, Adriana Moreo, Thomas A. Maier and Elbio Dagotto. *Structural phase transition, s±-wave pairing, and magnetic stripe order in bilayered superconductor $La_3Ni_2O_7$ under pressure*. Nature Communications, vol. 15, no. 1, page 2470, March 2024. doi:10.1038/s41467-024-46622-z.

[Zhou2023] Yazhou Zhou, Jing Guo, Shu Cai, Hualei Sun, Pengyu Wang, Jinyu Zhao, Jinyu Han, Xintian Chen, Yongjin Chen, Qi Wu, Yang Ding, Tao Xiang, Ho kwang Mao and Liling Sun. *Evidence of filamentary superconductivity in pressurized $La_3Ni_2O_7$*. November 2023. arXiv:2311.12361.

10 Additional results and perspectives

« To be, or not to be a Fermi-liquid, that is the question. »

Again freely adapted from *Hamlet*, Shakespeare

This chapter links the different works presented in this manuscript to highlight common aspects to the compounds investigated during this PhD thesis, adding some additional results, and gives directions for future work. Sec. 10.1 treats the self-doping tendency, and Sec. 10.2 discusses the spectral weights and the Fermi liquid nature of these nickelates. Finally, Sec. 10.3 discusses the reliability of the first-order *GW* corrections in nickelates.

10.1 Self-doping tendency

10.1.1 An effect triggered by both *GW* corrections and pressure

A common feature of the square-planar and RP nickelates is the tendency for one (or several) rare-earth bands to be lowered down with both pressure and *GW* corrections, which may induce self-doping if this (these) band reaches the Fermi level. In the infinite-layers, the self-doping by both the R-5d_{xy} band at Γ and the d_{z^2} band at A is already present at ambient pressure and at the DFT level, but is further enhanced by *GW* corrections (see Fig. 7.8) and by pressure (see Fig. 7.12). In the bilayer, the self-doping by the La-5$d_{x^2-y^2}$ band at the M point needs high pressure to occur, beyond 30 GPa at the *GW* level and beyond 80 GPa at the DFT level [Verraes2025]. Often overlooked by models, this self-doping effect might have an influence on superconductivity, either positive or detrimental, but it remains so far at the speculation level (see the discussion in Sec. 8.3.1.2). In the single-layer compound, as it was mentioned in Chap. 9 but not explicitly shown, the consideration of correlations at the *GW* level results in self-doping by the La-5$d_{x^2-y^2}$ at the M point (see Fig. 10.1). This underlines a non-trivial behavior of the rare-earth bands around the k_z direction, i.e. around the Γ and M points for the bilayer and the single-layer. It is obvious from Fig. 8.3a and Fig. 10.1 that while

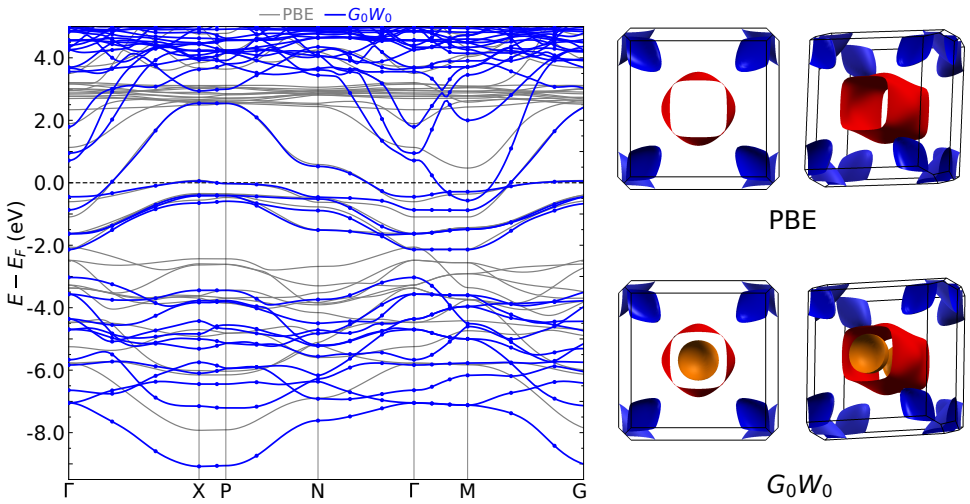

Figure 10.1: DFT (grey) and *GW* (blue) bandplots of La_2NiO_4 at 0 GPa in an enforced high-symmetry structure $I4/mmm$, with the Fermi surfaces associated. The new electron pocket is plotted in orange.

the rare-earth 5*d* manifold experiments, as the 4*f*, a substantial upper shift, around these two kpoints some of these bands are drastically lowered down at the *GW* level. In the infinite-layers, the self-doping enhancement is observed across the full Brillouin zone.

The isosurface corresponding to the La-5$d_{x^2-y^2}$ Bloch states at $\mathbf{k} = \mathrm{M}$ in the bilayer and in the single-layer are shown in Fig. 10.2. One see that these electrons are delocalized in the spacer, which explain the highly dispersive shape of the corresponding band. In the bilayer, this state is not occupied from 0 to 29.5 GPa, but becomes self-doping beyond 29.5 GPa, if one considered the *GW* calculation. On the other hand in the single-layer, this state is found occupied already at ambient pressure.

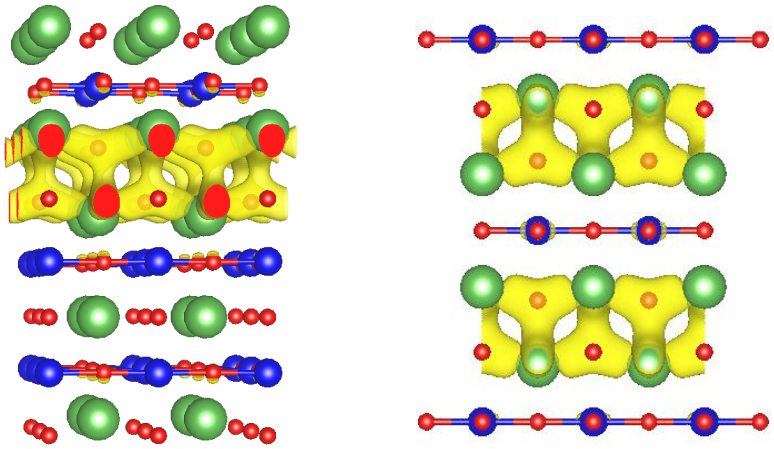

Figure 10.2: Iso-surfaces of the probability density $|\psi_{n\mathbf{k}}(\mathbf{r})|^2$ for the La-5$d_{x^2-y^2}$ Bloch states at $\mathbf{k}$=M in the bilayer (left) and in the single-layer (right).

10.1.2 Relative and absolute *GW* corrections

This renormalization of the rare-earth band is the most striking effect of the *GW* corrections on the DFT band structure, which otherwise is not so much renormalized. In the first place, we have thought to a failure of the DFT exchange-correlation potential V_{XC} which is then strongly corrected by the non-local and dynamical self-energy Σ in the subsequent *GW* calculation. But

interestingly, a careful study of the absolute corrections $\epsilon^{G_0W_0} - \epsilon^{\mathrm{KS}}$ reveals that this is not the rare-earth band which is renormalized, but rather all the Ni-3d bands which are shifted up in a relatively rigid manner. Fig. 10.3 shows this effect in the case of the bilayer and of the single-layer by plotting absolute energies instead of energies realigned on the Fermi level. One can notice that the oxygen manifold is also not too much renormalized if one consider absolute energies. This calls for further investigations on this typical many-body effect.

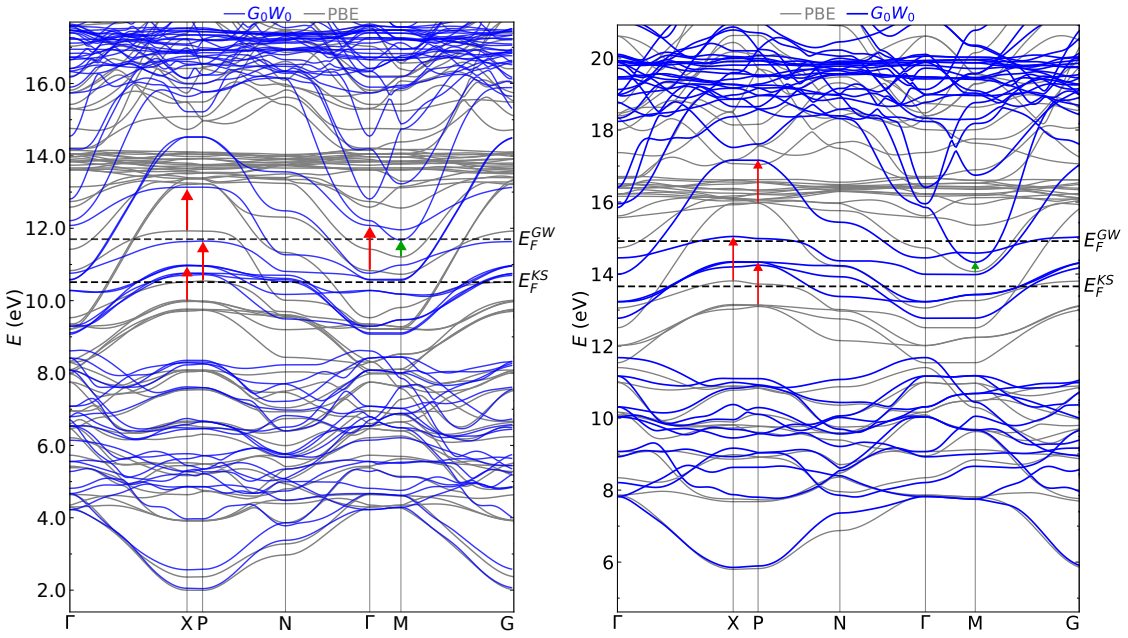

Figure 10.3: DFT (grey) and *GW* (blue) bandplots of $La_3Ni_2O_7$ at 29.5 GPa (left) and La_2NiO_4 at 0 GPa (right) showing absolute energies (i.e. without aligning the Fermi levels) in order to reveal the many-body corrections. The red arrows show the shift of the Ni-3d states of magnitude ∼1 eV, while the green arrow shows the shift of the rare-earth band at the M point, of magnitude ∼0.4 eV and ∼0.2 eV for the two compounds.

10.1.3 Sensitiveness to internal atomic positions

As already mention in Sec. 8.2.2, the electronic structure of the bilayer is extremely sensible to its crystal structure, and in particular to tiny displacements of the internal atomic positions. In our first attempt to calculate the electronic structures of the bilayer at 29.5 GPa, we used the experimental atomic positions determined by X-ray diffraction (XRD) given in the extended data table I in Sun et al. [Sun2023] (adapted to the $I4/mmm$ as in [Sakakibara2024]). The resulting DFT and *GW* Fermi surfaces show the appearance of a cylindrical Fermi sheet centered on Γ which is not observed in ARPES experiments [Yang2024]. This fake Fermi sheet originates precisely from the self-doping by the rare-earth band, as one can see in Fig. 10.4a for PBE and in Fig. 10.4b for *GW*. In this case, it has to be considered as an artifact due to a non-correct configuration of the internal atomic positions. Indeed, in XRD the accuracy on the internal atomic positions is in general lower than on the lattice parameters, especially concerning the oxygen atoms. Due to this drawback we decided to rather rely, in our work, on theoretical DFT-PBE relaxed internal atomic positions.

The DFT bandplot of the bilayer relaxed structure is shown on Fig. 10.4c and has to be compared with Fig. 10.4a corresponding to the experimental structure. In particular, we remark that the self-doping induced by the La-5$d_{x^2-y^2}$ band is absent for the relaxed structure. The Ni-e_g bands are less affected by these internal atomic positions differences, but quantitative

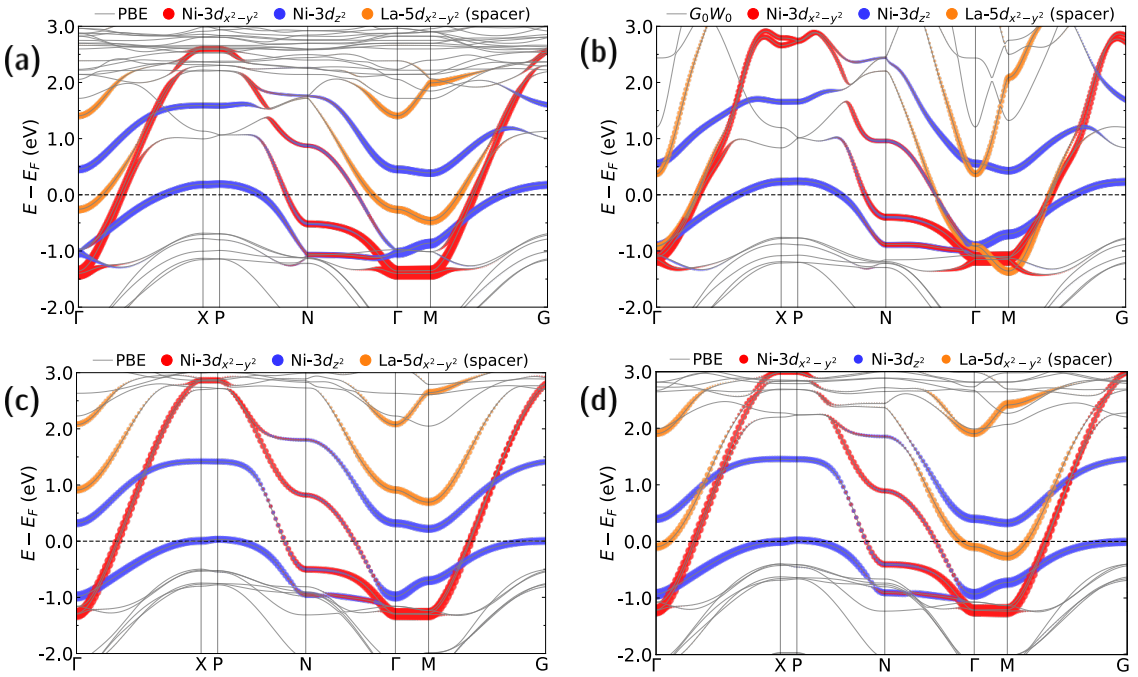

Figure 10.4: Bandplots of the bilayer $La_3Ni_2O_7$ at 29.5 GPa: **(a)** and **(b)** using experimental lattice parameters *as well as* experimental internal atomic positions from XRD [Sun2023], at the DFT (a) and *GW* level (b). **(c)** DFT bandplot calculated using experimental lattice parameters but relaxed internal atomic positions. We can really appreciate the large lowering of the La-5$d_{x^2-y^2}$ band when using XRD experimental atomic positions. The effect is further enhanced in *GW*. **(d)** DFT bandplot using relaxed internal atomic positions but with La atoms of the spacer artificially shifted away from the NiO_2 plane by an amount of 0.14 Å (right panel of Fig. 10.5), in order to reproduce the La-5$d_{x^2-y^2}$ band lowering.

discrepancies are visible, for example the size of the γ Fermi sheet. Some of these effects were already previously reported [Christiansson2023].

10.1.4 Band engineering

Since any real or fake modification of the electronic structure at the Fermi level may have important consequences for superconductivity, we tried to identify what precisely triggers the La-5$d_{x^2-y^2}$ band lowering. To this purpose we performed a "numerical experiment" of band engineering where we computed (at the DFT level only) the bandplot of a structure similar to the relaxed one, but with the La atoms in the spacer artificially shifted away from the NiO_2 plane by 0.14 Å, which corresponds to 0.7% of c (see Fig. 10.5). The associated bandplot is shown on Fig. 10.4d and reproduces well the self-doping behavior of the rare-earth band that is observed on the DFT bandplot of Fig. 10.4a.

We have also observed this effect in the single-layer, for which the same "numerical experiment" procedure via a shift of the spacer lanthanum atoms was carried out, as well as a shift of the spacer oxygen atoms in the opposite direction. The result are shown on Fig. 10.6. As one can see on the bottom panel, moving the apical oxygens of the spacer toward the NiO_2 planes changes the shape of the octahedron and the crystal field splitting. The Ni bands also look more dispersive.

What is described here is a large effect that depends on tiny shifts along the z direction of the internal atomic positions and which do not imply any symmetry breaking. Usually, atomic shifts of such tiny amplitude and without symmetry breakdown, should not affect the electronic

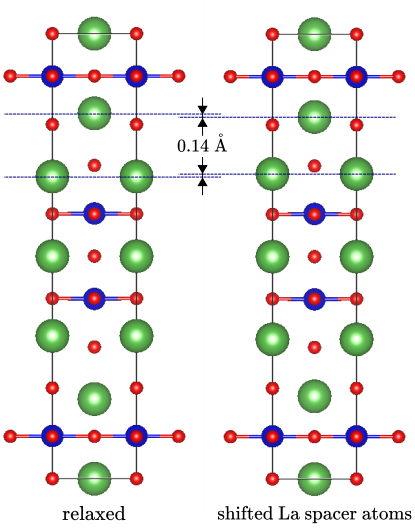

Figure 10.5: Comparison of $La_3Ni_2O_7$@29.5 GPa at the relaxed atomic positions (left) and with a 0.14 Å artificial shift of the La atoms of the spacer away from the NiO_2 planes introduced by hands (right)

.

structure with such large qualitative modifications. This is a first important indication that the electronic structure of these nickelates results from a delicate balance of many factors, already starting from internal atomic positions. Tiny atomic displacements, further enhanced by *GW* correlations, can provide self-doping and new Fermi surface pockets, bringing to a completely different Fermi level scenario. Future experiments, for example using other techniques like neutron diffraction measures, could be helpful in clarifying the internal atomic positions.

10.1.5 Sensitiveness to the tilt of the octahedra

We have seen that the application of hydrostatic pressure induces the lowering down of the rare-earth band toward the Fermi level. Interestingly, the effective internal pressure generated by an enforcement of the symmetry produces the same result, as shown in Fig. 10.7 in the case of the bilayer. The real structure of this compound at ambient pressure present tilted octhadera, but in the work presented in Chap. 8 we have preferred to work in the high-symmetry structure $I4/mmm$ where the octhadra are vertical, to better compare with the high-pressure calculation. This choice has almost no effect on the Ni bands in the Fermi level region and then do not affect the Fermi surface, but one see that the rare-earth band is strongly lowered down. The exact same effect is visible in Fig. 9.6 in the case of the single-layer La_2NiO_4, which also present a low symmetry structure with tilted octahedra and an higher symmetry one at higher pressure (see Fig. 9.1). As we know from its *GW* electronic structure shown in Fig. 10.1, this band is self-doping at ambient pressure, if one considers the enforced high-symmetry structure $I4/mmm$. Then, relaxing the structure can possibly suppress the self-doping in the single-layer at the *GW* level.

10.1.6 Electron-phonon coupling

These observations highlight the structural dependence of the self-doping, in particular to the specific phonon-mode X_3^+ corresponding to the octahedral tilting. It confirms the results of the naive "numerical experiment" described above. This is also totally consistent with the case of the infinite-layers, where the rare-earth band is the one with the highest e-ph coupling (see for

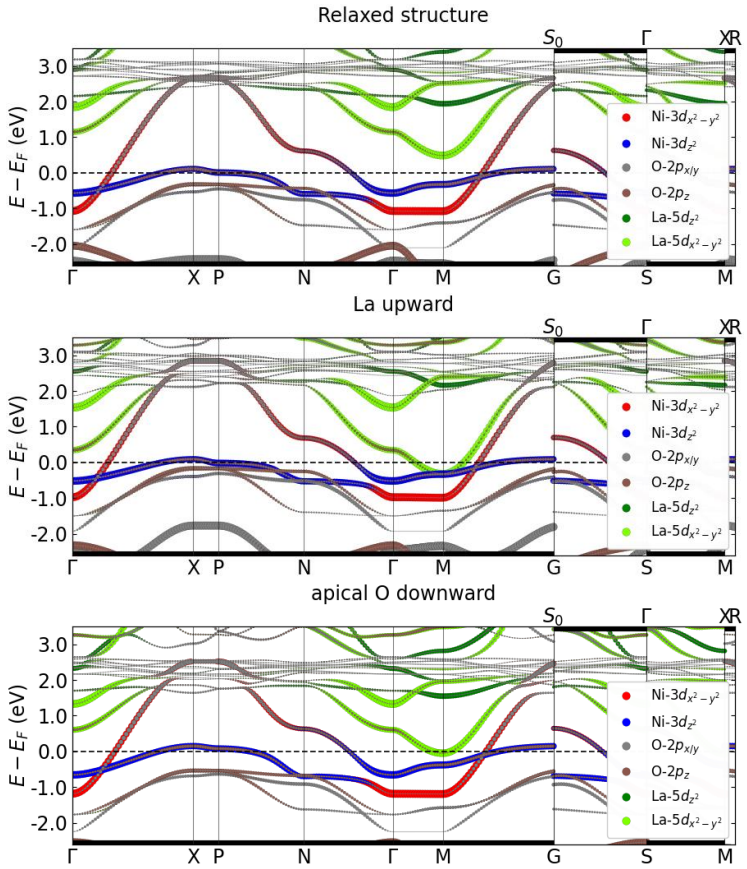

Figure 10.6: Bandplots of the single-layer La_2NiO_4 at 0 GPa: corresponding to the relaxed structure (top), with the band engineering resulting from an artificial shift of 13 Å of the lanthanum atoms *away* from the NiO_2 planes (middle), analogously to what was done in the bilayer (see Fig. 10.5) and finally with the band engineering resulting from an artificial shift of 13 Å of the oxygen atoms *toward* the NiO_2 planes (bottom). These two artificial shifts produces an analogous self-doping effect.

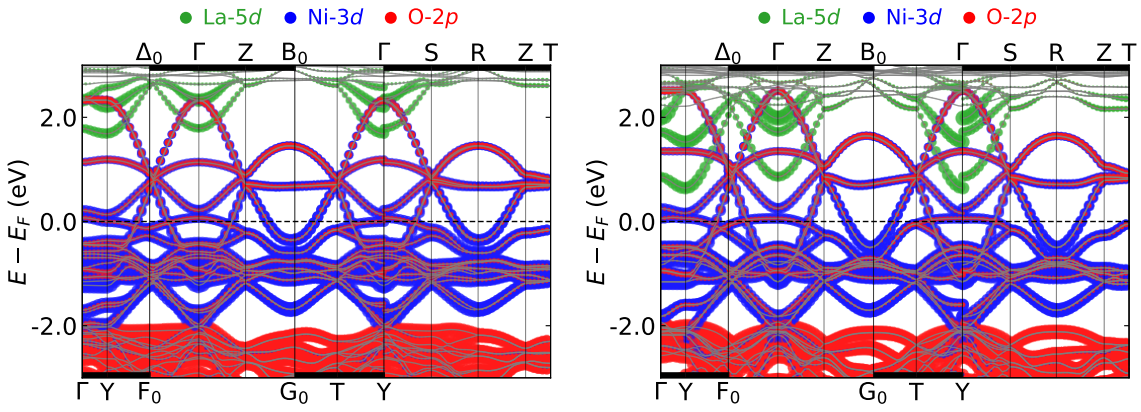

Figure 10.7: DFT bandplots with orbital characters of the bilayer $La_3Ni_2O_7$ at 0 GPa for the real low symmetry structure *Amam* (left) and for the enforced high-symmetry tetragonal structure $I4/mmm$ without the tilt of the octahedra (right). The calculations were both carried out in the unit cell corresponding to the *Amam* structure (*oS* base-centered orthorhombic). The *k*-path follows the convention given in [Hinuma2017]. In the *Amam* Brillouin zone, the Y point is equivalent to the M point of the $I4/mmmm$ Brillouin zone (see Fig. 8.2c). The lowering down of the rare-earth 5*d* band is evident at the Γ and Y points when suppressing the tilt.

example Fig. 2a of [Li2024]). The effect of the electron-phonon coupling on superconductivity have been investigated in the infinite-layers at the *GW* level (see Chap. 7). In the bilayer, DFT-based calculations did not conclude to an e-ph coupling sufficient to explain the superconducting T_c's [Ouyang2024]. A similar conclusion was given at the *GW* level [You2025]. In the latter work, *GW* was found to increase the e-ph matrix elements in comparison to DFT (like in the infinite-layers), but the reduction of the DOS by more than 50% at the *GW* level results in an overall weaker coupling constant λ. This decrease of the DOS from DFT to *GW* is confirmed by our calculations (see Fig. 8.2).

To summarize: hydrostatic pressure, octahedral tilting and *GW* corrections have the same effect on the self-doping band. These aspects worth to be further investigated.

10.2 Spectral weights behavior

In our work on the bilayer $La_3Ni_2O_7$, we have plotted the spectral weights Z with respect to the quasiparticle energies (Fig. 8.4) and have discussed about the Fermi liquid character of this compound (Sec. 8.3.1.4). The equivalent plot for the single-layer is shown in Fig. 10.8. The conclusion is the same, i.e. the minimal values are not small enough to speak about a Fermi liquid breakdown, the spectral weights ranging from ∼0.65 to 0.82 with the larger drop observed for the Ni-3*d* states, as for the bilayer.

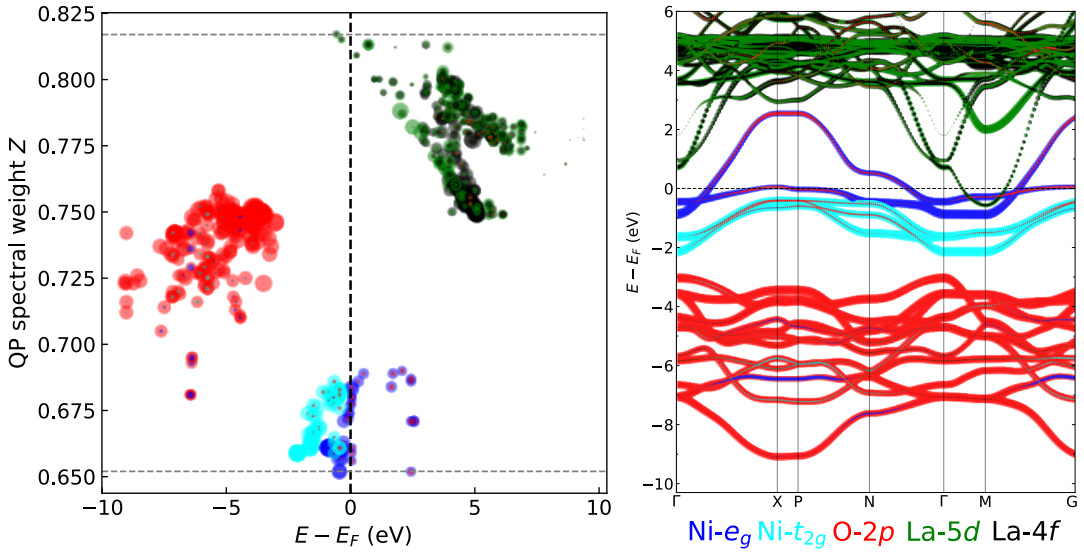

Figure 10.8: Results of the G_0W_0 electronic structure calculation for the single-layer La_2NiO_4 at 0 GPa, using the Godby-Needs plasmon-pole model. (left) Quasiparticle spectral weights Z with respect to the quasiparticle energy. (right) Associated G_0W_0 bandplot with orbital characters, defining the colors used on the left.

However, these two results were established from G_0W_0 calculations using the Godby-Needs (GN) plasmon-pole model (PPM) (see Sec. 5.5.2.1). In our investigations on the single-layer, we have tested other manners to treat the dynamical screening W, namely by using the contour deformation (CD) method and the Hybertsen-Louie (HL) PPM (see Sec. 7.4). Fig. 10.9 shows the spectrals weights for these three different treatments of the screening, in the case of $Nd_{0.8}Sr_{0.2}NiO_2$. The CD method gives the reference result, being numerically exact. The

spectral weights associated to Ni-3d states reach $Z \sim 0.5$. Beyond E_F, the spectral weights continue to increase, unlike the normal Fermi liquid decreasing trend. From a more technical point of view, one observes that the loss of spectral weight is underestimated by both plasmon-pole models, but this is spectacular for the HL PPM where the Z are almost constant. The GN PPM looks to be an intermediate result between the CD and the HL one, and seems therefore more reliable. One remarks that despite the different physics that are supposed to take place in the square-planar and in the Ruddlesden-Popper compounds, the order of magnitude of the spectral weights and the shape of their distribution is quite similar (if one compares GN PPM results). The question of the Fermi liquid nature of these material arises again, and the ability of the GW approximation and in particular one-shot G_0W_0 to capture many-body correlations needs to be further investigated.

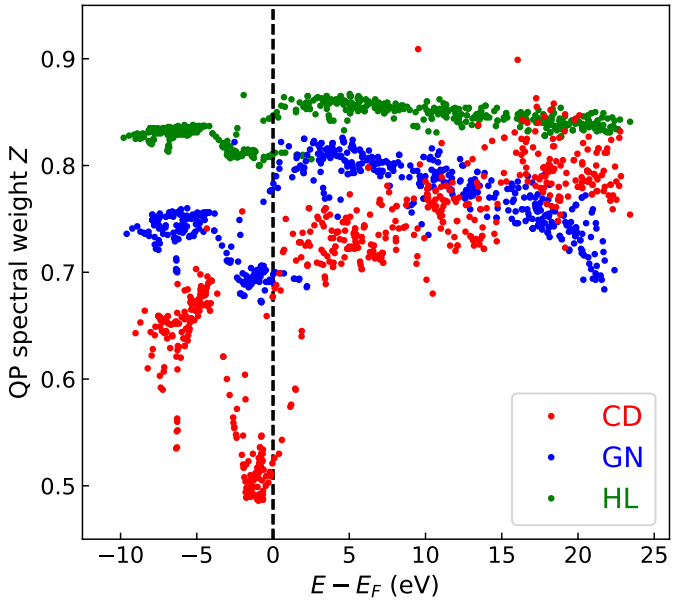

Figure 10.9: Quasiparticle spectral weights Z with respect to the quasiparticle energies for different screening treatments, as calculated in the infinite-layer $Nd_{0.8}Sr_{0.2}NiO_2$. The HL result correspond to the calculation with 1400 bands (see Sec. 7.4).

10.3 Stability of the *GW* corrections

In Sec. 7.6 we have highlighted the fact that the first order GW corrections converges toward the same results even for different starting DFT functionals. This is a really important point: one could have obtain diverging results, indicating that the GW approximation fails to capture the physics. Although we have not carried out this study for two other nickelates investigated in this manuscript, the GW corrections are often only slightly renormalizing the Kohn-Sham energies (except for the rare-earth band discussed above). It validates *a posteriori* the use of the one-shot G_0W_0 method on nickelates. To fully test this reliability, further investigations are required to explore the different aspects of the GW method, among other the effect of self-consistency and the spectral properties.

References

[Christiansson2023] Viktor Christiansson, Francesco Petocchi and Philipp Werner. *Correlated Electronic Structure of $La_3Ni_2O_7$ under Pressure*. Physical Review Letters, vol. 131, no. 20, page 206501, November 2023. doi:10.1103/PhysRevLett.131.206501.

[Hinuma2017] Yoyo Hinuma, Giovanni Pizzi, Yu Kumagai, Fumiyasu Oba and Isao Tanaka. *Band structure diagram paths based on crystallography*. Computational Materials Science, vol. 128, pages 140–184, February 2017. doi:10.1016/j.commatsci.2016.10.015.

[Li2024] Zhenglu Li and Steven G. Louie. *Two-Gap Superconductivity and the Decisive Role of Rare-Earth d Electrons in Infinite-Layer Nickelates*. Physical Review Letters, vol. 133, no. 12, page 126401, September 2024. doi:10.1103/PhysRevLett.133.126401.

[Ouyang2024] Zhenfeng Ouyang, Miao Gao and Zhong-Yi Lu. *Absence of electron-phonon coupling superconductivity in the bilayer phase of $La_3Ni_2O_7$ under pressure*. npj Quantum Materials, vol. 9, no. 1, pages 1–6, October 2024. doi:10.1038/s41535-024-00689-5.

[Sakakibara2024] Hirofumi Sakakibara, Naoya Kitamine, Masayuki Ochi and Kazuhiko Kuroki. *Possible High T_c Superconductivity in $La_3Ni_2O_7$ under High Pressure through Manifestation of a Nearly Half-Filled Bilayer Hubbard Model*. Physical Review Letters, vol. 132, no. 10, page 106002, March 2024. doi:10.1103/PhysRevLett.132.106002.

[Sun2023] Hualei Sun, Mengwu Huo, Xunwu Hu, Jingyuan Li, Zengjia Liu, Yifeng Han, Lingyun Tang, Zhongquan Mao, Pengtao Yang, Bosen Wang, Jinguang Cheng, Dao-Xin Yao, Guang-Ming Zhang and Meng Wang. *Signatures of superconductivity near 80 K in a nickelate under high pressure*. Nature, vol. 621, no. 7979, pages 493–498, September 2023. doi:10.1038/s41586-023-06408-7.

[Verraes2025] Daan Verraes, Tom Braeckevelt, Nick Bultinck and Veronique Van Speybroeck. *Evidence for strongly correlated superconductivity in $La_3Ni_2O_7$ from first principles*, February 2025. arXiv:2502.19501.

[Yang2024] Jiangang Yang, Hualei Sun, Xunwu Hu, Yuyang Xie, Taimin Miao, Hailan Luo, Hao Chen, Bo Liang, Wenpei Zhu, Gexing Qu, Cui-Qun Chen, Mengwu Huo, Yaobo Huang, Shenjin Zhang, Fengfeng Zhang, Feng Yang, Zhimin Wang, Qinjun Peng, Hanqing Mao, Guodong Liu, Zuyan Xu, Tian Qian, Dao-Xin Yao, Meng Wang, Lin Zhao and X. J. Zhou. *Orbital-dependent electron correlation in double-layer nickelate $La_3Ni_2O_7$*. Nature Communications, vol. 15, no. 1, page 4373, May 2024. doi:10.1038/s41467-024-48701-7.

[You2025] Jing-Yang You, Zien Zhu, Mauro Del Ben, Wei Chen and Zhenglu Li. *Unlikelihood of a phonon mechanism for the high-temperature superconductivity in $La_3Ni_2O_7$*. npj Computational Materials, vol. 11, no. 1, pages 1–8, January 2025. doi:10.1038/s41524-024-01483-4.

Conclusion

During this PhD work, several nickelates were studied using density functional theory and many-body perturbation theory within the *GW* approximation. As the literature on these materials has been evolving very rapidly, the choice of topics and compounds we focused on was often guided by the current developments in the field of nickelates.

I started my PhD by studying the fluorine compound La_2NiO_3F, derived from the single-layer La_2NiO_4, which initially appeared as a promising candidate for superconductivity [Bernardini2021]. Although this study was finally left aside during the thesis, it provided me experience in performing DFT and *GW* calculations. The calculations related to the single-layer compound had been performed at this occasion and were later re-visited in light of the discovery of superconductivity in the multilayer members of the Ruddlesden-Popper serie.

In the autumn of 2022, our group rapidly shifted towards the study of electron–phonon coupling in infinite-layer compounds, in response to a preprint by Li and Louie who, based on *GW* calculations, had suggested the possibility of phonon-mediated superconductivity in these nickelates [Li2022]. This work questioned their supposed unconventional character, a feature that, although only hypothesized, is at the basis of the excitement surrounding these materials, believed to host a superconductivity analogous to that of the cuprates. Moreover, inconsistencies were found between their work and the electronic structure calculated in the early *GW* work by the supervisors of this thesis [Olevano2020]. Therefore, our first step was to reproduce the electronic structure reported by Li and Louie, which allowed us to identify several technical aspects of the *GW* method that are critical for determining the electronic structure near the Fermi level. In particular, we analyzed the role of the plasmon-pole model, the convergence of the self-energy with respect to this choice, and the use of the on-shell or off-shell approximations in its evaluation. The sum of these technicalities had the effect to overestimate the density of states near E_F in the Li and Louie's work, and consequently the electron–phonon coupling. Based on these conclusions, we carried out our own study of this coupling and obtained extremely small values, incompatible with the experimentally observed critical temperatures. At this point, the discrepancy between our result and Li and Louie's result could still be due to technicalities and methodological differences. Since an experimental result had shown a monotonic enhancement of T_c with pressure, we decided to study the behavior of the electron-phonon coupling with respect to the latter. We found that the trend in the calculated T_c's was inconsistent with this experimental trend, decreasing instead of increasing with pressure. Therefore, the electron–phonon coupling does not appear to be responsible for superconductivity in infinite-layer nickelates, and is most likely preempted by another pairing mechanism, this one unconventional. To ensure the robustness of our G_0W_0 electronic structures, we investigated their variability with respect to the exchange–correlation functional used in the starting DFT calculations. We observed a consistent behavior of the G_0W_0 corrections, which seem to converge towards a common result. This suggests, in a broader perspective than the one specific to this work, that perturbation theory is well suited for studying nickelates, accordingly to the intuition that originally motivated this PhD.

The discovery of superconductivity in the bilayer compound at the beginning of 2023, at a much higher temperature than in the infinite-layer compounds, naturally led us to investigate it,

starting from summer 2024. Numerous theoretical works based on models fitted on DFT band-structures were emerging in the literature, speculating in particular about the symmetry of the superconducting gap in this compound. It therefore appeared important to clarify its electronic structure, especially since only one *GW*-level study had addressed it at that time [Christiansson2023]. We studied this compound as a function of pressure and epitaxial strain – two experimental parameters affecting superconductivity – and compared our results with the first ARPES measurements that were starting to appear. The main conclusion of this work is that the *GW* approximation yields an electronic structure consistent with the experimental Fermi surface, in particular with the absence of the Ni-d_{z^2} band at the Fermi level, which was present at the DFT level. Compared to DFT, we also observed a characteristic lowering of a 5*d* band associated with the rare-earth element, an effect that increases with pressure and can even lead to self-doping. This phenomenon is not specific to the bilayer and is also found in the infinite-layer and single-layer compounds. Interestingly, this band is extremely sensitive to the position of the rare-earth atom, which should result in a strong electron–phonon coupling, as it was observed in the infinite-layer compound. This effect has not yet been explained, and although certain coincidences have been noticed between its pressure dependence and that of superconductivity, its possible connection with the latter remains unclear.

At the occasion of this work on the bilayer compound, we also investigated the G_0W_0 spectral weights and observed a significant reduction for the Ni 3*d* states near E_F, indicating a noticeable deviation from standard Fermi-liquid behavior. We later found that this reduction of spectral weight is a common feature among the three nickelates studied in this thesis. For the infinite-layer compound, for which we had a calculation performed with the numerically exact contour-deformation method, we observed an even stronger decrease of spectral weights, suggesting that they may be overestimated when a plasmon-pole model is used. This intriguing effect, which we discovered recently, deserves further investigation and could provide important insights into the Fermi-liquid character of these nickelates, as well as the ability of the G_0W_0 approach to accurately describe it.

As mentioned earlier, we had already considered the single-layer compound at the beginning of the thesis. Since most of the current literature focuses on the infinite, bi, and trilayer compounds, all of them being superconducting, studying the single-layer system represented a step aside. However, as superconductivity has not been observed in this compound so far, it might help to disentangle which features are responsible for superconductivity and which are not. Moreover, the existence of polymorphs consisting of alternating single-trilayer or single-bilayer has been frequently discussed in the literature, and further motivates the study of this member of the serie. We first focused on the structural transition from the low-symmetry *Bmab* phase to the high-symmetry $I4/mmm$ phase, the latter appearing necessary for superconductivity to emerge in the multilayer compounds. We showed that barium doping stabilizes this high-symmetry phase in a similar way than pressure, and could therefore provide an alternative route to achieve it. We also found that barium inclusion, besides making the electronic configuration of the system more similar to that of the bilayer, makes its Fermi surface more two-dimensional. The parent compound being a magnetic insulator (unlike the multilayer members, which are paramagnetic metals), spin-polarized DFT+U calculations were required to open a gap and reproduce this behavior, predicting an antiferromagnetic order in the parent phase. However, the insulating character does not survive under pressure or Ba doping, the system recovering a metallic behavior. We recently realized that structural relaxations performed with spin-polarized DFT, while not changing the previous conclusions on the equivalence between pressure and Ba doping, enables us to reproduce the non-trivial behavior of the lattice parameters of this compound, highlighting the importance of magnetism in this compound.

In conclusion, a wide range of aspects of nickelate physics have been explored during this PhD thesis, making it a snapshot of our current understanding about these materials, an understanding that will surely continue to evolve (most likely rapidly!) in the coming years. In addition, several technical aspects of the *GW* method were investigated, and their influence on physical predictions highlighted, which certainly open interesting directions for future research.

References

[Bernardini2021] F. Bernardini, A. Demourgues and A. Cano. *Single-layer T'-type nickelates: Ni^{1+} is Ni^{1+}*. Physical Review Materials, vol. 5, no. 6, page L061801, June 2021. doi:10.1103/PhysRevMaterials.5.L061801.

[Christiansson2023] Viktor Christiansson, Francesco Petocchi and Philipp Werner. *Correlated Electronic Structure of $La_3Ni_2O_7$ under Pressure*. Physical Review Letters, vol. 131, no. 20, page 206501, November 2023. doi:10.1103/PhysRevLett.131.206501.

[Li2022] Zhenglu Li and Steven G. Louie. *Two-gap superconductivity and decisive role of rare-earth d electrons in infinite-layer nickelates*, October 2022. arXiv:2210.12819.

[Olevano2020] Valerio Olevano, Fabio Bernardini, Xavier Blase and Andrés Cano. *Ab initio many-body GW correlations in the electronic structure of $LaNiO_2$*. Physical Review B, vol. 101, no. 16, page 161102, April 2020. doi:10.1103/PhysRevB.101.161102.

Conclusion (en français)

Durant cette thèse, plusieurs nickélates ont été étudiés au moyen de la théorie de la fonctionnelle de la densité et de la théorie des perturbations à N-corps dans l'approximation GW. La littérature sur ces matériaux évoluant très rapidement, le choix des sujets et des composés sur lesquels nous avons travaillé a souvent été fait par rapport à l'actualité des nickélates.

J'ai commencé ma thèse par étudier le composé fluoré La_2NiO_3F dérivé du monocouche La_2NiO_4, qui semblait prometteur pour la supraconductivité [Bernardini2021]. Cette étude n'a pas abouti, mais m'a en tout cas permis de me faire la main sur les calculs DFT et GW. Les calculs associés au monocouche avaient en tout cas déjà été effectués et ont été analysés plus tard, à l'aune de la découverte de la supraconductivité dans les membres multicouches de la série de Ruddlesden-Popper.

A l'automne 2022, notre groupe a rapidement bifurqué sur l'étude du couplage électron-phonon dans les composés à infinité de couche, en réaction à une prépublication de Li et Louie qui, s'appuyant sur des calculs GW, avaient suggéré la possibilité d'une supraconductivité médiée par les phonons dans ces nickélates [Li2022]. Ce travail remettait en cause leur caractère non-conventionnel, caractère certes supposé mais qui est tout de même à la base de l'engouement autour de ces matériaux, supposés héberger une supraconductivité analogue à celle des cuprates. De plus, des incohérences ont été relevées entre leur travail et la structure électronique GW calculée dans un travail antérieur par les encadrants de cette thèse [Olevano2020]. Notre première tâche a donc été de tenter de reproduire la structure électronique publiée par Li et Louie, et nous a permis d'identifier certains aspects techniques liés à la méthode GW qui sont critiques dans la détermination de la structure électronique proche du niveau de Fermi, à savoir le choix du modèle de plasmon, la convergence de la self-énergie en fonction de ce choix, et l'utilisation des approximations on-shell ou off-shell pour l'évaluation de celle-ci. Ces détails techniques cumulés avaient pour effet de surestimer la densité d'état proche de E_F dans le travail de Li et Louie, et donc le couplage électron-phonon. Suite à ces conclusions, nous nous sommes lancés dans notre propre étude de ce couplage, et avons obtenu des valeurs extrêmement faibles non compatibles avec les températures critiques observées expérimentalement. A ce moment-là, les différences entre nos résultats et ceux de Li et Louie pouvaient toujours être dues à des différences techniques ou méthodologiques. Etant donné qu'un travail expérimental avait montré une augmentation monotone de la T_c avec la pression, nous avons décidé d'étudier le comportement du couplage électron-phonon en fonction de celle-ci. Nous avons montré que l'évolution des T_c calculées allait à l'encontre de la tendance expérimentale observée. Le couplage électron-phonon ne semble donc pas responsable de la supraconductivité dans les nickélates à infinité de couche, et est donc selon toute vraisemblance devancé par un autre mécanisme de couplage, non-conventionnel celui-là. Afin d'attester la robustesse de nos structures électroniques G_0W_0, nous avons étudié la variabilité de celles-ci en fonction de la fonctionnelle d'échange-corrélation utilisée dans le calcul DFT initial. Nous avons observé un comportement cohérent des corrections G_0W_0, qui semblent converger vers un même résultat. Cela montre, dans une perspective plus large que celle spécifique à ce travail, que la théorie des perturbations semble bien adaptée à l'étude des nickélates, donnant du crédit à l'intuition qui avait motivé de cette thèse.

La découverte de la supraconductivité dans le composé bicouche début 2023 à une température bien plus élevée que dans les composés à infinité de couches nous a évidemment poussé à nous y intéresser, à partir de l'été 2024. Beaucoup de travaux théoriques basés sur des modèles ajustés sur des structures électroniques DFT commençaient à fleurir dans la littérature, spéculant en particulier sur la symétrie du gap supraconducteur de ce composé. Il nous est alors paru important de clarifier sa structure électronique, sachant qu'un seul travail s'y était jusqu'alors intéressé au niveau *GW* [Christiansson2023]. Nous l'avons étudié en fonction de la pression ainsi que de la contrainte épitaxiale, deux variables expérimentales affectant la supraconductivité, et avons également pu la comparer avec les premières mesures ARPES qui commençaient à être publiées. La conclusion principale de ce travail est que l'approximation *GW* donne une structure électronique en accord avec la surface de Fermi expérimentale, avec notamment l'absence de la bande Ni-d_{z^2} au niveau de Fermi, qui était présente au niveau DFT. Toujours par rapport à la DFT, nous avons également relevé un abaissement caractéristique d'une bande 5*d* associée à la terre rare, cet effet augmentant avec la pression et pouvant aller jusqu'à l'auto-dopage. Il se trouve que cet effet n'est pas spécifique au bicouche et se retrouve dans le composé à infinité de couches ainsi que dans le composé monocouche. Fait intéressant, cette bande est extrêmement sensible à la position de l'atome de terre-rare associé, ce qui devrait se traduire par un fort couplage électron-phonon, d'ailleurs remarqué dans le cas du composé à infinité de couches. Cet effet n'a pas pu être expliqué, et bien que certaines coïncidences dans son comportement en pression et celui de la supraconductivité aient été remarqués, son lien avec cette dernière, si tant est qu'il existe, n'est pas clair.

A l'occasion de ce travail sur le bicouche, nous nous sommes intéressés aux poids spectraux calculés en G_0W_0, et avons constaté une baisse relativement importante pour les états 3*d* du nickel proche de E_F, ce qui constitue une déviation notable du caractère liquide de Fermi. Nous avons ensuite constaté que ce comportement des poids spectraux était commun aux deux autres nickélates étudiés pendant cette thèse. Disposant dans le cas du composé à infinité de couche d'un calcul effectué avec la méthode numériquement exacte de déformation de contour, nous avons remarqué que celle-ci avait tendance à abaisser davantage les poids spectraux, qui semblent donc surestimés lorsqu'un modèle de plasmon est utilisé. Cet effet intrigant, que nous avons découvert récemment, mérite d'être étudié plus en profondeur et pourrait apporter d'importantes indications sur le caractère liquide de Fermi de ces nickélates, ainsi que sur la capacité de l'approche G_0W_0 d'en décrire correctement le comportement.

Comme mentionné plus haut, nous avions déjà abordé le composé monocouche au début de la thèse. La majorité de la littérature se concentrant actuellement sur les composés à infinité de couche, bicouche et tricouche, tous supraconducteurs, étudier le monocouche représentait un pas de côté. Mais celui-ci, dans lequel la supraconductivité n'a jusque-là pas été observée, pourrait justement permettre de démêler les éléments responsables à la supraconductivité de ceux qui ne le sont pas. De plus, l'existence de composés polymorphes constitués d'une alternance de monocouche-tricouche ou de monocouche-bicouche est fréquemment évoquée dans la littérature, ce qui renforce l'intérêt d'étudier ce membre de la série. Nous sous sommes tout d'abord intéressé à la transition structurale de la phase de basse symétrie *Bmab* vers la phase de haute symétrie $I4/mmm$, cette dernière semblant nécessaire à l'émergence de la supraconductivité dans les composés multicouches. Nous avons montré qu'un dopage au baryum avait pour effet de stabiliser cette phase de la même manière que la pression, et pouvait donc être une solution pour s'affranchir de cette dernière. Nous avons aussi montré que l'inclusion du baryum, en plus faire tendre la configuration électronique du système vers celle du bicouche, avait pour effet de rendre sa surface de Fermi plus bidimensionnelle. Le composé parent étant un isolant magnétique, à l'inverse des membres multicouches de la série qui sont des métaux paramagnétiques, des calculs DFT+U polarisés en spin ont permis d'ouvrir un gap afin de reproduire ce

comportement, prédisant un ordre antiferromagnétique dans la phase parent. Toutefois, le caractère isolant ne survit pas à l'application de la pression ou à l'inclusion de baryum, le système étant ramené à un comportement métallique. Nous nous sommes rendu compte récemment que des relaxations structurales effectuées au moyen de calculs DFT polarisés en spin permettaient, sans remettre en cause les résultats précédemment évoqués sur l'équivalence entre pression et dopage au baryum, de reproduire le comportement non trivial des paramètres de maille de ce composé, soulignant l'importance de la prise en compte du magnétisme pour aborder ce composé.

En conclusion, des aspects très divers de la physique des nickélates ont été abordées durant cette thèse, qui est représentative de l'état de nos connaissances et de notre compréhension de ces matériaux à l'instant t, compréhension qui sera sûrement amenée à évoluer (très rapidement !) dans les prochaines années. D'autre part, des aspects techniques de la méthode *GW* ont été étudiés et leurs influences sur les prédictions physiques remarquées, ce qui constitue très certainement des directions intéressantes à explorer dans de futurs travaux.

List of publications

Three articles based on the work realized during this PhD thesis have been published. The first one addresses the electron-phonon coupling in the infinite-layer nickelates [Meier2024], the second addresses the bilayer electronic structure and its pressure dependence [de Vaulx2025a] and the last one addresses the single-layer nickelate with its pressure and doping dependence [de Vaulx2025b]. They correspond to chapters 7, 8 and 9, respectively.

[Meier2024] Q. N. Meier, J. B. de Vaulx, F. Bernardini, A. S. Botana, X. Blase, V. Olevano and A. Cano. *Preempted phonon-mediated superconductivity in the infinite-layer nickelates*. Physical Review B, vol. 109, no. 18, page 184505, May 2024. doi:10.1103/PhysRevB.109.184505.

[de Vaulx2025a] J.B. de Vaulx, Q.N. Meier, P. Toulemonde, A. Cano and V. Olevano. *Pressure and strain effects on the ab initio GW electronic structure of $La_3Ni_2O_7$*. Physical Review B, vol. 112, no. 8, page 085143, August 2025. doi:10.1103/q5ym-hf5k.

[de Vaulx2025b] J. B. de Vaulx, F. Bernardini, V. Olevano, Q. N. Meier and A. Cano. *Pressure and doping effects on the electronic structure and magnetism of the single-layer nickelate La_2NiO_4*. Physical Review Materials, vol. 9, no. 11, page 114804, November 2025. doi:10.1103/94sd-ssbw.

List of symbols

In the all manuscript, atomic units ($\hbar = m_e = e^2/4\pi\epsilon_0 = 1$) are used, i.e. lengths are in bohr and energies in hartree.

Symbol	Description
n	number of consecutive nickel oxide layers in Ruddlesden-Popper or square-planar nickelates
$\mathbf{r}$	Position in 3D real space
t	Time
σ	Spin variable
$q = \mathbf{r}\sigma$	Short-notation for space-spin variables
$1 = (\mathbf{r}_1, t_1, \sigma_1)$	Short notation for space, time, and spin variables
ω	Angular frequency (often referred to as frequency or energy)
$\mathbf{k}$	Wavevector in 3D reciprocal space. In infinite periodic systems, refers to the crystal momentum within the first Brillouin zone (FBZ)
$\mathbf{q}$	Wavevector difference in 3D reciprocal space (used for the dielectric function and for phonons)
$\mathbf{G}$	Reciprocal lattice vector
N	Number of electrons in the system (in the unit cell for a crystal). When starred (N^*) it refers to the effective number of electrons taken into account by the pseudopotentials used.
n, m	Subscripts for electrons, ranging from 1 to N
Ψ, $\lvert\Psi\rangle$, $\lvert N\rangle$	Many-body wavefunction of N electrons and its associated state
i, j	Subscripts for many-body eigenstates
ϕ	Spin-orbital
ψ	Spacial part of a single-particle wavefunction. May describes quasi-particles.
χ	Spin part of a single-particle wavefunction
ℓ, m	Subscripts for generic single-particle eigenstates
$\psi_{n\mathbf{k}}$	Bloch state with band index n and crystal momentum $\mathbf{k}$
$n(\mathbf{r})$	Electronic density
$\hat{H}$	Many-body hamiltonian
$\hat{h}$	Single-particle hamiltonian
E	Total energy of the electronic system (i.e. eigenenergy of the many-body hamiltonian). In the DFT context, refers only to the ground-state.
ϵ	Single-particle eigenenergy

E_F	Fermi energy (chemical potential μ at $T=0$)
v	Bare Coulomb potential
W	Dynamically screened Coulomb potential
V_{ext}	External potential
V_{H}	Hartree potential
$\hat{V}_{\text{X}}$	Fock exchange operator
V_{XC}	Exchange-correlation potential of Kohn-Sham DFT
Σ	Generic self-energy
$\hat{\psi}^\dagger(\mathbf{r})$, $\hat{\psi}(\mathbf{r})$	electronic creation and annihilation field operators
$\hat{c}_\ell^\dagger$, $\hat{c}_\ell$	electronic creation and annihilation operators for state ℓ
G	Green's function (time-ordered if not specified)
η	Infinitesimal quantity (used in particular in the denominator of the Green's function)
$f_i(\mathbf{r})$	Lehmann amplitude
Z	Quasiparticle spectral weight
A	Spectral function
P	Irreducible polarizability
ε	Dielectric function
$V_{\mathbf{k}\mathbf{k}'}$, V	Matrix elements of the BCS effective interaction and its magnitude in the isotropic approximation.
N_F	Density of states at the Fermi level
λ	Electron-phonon coupling constant
T_c	Critical temperature of the superconducting transition
Δ	Superconducting gap

List of abbreviations

Abbreviation	Description
AFM	Antiferromagnetic
ARPES	Angle-resolved photoemission spectroscopy
BL	Bilayer
CD	Contour deformation
DFT	Density functional theory
DOS	Density of states
e-ph	electron-phonon
FBZ or BZ	First Brillouin zone
FL	Fermi liquid
FM	Ferromagnetic
GGA	Generalized gradient approximation
GN	Godby-Needs
GS	Ground-state
HEG	Homogeneous electron gas
HF	Hartree-Fock
HK	Hohenberg-Kohn
HL	Hybertsen-Louie
HSE	Heyd, Scuseria, Ernzerhof (functional)
IL	Infinite-layer
KS	Kohn-Sham
LDA	Local density approximation
MBPT	Many-body perturbation theory
MBSE	Many-body Schrödinger equation
MF	Mean-field
MLWF	Maximally-localized Wannier functions
PBE	Perdew, Burke, Ernzerhof (functional)
PDOS	Partial (or projected) density of states
PL	Pentalayer
PPM	Plasmon-pole model
PWF	Projected Wannier functions
QP	Quasiparticle
RPA	Random-phase approximation

RP	Ruddlesden-Popper
SCF	Self-consistent field
SL	Single-layer
SP	Square-planar
TL	Trilayer
XC	Exchange-correlation



Personal version of the Feynman diagram associated to the *GW* self-energy (credit: Bilal Kousar).